

**DETERMINATION OF THE TRIBOLOGICAL  
FUNDAMENTALS OF SOLID LUBRICATED CERAMICS  
PART III: MOLECULAR ENGINEERING OF  
RUTILE ( $\text{TiO}_{2-x}$ ) AS A LUBRICIOUS OXIDE**

M. N. Gardos  
Hughes Aircraft Company  
El Segundo, Ca 90245

October 1994

Final Report for Period 01 August 1990 - 31 July 1993.

Approved for public release; distribution is unlimited.

DTIC QUALITY INSURED 8

**MATERIALS DIRECTORATE  
WRIGHT LABORATORY  
AIR FORCE MATERIEL COMMAND  
WRIGHT-PATTERSON AIR FORCE BASE, OH 45433-7734**

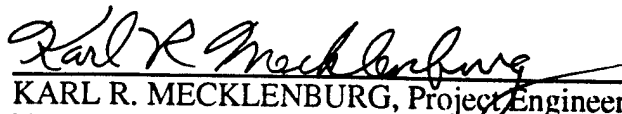
19950620 121


## NOTICE

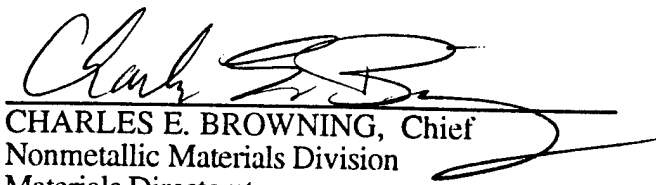
When Government drawings, specifications, or other data are used for any purpose other than in connection with a definitely Government-related procurement, the United States Government incurs no responsibility or any obligation whatsoever. The fact that the government may have formulated or in any way supplied the said drawings, specifications, or other data, is not to be regarded by implication, or otherwise in any manner construed, as licensing the holder, or any other person or corporation; or as conveying any rights or permission to manufacture, use, or sell any patented invention that may in any way be related thereto.

This report is releasable to the National Technical Information Service (NTIS). At NTIS, it will be available to the general public, including foreign nations.

This technical report has been reviewed and is approved for publication.

  
KARL R. MECKLENBURG, Project Engineer  
Nonstructural Materials Branch  
Nonmetallic Materials Division

  
KENT J. EISENTRAUT, Chief  
Nonstructural Materials Branch  
Nonmetallic Materials Division

  
CHARLES E. BROWNING, Chief  
Nonmetallic Materials Division  
Materials Directorate

If your address has changed, if you wish to be removed from our mailing list, or if the addressee is no longer employed by your organization please notify WL/MLBT, WPAFB, OH 45433-7750 to help us maintain a current mailing list.

Copies of this report should not be returned unless return is required by security considerations, contractual obligations, or notice on a specific document.

REPORT DOCUMENTATION PAGE			Form Approved OMB No. 0704-0188	
<small>Public reporting burden for this collection of information is estimated to average 1 hour per response, including the time for reviewing instructions, searching existing data sources, gathering and maintaining the data needed, and completing and reviewing the collection of information. Send comments regarding this burden estimate or any other aspect of this collection of information, including suggestions for reducing this burden, to Washington Headquarters Services, Directorate for Information Operations and Reports, 1215 Jefferson Davis Highway, Suite 1204, Arlington, VA 22202-4302, and to the Office of Management and Budget, Paperwork Reduction Project (0704-0188), Washington, DC 20503.</small>				
1. AGENCY USE ONLY (Leave blank)		2. REPORT DATE Oct. 1994	3. REPORT TYPE AND DATES COVERED Final 08/01/90 - 07/01/93	
4. TITLE AND SUBTITLE Determination of the Tribological Fundamentals of Solid Lubricated Ceramics, Part III: Molecular Engineering of Rutile ( $\text{TiO}_{2-x}$ ) As a Lubricious Oxide			5. FUNDING NUMBERS C: F33615-85-C-5087 PE: 61101 PR: 5177 TA: 00 WU: 01	
6. AUTHOR(S)  M.N. Gardos				
7. PERFORMING ORGANIZATION NAME(S) AND ADDRESS(ES) Hughes Aircraft Company Aerospace and Defense Sector Electro-Optical Systems P.O. Box 902, El Segundo, CA 90245			8. PERFORMING ORGANIZATION REPORT NUMBER	
9. SPONSORING / MONITORING AGENCY NAME(S) AND ADDRESS(ES) Materials Directorate (WL/MLBT) Wright Laboratory Air Force Materiel Command Wright-Patterson Air Force Base, Ohio 45433-7734			10. SPONSORING / MONITORING AGENCY REPORT NUMBER  WL-TR-94-4108	
11. SUPPLEMENTARY NOTES				
12a. DISTRIBUTION / AVAILABILITY STATEMENT  Approved for public release; distribution is unlimited.			12b. DISTRIBUTION CODE	
13. ABSTRACT (Maximum 200 words) <p>A study was conducted to (a) confirm a Hughes hypothesis correlating the oxygen stoichiometry of rutile Magnèli phases (<math>\text{Ti}_n\text{O}_{2n-1}</math>) with their tribological behavior, and (b) show feasibility of controlling the stoichiometry (and thus the tribological performance) by doping specifically with <math>\text{Cu}^{2+}/\text{Cu}^{1+}</math> and other selected cations. Variable temperature (from R.T. to 1000°C) SEM tribometry completed on fully stoichiometric, single-crystal and polycrystalline rutile samples and other polycrystalline specimens reduced into narrow stoichiometric ranges confirmed that the shear strength and the resultant friction are highly dependent on oxygen-content-controlled development of various crystallographic shear planes (the <math>\text{Ti}_n\text{O}_{2n-1}</math> Magnèli phases). However, the high sensitivity of these phases to structural changes induced by the variation of the sample temperature and the partial pressures of oxygen around the sample render the rutile polymorph of <math>\text{TiO}_{2.00}</math> a tribooxidatively unstable material. Polycrystalline rutile was subsequently doped with cations predicted to stabilize or fail to stabilize stoichiometry. X-ray diffraction combined with four-point electrical conductivity measurements of model rutile compositions doped with CuO indicated the predicted feasibility of generating chemically induced crystallographic shear planes through the creation of a Ti-Cu bronze equivalent in behavior to a <math>\text{TiO}_{1.89}</math> Magnèli phase. SEM tribometry, combined with other high temperature tribotests performed with an engineering-type friction and wear bench tester, demonstrated the enhanced tribooxidative stability of the copper-doped, <math>\text{TiO}_{1.89}</math>-like doped lubricious oxide prototype. The data indicate the feasibility of molecularly engineering rutile, and possibly other selected oxides capable of Magnèli phase formation, as oxidatively stable tribomaterials useful for wide environmental range applications.</p>				
14. SUBJECT TERMS Solid lubricants, lubricious rutile, $\text{TiO}_2$ , high temperature, oxygen stoichiometry, Magnèli phases, crystallographic shear planes, characteristic shear strength, oxidation resistance, stoichiometry stabilization, cation doping, molecular engineering.			15. NUMBER OF PAGES 194	
			16. PRICE CODE	
17. SECURITY CLASSIFICATION OF REPORT Unclassified	18. SECURITY CLASSIFICATION OF THIS PAGE Unclassified	19. SECURITY CLASSIFICATION OF ABSTRACT Unclassified	20. LIMITATION OF ABSTRACT UL	

## FOREWORD

The objective of this 39-month, PART III add-on to the "Determination of the Tribological Fundamentals of Solid Lubricated Ceramics" program (Contract No. F33615-85-C-5087, Parts I and II) was to provide the knowledge base needed for the development of lubricious titanium dioxide compounds for high temperature (~ 850°C) moving mechanical assemblies operating in various atmospheric environments. The title of the Part III program is "Molecular Engineering of Rutile (TiO<sub>2-x</sub>) as a Lubricious Oxide", with a start date of 01 August 1990. This report covers the work accomplished between that date and 31 July 1993.

Under this Part III effort, based on the initial findings of the Part I program segment, an attempt was made to formulate rutile into a controlled shear strength bearing material by doping. The main objective was to demonstrate the possibility of producing at least a prototype of an environmentally stable, lubricative oxide.

The work was performed by selected members of the same Hughes team of tribologists who have been involved with the Part I and Part II program sequences, as assisted by in-house and subcontractor experts. The overall effort was spearheaded by Dr. Michael N. Gardos serving as the Principal Investigator of all three parts of the "Tribological Fundamentals" program. Ms. Bonnie L. Soriano, Messrs. Patrick S. Davis, Bruce W. Buller, Gerald R. Meldrum and Dr. Daniel A. Demeo were responsible for the tribological and chemical characterization of the model compounds. Key subcontractor representatives were Dr. Andre Ezis of CERCOM Inc. (Vista, CA), Dr. Robert L. Clarke of ICI/Ebonex and Dextra Associates (Orinda, CA) working in concert with Dr. Vaughan White of The New Zealand Institute for Industrial Research and Development (Lower Hutt, New Zealand), and Dr. Kevin Kendall of ICI (now with the U. of Keele, Keele, England). Mr. Earl B. Holst and Dr. Gardos served as Program Managers, supported by Ms. Patricia Schmidt as the Hughes Contract Administrator.

Key government personnel monitoring all parts of the "Tribological Fundamentals" program were Messrs. Bobby D. McConnell and Karl R. Mecklenburg of WL/MLBT (Wright-Patterson AFB, OH) acting as the US Air Force Project Engineers.

Accession For	
NTIS	CRA&I <input checked="checked" type="checkbox"/>
DTIC	TAB <input type="checkbox"/>
Unannounced	<input type="checkbox"/>
Justification .....	
By .....	
Distribution /	
Availability Codes	
Dist	Avail and/or Special
A-1	



## CONTENTS

	<u>Page</u>
1.0 EXECUTIVE SUMMARY .....	1
2.0 INTRODUCTION .....	5
3.0 OXYGEN CONTENT-DRIVEN TRIBOLOGICAL BEHAVIOR OF RUTILE ....	6
3.1 Magnèli Phase-Controlled Friction of Rutile .....	6
3.2 Control of Magnèli Phases by Pre-reduction and Variable Temperature SEM Tribometry.....	10
3.2.1 Test Equipment and Methodology .....	10
3.2.2 SEM Tribometry of Single Crystal Rutile vs. Polycrystalline $\alpha$ -SiC .....	17
3.2.3 SEM Tribometry of Polycrystalline Rutile vs. Polycrystalline $\alpha$ -SiC .....	26
3.2.4 SEM Tribometry of Polycrystalline Rutile vs. Polycrystalline Rutile .....	33
4.0 MOLECULAR ENGINEERING OF POLYCRYSTALLINE RUTILE .....	48
4.1 Control of Magnèli Phases by Doping with Aliovalent Cations .....	48
4.2 A Simple Preparation Method for Cation Doped Rutile .....	53
4.2.1 Doping with CuO .....	54
4.2.2 Doping with Fe <sub>2</sub> O <sub>3</sub> , CoO and NiO.....	65
4.3 Variable Temperature SEM Tribometry of CuO-doped Rutile .....	66
4.3.1 Friction Behavior in Vacuum .....	67
4.3.2 Friction Behavior in Partial Pressures of Oxygen .....	71
4.3.3 Wear Behavior in Vacuum and Partial Pressures of Oxygen .....	83
4.4 Tester 2A Tribometry of Undoped and CuO-doped Rutile .....	108
5.0 CONCLUSIONS AND RECOMMENDED FUTURE WORK .....	125
6.0 REFERENCES .....	127
7.0 APPENDICES	
APPENDIX A - "Summary of Lubricious Oxide Development, Job# 915050," Preliminary and Summary Reports, CERCOM Inc., Vista, CA, 24 December 1991, and 04 June 1992 .....	134
APPENDIX B - R. L. Clarke, Technical Letter to Hughes, HAC P.O.# S9-333846-SAA, Dextra Assoc., Orinda, CA, 9 March 1992, with a Technical Addendum DSIR Chemistry, New Zealand, 6 March 1992 .....	138

## **CONTENTS (Concluded)**

	<u>Page</u>
APPENDIX C - D. A. Demeo, "Surface Analysis Examination of 988-3 Samples," Hughes Interdepartmental Correspondence No. 7621.10/09, 14 May 1992 .....	148
APPENDIX D - R. L. Clarke, Technical Letter to Hughes HAC P.O.# S9-333846-SVX, Rev. A, Dextra Assoc., Orinda, CA 20 October 1992 .....	169
APPENDIX E - R. L. Clarke, Technical Letter to Hughes, HAC P.O.# S9-333846-SVX, Rev. A, Dextra Assoc., Orinda, CA, 30 November 1992, with a Technical Addendum from DSIR Chemistry, New Zealand, 16 November 1992 .....	172
APPENDIX F - R. L. Clarke, Technical Letter to Hughes, HAC P.O.# S9-333846-SVX, Rev. A Dextra Assoc., Orinda, CA, 30 March 1992 .....	178

## FIGURES

Figure		Page
1	Shear strength vs. stoichiometry of rutile (14, 15) .....	8
2	Electrical conductivity and weight loss vs. stoichiometry of rutile (16, 17) .....	8
3	Vickers microhardness ( $H_V$ ) of (110) rutile vs. stoichiometry (18) .....	9
4	Schematic of the SEM tribometer (a), with idealized friction traces depicting the measurement of COF (the average coefficient of kinetic friction) and MAX. COF [the maximum (or break-away) coefficient of static friction] .....	11
5	Qualitative depiction of change in oxygen stoichiometry of a rutile triboflat surface as a function of SEM tribometer test parameters .....	12
6	UTI-100 residual gas analyses of the SEM tribometer vacuum atmosphere at $\sim 1 \times 10^{-5}$ torr (pressure measured by a Bayard-Alpert ion gage) .....	13
7	Near-room-temperature (30°C) adsorption isotherms for water on vacuum-reduced rutile (at 400°C) from (19) .....	14
8	Hughes hypothesis on the shear strength of rutile, and the concept of duplicating the shear strength trend by measuring the coefficient of friction (COF) trend of rutile samples in the SEM tribometer during temperature upramp (solid arrow on the bottom of the shear strength function) while the oxygen stoichiometry is reduced, and during temperature downramp (broken arrow on top of the function) while the oxygen stoichiometry is increased. The anticipated changes should occur both in vacuum ( $\sim 1 \times 10^{-5}$ torr) and in various partial pressures of oxygen gas ( $P_{Ox}$ ) .....	16
9	Coefficient of friction (COF) of a slightly-reduced single-crystal (001) rutile SEM triboflat sliding against a polycrystalline $\alpha$ -SiC pin in the [110] direction, from (14); Figure 8 is reproduced for ease of data interpretation ...	18
10	Vickers microhardness ( $H_V$ ) of (110) rutile during thermal exposure to vacuum ( $10^{-5}$ torr) at 800°C; from (18) .....	19
11	Optical photomicrograph of single crystal (001) [110] rutile triboflat and mating $\alpha$ -SiC pin after several SEM tribotests [from (12) and (14)] .....	20
12	Rutile surface shear strength ( $\tau_s$ ) estimates based on the friction forces measured from Fig. 9 and the real area of pin-flat contact ( $A_r$ ) estimated from Fig. 11 .....	22
13	Vickers microhardness ( $H_V$ ) for stoichiometric and reduced (110) rutile as a function of indentation temperature; from (18) .....	23
14	Vickers microhardness ( $H_V$ ) of 12 nm average grain-sized $TiO_2$ (rutile) samples measured at room temperature as a function of one-half hour sintering at successively high temperatures in air, as compared to a sample prepared via normal nanophase processing route using vacuum compaction, with no exposure to air; from (20) .....	24

## FIGURES (Continued))

Figure		Page
15	Temperature and atmospheric pressure effects on the deformation of single crystals of rutile: (a) engineering stress-strain curves; (b) the critical resolved shear stress function of the {101} <101> system; from (12), (13) and (21) ....	25
16	SEM photomicrographs of identically SEM-tribotested portions of rutile triboflats: the fully stoichiometric TiO <sub>2.00</sub> (001) [110] single crystal and polycrystalline flats and the reduced polycrystalline TiO <sub>1.95-2.00</sub> flat, at various magnifications .....	27
17	Surface shear strength ( $\tau_s$ ) estimates of an SEM-tribotested, fully stoichiometric (TiO <sub>2.00</sub> ) polycrystalline rutile triboflat sliding against a polycrystalline $\alpha$ -SiC pin, based on the measured friction forces and the real area of pin-flat contact ( $A_r$ ) estimated from Fig. 16 .....	28
18	Surface shear strength ( $\tau_s$ ) estimates of an SEM-tribotested, reduced-polycrystalline TiO <sub>1.95-2.00</sub> rutile triboflat sliding against a polycrystalline $\alpha$ -SiC pin, based on the measured friction forces and the real area of pin-flat contact ( $A_r$ ) estimated from Fig. 16 .....	29
19	Phase diagram of TiO <sub>2</sub> - SiO <sub>2</sub> ; from (23) .....	31
20	SEM tribometry results of polycrystalline rutile pin/flat combinations preconditioned to five different oxygen stoichiometry ranges, as indicated. Horizontal line markers of environmental atmospheric pressure are there only to show changes and their steps are not drawn to scale .....	35
21	A collage of indentation hardness- and hardness-related data on an (001) single crystal rutile plane and on nanophase TiO <sub>2</sub> sintered at various temperatures, in vacuum; from (30) .....	40
22	Indentation hardness measurements of EBONEX® ~Ti <sub>4</sub> O <sub>7</sub> (~TiO <sub>1.75</sub> ): (a) Knoop at 300 g. load, 500x mag.; (b) Vickers at 5 kg load, 200x mag., (c) Vickers at 20 kg load, 50x mag.; (also see Table 1) .....	41
23	SEM photomicrograph pairs of SEM tribometer pin (top) and mating flat (bottom) wear scars corresponding to the TiO <sub>2.00</sub> tests described in Fig. 20 ..	43
24	Same as Fig. 22 for TiO <sub>1.95-2.00</sub> .....	44
25	Same as Fig. 22 for TiO <sub>1.90-1.95</sub> .....	45
26	Same as Fig. 22 for TiO <sub>1.80-1.85</sub> .....	46
27	Same as Fig. 22 for TiO <sub>1.70-1.75</sub> .....	47
28	Schematic representation of oxygen vacancy formation in TiO <sub>2.00</sub> by doping with the aliovalent Cu <sup>2+</sup> cation .....	50
29	Dielectric polarizabilities of M <sup>2+</sup> , M <sup>3+</sup> and M <sup>3+</sup> cations vs. (crystal radius); from (46) .....	51

## FIGURES (Continued)

Figure		Page
30	IR, Ltd. X-ray diffractogram of CuO-pressed, polycrystalline rutile [(Ti + Cu)O <sub>1.80</sub> theoretical blend, hot-pressed + annealed] compared to the diffractograms of V <sub>3</sub> Ti <sub>6</sub> O <sub>17</sub> and pure rutile (also see Table 2 for sample identification) .....	57
31	Electrical conductivity-indicated stoichiometry of CuO-doped rutile [(Ti + Cu)O <sub>1.80</sub> theoretical blend, hot-pressed annealed]; (also see Table 2 for sample identification) .....	60
32	Copper-oxygen phase diagrams from Ref. 74 (left) and Ref. 75 (right) .....	63
33	The results of isothermal annealing CuO in $2 \times 10^{-7}$ torr vacuum: (a) oxygen content of copper oxide thin films vs. time of isothermal annealing from 375° to 555°C and (b) the transformed mole fraction of the Cu <sub>2</sub> O phase vs. annealing times corresponding to (a); from (76) .....	64
34	SEM tribometer-measured average coefficients of kinetic friction (COF) of hot-pressed, undoped rutile (slightly reduced during the hot-pressing process) sliding against itself, in vacuum. Figure 8 is reproduced for ease of data interpretation .....	68
35	SEM tribometer COF results of undoped and CuO-doped rutile samples sliding against themselves in vacuum, presented together to allow comparison of COF behavior under identical test conditions .....	70
36	Duplicate SEM tribometer COF results of CuO-doped rutile samples [(Ti + Cu)O <sub>1.80</sub> theoretical blend, hot-pressed + annealed] sliding against themselves in vacuum (two new sets of specimens) .....	72
37	MAX. COF results associated with the tests described in Fig. 35 to allow comparison of COF (average kinetic friction) with MAX. COF (maximum break-away or static friction) behavior of the same counterfaces as a function of temperature, in vacuum .....	73
38	SEM tribometer-measured average coefficient of kinetic friction (COF) of hot-pressed, undoped rutile (slightly reduced during the hot-pressing process) sliding against itself in various partial pressures of oxygen (P <sub>Ox</sub> ). Figure 8 is reproduced for ease of data interpretation .....	74
39	SEM tribometer COF results of undoped and CuO-doped rutile samples sliding against themselves in P <sub>Ox</sub> , presented together to allow comparison of COF behavior under identical test conditions .....	77
40	Duplicate SEM tribometer COF results of CuO-doped rutile samples [(Ti + Cu)O <sub>1.80</sub> theoretical blend, hot-pressed] sliding against themselves in P <sub>Ox</sub> (two new sets of specimens) .....	78
41	MAX. COF results associated with the tests described in Fig. 39, to allow comparison of COF (average kinetic friction) with MAX. COF (maximum break-away or static friction) behavior of the same counterfaces as a function of temperature, in P <sub>Ox</sub> .....	79

## FIGURES (Continued))

Figure		Page
42	Regression-smoothed COF functions from Figures 35 and 37 to allow COF comparison of all typical and equivalent tests on undoped and doped rutile, as a function of test temperature and atmospheric environment .....	81
43	Regression-smoothed MAX. COF functions from Figures 39 and 41, to allow MAX. COF comparison of all typical and equivalent tests on undoped and doped rutile, as a function of test temperature and atmospheric environment .....	82
44	Low magnification SEM photomicrographs of pin (P) tip and flat (F) wear scars associated with all the vacuum tribotests described in Figs. 42 and 43, showing generally lower wear rates in $P_{Ox}$ . Double-headed arrow indicates direction of oscillatory sliding .....	84
45	Energy dispersive X-ray spectrum (EDS) of the undoped rutile pin tested in $P_{Ox}$ .....	85
46	Low magnification SEM photomicrographs (backscattered electron images) of pin tip wear scars associated with vacuum tribotests, showing rougher surface structure that developed on CuO-doping. Double-headed arrow indicates direction of oscillatory sliding .....	86
47	High magnification SEM photomicrographs of unused pin (P) tip and flat (F) portions of vacuum-tribotested specimen surfaces (also see Figs. 35 and 37), showing grain growth due to CuO-doping .....	87
48	High magnification SEM photomicrographs of unused pin (P) tip and flat (F) portions of duplicate-vacuum-tribotested specimen surface sets (also see Fig. 36), showing consistency of grain growth due to CuO-doping .....	88
49	High magnification SEM photomicrograph equivalents of Fig. 44 pin tip and flat wear scars tested in vacuum. Tip scars include entire areas of apparent contact; flat scar photos taken full-width at midstroke. Double-headed arrow indicates direction of oscillatory sliding .....	90
50	Shallow angle, high magnification SEM photomicrographs of typical areas of pin (P) tip and flat (F) wear scars tested in vacuum from Fig. 49, showing smaller real areas of contact ( $A_r$ ) on the flats' wear path due to CuO-doping-caused grain growth. Double-headed arrow indicates direction of oscillatory sliding .....	91
51	Shallow angle, high magnification SEM photomicrographs of typical, unused portions of the heat-treated Ti-Cu-bronze pin (P) tip and flat (F) tested in $P_{Ox}$ , showing heavy surface accumulation of $Cu_2O$ on the heated flat (F) but no accumulation on the unheated pin (P) .....	92
52	High magnification SEM photomicrographs of unworn areas of duplicate CuO-doped rutile flats [(Ti + Cu) $O_{1.80}$ theoretical blend, hot-pressed], with accompanying EDS spectra at ultrahigh magnifications showing accumulation of the cubic $Cu_2O$ during $P_{Ox}$ tribotests .....	93

## FIGURES (Continued)

Figure		Page
53	Low magnification SEM photomicrographs and high magnification EDS spectra of areas in and out of the flat's wear scar of one of the two $P_{OX}$ tests shown in Fig. 52. Slight accumulation of the smeared $Cu_2O$ in the wear track is indicated .....	94
54	Low magnification SEM photomicrographs and high magnification EDS spectra of areas in and out of the flat's wear track of the second of the two $P_{OX}$ tests shown in Fig. 52. Slight accumulation of the smeared $Cu_2O$ in the wear tracks is indicated .....	95
55	Comparison of in-wear-track, high magnification, EDS spectra of vacuum- and $P_{OX}$ -tested flats fabricated from $CuO$ -doped rutile $[(Ti + Cu)O_{1.80}]$ theoretical blend, hot-pressed], showing preferential accumulation of $Cu_2O$ in $P_{OX}$ .....	96
56	Comparison of in-and-out-of-wear-track, high magnification EDS spectra of vacuum- and $P_{OX}$ -tested flats fabricated from the heat-treated $Ti-Cu$ -bronze, showing minimal (if any) copper compound accumulation in either environment. Source of trace iron contamination of $P_{OX}$ -tested sample is unknown .....	97
57	Shallow angle, high magnification photomicrographs of all worn pin tips, showing reduced charging of the wear scars associated with $CuO$ -doped rutile tested in $P_{OX}$ only. Double-headed arrow indicates direction of sliding .....	98
58	Low magnification SEM photomicrographs of duplicate vacuum tribotest pin (P)/flat (F) wear scars associated with the tests described in Fig. 36, showing repeatable wear scar appearance. Double-headed arrow indicates direction of sliding .....	100
59	High magnification SEM photomicrograph equivalents of Fig. 56 [(P) = pin scar, (F) = flat wear track]. Double-headed arrow indicates direction of sliding .....	101
60	Shallow angle, SEM photomicrographs of Fig. 59 pin (P)/flat (F) wear scars at even higher magnification. Double headed arrow indicates direction of sliding .....	102
61	Shallow angle, high magnification SEM photomicrographs of pin wear scars (also see Fig. 58), showing repeatable alignment and appearance of the scars. Double-headed arrow indicates direction of sliding .....	103
62	Low magnification SEM photomicrographs of duplicate $P_{OX}$ tribotest pin (P)/flat (F) wear scars associated with the tests described in Fig. 40 showing repeatable scar appearance. Double-headed arrow indicates direction of sliding .....	104
63	High magnification SEM photomicrograph equivalents of Fig. 62 [(P) = pin scar; (F) = flat wear track]. Double-headed arrow indicates direction of sliding .....	105

## FIGURES (Continued)

Figure		Page
64	Shallow angle, high magnification SEM photomicrographs of Fig. 63 pin (P)/flat (F) wear scars at even higher magnification. Double-headed arrow indicates direction of sliding .....	106
65	Shallow angle, high magnification SEM photomicrographs of pin wear scars (also see Fig. 62), showing repeatable alignment of the scars. Double-headed arrow indicates direction of sliding .....	107
66	Schematic of the Hughes Tester 2A high temperature tribometer .....	109
67	Hughes-modified engineering drawing of the NTN-Bower rolling contact fatigue (RCF) rod for Tester 2A use .....	110
68	Engineering drawing of the Tester 2A (modified) rubshoe .....	111
69	Detailed schematic of the Hughes Tester 2A high temperature tribometer ....	112
70	Photograph of the Tester 2A with dedicated computer for data logging and analysis .....	114
71	Tester 2A friction traces of Kyocera rutile rubshoes tested against an $\alpha$ -SiC RCF rod, under standard test conditions (see Table 4); from (12) .....	116
72	Appearance of used Tester 2A Kyocera rutile rubshoes tested against an $\alpha$ -SiC rod, under standard test conditions (see Table 4); from (12). Arrow was added to original figure to indicate the direction of counterface sliding .....	117
73	Tester 2A friction traces of <i>rutile</i> rubshoes tested against an $\alpha$ -SiC RCF rod under standard test conditions (see Table 4) .....	119
74	Tester 2A friction traces of <i>mix</i> rubshoes tested against an $\alpha$ -SiC RCF rod, under standard test conditions (see Table 4) .....	120
75	Tester 2A friction traces of <i>bronze</i> rubshoes tested against an $\alpha$ -SiC RCF rod, under standard test conditions (see Table 4) .....	121
76	Low magnification optical photomicrographs of used Tester 2A <i>rutile</i> , <i>mix</i> , and <i>bronze</i> rubshoes associated with the test described in Figures 73, 74 and 75 (7.9x mag.). Arrow indicates the direction of counterface sliding .....	122
77	Typically representative SEM photomicrographs of the used rubshoes shown in Figure 76, taken in and out of the wear tracks .....	123



## **TABLES**

Table		Page
1	Typical properties of the EBONEX® substoichiometric rutile electrode material .....	34
2	Results of the first successful heat-treatment study .....	56
3	Results of the second heat-treatment study to further elucidate pressing and curing temperatures .....	61
4	Test conditions for Tester 2A experiments .....	115

## 1.0 EXECUTIVE SUMMARY

Stable oxides would be ideal (and in certain cases, the only feasible) high temperature lubricants for critical applications in air. Unfortunately, most stable metal oxides are high-friction, abrasive materials. Those that are not are either tribochemically unstable (i.e., they react with a variety of ceramic substrates to form glasses or brittle interface compounds) or volatile, or both.

The quest for thermo- and tribo-oxidatively stable, low surface shear strength ( $\tau_s$ ) and low friction oxides has been significantly advanced by a major breakthrough of the recently completed Part I portion of the "Tribological Fundamentals " program. Using the rutile polymorph of titanium dioxide as a model compound, the work demonstrated that the crystallographic shear (CS) plane structures also known as the  $\text{Ti}_n\text{O}_{2n-1}$  Magnèli phases that form during progressive reduction of rutile exhibit distinctly different  $\tau_s$ . It was hypothesized that the predictably changing Magnèli phases either reduce or increase the lattice strain energy ( $E_l$ ) and the commensurately smaller and larger  $\tau_s$ -controlled friction of rutile. In particular, two low  $E_l$ ,  $\tau_s$  and friction regimes were predicted near  $\text{TiO}_{1.93}$  to  $\text{TiO}_{1.98}$  and at  $\text{TiO}_{1.70}$ , surrounding a four-to-five times higher peak of those values at  $\text{TiO}_{1.80}$ .

The present study continued this research in two major parts. During the first part, variable temperature range (room temperature to 1000°C) scanning electron microscope (SEM) tribometry was completed on (a) fully stoichiometric, single-crystal and polycrystalline rutile samples, as well as (b) polycrystalline rutile reduced into narrow oxygen stoichiometric ranges. The friction and wear experiments were performed in test atmospheres consisting of the  $\sim 1.33 \times 10^{-3} \text{ Pa} = 1 \times 10^{-5} \text{ torr}$  SEM column vacuum and various controlled partial pressures of oxygen ( $P_{\text{Ox}}$ ) ranging from 0.2 to  $\sim 3.4 \text{ torr}$ . In addition to a few tribotests with single crystal and polycrystalline rutile specimens sliding against polycrystalline  $\alpha$ -SiC, five different sliding pairs of polycrystalline  $\text{TiO}_{2.00}$ ,  $\text{TiO}_{1.95-2.00}$ ,  $\text{TiO}_{1.90-1.95}$ ,  $\text{TiO}_{1.80-1.85}$  and  $\text{TiO}_{1.70-1.75}$  triboflats were oscillated against self-similar hemispherical pins, under the standard 0.49 N normal load. The results confirmed the predicted, oxygen-vacancy-controlled creation of high and low  $E_l$  Magnèli phases exhibiting high and low  $\tau_s$  (and friction), respectively. The  $\text{TiO}_{1.70}$  was shown particularly promising as a low friction lubricious oxide, in contrast with the high friction  $\text{TiO}_{1.80}$  counterpart. However, the tendency of the narrow stoichiometric ranges to shift as a function of temperature and  $P_{\text{Ox}}$  causes purposely reduced rutile to be a thermo-oxidatively unstable tribomaterial for extreme environmental applications.

The second part of the present program consisted of an attempt to generate stable Magnèli phases of the desired kind(s) by doping rutile with selected cations similar in size and polarizability to the  $\text{Ti}^{4+}$ , but with lower valencies. Doping with these aliovalent cations was predicted to cause chemical expulsion of oxygen from the rutile lattice to maintain charge balance and to generate specific CS plane structures. Additional SEM tribometric experiments, similar to the ones completed during the first portion of the program, were done in vacuum and in various  $P_{\text{Ox}}$  of 99.995% pure oxygen gas on undoped hot-pressed polycrystalline rutile and rutile blended and hot-pressed with CuO to an ideal stoichiometry of  $(\text{Ti}+\text{Cu})\text{O}_{1.80}$ . Copper was selected as the dopant of choice because both the theoretical predictions and doping studies with other candidate cations indicated that  $\text{Cu}^{2+}$  and/or  $\text{Cu}^{1+}$  had the best chance of immediately satisfying program requirements.

The analyses of the hot-pressed molds and the results of the SEM tribometer tests indicated that only copper could be made to enter the rutile lattice using our simple preparation technique. The reaction is not stoichiometric, however. While some of the residual dopant evaporated (or remained) as  $\text{Cu}_2\text{O}$  or was left behind as metallic copper ( $\text{Cu}^0$ ), a small portion did react to generate Magnèli phases. A never-before-created titanium-copper bronze was formed, equivalent to an analogous compound resembling the X-ray diffractogram of  $\text{V}_3\text{Ti}_6\text{O}_{17}$ . This titanium-vanadium bronze is a known rutile-based electrode and catalyst material equivalent to the cation-to-oxygen ratio of  $\text{TiO}_{1.89}$ . It also exhibited the electrical conductivity of undoped rutile electrodes reduced to  $\text{TiO}_{1.89}$ . The SEM tribometer data consistently showed, both in vacuum and in  $P_{\text{Ox}}$  test atmospheres, that this titanium-copper bronze did lower the magnitude of the frictional increase as the stoichiometry was changed to and through  $\text{TiO}_{1.80}$  by virtue of its chemically de-oxygenated nature. This proof of higher thermooxidative stability was shown to occur during every SEM tribometer test.

Additional bench-top friction and wear testing in air with a dual rubshoe vs.  $\alpha$ -SiC rod-type, high temperature tribotester, confirmed the SEM tribometer results in that the copper-titanium bronze's friction response is less temperature sensitive than the response of the undoped rutile. However, these engineering-type friction and wear tests indicated that neither the bronze nor its precursors are practical lubricious oxides yet for use in high temperature air. Their friction is still too high (~0.6 to 0.7). The high but essentially unchanging friction of the bronze, at all test temperatures, may still render it useful as a wide temperature range ceramic brake material.

The  $\text{TiO}_{1.89}$ -like titanium-copper bronze exhibiting the rutile crystal structure has served well as an ideal model compound for the experimental confirmation of the Hughes hypothesis. It was demonstrated that doping-induced molecular engineering of lubricious oxides is possible.

## 2.0 INTRODUCTION

Stable oxides would be ideal (and in certain cases, the only feasible) high temperature lubricants for critical applications in air. There are several national programs which need such lubricious oxides. Examples of these programs are the Integrated High Performance Turbine Engine Technology or IHPTET (1), the Advanced Turbine Technology Application Project or ATTAP (2), and the Advanced Gas Turbine (AGT) project (3). The IHPTET initiative's goal is to double propulsion performance. This will be achieved through innovative designs attaining higher cycle temperatures through the use of advanced materials. Parallel to this initiative, the ATTAP is intended to advance the technological readiness for the commercialization of an automotive ceramic gas turbine engine, the feasibility of which was demonstrated during the recently concluded AGT. There is also an urgent need for cryogenic tribomaterials capable of operating in the liquid oxygen (LOX) turbopumps of the Space Shuttle Main Engine (both the current and the upgraded designs) and the engines being currently designed for the Advanced Launch System (ALS)/National Launch System (NLS) and the National AeroSpace Plane (NASP); (4 - 11). Unfortunately, most stable metal oxides are not suitable as high temperature lubricants, because they are high-friction, abrasive materials. Those that are not are either tribochemically unstable (i.e., they react with a variety of ceramic substrates to form glasses or brittle interface compounds) or volatile, or both.

The quest for thermo- and tribo-oxidatively stable, low surface shear strength ( $\tau_s$ ) and low friction oxides has been significantly advanced by a major breakthrough of the recently completed Part I portion of the "Tribological Fundamentals " program (12 - 15). An assessment and interpretation of literature data identified the oxygen deficient crystal structures of rutile ( $\text{TiO}_{2-x}$ ) as promising model compounds for fundamental friction and wear studies on lubricious oxides. In oxygen-deficient or reducing environments, especially at high temperatures, a progressively larger number of oxygen vacancies are generated both on the surface and in the bulk of the rutile lattice. Vacancy generation leads to the creation of new crystallographic shear (CS) systems also known as the  $\text{Ti}_n\text{O}_{2n-1}$  Magnèli phases. The high index planes of these phases shift with oxygen content and dominate the actions of the natural (low index) cleavage planes, determining the surface shear strength ( $\tau_s$ ) and the  $\tau_s$ -controlled friction force. It was hypothesized that the predictably changing Magnèli phases either reduce or increase the lattice (strain) energy ( $E_l$ ) and, commensurately, the  $\tau_s$ -controlled friction of rutile. In particular, two low  $E_l$ ,  $\tau_s$  and friction regimes were predicted near  $\text{TiO}_{1.93}$  to  $\text{TiO}_{1.98}$  and at  $\text{TiO}_{1.70}$ , surrounding a four-to-five times higher peak of those values at  $\text{TiO}_{1.80}$ .

Building on this discovery, it became possible to conduct a molecular engineering study of lubricious oxides for high temperature air applications. The present study consisted of two major parts. During the first portion, variable temperature (room temperature to 1000°C) scanning electron microscope

(SEM) tribometry was completed on (a) fully stoichiometric, single crystal and polycrystalline rutile samples, as well as (b) polycrystalline rutile samples reduced into narrow oxygen stoichiometry ranges, to examine the validity of the Hughes hypothesis. Friction and wear experiments were performed in test atmospheres consisting of  $\sim 1.33 \times 10^{-3}$  Pa =  $1 \times 10^{-5}$  torr SEM column vacuum and various controlled partial pressures of oxygen ( $P_{Ox}$ ) ranging from 0.2 to  $\sim 3.4$  torr. In addition to a few tribotests with single crystal and polycrystalline rutile sliding against polycrystalline  $\alpha$ -SiC, five different sliding pairs of polycrystalline  $TiO_{2.00}$ ,  $TiO_{1.95-2.00}$ ,  $TiO_{1.90-1.95}$ ,  $TiO_{1.80-1.85}$  and  $TiO_{1.70-1.75}$  triboflats were oscillated against self-similar hemispherical pins, under the standard 0.49 N normal load. The results confirmed the predicted, oxygen-vacancy-controlled creation of high and low  $E_f$  Magnèli phases exhibiting high and low  $\tau_s$  (and friction), respectively. The  $TiO_{1.70}$  is particularly promising as a low friction lubricious oxide, in contrast with the high friction  $TiO_{1.80}$  counterpart. However, the tendency of the narrow stoichiometric ranges to shift as a function of temperature and  $P_{Ox}$  causes purposely reduced rutile to be a thermo-oxidatively unstable tribo-material for extreme environmental applications.

The second portion of the present program consisted of an attempt to generate stable Magnèli phases of the desired kind(s) by doping rutile with selected cations similar in size and polarizability to the  $Ti^{4+}$ , but with lower valencies. Doping with these aliovalent cations was predicted to cause chemical expulsion of oxygen from the rutile lattice to maintain charge balance and to generate specific CS plane structures. Additional SEM tribometric experiments, similar to the ones completed during the first portion of the program, were done in vacuum and in various  $P_{Ox}$  of 99.995% pure oxygen gas, using specimens fabricated from hot-pressed, undoped polycrystalline rutile and rutile blended and hot-pressed with CuO to an ideal stoichiometry of  $(Ti+Cu)O_{1.80}$ . Copper was selected as the dopant of choice because both the theoretical predictions and doping studies with other candidate cations indicated that  $Cu^{2+}$  and/or  $Cu^{1+}$  had the best chance of immediately satisfying program requirements. The tribotests and the attendant techniques used to analyze the chemistry and crystal structure of the specimens [e.g., X-ray diffraction (XRD), 4-point conductivity measurement, some X-ray photoelectron spectroscopy (XPS)] had to resolve the following questions:

1. Can the copper ions, embodied in pulverized CuO, be made to enter the rutile lattice by the relatively simple and inexpensive preparation technique of ball milling, drying, hot-pressing and high temperature annealing in controlled atmospheric environment (i.e., by thermal diffusion)?
2. If yes, is the reaction stoichiometric, i.e., has all or only a portion of the dopant succeeded in chemically expelling a controlled part of the oxygen from the rutile lattice to induce the formation of friction-specific Magnèli phases?

3. Would the hot-pressed molds exhibit sufficient structural integrity to allow fabrication and testing of specimens?
4. Can the copper ions, in a desirably reacted form, influence the tribological behavior of rutile under extreme environmental conditions, as predicted by the Hughes hypothesis?
5. Could  $\text{Fe}^{3+}$ ,  $\text{Co}^{2+}$  and  $\text{Ni}^{2+}$  act as likely dopants similar to copper?

A successful, fundamental approach to answering the above questions and leading to the validation of the doping hypothesis is described in the present report.

### **3.0 OXYGEN-CONTENT DRIVEN TRIBOLOGICAL BEHAVIOR OF RUTILE**

#### **3.1 Magnèli Phase-Controlled Friction of Rutile**

As discussed in (12 - 15), anything that is done to an oxide surface can, and often will, change its composition. In almost all cases, the surface becomes oxygen-deficient. Rutile is no exception to this rule.

The O/Ti ratio as the function of various surface treatments (e.g., heating in air, in vacuum or in reducing environment such as hydrogen, by ion bombardement or even by mechanical shock) indicates that oxygen is removed preferentially even from the most thermodynamically stable cleavage planes. When an oxygen is lost from the surface, two electrons are left in the vacancy to maintain charge balance. Initially, the electrons may occupy the vacancies formed. As the reduction proceeds, a neighboring  $\text{Ti}^{4+}$  may change its charge state to  $\text{Ti}^{3+}$ ; the other electron is essentially free to act as a charge carrier. The color of the oxide changes from the ivory-yellow-white of the fully stoichiometric version to the progressively darker, blue-black coloration of the more anion-deficient sample. The color change is caused by the absorption of red light by the conduction electrons, signaling the transformation from a large band gap insulator to an *n*-type semiconductor.

There will be vacancy point defects even on the most stable (110) cleavage plane. These can act as chemisorption sites for a variety of gases. The dissociation of molecular oxygen and other oxygen-containing moieties such as water occurs at these active sites even at low temperatures. With the annihilation of the vacancies the conduction electrons become depleted and the color changes back to ivory-white.

The effectiveness of anion vacancy annihilation highly depends on the gas content of the atmosphere in contact with the substoichiometric rutile surface, the temperature of the sample and the duration of gas exposure. Beyond the maximum temperature of thermal desorption, oxygen or other oxygenated species react directly from the gas phase to anneal out the surface vacancies. Diffusion in the direction of the electrochemical potential gradient rapidly anneals the vacancies in the subsurface region also. For example, heating stoichiometric rutile to several hundred degrees Centigrade in vacuum or in a reducing atmosphere results in a small number of oxygen vacancies in the bulk. These can be annealed out by heating in air or in oxygen, at temperatures to 1000°C for several hours.

Surface anion vacancies can also be annihilated by oxygen migration from the bulk. Here, the electrochemical potential gradient changes direction. Therefore, at any temperature, at the various  $P_{\text{Ox}}$

above the  $\text{TiO}_{2-x}$  surface, the surface concentration of oxygen vacancies is determined by two competing processes: adsorption and diffusion in reversible directions (i.e., the escape or capture of oxygen at the surface, as well as the diffusion of the oxygen from the bulk to the surface or from the surface to the bulk).

The generation of oxygen vacancies on the rutile surface will not necessarily lead to the formation of Magnéli phases. Some of the anion removal processes are not sufficiently energetic to induce the diffusion of the vacancies into the bulk. This diffusion is important, because the self-arrangement of the vacancies into ordered, planar arrays is the dominant mechanism for creating the various CS planes. The low and high  $\tau_s$  Magnéli phases exhibit the changing shear strength gradient because of the interaction and structural modulation of the charge density waves produced by corner- and edge-sharing  $[\text{TiO}_6]$  octahedra. The layer-to-layer attraction or repulsion of the various phases can be decomposed into contributions from different sets of one-dimensional chains of these variously assembled octahedra. For example, those derived from edge-shared chains have shorter Ti-Ti distances and stronger interaction (thus higher  $\tau_s$ ) than in the case of layers comprised by corner-sharing octahedral chains.

The first numerical estimation of  $\tau_s$  as the function of oxygen stoichiometry (Fig. 1) was made by SEM tribometric results on XTL rutile sliding against poly-XTL  $\alpha$ -SiC, backed by theoretical calculations of charge density wave interactions (13,15). Strong confirmation of at least the accuracy of the predicted trend of  $\tau_s$  changes came from electrical conductivity measurements done on reduced-rutile electrode materials (see Fig. 2); (16,17). Recent NASA Lewis Research Center indentation microhardness tests of stoichiometric and reduced rutile XTL performed at 25° and 800°C further corroborated the Hughes hypothesis (Fig. 3).

The next subsection contains the summary of all previous SEM tribometer tests on rutile specimens to lay the groundwork for the series of similar experiments performed during the present program. In addition, new SEM tribometric data are presented on poly-XTL rutile specimens prepared to be in the stoichiometric ranges of  $\text{TiO}_{2.00}$ ,  $\text{TiO}_{1.95-2.00}$ ,  $\text{TiO}_{1.90-1.95}$ ,  $\text{TiO}_{1.80-1.85}$  and  $\text{TiO}_{1.70-1.75}$ . The last four types of specimens were prepared by pre-reduction in hydrogen, using a standard preparation method for oxygen-deficient rutile electrodes.



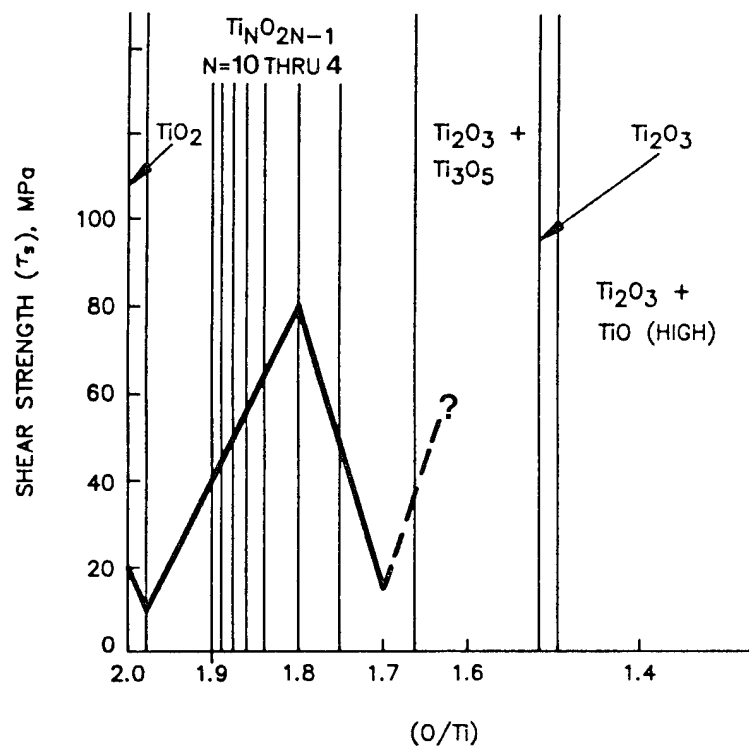


Figure 1. Shear strength vs. stoichiometry of rutile (14, 15).

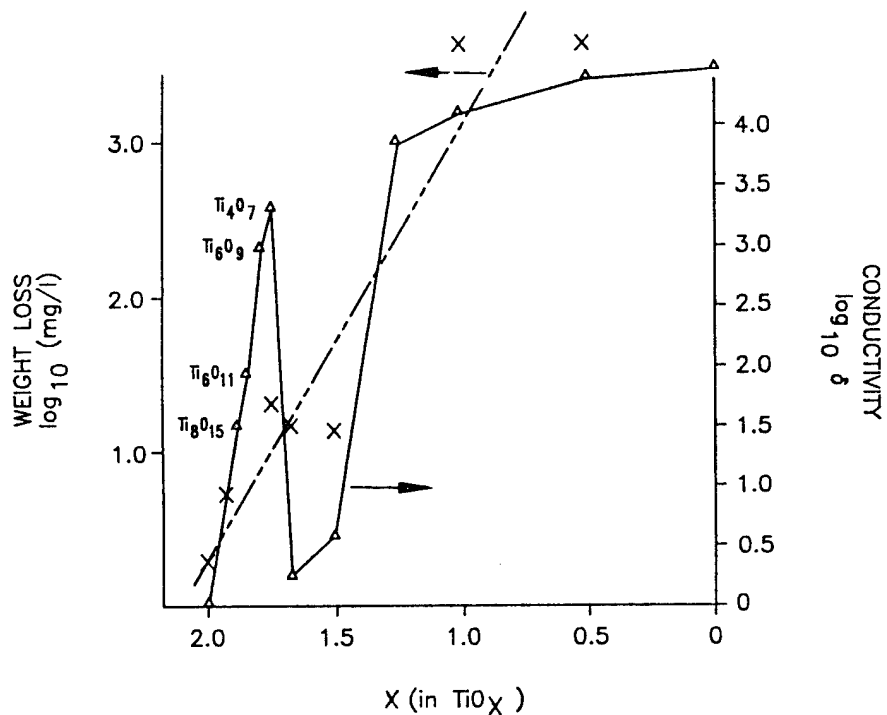


Figure 2. Electrical conductivity and weight loss vs. stoichiometry of rutile (16, 17).

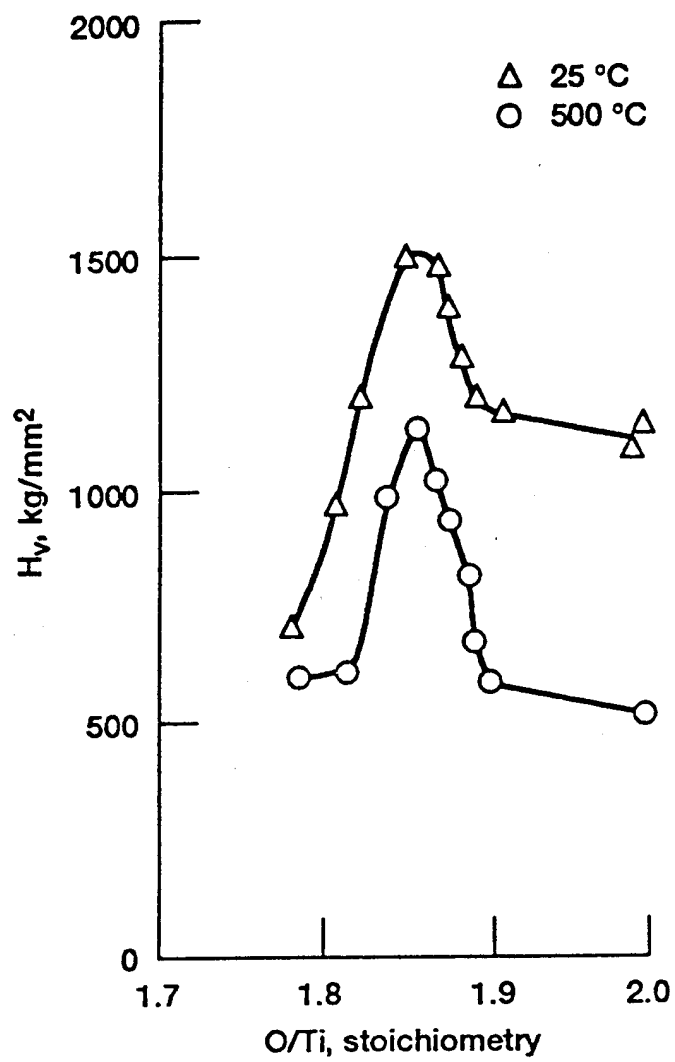


Figure 3. Vickers microhardness ( $H_V$ ) of (110) rutile vs. stoichiometry (18).

## 3.2 Control of Magnèli Phases by Pre-reduction and Variable Temperature

### SEM Tribometry

#### 3.2.1 Test Equipment and Methodology

During SEM tribometry, a 7 mm x 5 mm x 2 mm triboflat is oscillated against a 2 mm diameter, 10 mm long tribopin under a 0.49 N (50 gram-force) normal load, as depicted by the schematic in Fig. 4a. The test apparatus and procedure have been adequately described before (12, 14). The objective of each test is to observe the  $\tau_s$  vs. stoichiometry-controlled changes in friction trends, as predicted in Fig. 1. Since (a) the coefficient of friction is a systems parameter in that it is equal to  $\tau_s/P_y$ , where  $P_y$  is the yield strength of the substrate, and (b) both  $\tau_s$  and  $P_y$  are directly proportional to the  $E_l$  of a given set of CS planes belonging to a particular Magnèli phase, on the first order the  $\tau_s$  and the development of its trend as a function of oxygen stoichiometry is accurately reflected by the changes in the value of the coefficient of friction.

In the present case, both the average coefficient of kinetic friction (COF) and the coefficient of static (maximum or break-away) friction (MAX.COF) are values of interest, as measured by the SEM tribometer (Fig. 4b). Note that the above quoted equality applies to both type of friction coefficients, provided the tribo-environmental factors influence both the  $\tau_s$  and the  $P_y$  equally.

Theoretically, each untested triboflat should exhibit a given, homogeneous stoichiometry throughout its cross-section. Depending on the degree of pre-reduction and the environmental condition above the flat, it should be either easy or difficult to remove additional amounts of oxygen from the surface of the flat by heating at low atmospheric pressures. Taking the fully stoichiometric baseline sample as an example in Fig. 5 (top), the surface becomes more anion deficient than the bulk during temperature upramp (Fig. 5, middle). During thermal downramp of the gradually cooled flat, the residual gas species in the SEM column (with the SEM tribometer lid off) or the oxygen molecules in the fully-lidded version begin to increasingly interact with the highly reactive vacancy sites on the surface. As previously mentioned, these are strong Lewis acid sites, consisting of five-, four- and possibly three-fold-coordinated titanium ions. The coordination (and the reactivity) depends on which crystal plane is being exposed on the surface of the many-grained, poly-XTL sample. Since (a) these highly active dangling bonds are capable of splitting both oxygen and water to their atomic constituents, (b) most of the residual gases in the  $\sim 1 \times 10^{-5}$  torr vacuum of the SEM column is over 90% moisture with nitrogen and oxygen essentially comprising the rest (Fig. 6), and (c) in such low partial pressures of water reduced rutile sorbs the  $H_2O$  molecules readily by dissociative chemisorption [see Fig. 7 taken from (19)], the surface of the cooled rutile flat becomes oxygen-rich. Now the oxygen stoichiometry of the flat cross-section becomes more

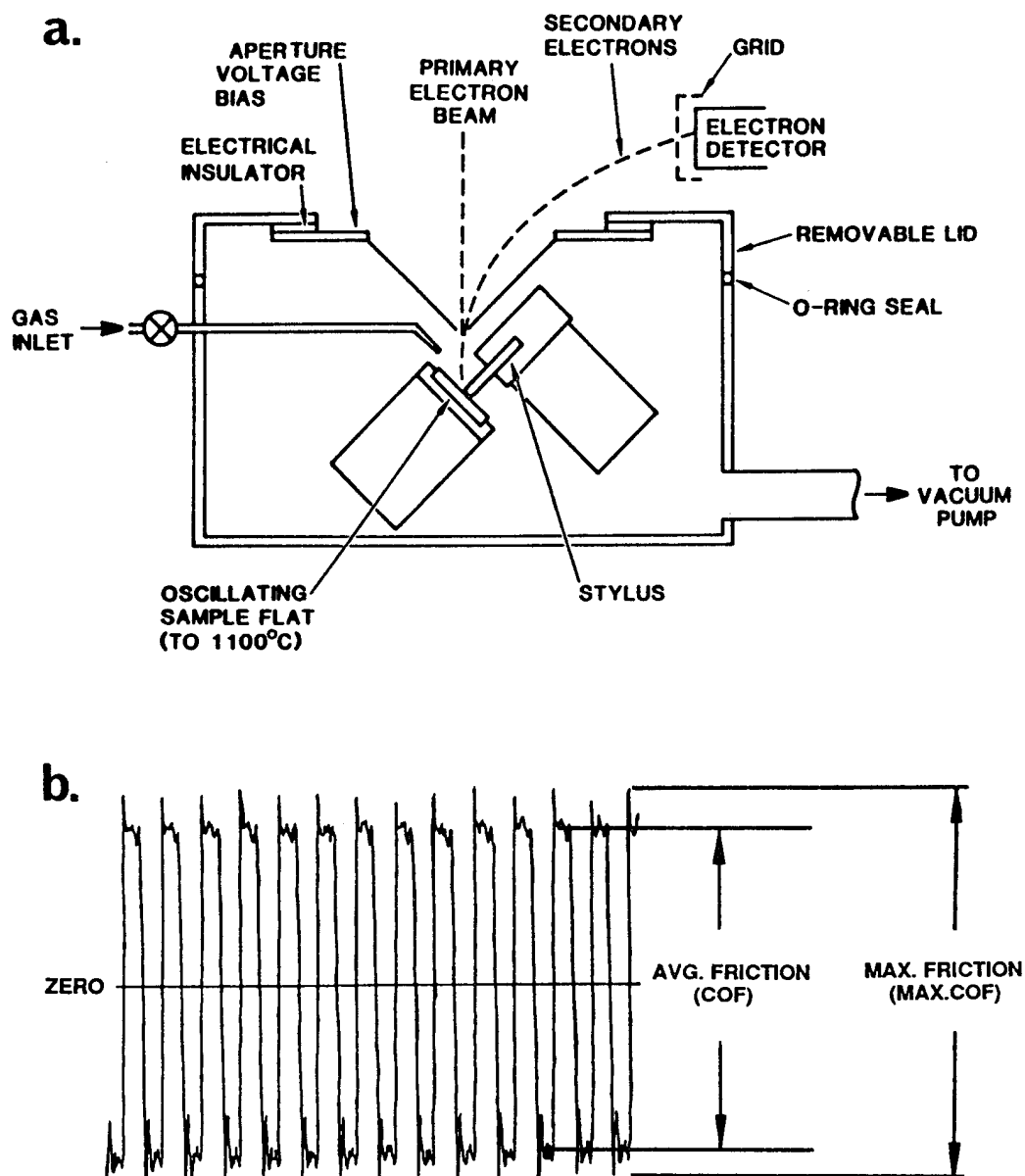
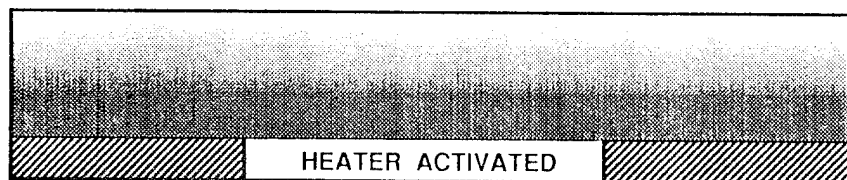


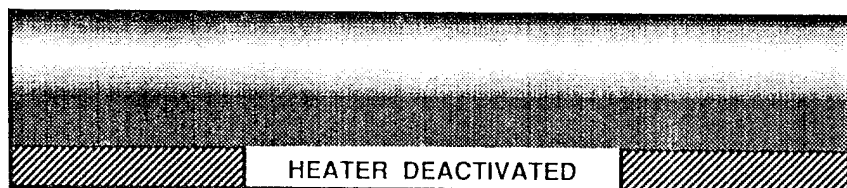
Figure 4. Schematic of the SEM tribometer (a) with idealized friction traces depicting the measurement of COF (the average coefficient of kinetic friction) and MAX. COF [the maximum (or break-away) coefficient of static friction].



ORIGINAL



THERMAL UPRA  
MP  
IN VACUUM



THERMAL DOWNRA  
MP  
IN P<sub>gas</sub>

Figure 5. Qualitative depiction of change in oxygen stoichiometry of a rutile triboflat surface as a function of SEM tribometer test parameters.

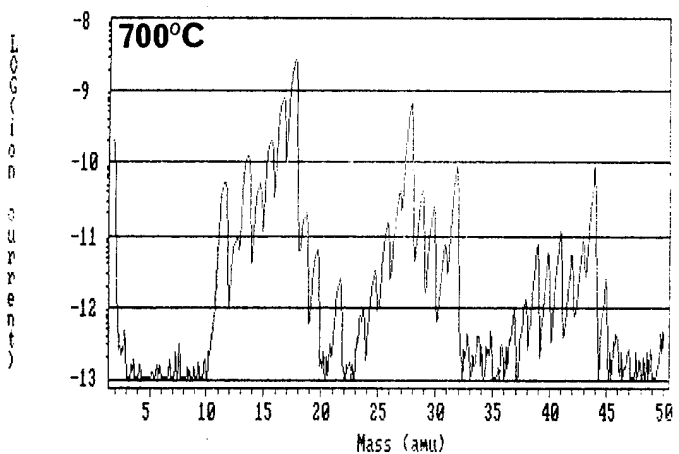
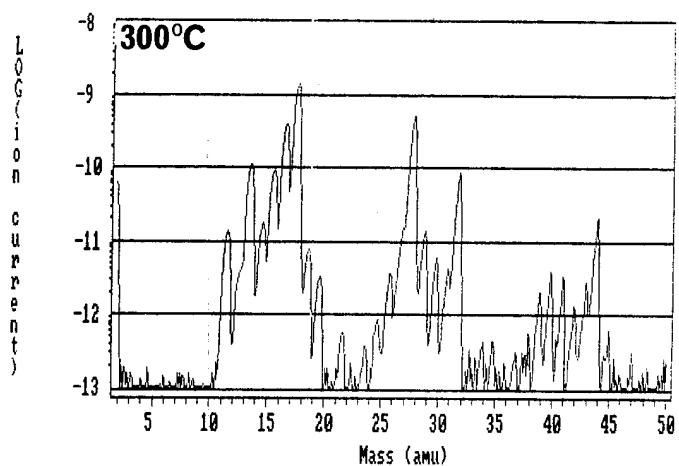
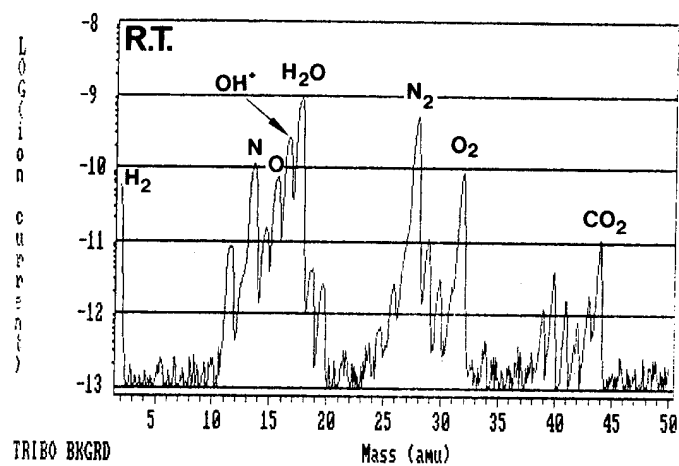


Figure 6. UTI-100 residual gas analyses of the SEM tribometer vacuum atmosphere at  $\sim 1 \times 10^{-5}$  torr (pressure measured by a Bayard-Alpert ion gage).

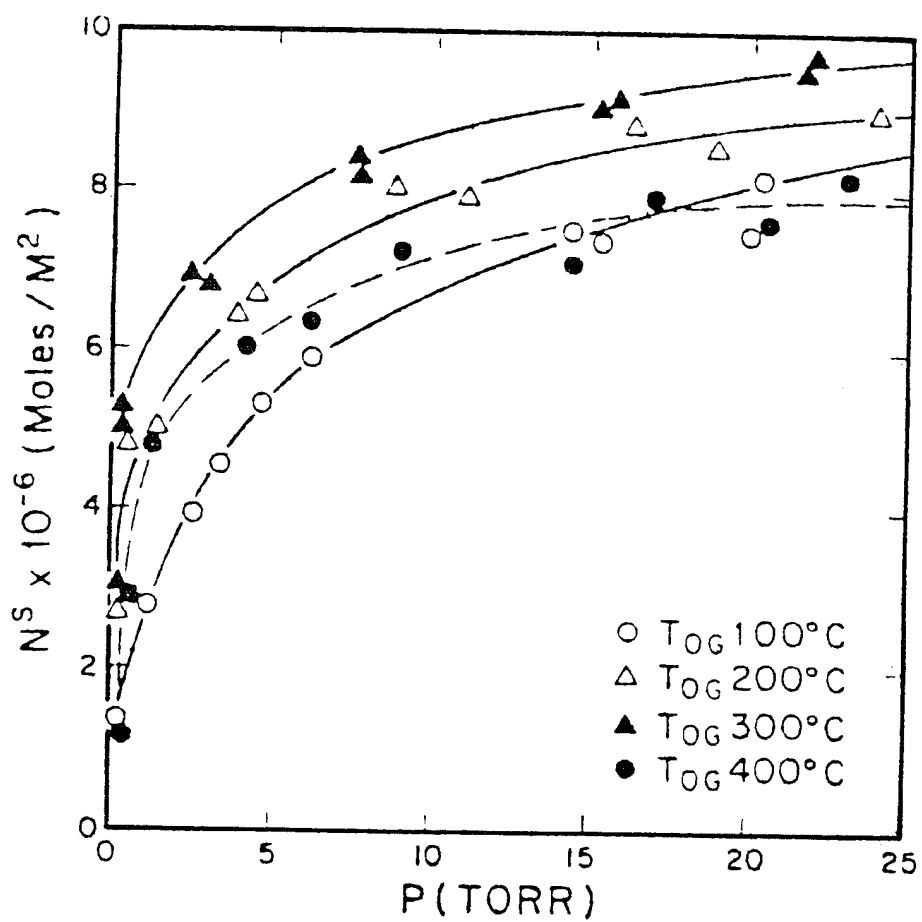


Figure 7. Near-room-temperature (30°C) adsorption isotherms for water on vacuum-reduced rutile (at 400°C) from (19).

like that depicted in Fig. 5 (bottom). In the much higher  $P_{\text{Ox}}$  of the lid-covered tribometer, ranging from 0.1 to ~3.4 torr, filling the oxygen vacancies is easier yet.

As previously stated, the main objective of each SEM tribometer experiment is to further examine the validity of the  $\tau_s$  vs. oxygen stoichiometry function. The  $\tau_s$  and the associated friction forces may be manipulated by first heating, then cooling the rutile triboflat in  $\sim 1 \times 10^{-5}$  torr vacuum or in various  $P_{\text{Ox}}$  of 99.997% pure oxygen gas. The controlled amounts of oxygen are introduced through a variable leak valve to maintain given levels of  $P_{\text{Ox}}$  in the continuously pumped, lidded tribometer subchamber (see Fig. 4a).

Therefore, the first (heated) part of the predicted  $\tau_s$  and friction trend in Fig. 8 (an appropriately modified version of Fig. 1) should follow the solid-arrow-indicated direction, towards and past the  $\text{TiO}_{1.80}$   $\tau_s$  peak. The vacuum- (or low  $P_{\text{Ox}}$ )-exposed and heated rubbing surface is always the most oxygen-poor at the end of the thermal upramp and heated portion of the test.

The rate and degree of any oxygen loss from either a fully stoichiometric or purposely reduced flat's surface, as well as any anionic concentration gradient resulting therefrom, depend on (a) the degree of initial reduction, (b) the time-at-temperature of the heated flat, (c) the partial pressure of the oxygen-producing gases around the sliding interface, and (d) the characteristic self-diffusion of oxygen ions through the rutile lattice towards the vacuum-exposed surface, as driven by the specific electrochemical potential gradient set up by the concentration and Magnéli phase gradients.

The same argument applies to the stoichiometric and  $\tau_s$  changes that occur during adsorbate-caused annihilation of the anion vacancies on the cooled triboflat. It follows that during temperature downramp, the broken-arrowed-direction in Fig. 8 should prevail. The changes in the tribological behavior of the surface should also be highly dependent on whether the thermal downramp portion of the test is run in the SEM column vacuum (with the tribometer lid off) or in  $P_{\text{Ox}}$  (with the tribometer lid on). At the lower concentration of the oxygen species in the column vacuum, removing oxygen from the surface is faster and easier than in the higher  $P_{\text{Ox}}$  of the lidded tribometer. In contrast, regaining oxygen in vacuum is slower than in  $P_{\text{Ox}}$ .

During all tests, the flats were oscillated against the hemispherical pin tips with a normal load  $F_n = 0.49$  N. The standard wear path length is 3.5 mm. Each oscillatory cycle equals twice the path length. At 40 cpm, the average oscillatory velocity is  $4.66 \times 10^{-3}$  m/s. During each test, thermal cycling began at room temperature (R.T.), followed by heating to a predetermined (near 1000°C) temperature and finally cooling back to near R.T.. The wear path was imaged by video throughout the tests.



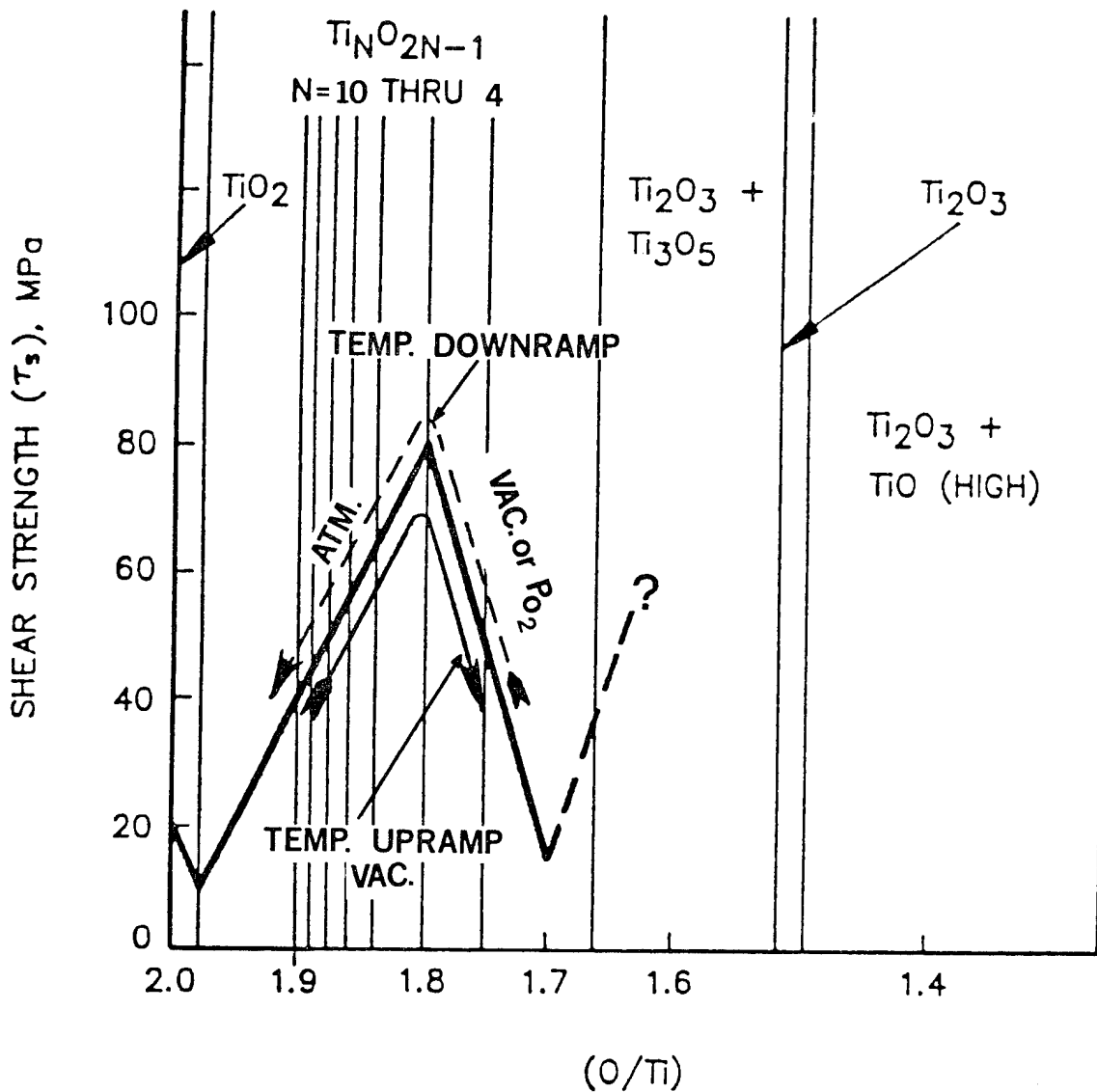


Figure 8. Hughes hypothesis on the shear strength of rutile, and the concept of duplicating the shear strength trend by measuring the coefficient of friction (COF) trend of rutile samples in the SEM tribometer during temperature upramp (solid arrow on the bottom of the shear strength function) while the oxygen stoichiometry is reduced, and during temperature downramp (broken arrow on top of the function) while the oxygen stoichiometry is increased. The anticipated changes should occur both in vacuum ( $\sim 1 \times 10^{-5}$  torr) and in various partial pressures of oxygen gas ( $P_{Ox}$ ).

### 3.2.2 SEM Tribometry of Single Crystal Rutile vs. Polycrystalline $\alpha$ -SiC

The most significant data from (12,14,15) are reproduced here in Fig. 9. The COF function faithfully follows the predictions proposed in Fig. 8. At the onset of sliding in vacuum at R.T., the initial reduction in COF agrees with the predicted reduction in  $\tau_s$  (to ~350 cycles). The sudden friction rise at the onset of heating (i.e., rapid oxygen loss from the surface) is followed by a reduction in friction on further heating at ~1000°C (see solid-arrowed direction in Fig. 8). This temporary increase in  $E_1$  (and thus hardness and abrasiveness) was also noted by DellaCorte and Deadmore during hot microhardness indentation of XTL rutile in vacuum (18); (see Fig. 10).

It is important to note that this trend in Fig. 9, using the (001)[110] XTL rutile SEM triboflat surface sliding against the ceramic pin, developed clearly only after two similar tests with the same flat. As the experiments were performed one after another, we were able to observe a definite darkening of the flat prior to the third (the present) test. It seemed that some pre-reduction is necessary to set up an initial electrochemical potential gradient for more ready oxygen loss on heating. There was still a net loss of oxygen by prior heating (twice) in vacuum, even though that during the respective cooling cycles some vacancy annihilation had to have occurred. Such gradient-driven enhancement of oxygen loss from already reduced samples was also observed with the other tests described in 3.2.3 herein.

On cooling, the predicted trend of COF changes follows the broken-arrowed direction shown in Fig. 8. However, the measured COF increased to its highest level on cooling, not on heating. The meaning of this experimental artifact did not become clear until the other tribotests were completed on poly-XTL rutile samples sliding against themselves, both in vacuum and in  $P_{Ox}$  (see 3.2.4). It is believed that the loss of surface oxygen on heating in vacuum is sufficiently rapid for the gradually changing friction forces to bypass the peak value at  $TiO_{1.80}$ . However, the replenishment of surface oxygen by dissociative chemisorption of the residual water and oxygen while cooling in vacuum is much slower than the oxygen loss during heating. As a consequence, the gradual change in the friction-controlling Magnèli phases is sufficiently slow during the cooling cycle to allow the development of the highest possible  $\tau_s$  and COF maximum at  $TiO_{1.80}$ . In  $P_{Ox}$  the trend reverses itself; it is more difficult to lose oxygen from the surface by heating at higher partial pressures of oxygen, but much easier to resorb oxygen on cooling. This phenomenon persisted during all other SEM tribometer tests also, lending credence to its proposed cause.

As previously discussed in (12,14), all the surface softening/hardening changes occurred within a thin surface region (~2  $\mu m$ ) of the low wear rate rutile XTL (Fig. 11). Consequently, the  $P_y$  did not change significantly throughout the test. With a relatively stable yield strength combined with (a) our ability

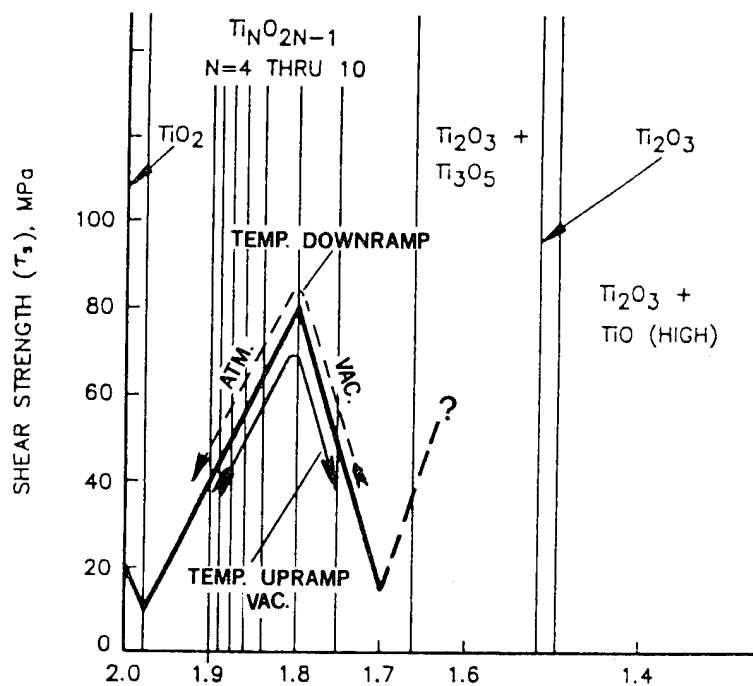
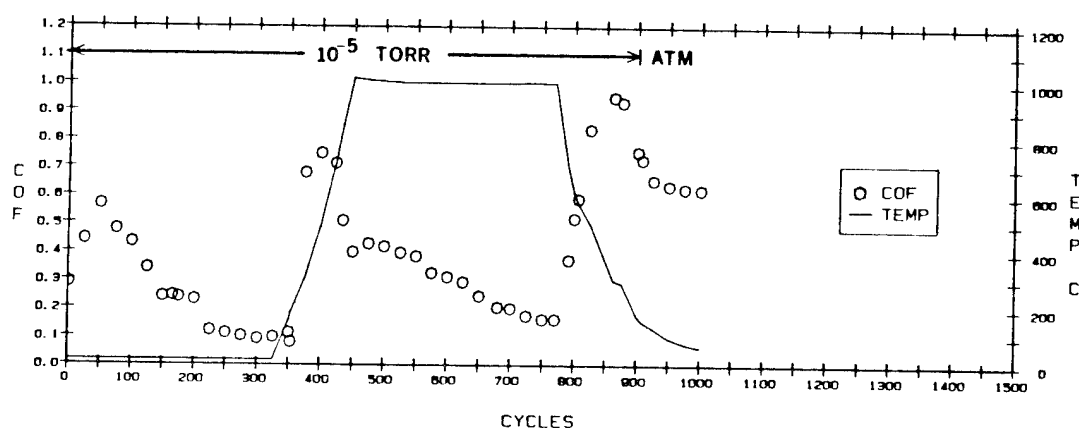


Figure 9. Coefficient of friction (COF) of a slightly-reduced single-crystal (001) rutile SEM triboflat sliding against a polycrystalline  $\alpha$ -SiC pin in the [110] direction, from (14); Figure 8 is reproduced for ease of data interpretation.

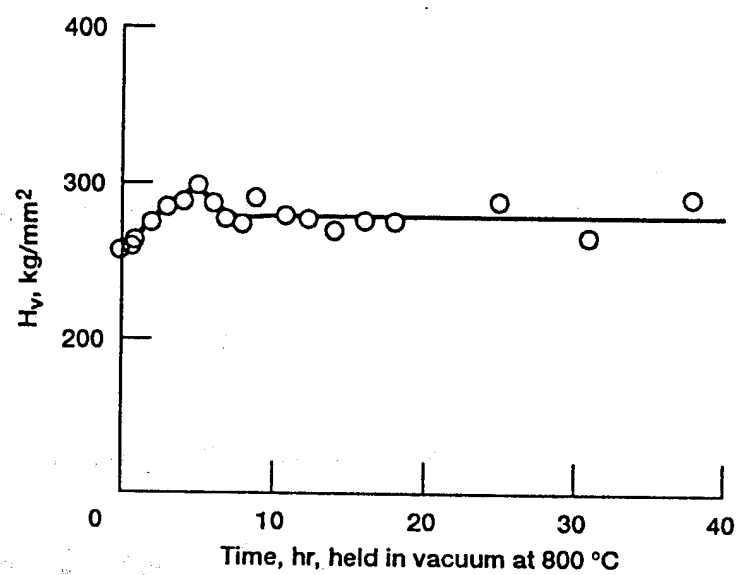


Figure 10. Vickers microhardness ( $H_V$ ) of (110) rutile during thermal exposure to vacuum ( $10^{-5}$  torr) at  $800^\circ\text{C}$ ; from (18).



← SINTER + HIP  $\alpha$ -SiC PIN

VS.

← (001)[110]  $\text{TiO}_{2-x}$  (RUTILE) FLAT

$$P_{\text{Hertz}} \approx 1.0 \text{ GPa}$$

$$P_{\text{final}} \approx 85 \text{ MPa}$$

$$\dot{V}_{\text{SiC}} \approx 7.3 \times 10^{-18} \text{ m}^3/\text{m}$$

• PIN (4 TESTS  $\approx$  5K-CYC  $\approx$  3511)

• FLAT (2 TESTS = 2.6 K-CYC)

Figure 11. Optical photomicrograph of single crystal (001) [110] rutile triboflat and mating  $\alpha$ -SiC pin after several SEM tribotests [from (12) and (14)].

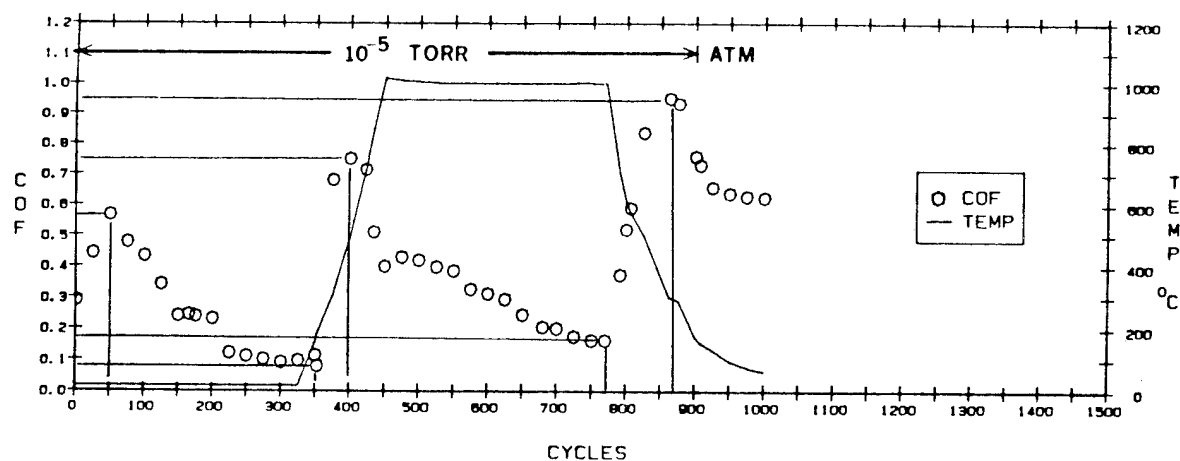
to measure the friction force ( $F_k$ ) accurately, and (b) the real area of contact ( $A_r$ ) with some degree of accuracy from the photographs (e.g., see Fig. 11),  $\tau_s$  may be estimated by using the equation similar to measuring viscosity:  $\tau_s = F_k/A_r$ . These shear strength estimates, fitted to the predictions of Fig. 8, are presented in Fig. 12.

A more accurate estimate of  $\tau_s$  could be obtained if we knew  $P_y$  as a function of temperature. One well-known estimate is  $P_y = H_v/3$  for ductile materials and  $H_v/35$  for brittle materials (12). As also discussed in (12), the problem of approximating  $P_y$  with these simple formulae lies in the uncertainties of determining whether a material of interest is brittle or ductile at a given temperature. Since the  $E_I$  goes through several strong-weak (hard-soft) changes, the hot-hardness tests in (18) (see Figs. 3 and 13) and those from (20) (Fig. 14), *qualitatively* confirm the Hughes hypothesis. The data could be made quantitative only if the indentation hysteresis loop energy and the related "true hardness" parameter had been determined for the various crystallographic orientations, and the effective resolved shear stresses for the slip (and twinning) systems were calculated and applied to the indentation behavior. Some of these steps were already taken and the remaining shortcomings were discussed in (18).

In Fig. 14, the hardness of nanocrystalline rutile is shown to increase as the air-sintering temperature increases (due to some oxygen loss from the surface). After hot-sintering in vacuum, where oxygen loss is even more efficient, the hardness is even higher. These results are also in accordance with the predictions in Figs. 1 and 8.

The  $P_y$  of rutile may be estimated better from the stress-strain curves of XTL samples taken from (21) and reproduced here as Fig. 15. The yield stress was measurable only at 650°C (~100 MPa at  $10^{-5}$  torr). Below that temperature the compressed specimens shattered. Near 1000°C,  $P_y$  dropped to ~80 MPa at the same low atmospheric pressure. Johnson et al, (22) also found that the lowest temperature at which detectible plastic deformation of a fully stoichiometric rutile XTL occurred (in air) was 572°C, with a value of 103 MPa. Therefore, taking  $P_y$  as approximately 100 MPa for at least the XTL samples and using the previously presented equality of  $\text{COF} = \tau_s/P_y$ ,  $\tau_s$  may be estimated by multiplying the measured COF by 100. The hardness data from Fig. 13 indicate that the yield strength of poly-XTL rutile would be somewhat lower than 100 MPa. It might be less by anywhere from 10 to 40%, depending on the temperature and the microcrystallinity.

Using this simple method of  $\tau_s$  estimation and comparing the values so calculated with the  $\tau_s = F_k/A_r$  method in Fig. 12, the two values are reasonably close: 25 vs. 29 MPa at  $\text{TiO}_{2.00}$ , 7 vs. 8 MPa at  $\sim\text{TiO}_{1.98}$ , 62 vs. 75 MPa (obtained during the heating cycle) and 78 vs. 95 MPa (obtained during the cooling cycle) at  $\text{TiO}_{1.80}$ , and 15 vs. 17 MPa at the predicted stoichiometry of  $\text{TiO}_{1.70}$ . These approximate values provided the general basis of preparing Fig. 1 (and Fig. 8).



NO. OF CYCLES	$f_k$	SCAR WIDTH (mm)	$F'_k$ (kg)	$A$ (mm <sup>2</sup> )	$\tau$ (MPa)	OXYGEN STOICHIOMETRY
2	0.29	$90 \times 10^{-3}$	$15 \times 10^{-3}$	$6 \times 10^{-3}$	25	2.00
350	0.08	$90 \times 10^{-3}$	$4 \times 10^{-3}$	$6 \times 10^{-3}$	7	~1.98
400	0.75	$90 \times 10^{-3}$	$38 \times 10^{-3}$	$6 \times 10^{-3}$	62	1.80
870	0.95	$90 \times 10^{-3}$	$48 \times 10^{-3}$	$6 \times 10^{-3}$	78	1.80
770	0.17	$90 \times 10^{-3}$	$9 \times 10^{-3}$	$6 \times 10^{-3}$	15	1.70

Figure 12. Rutile surface shear strength ( $\tau_s$ ) estimates based on the friction forces measured from Fig. 9 and the real area of pin-flat contact ( $A_r$ ) estimated from Fig. 11.

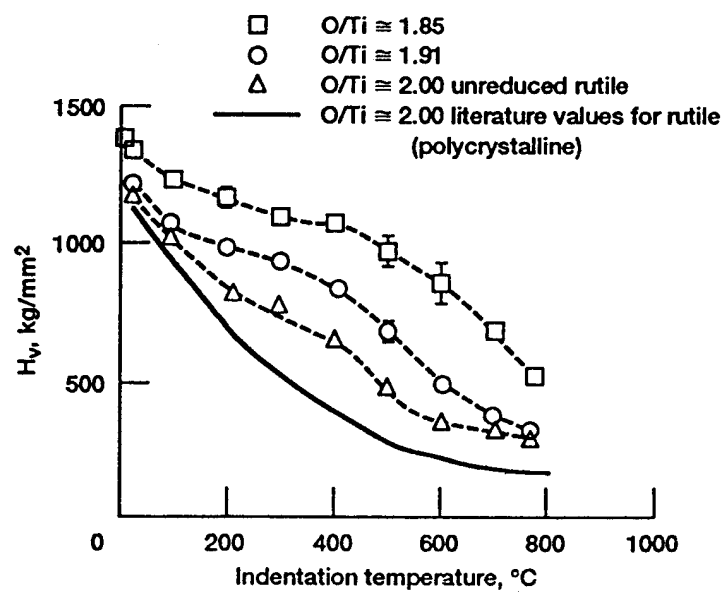


Figure 13. Vickers microhardness ( $H_v$ ) for stoichiometric and reduced (110) rutile as a function of indentation temperature; from (18).



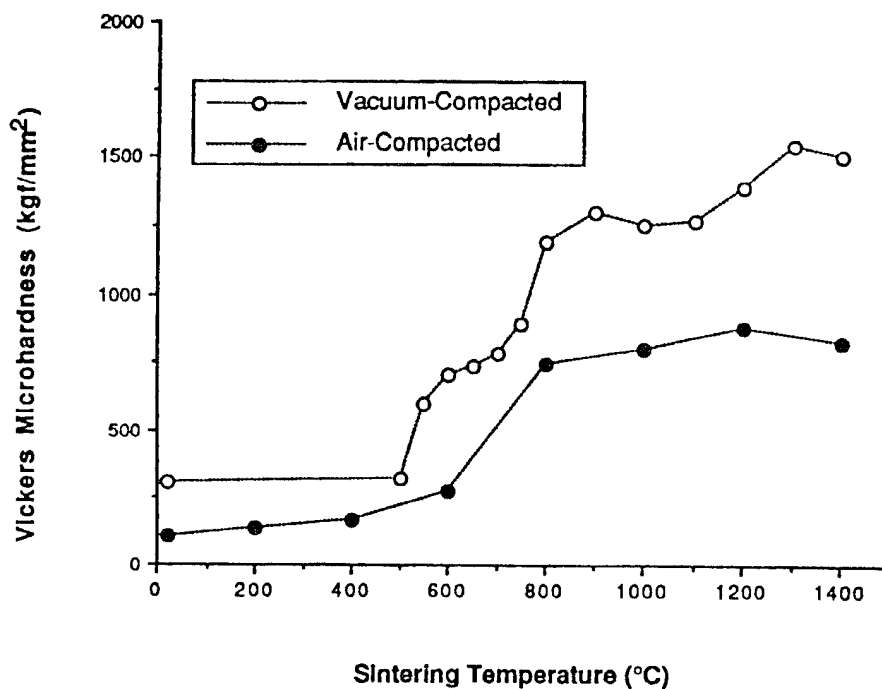


Figure 14. Vickers microhardness ( $H_V$ ) of 12 nm average grain-sized  $\text{TiO}_2$  (rutile) samples measured at room temperature as a function of one-half hour sintering at successively high temperatures in air, as compared to a sample prepared via normal nanophase processing route using vacuum compaction, with no exposure to air; from (20).

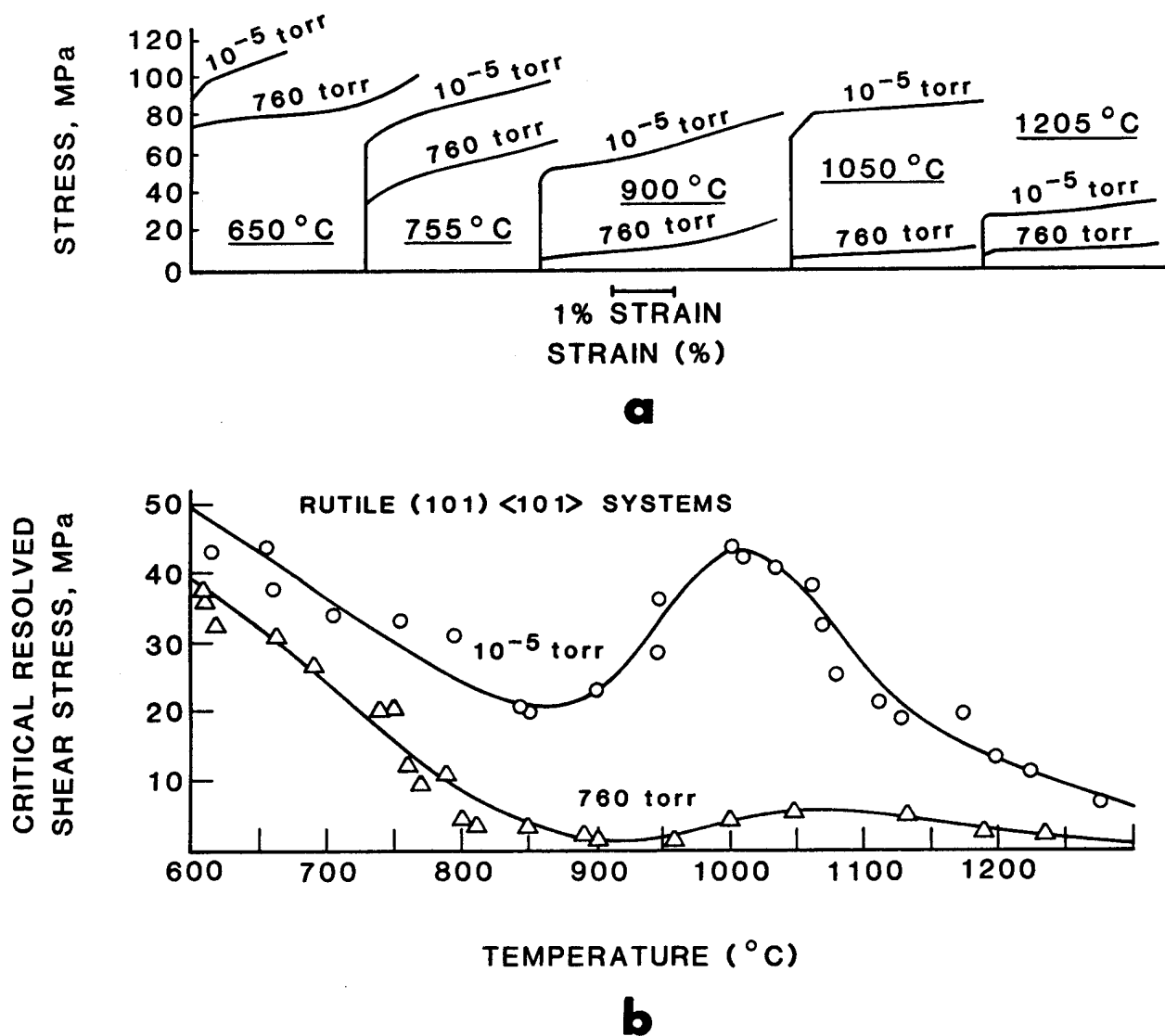


Figure 15. Temperature and atmospheric pressure effects on the deformation of single crystals of rutile: (a) engineering stress-strain curves; (b) the critical resolved shear stress function of the  $\{101\} \langle 101 \rangle$  system; from (12), (13) and (21).

### 3.2.3 SEM Tribometry of Polycrystalline Rutile vs. Polycrystalline $\alpha$ -SiC

SEM tribotests were also completed with two stoichiometries of the five pressureless-sintered rutile triboflat and pin sets prepared for us by Dr. Kevin Kendall of the Imperial Chemical Industries (ICI), Ltd., England (now with the University of Keele, England), with the assistance of Dr. Robert L. Clarke of Ebonex (then a senior executive with that ICI subsidiary in the U.S.; now the President and CEO of Dextra Associates, Orinda, CA). The respective stoichiometries of the test flats were  $\text{TiO}_{2.00}$  and  $\text{TiO}_{1.95-2.00}$ . The test procedure was identical with the one previously used for the XTL specimen.

The wear scar appearance of the fully stoichiometric XTL flat is compared to those of the poly-XTL rutile flats in Fig. 16. The  $A_r$  estimates based on the scar conditions continually measured by *in situ* video (12), combined with the respective COF data comprised the basis for the  $\tau_s$  estimates in Figs. 17 and 18 [also taken from (12)]. The COF charts exhibited the characteristic and clear-cut friction trends previously observed with the XTL sample only during the third experiment on the same flat, as found before. Since Fig. 18 is associated with a flat already pre-reduced to a mildly oxygen-deficient state of  $\text{TiO}_{1.95-2.00}$ , the efficiency of oxygen loss by heating in vacuum may require a potential gradient set up by a surface which is at least, or more, substoichiometric than  $\sim\text{TiO}_{1.975}$ .

The  $\tau_s = F_k/A_r$  data of the  $\text{TiO}_{2.00}$  flat indicated lower values than those measured with the XTL equivalent, although the COF trend generally followed the prediction. The data of  $\text{TiO}_{1.95-2.00}$  were more in line with the  $\tau_s$  predicted in Figs. 1 and 8. This is significant because the XTL flat was purposely roughened by stroking with a fine diamond paper normal to the direction of sliding, (see 12,14), while the roughness of the purposely pre-reduced flat was higher. A rougher surface was generated by the grain growth that occurs during the heating and post-baking steps of the preparation process of substoichiometric rutile electrodes. Higher COF measured with rougher surfaces which exhibit smaller  $A_r$  indicate profound changes in the  $\tau_s$  of the exposed asperities. Furthermore, since the  $P_y$  of a poly-XTL  $\text{TiO}_{2.00}$  rutile should be lower than that of an XTL sample just as its hardness commensurately is (see Fig. 13), multiplying the lower COF of the fully stoichiometric sample with something less than the previously estimated  $P_y = 100$  MPa factor will result in low  $\tau_s$  values.

The data in Figs. 17 and 18 show that only the pre-reduced sample exhibits a higher COF on cooling than on heating. Since none of these samples received duplicate testing, it is not known whether this anomaly is attributed to a repeatability problem or a real experimental artifact.

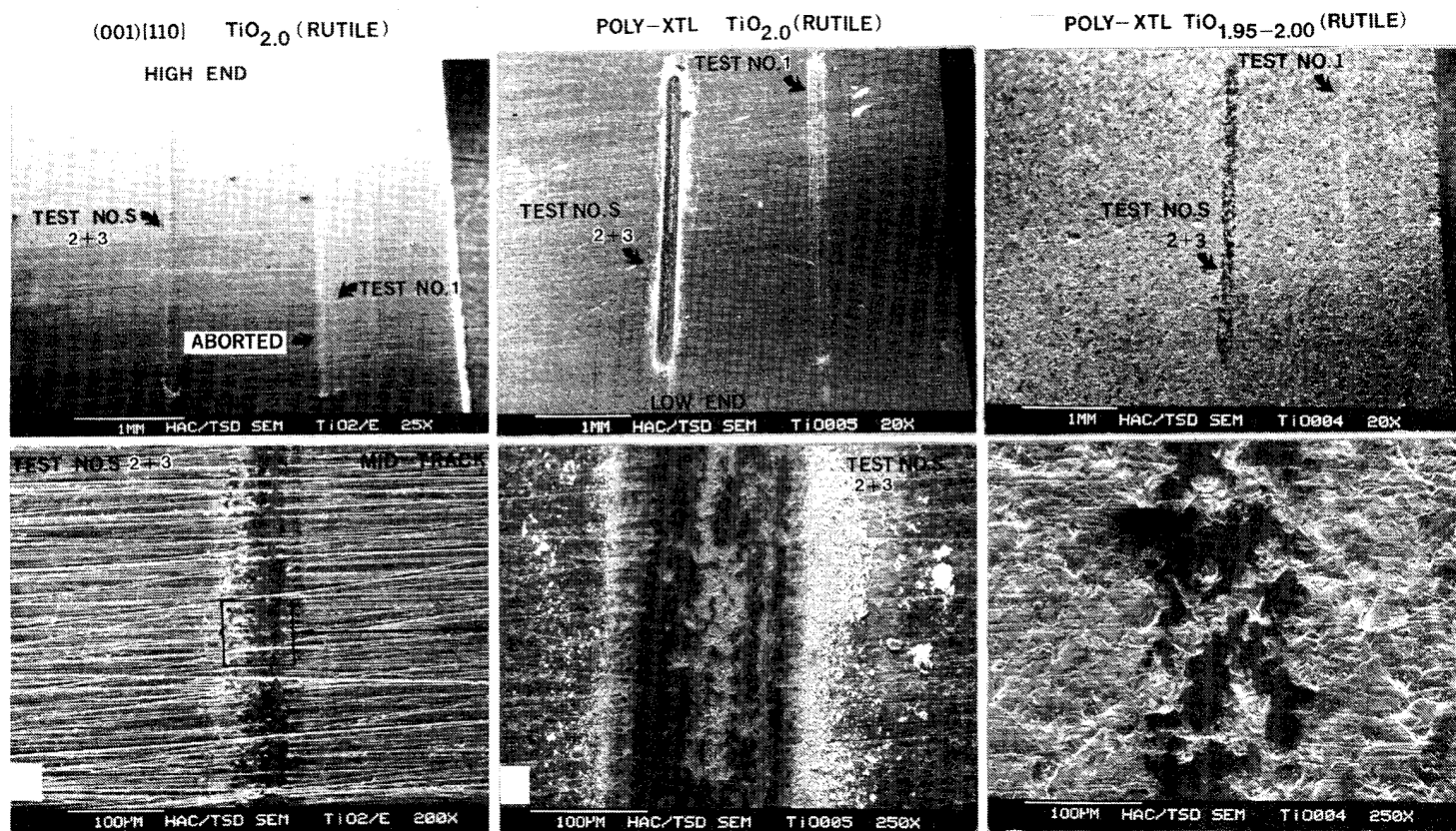
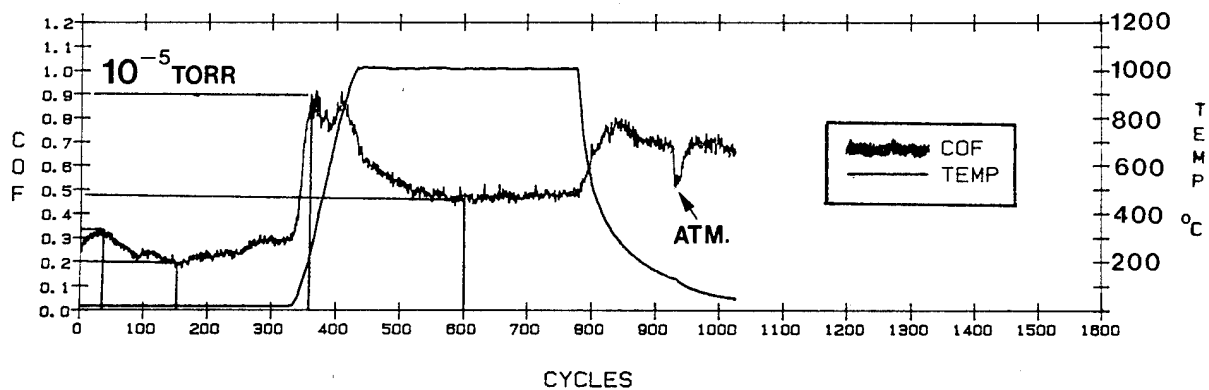
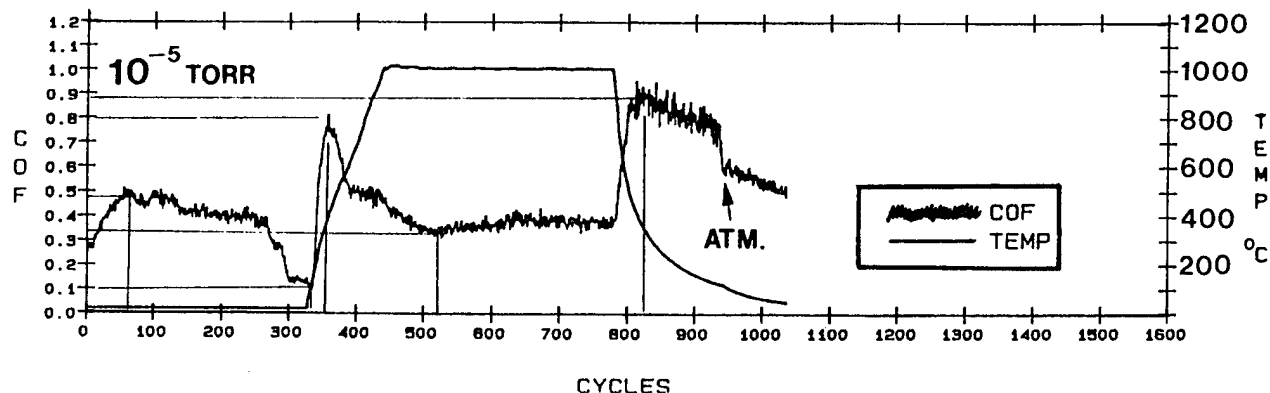


Figure 16. SEM photomicrographs of identically SEM-tribotested portions of rutile triboflats: the fully stoichiometric  $\text{TiO}_{2.00}$ (001) [110] single crystal and polycrystalline flats and the reduced polycrystalline  $\text{TiO}_{1.95-2.00}$  flat, at various magnifications.



NO. OF CYCLES	$f_k$	SCAR WIDTH (mm)	$F'_k$ (kg)	A (mm <sup>2</sup> )	$\tau$ (MPa)	OXYGEN STOICHIOMETRY
2	0.25	$102 \times 10^{-3}$	$17 \times 10^{-3}$	$8 \times 10^{-3}$	21	2.00
150	0.20	$108 \times 10^{-3}$	$10 \times 10^{-3}$	$9 \times 10^{-3}$	11	~1.98
370	0.90	$120 \times 10^{-3}$	$45 \times 10^{-3}$	$11 \times 10^{-3}$	40	1.80
600	0.48	$132 \times 10^{-3}$	$24 \times 10^{-3}$	$14 \times 10^{-3}$	17	1.70

Figure 17. Surface shear strength ( $\tau_s$ ) estimates of an SEM-tribotested, fully stoichiometric ( $\text{TiO}_{2.00}$ ) polycrystalline rutile triboflat sliding against a polycrystalline  $\alpha$ -SiC pin, based on the measured friction forces and the real area of pin-flat contact ( $A_f$ ) estimated from Fig. 16.



NO. OF CYCLES	$f_k$	SCAR WIDTH (mm)	$F_k$ (kg)	$A$ (mm <sup>2</sup> )	$\tau$ (MPa)	OXYGEN STOICHIOMETRY
55	0.48	$80 \times 10^{-3}$	$24 \times 10^{-3}$	$5 \times 10^{-3}$	47	2.00
335	0.10	"	$5 \times 10^{-3}$	"	10	~1.98
350 / 825	0.80 / 0.88	"	$\frac{40 \times 10^{-3}}{44 \times 10^{-3}}$	"	78 / 86	1.80
530	0.34	"	$17 \times 10^{-3}$	"	33	1.70

Figure 18. Surface shear strength ( $\tau_s$ ) estimates of an SEM-tribotested, reduced-polycrystalline  $\text{TiO}_{1.95-2.00}$  rutile triboflat sliding against a polycrystalline  $\alpha$ -SiC pin, based on the measured friction forces and the real area of pin-flat contact ( $A_r$ ) estimated from Fig. 16.

The tribological behavior of rutile sliding against  $\alpha$ -SiC has important practical implications. Lubricious rutile is one possible alternative to pyrocarbon and h-BN coatings deposited onto the SiC fiber reinforcement of ceramic-ceramic composites. These coatings provide controlled break-away between the fiber and the matrix, enhancing the fracture toughness of the composite. The reactivity of such coatings with either the fiber or the matrix in the presence of an often oxidative environment frequently results in brittle interlayers, which no longer serve as lubricious solid films.

SiC fibers are invariably coated with a thin layer of silica. Therefore, the interaction between  $\text{TiO}_2$  and  $\text{SiO}_2$  is of interest. Although the solubility of silica in titania is too small to be detected up to the  $1550^\circ\text{C}$  eutectic temperature (Fig. 19) by XRD lattice parameter measurements and by infrared (IR) spectroscopy (23), it may be an important factor in defect-related transport where parts-per-million quantities could influence interfacial properties. Substitutional replacement of  $\text{Si}^{4+}$  for  $\text{Ti}^{4+}$  would not cause changes in diffusive transport on the basis of well-established aliovalent defect models. However, the same  $\text{Si}^{4+}$  acting as an interstitial ion could displace a  $\text{Ti}^{4+}$  interstitial and would require a greater electron concentration for electroneutrality.

Since (a) titania and silica are commonly used in optical thin film (rugate) filters in the visible and the near-IR wavelength ranges, and (b) optical coatings can be subjected to high temperatures during processing (e.g., annealing) or in use (e.g., as exposed to laser or energetic particle irradiation), one can turn to the literature dealing with these disciplines to predict the extent of any interfacial reaction.

A Raman study of silica-titania sol-gel glasses (24) showed that after heat-treating these glasses containing higher  $\text{TiO}_2$  concentrations at temperatures to  $700^\circ\text{C}$ , some  $\text{Ti}^{4+}$  ions do become incorporated into the silica network. Also, Raman intensity bands were associated with vibrational modes involving  $[\text{SiO}_4]$  units linked with titanium atoms (24). The increased number of Si-O-Ti bridges were attributed to the continuous hydrolytic polycondensation reactions strengthening the network during thermal treatment. Elevated temperature processing results in a larger number of  $\text{Ti}^{4+}$  ions incorporated into the network, possibly stressing the structure by distorting the tetrahedral units of silica. However, the characteristic absorption bands for the Si-O-Ti bridges completely disappeared after heating at  $950^\circ\text{C}$  for 10 hours and the exsolved  $\text{TiO}_2$  crystallized out to form anatase. After thermal treatment at  $1200^\circ\text{C}$  for 24 hours, there was an anatase-to-rutile phase transformation.

A more recent study on coprecipitated silica-titania mixtures calcined at  $450^\circ\text{C}$  confirmed the entrance of  $\text{Ti}^{4+}$  ions, in small amounts, into the silica network (25). Even though the resulting  $\text{SiO}_2$ - $\text{TiO}_2$  was still regarded as a mechanical blend, the incomplete tetrahedral coordination of the normally octahedrally coordinated  $\text{Ti}^{4+}$  ions exposed on the surfaces did form strong Lewis acid sites. Since silica

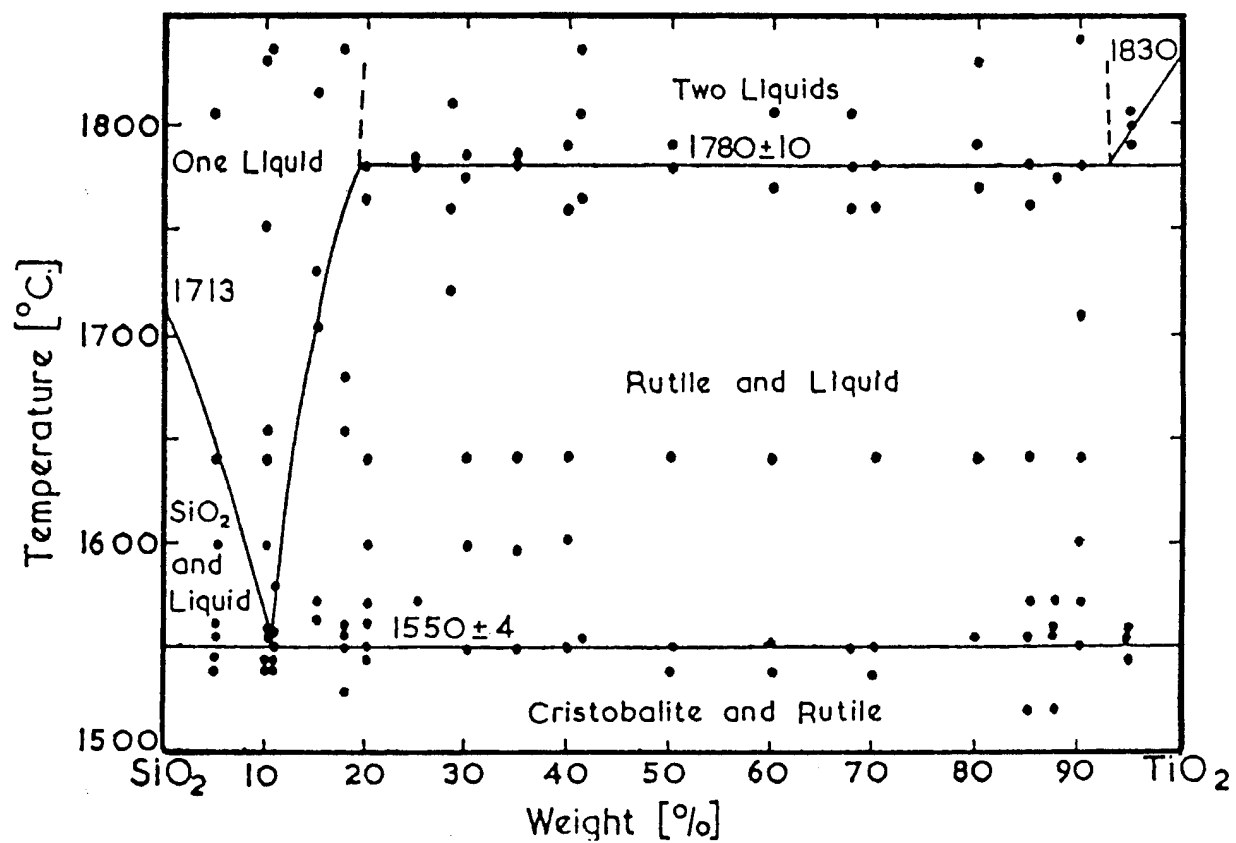


Figure 19. Phase diagram of  $\text{TiO}_2$  -  $\text{SiO}_2$ ; from (23).



displays Lewis acidity at high temperatures in vacuum, what happens here differs very little from what would transpire at a doped rutile (also containing Lewis acid sites) vs. silica-coated SiC fiber interface.

The observation of alternating-layered thin films of pure  $\text{SiO}_2$  and  $\text{TiO}_2$  heated to  $1100^\circ\text{C}$  showed that such sandwiched layers behave differently from codeposited phases. While the codeposited films were transformed to rutile [as observed in (24)], the alternating layers remained as anatase. Prolonged annealing at  $900^\circ\text{C}$  left a  $1000\text{\AA}$   $\text{TiO}_2$  layer with only very weak rutile diffraction lines (26). The effect of sorbed water in these films appears to be negligible at our temperatures of interest [i.e., at  $700^\circ\text{C}$  and above, see (27)].

While the above data indicate little possibility of adverse reactions between the thin  $\text{SiO}_2$  and  $\text{TiO}_2$  layers, the most convincing data are provided by an ion-mixing study of thin Ti and  $\text{TiO}_y$  films deposited on  $\text{SiO}_x$  substrates (28). While ion implantation resulted in a ten-fold increase in adhesion at the Ti/ $\text{SiO}_x$  interface, there was no similar increase at the  $\text{TiO}_y/\text{SiO}_x$  junctions. The adhesion enhancement in the former case was ascribed to increased Si-O-Ti bonding. The absence of adhesion at the latter interface stemmed from the separation of the titania and silica phases.

In the absence of the silica interlayer or at the high temperatures where SiC fiber-reinforced ceramic-ceramic or ceramic-glass composites are prepared (e.g.,  $1200^\circ$  to  $1350^\circ\text{C}$ ), reduction-oxidation reactions can occur between SiC and  $\text{Ti}_n\text{O}_{2-n}$  rutile phases. During hot-pressing of such composites, the titania additive in a glass matrix reacted with the silicon carbide fibers, forming a titanium silicide phase that severely degraded fiber strength (29). There are also solid carbon and CO gas formed as byproducts of the reaction.

It may be concluded that there should be no harmful increase in adhesion resulting from any minor interfacial reaction between  $\text{SiO}_2$  and a rutile layer. The low  $\tau_s$  of the rutile layer would ideally be controlled by the molecularly engineered rutile + dopant chemistry. Any minor diffusion into the silica network would be retarded by the equilibrium electrochemical potential field that exists in the doped rutile's lattice. As such, the shear strength of the interface is not interfacial-reaction-dependent, but would be controlled by the engineered  $\tau_s$  of the doped rutile layer. However, this hypothesis would be accurate only if the dopant did not enter or catalyze the reaction in any way.

### 3.2.4 SEM Tribometry of Polycrystalline Rutile vs. Polycrystalline Rutile

ICI/Ebonex's capabilities to exercise some control over the stoichiometry of rutile tribospecimens were employed to prepare SEM flats and pins in five stoichiometries or stoichiometric ranges:  $\text{TiO}_{2.00}$ ,  $\text{TiO}_{1.95-2.00}$ ,  $\text{TiO}_{1.90-1.95}$ ,  $\text{TiO}_{1.80-1.85}$  and  $\text{TiO}_{1.70-1.75}$ . As previously shown in Figs. 1 and 2, the degree of reduction may be estimated by weight loss. Although the physical properties of the individual groups were not measured, they can be estimated by the properties of the standard Ebonex electrode material. It consists of primarily the  $\text{Ti}_4\text{O}_7$  ( $\text{TiO}_{1.75}$ ) and  $\text{Ti}_5\text{O}_9$  ( $\text{TiO}_{1.80}$ ) suboxides, having the highest conductivity (see Table 1). One new pair of pin-flat combination was tested in vacuum and in  $P_{\text{O}_x}$ , as shown in Fig. 20.

All vacuum tests followed the same procedure. Sliding was started at a chamber pressure was reduced to  $\sim 1 \times 10^{-5}$  torr, at room temperature. Thermal upramp to  $\sim 1000^\circ\text{C}$  began at 325 cycles, reaching the maximum test temperature in about 100 additional cycles. Sliding at the highest temperature continued to 900 cycles before the temperature was downramped. At 1125 cycles, laboratory air was admitted into the SEM chamber to observe differences in sliding behavior as a function of high  $P_{\text{O}_x}$  and the presence of atmospheric humidity. A test ends at 1200 cycles.

All  $P_{\text{O}_x}$  experiments were started in the lowest subchamber pressure provided by a mechanical vacuum pump ( $\leq 1 \times 10^{-2}$  torr). As with the vacuum tests, thermal upramp was initiated at 325 cycles. At 625 cycles, 0.2 torr of 99.997% pure oxygen was admitted into the lidded subchamber, allowing a continually replenished and pumped  $P_{\text{O}_x}$  atmosphere to sweep over the hot triboflat. The thermal upramp was started at 925 cycles (as before), but now in the continued presence of 0.2 torr of oxygen. Three out of the five tests continued under this pressure to 1125 cycles, at which time atmospheric air was admitted into the SEM chamber and into the subchamber. Sliding was stopped after 1200 cycles, having rubbed the cooled interface in atmospheric air for  $\sim 75$  cycles prior to test termination. Two of the five tests ran longer (for 1500 cycles), having received a higher (3.4 torr) oxygen dose onto the cooled flat near 1250 cycles and the customary full dose of atmospheric air at  $\sim 1400$  cycles.

All the vacuum-to-atmosphere and  $P_{\text{O}_x}$ -to-atmosphere COF data are presented together in Fig. 20. The vacuum test results given on the left side of this illustration indicate the following:

Table 1. Typical properties of the EBONEX<sup>®</sup> substoichiometric rutile electrode material.

PROPERTY	TYPICAL VALUES	TEST METHOD
Chemical Formula	TiO <sub>x</sub> - Titanium suboxides Primarily TiO <sub>2</sub> O <sub>3</sub> & Ti <sub>2</sub> O <sub>3</sub>	XRD
Impurities	<0.5%	AA
Bulk Resistivity	<10 m -cm	4-Pt Probe
Bulk Density	3.15 +/- 0.3 g/cm <sup>3</sup>	ASTM C373-2
Water Absorption (Porosity)	0 -25%	ASTM C373-2
Permeability	0.33 cm <sup>3</sup> /(cm <sup>2</sup> . sec.MPa)	ASTM F417-78 3 Pt Bend
Flexural Strength	60 - 180 MPa	ASTM F417-78 1.2 Kg load
Hardness	230 H <sub>v</sub> (Vickers)	ASTM E18 -67 1.2 Kg load
Pore Size	1 - 2 um	
Surface Finish	R <sub>a</sub> = 2.5 um	Talysurf
Coefficient of thermal expansion	6 * 10 <sup>-4</sup> /°C @ ambient temperatures	ASTM C408-58
Thermal Conductivity	10-20 W/(m-K)	ASTM C408-58
Specific Heat	0.75 J/(gk)	ASTM C3511 - 61
Machinability	satisfactory with water cooled diamond saw and drill	

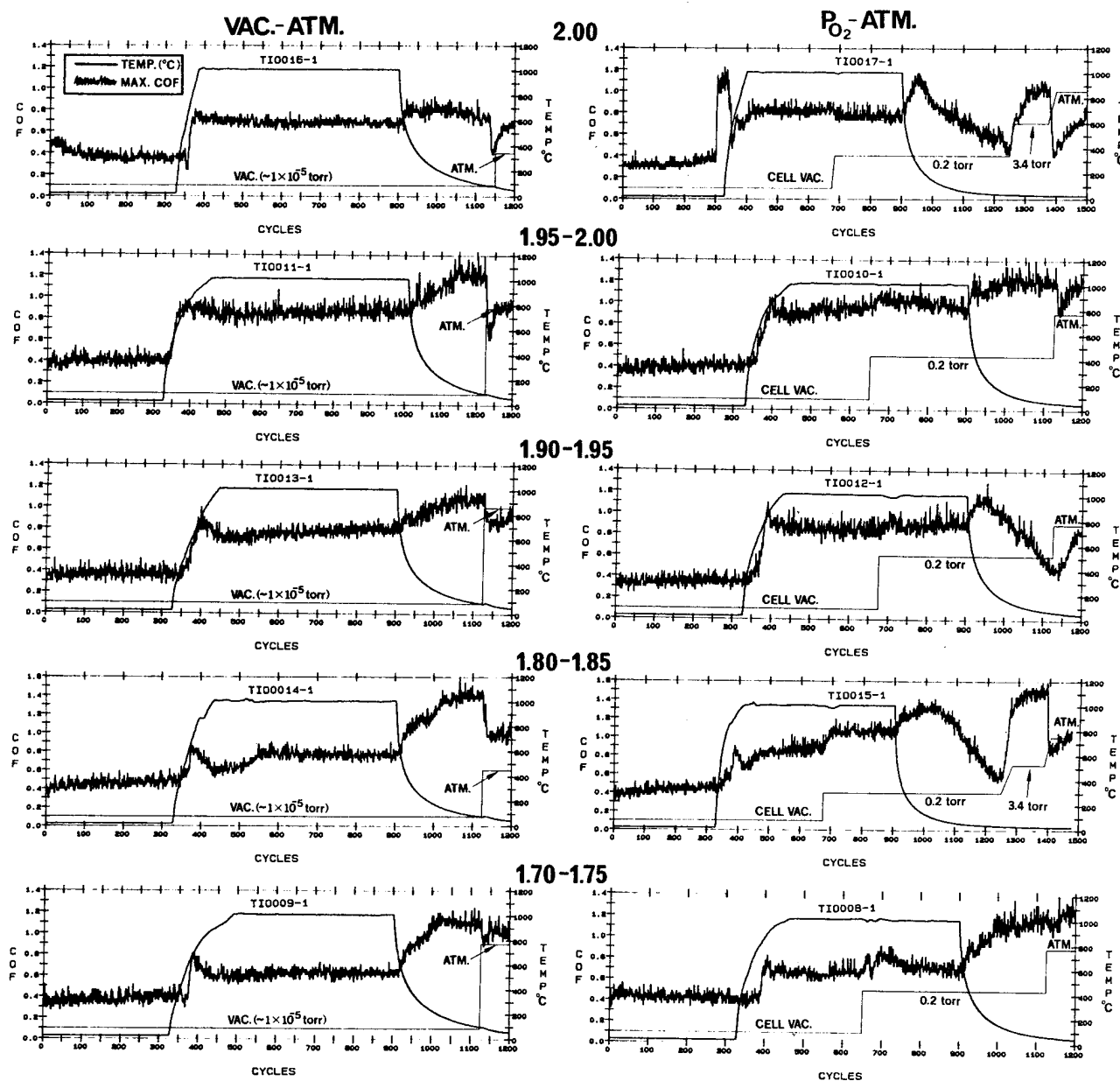


Figure 20. SEM tribometry results of polycrystalline rutile pin/flat combinations preconditioned to five different oxygen stoichiometry ranges, as indicated. Horizontal line markers of environmental atmospheric pressure are there only to show changes and their steps are not drawn to scale.

1. Heating the triboflats always causes a sudden rise in COF. The frictional increase on oxygen removal occurred as before with the XTL flat shown in Fig. 8. This increase is the largest with the least reduced samples ( $\text{TiO}_{1.95-2.00}$  and  $\text{TiO}_{1.90-1.95}$ ) and the smallest with the most reduced ones ( $\text{TiO}_{1.80-1.85}$  and  $\text{TiO}_{1.70-1.75}$ ). Samples that had been pre-reduced to a larger degree lose oxygen with progressively greater difficulty. Some pre-reduction appears to be necessary to set up an initial electrochemical potential gradient conducive for more ready oxygen loss from the flat on heating. This phenomenon was observed with the XTL flat also.
2. The COF curves exhibit the characteristic friction peak predicted by the solid-arrowed direction shown in Fig. 8, especially as pre-reduction became more severe. The exact nature of the mechanism governing the differences in peak sizes and shapes cannot be speculated upon at this time. It is suspected that the initial stoichiometry, any storage-generated "skin" with a slightly different stoichiometry and some wear of the changing surface all have control over the parameters.
3. The  $\tau_s$  function in Figs. 1 and 8 predicts that rutile reduced to  $\sim\text{TiO}_{1.70}$  should have lower friction than a sample reduced to  $\sim\text{TiO}_{1.80}$ . As shown by the data, this is indeed the case. The most reduced sample has the lowest steady-state COF under continued heating.
4. The COF increased to the highest level during each test as the triboflat was cooled near room temperature. As shown in Figs. 1 and 8, this increase is predicted to occur only if the stoichiometry of the thermally downramped flat was less than  $\text{TiO}_{1.80}$ . This increase is defined by the first part of the broken-arrowed direction in Fig. 8. The slowly condensing and dissociatively chemisorbing molecular oxygen gradually annihilates the vacancies, sending the  $\tau_s$  and COF values back up the negative slope of Fig. 8. An identical trend was observed with the XTL rutile flat. The degree of oxygen sorption (or that of the other oxygenated species, like residual water) realized in vacuum appears to be limited. Vacancy annihilation seems to be the most effective with the sample already nearest to its maximum predicted COF and  $\tau_s$  value (the  $\text{TiO}_{1.80-1.85}$  flat).
5. Introducing atmospheric air into the SEM chamber reduced the COF in each and every case. This is predicted by the second part of the broken-arrowed direction shown in Fig. 8. The extent of reduction depends on the equilibrium stoichiometry reached by a given sample during cooling in vacuum, before bleeding in air from the lab atmosphere.

These findings are now compared with the results of the  $P_{Ox}$  tests presented on the right side of Fig. 20:

1. An increase of pressure several orders of magnitude notwithstanding, there is still a sudden rise in COF when heating the flats. During thermal upramp and at 1000°C, the oxygen loss from the surface leading to another characteristic stoichiometric equilibrium appears to be more a function of the temperature than the pressure. It can be seen, however, that a higher pressure does postpone the onset of the sudden COF increase to higher temperatures (i.e., this sudden rise occurs at a larger number of cycles). In fact, the oxygen loss from the fully stoichiometric sample was slowed down to the point where the oxygen content vs. COF curve was able to climb at least a portion of the predicted  $TiO_{1.80}$  COF increase hill. There was no observable thermal upramp COF peak during the equivalent vacuum test. The maximum COF must have been bypassed rapidly due to a more effective oxygen removal process in higher vacuum: the oxygen equilibrium of the vacuum-heated flat's surface quickly landed somewhere on the negative slope of the function shown in Fig. 8.
2. The introduction of 0.2 torr of oxygen onto the hot flat allowed observing our ability to increase the COF, as predicted by the first portion of the broken-arrowed direction in Fig. 8. Depending on the affinity of the reduced surfaces to oxygen even at the highest temperature, the presence of suddenly introduced oxygen should increase (or at the very least not change) the stoichiometry of the sliding surface. Some commensurate COF increases are observed in each case, with the exception of the fully stoichiometric sample. The greatest COF increases occurred with the most reduced triboflats.
3. The sticking coefficient of oxygen or moisture on a triboflat can be increased by higher pressures at a given temperature or, even better, by reducing the surface temperature at a given pressure. During every test, the latter method was effective in raising the COF by cooling the triboflats in the 0.2 torr oxygen environment. This rise is commensurate with the onset of the broken-arrowed direction to the  $TiO_{1.80}$  stoichiometry in Fig. 8. Again, the highest growth in COF was observed with the most reduced flats. In three out of the five tests, these COF values did not attain equilibrium values. This disturbance of the equilibrium could be caused by two separate (synergistic or antagonistic) phenomena, as described in 4. below.

4. The gradual (unexpected and puzzling) drop in COF on continued cooling of the  $\text{TiO}_{2.00}$ ,  $\text{TiO}_{1.90-1.95}$  and  $\text{TiO}_{1.80-1.85}$  flats could be caused by spalling wear or by in-diffusion of oxygen. The possible (and unpredictably random) spalling or excessive wear of a newly developing surface layer is one explanation. This new surface is the yet-unchanged subsurface exposed by the sliding action. A competing hypothesis presumes that on thermal downramp the subsurface is more oxygen deficient than the re-enriched surface skin. The attractive forces set up by the internal electrochemical potential gradient (the depleted rutile lattice always hungers for more oxygen) can become greater than the rate of oxygen resupply to the surface from the low  $P_{\text{O}_2}$  environment. As shown later in this section, the pin tip and flat wear data could not separate the influence of these two variables unambiguously.
5. Whether or not just one, the other or both mechanisms hypothesized in 4. above are operative, injecting the even higher 3.4 torr  $P_{\text{O}_2}$  onto the cooled flat (see the  $\text{TiO}_{2.00}$  and  $\text{TiO}_{1.80-1.85}$  tests) increases COF even closer to the maximum value predicted to be at  $\text{TiO}_{1.80}$ . This increase parallels a similar one that occurred during the vacuum tests, just by cooling the flat in a more rarified atmosphere. The increase can be explained, as before, by the first portion of the broken-arrowed direction in Fig. 8. In fact, the higher  $P_{\text{O}_2}$  may have caused a reverse bypass of the largest possible COF value; the highest measured COF among all of the experiments (i.e., the  $\text{TiO}_{1.80-1.85}$  samples, on cooling the flats) occurred in vacuum, not in the 3.4 torr oxygen. The fact that the introduction of atmospheric air brought the COF down significantly during both tests indicates that the second part of the broken-arrowed direction was followed in each case. Two of the remaining three tests also exhibited some COF reduction on atmospheric bleed-in.

Since the actual stoichiometry of the rubbed triboflat surfaces could not be measured *in situ*, and there was no reliable way to estimate it as the tests progressed, by definition the measured friction trends are only qualitative proof of the Hughes hypothesis. Yield strength data combined with hot hardness results on the various rutile samples could have helped converting the measured COF values (representing a systems parameter) to  $\tau_s$  data (representing a fundamental material parameter). Then, the predictions shown here in Figs. 1 and 8 could be confirmed not just qualitatively, but quantitatively as well.

At first glance, the microindentation measurements in Fig. 3 might indicate some promise to connect hardness with yield strength and surface shear properties, as previously discussed with the XTL specimen. Unfortunately, one cannot ignore the high tangential shear forces (greater abrasiveness) and the inelastic strain caused by the sliding contacts fabricated from pressureless-sintered titania exhibiting

low tensile strength and fracture toughness. In the wake of the high COF tribocontact, the tensile cracks normal to the direction of sliding can cause a great deal of wear, even if the hardness of the ceramic were high. Nevertheless, one might attempt to make some predictions about the wear behavior of XTL vs. poly-XTL rutile by employing the data in Figs. 3 and 21 (30).

According to these data, the hardness and modulus of poly-XTL (nanophase) rutile are significantly less than those of the XTL. The strain rate sensitivity is, however, greater. This means that the polycrystalline-nanophase rutile is more ductile than the XTL. Higher ductility (lower hardness) of ceramics usually goes hand-in-hand with higher fracture toughness and lower wear. Yet, in the case of at least the nanophase rutile, the increased hardness with increasing sintering temperature is commensurate with an *increase* in fracture toughness. The toughness became higher even though the strain rate sensitivity was reduced on an increase in sintering temperature: at 600°C  $K_{Ic}$  (the critical stress intensity factor) is only  $1.0 \text{ MPa}\cdot\text{m}^{0.5}$ , while at 800°-to 1000°C  $K_{Ic}$  increases to  $2.8 \text{ MPa}\cdot\text{m}^{0.5}$  (31).

All this comes about through grain growth during prolonged heating in vacuum. An agglomeration of progressively larger grains bring the physical property values closer to those of the XTL, as shown in Fig. 21. There is less grain boundary sliding. In the case of the Ebonex electrode material (Table 1), the hardness ( $H_v = 260 \text{ kg/mm}^2 = 255 \text{ GPa}$ ) is low compared to the hardness of the high temperature-sintered nanophase versions. The low hardness of the Ebonex electrode material is somewhat surprising, because the ceramic is heated three times during its fabrication cycle to high temperatures: once during pressureless sintering, once during the hydrogen reduction cycle and once during heating in argon afterwards, to even out the stoichiometry throughout a mold by the diffusion of the oxygen vacancies.

This reportedly low hardness value was double-checked by Knoop indentation hardness measurements per ASTM C-849, using a 300 gram load (Fig. 22a). Six measurements yielded a Knoop hardness of  $508 \pm 34 \text{ kg/mm}^2$ , equivalent to a Vickers hardness value of  $\sim 300 \text{ kg/mm}^2$  (a reasonable correlation; see Table 1). However, this value is only about one-third the hardness of Kyocera's commercially available T-792 grade  $\text{TiO}_2$  and one-fourth the hardness of the harder and stronger T-744  $\text{TiO}_{2-x}$  (32). The structural integrity of the Ebonex electrode material is high enough to serve as a useful electrode, but does not appear to be high enough to act as a practical tribomaterial. Note that its fracture toughness could not be determined reliably using the Vickers indentation method (Figs. 22b and c), because the high porosity disturbed the induced stress field. A network of fine, branched cracks formed instead of straight and measurably extended cracks at the apexes. Repeated attempts to fabricate this electrode material into SEM tribometer specimens failed due to breakage and crumbling of the mold during machining.



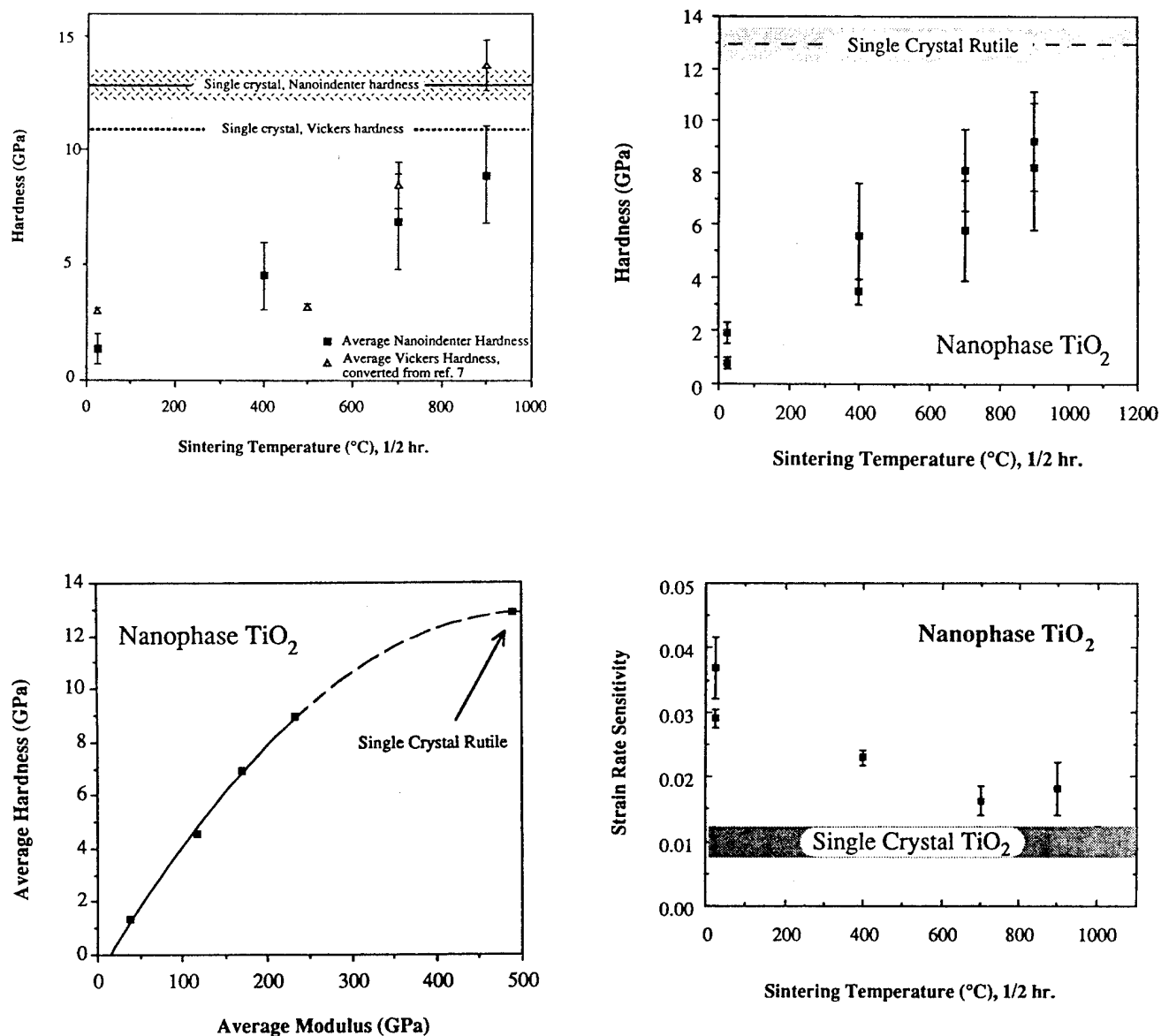


Figure 21. A collage of indentation hardness- and hardness-related data on an (001) single crystal rutile plane and on nanophase  $\text{TiO}_2$  sintered at various temperatures, in vacuum; from (30).

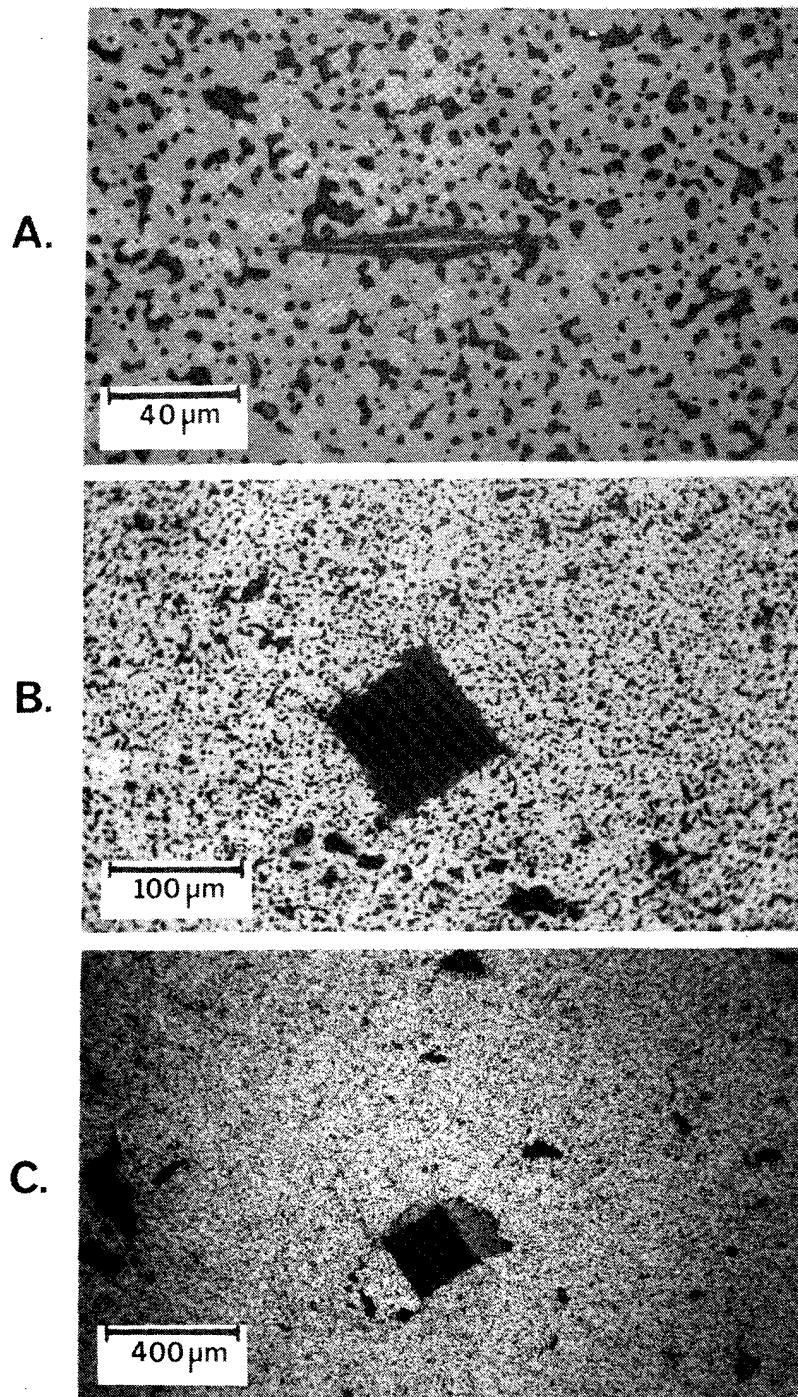


Figure 22. Indentation hardness measurements of EBONEX® ~Ti<sub>4</sub>O<sub>7</sub> (~TiO<sub>1.75</sub>): (a) Knoop at 300 g. load, 500x mag.; (b) Vickers at 5 kg load, 200x mag., (c) Vickers at 20 kg load, 50x mag.; (also see Table 1).

Clearly, predicting the wear of substoichiometric, pressureless sintered tribospecimens is not possible by the sometimes conflicting rules-of-thumb of ceramic tribology. Poor predictability is exacerbated by the less-than-ideal structural integrity of the model compounds. Our inability to predict wear and check the predictions against data notwithstanding, the ICI/Ebonex-reduced samples played a valuable role in elucidating friction and  $\tau_s$  behavior of XTL vs. polycrystalline rutile.

The pin-flat wear scars associated with the tests described in Fig. 20 are presented in Figs. 23 through 27. Outlining of the respective scars by black-and-white dots or lines was necessary, because even at the clear magnifications afforded by the SEM, sharp scar boundaries could not be discerned. Even with the boundaries highlighted, the identically magnified pin scars and the respective wear tracks on the flats do not match up exactly in terms of comparable widths. Nevertheless, the respective scar couples are similar in size and depict the same wear trend. The width or the wear plateau appearance of the scars is only a very rough approximation of  $A_r$  (the real area of contact) between each pin/flat combination and cannot be used for estimating  $\tau_s$  with the same confidence as in the previous case with the XTL sample. Moreover, the SEM tribometer assembly cannot heat the pin, whose scar size is the only means to measure wear by geometric (volume loss) considerations. Although one can estimate the temperature of the pin tip as the temperature of the contacting (and heated) flat, it is only an approximation. With these caveats in mind, the SEM photomicrographs in Figs. 23 through 27 indicate the following:

1. The preparation process to reduce rutile into substoichiometric ranges causes grain growth and porosity. The contact zone changes from a small apparent area of contact ( $A_{app}$ ) consisting of numerous small plateaus (see Fig. 23) to a large  $A_{app}$  consisting of fewer but larger plateaus (see Fig. 26). The respective  $A_r$  cannot be estimated without extensive computer-assisted image analysis. Because of the influence of all the other wear-measurement-influencing factors, such analysis did not seem to be warranted in the present case.
2. The respective scars of  $TiO_{2.00}$ ,  $TiO_{1.95-2.00}$  and  $TiO_{1.90-1.95}$  are smaller than those of  $TiO_{1.80-1.85}$  and  $TiO_{1.70-1.75}$ . The high friction materials had somewhat lower wear. The lowest friction material ( $TiO_{1.70-1.75}$ ) exhibited the highest pin tip wear. There is strong evidence for the spalling-type wear of all the substoichiometric rutiles, especially with the latter two samples.
3. Pressureless sintering is not an acceptable method of fabricating highly dense and strong lubricious rutiles.

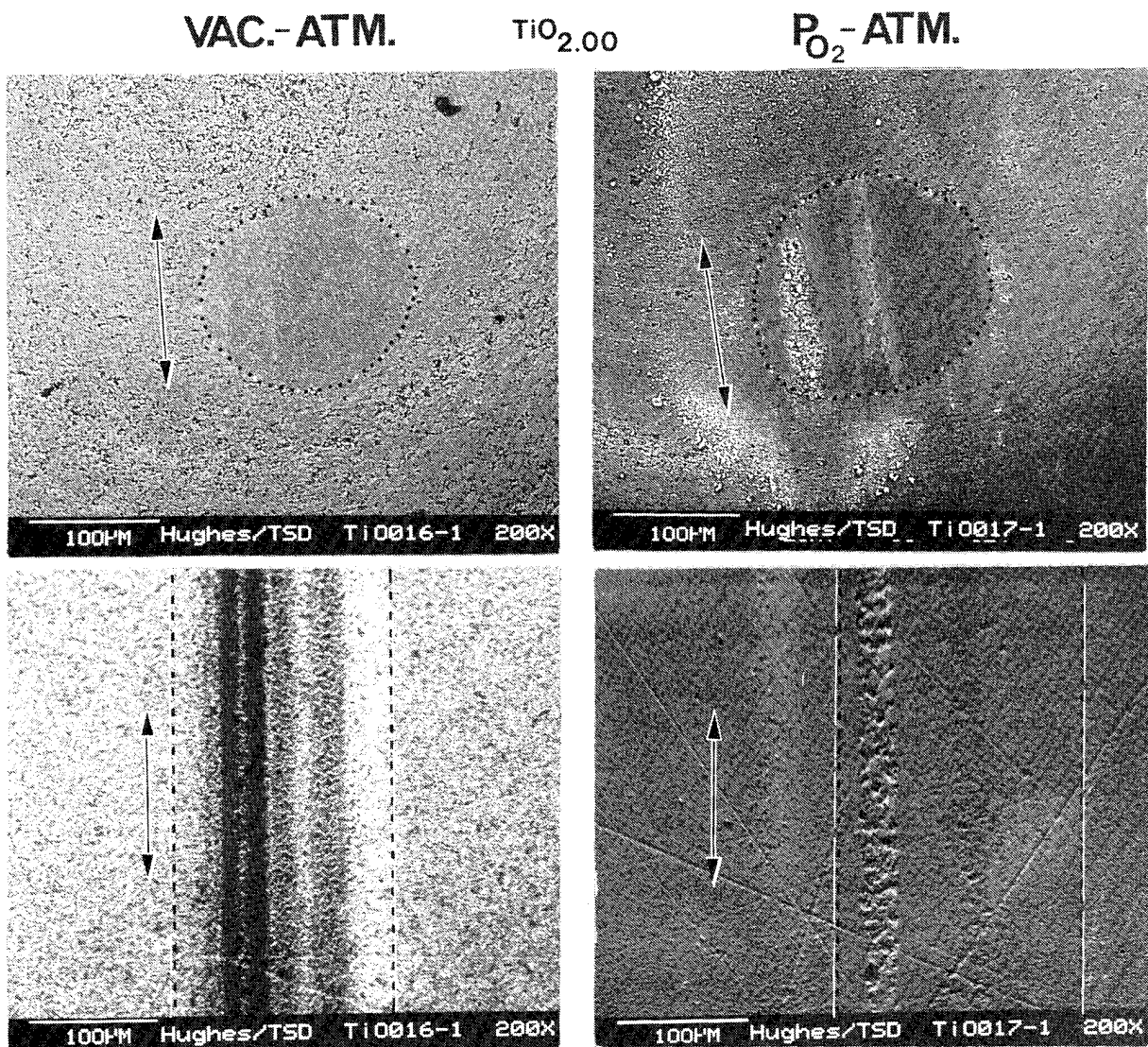


Figure 23. SEM photomicrograph pairs of SEM tribometer pin (top) and mating flat (bottom) wear scars corresponding to the  $\text{TiO}_{2.00}$  tests described in Fig. 20.

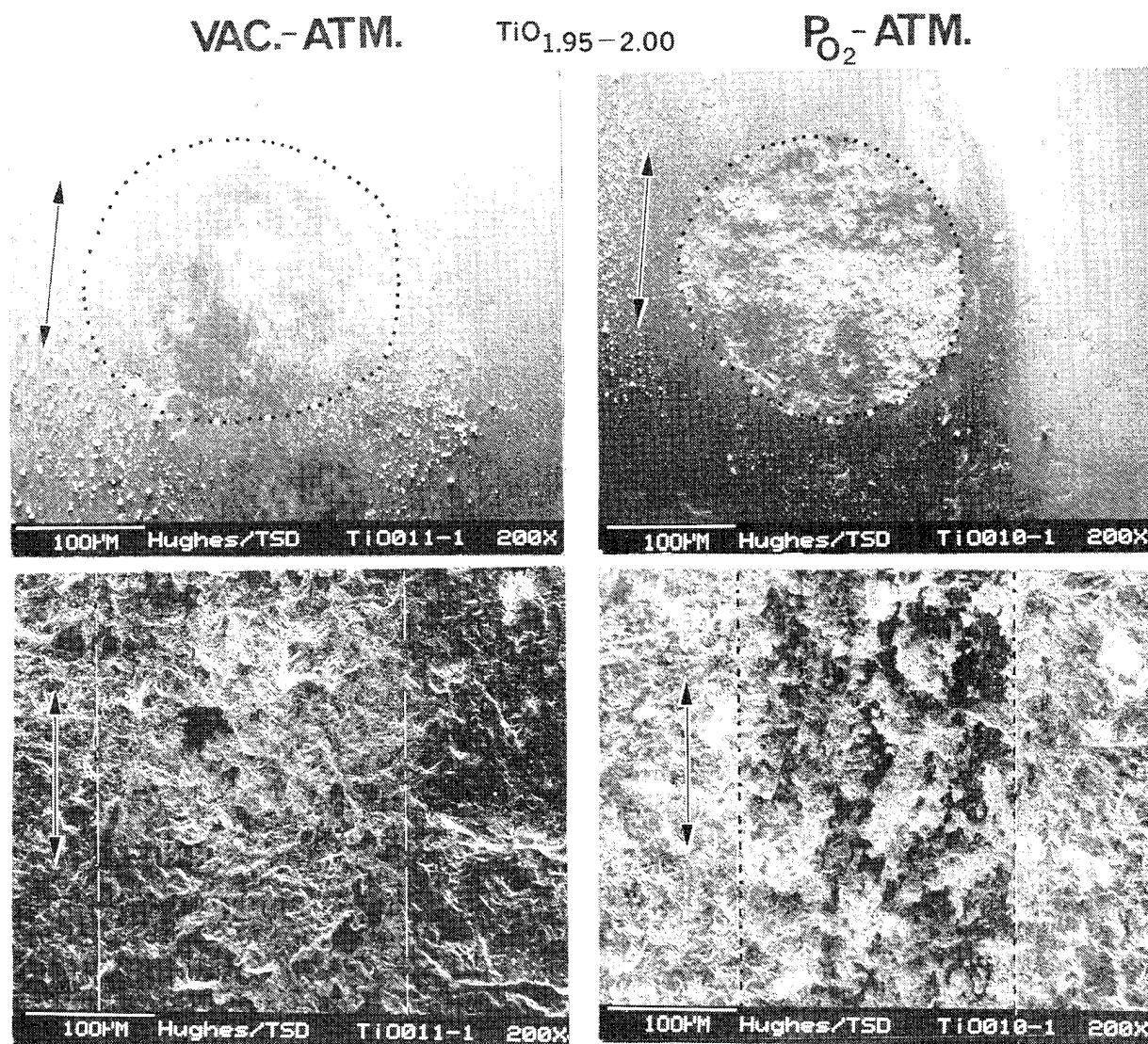


Figure 24. Same as Fig. 22 for  $\text{TiO}_{1.95-2.00}$ .



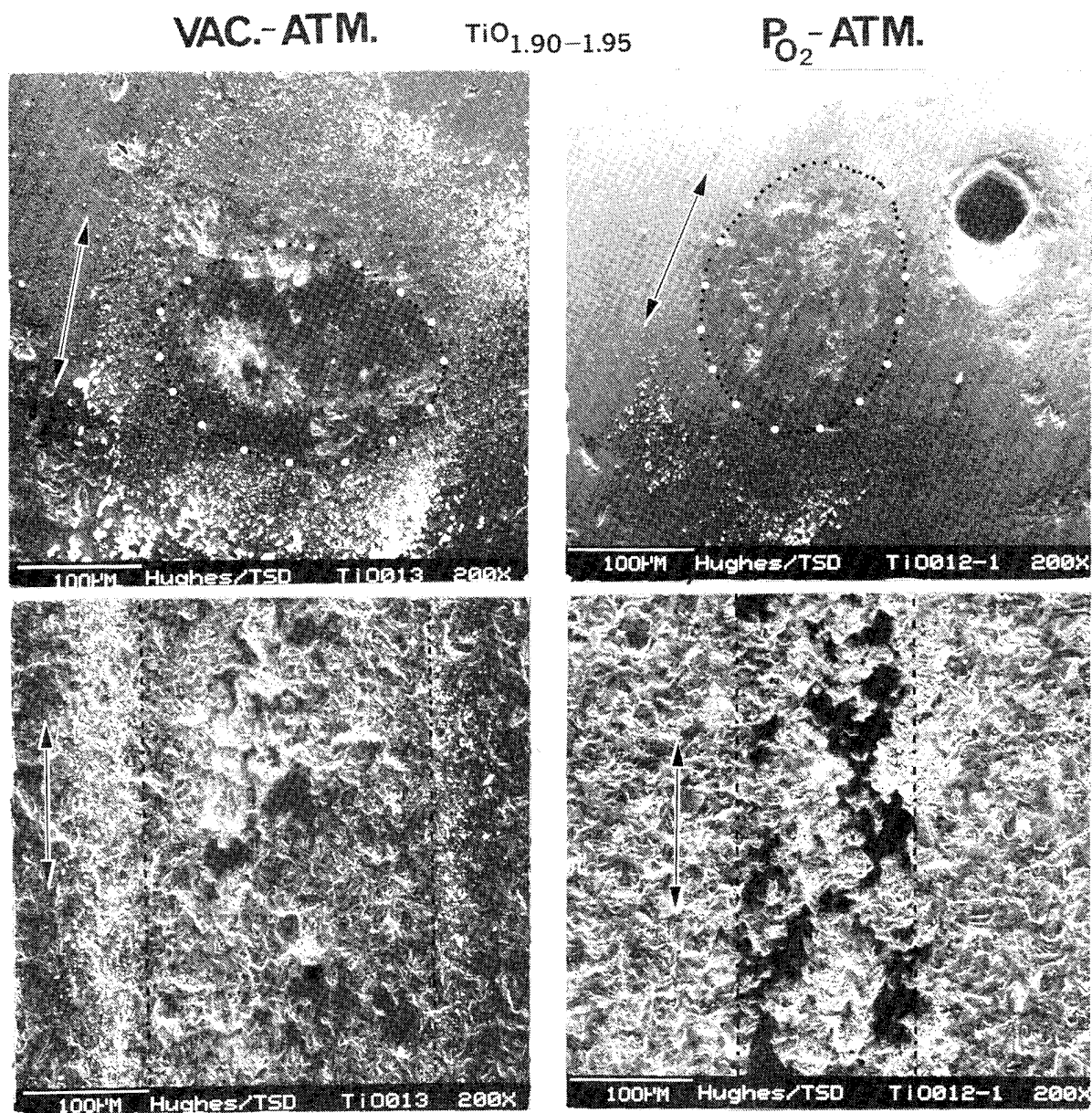


Figure 25. Same as Fig. 22 for  $\text{TiO}_{1.90-1.95}$ .

VAC.-ATM.

$\text{TiO}_{1.80-1.85}$

$\text{P}_{\text{O}_2}$ -ATM.

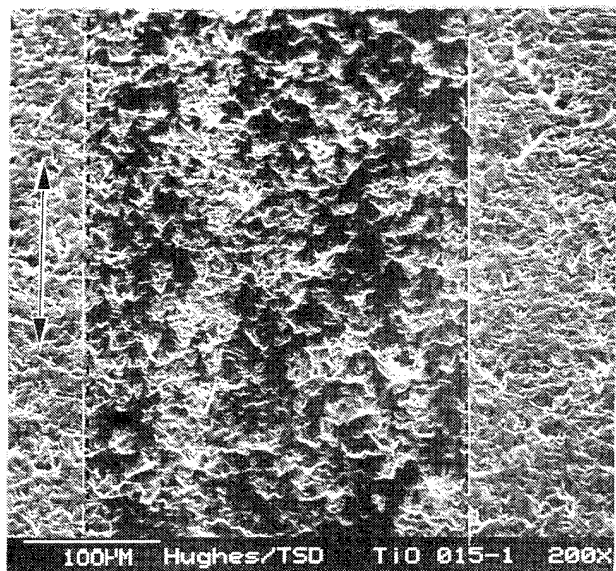
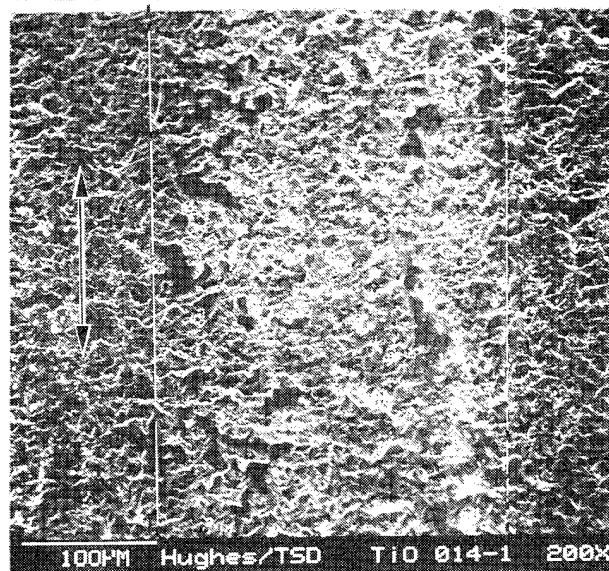
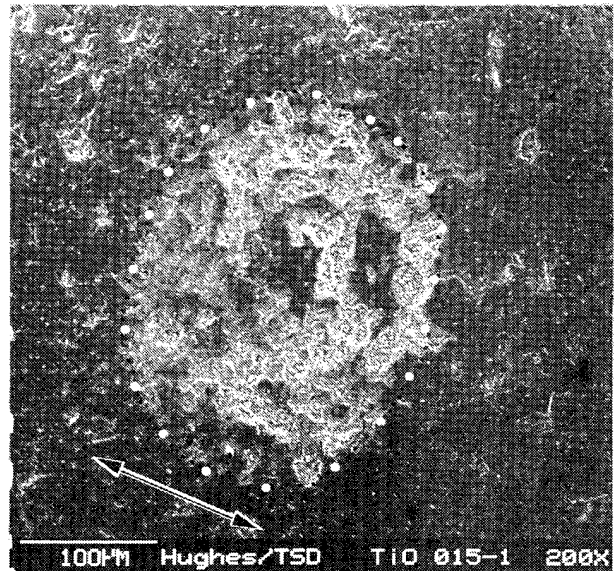
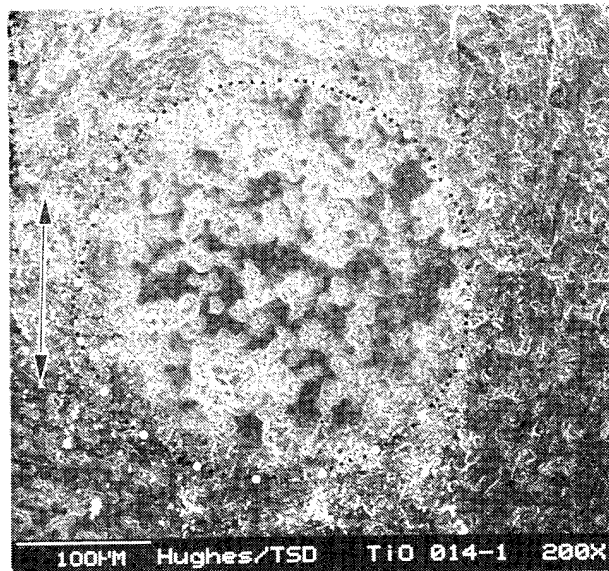


Figure 26. Same as Fig. 22 for  $\text{TiO}_{1.80-1.85}$ .

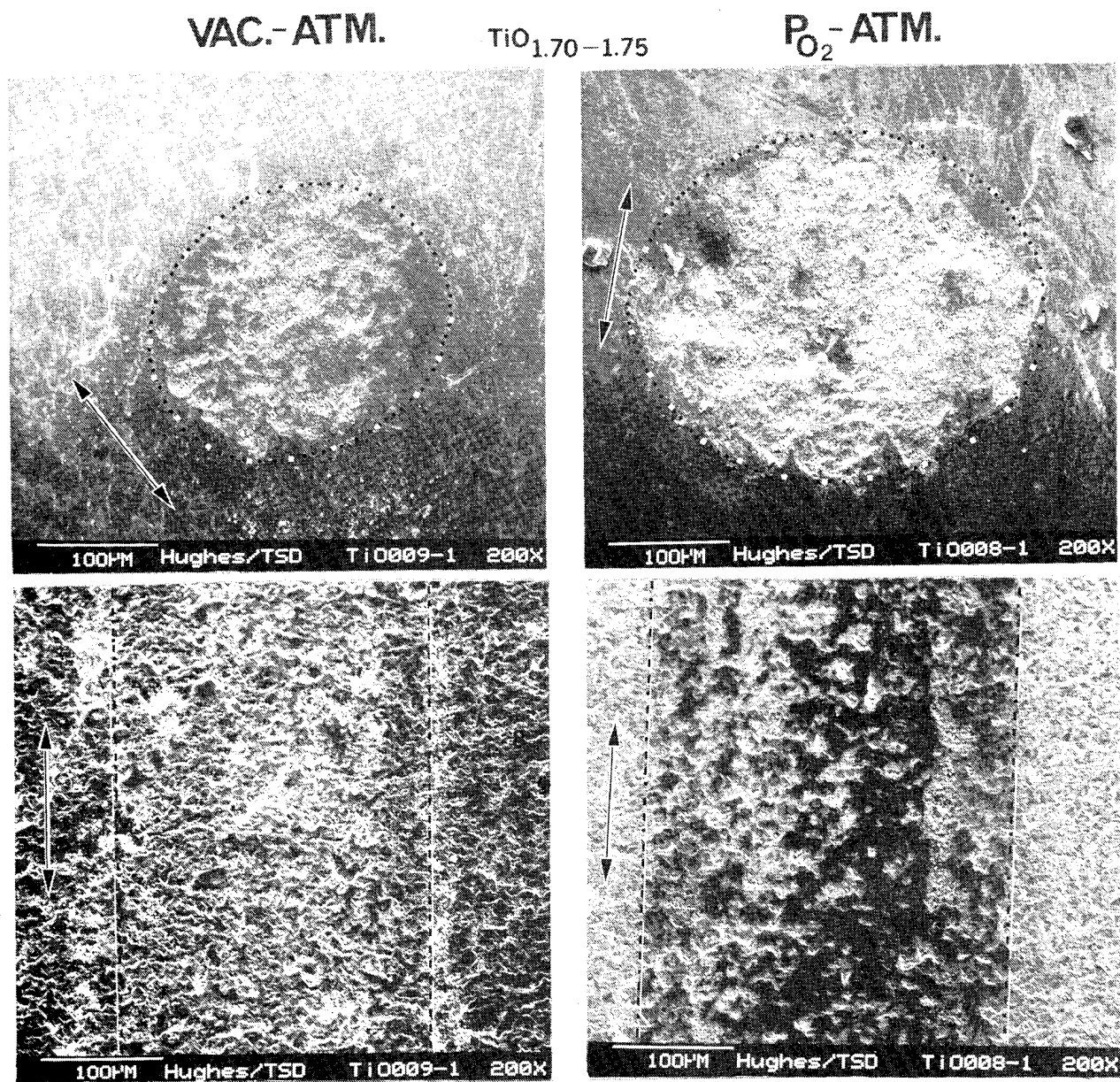


Figure 27. Same as Fig. 22 for  $\text{TiO}_{1.70-1.75}$ .



## 4.0 MOLECULAR ENGINEERING OF POLYCRYSTALLINE RUTILE

### 4.1 Control of Magnéli Phases by Doping with Aliovalent Cations

Monolithic rutile bearings would not perform satisfactorily in extreme environments, even if the base material were reduced to the right stoichiometric range or if the consolidation process could provide a high structural integrity substrate. The changing stoichiometry of rutile either in air or LOX (possible oxygen enrichment) or in vacuum (possible oxygen loss) would prevent protracted thermo/tribo-oxidative stability. Ideally, the desired Magnéli phases should be induced chemically (i.e., by doping), so the oxygen content and the crystal structure could be tailored *à priori* and made impervious to environmental effects.

Our basic concept of how to achieve stability by doping is similar to that of the preparation of high temperature superconductive oxides (33). In order to control the superconductive properties, it is essential to regulate the defect concentration by doping with selected aliovalent cations and changing the oxygen content. Most of the studies carried out so far on these superconductive oxides (e.g., the Y-Ba-Cu-O and Bi-Sr-Ca-Cu-O compounds) have reported that the incommensurate modulation structure was associated with the doping, causing the superconductivity. In other words, on doping rutile intentionally with impurity cations, the ions must not enter the lattice as simple and isolated substitutionals but instead enter the lattice as part of a complex. The Magnéli phases are the building blocks of this desired complex, consisting of the orderly arrangements of CS planes.

An essential part of this concept is determining the correct valence and ionic radius (i.e., the electronic structure- and ionic size-governed polarizability) and the quantity of the cations introduced into the rutile lattice. We must also know whether they are introduced substitutionally or interstitially.

The initial literature survey uncovered several references regarding the CS plane-forming ability of certain cations. For example, doping with trace amounts of  $\text{Fe}^{3+}$  and  $\text{Fe}^{2+}$  contained in iron oxides did create {132} planes (the kind we demonstrated to have low shear strength properties) in rutile (34,35). Similarly, doping with gallium oxide created a homologous series of  $\text{Ga}_4\text{Ti}_{n-4}\text{O}_{2n-2}$  structures comprised of a new type of CS plane system of  $\beta\text{-Ga}_2\text{O}_3$  coherently intergrown with rutile (36). The implantation of metallic ions also induced defect structures (37,38,39). Studies also dealt with the effects of cations on the anatase-to-rutile transformation (40,41,42). As an example, the addition of only 1% CuO caused ready transformation of anatase into rutile. Additions of this small amount of dopant outperformed conventional reduction methods which could achieve the same transformation, such as heating in air or in progressively higher partial pressures of hydrogen (40). Note that this polymorphic change into the

denser rutile structure could not occur without some removal and rearrangement (diffusion) of the oxygen vacancies.

As far as the valency of the likely dopant cations concerned, each  $\text{Ti}^{4+}$  in the rutile lattice is associated with two  $\text{O}^{2-}$ , arranged in the  $[\text{TiO}_6]$  octahedra linked by two common edges to form chains parallel to the  $c$ -axis. Where a titanium ion is replaced substitutionally by an aliovalent cation of similar ( $\sim \pm 15\%$ ) size but lower valency, anion vacancies will form and oxygen will be liberated. Clearly, monovalent cations produce  $3/2$  vacancies per cation, divalent ones (such as  $\text{Cu}^{2+}$  in Fig. 28) produce one vacancy and trivalent cations are the least efficient: they create only  $1/2$  vacancy per cation.

Since the diameter of a  $\text{Ti}^{4+}$  ion is  $0.68 \text{ \AA}$ , on size considerations alone,  $\text{Co}^{3+}$  ( $0.63 \text{ \AA}$ ),  $\text{Cr}^{3+}$  ( $0.63 \text{ \AA}$ ),  $\text{Fe}^{3+}$  ( $0.64 \text{ \AA}$ ),  $\text{Mn}^{3+}$  ( $0.66 \text{ \AA}$ ),  $\text{Li}^{1+}$  ( $0.68 \text{ \AA}$ ) and  $\text{Ni}^{2+}$  ( $0.69 \text{ \AA}$ ) should be most effective, followed by  $\text{Cu}^{2+}$  ( $0.72 \text{ \AA}$ ),  $\text{Co}^{2+}$  ( $0.74 \text{ \AA}$ ) and  $\text{Zn}^{2+}$  ( $0.74 \text{ \AA}$ ). Size is very important not only from the standpoint of lattice fit with minimum distortion, but also because cations bigger than  $0.77 \text{ \AA}$  (the size of the largest interstitial channels in the rutile lattice) simply cannot diffuse into the structure (43). If the solute cation is much smaller than the  $\text{Ti}^{4+}$  (e.g.,  $\text{Al}^{3+} = 0.51 \text{ \AA}$ ), it tends to be interstitial.

The bonding state (polarizability) of the dopant must also be similar enough to that of  $\text{Ti}^{4+}$  so that the Fermi surface interaction in the 2D structure of the CS planes (44) will be minimally disturbed. The planar structures of the cation and the anion sublattices interact similar to metal-semiconductor surfaces forming Schottky barriers or ohmic contacts. For example, as explained in (45), the bonding of titanium, copper and platinum to SiC is influenced by the hybridization of the metal-semiconductor bonding orbitals as well as the charge transfer from one valence level to the other. If the valence levels are of nearly equal energies hybridization dominates and if they are apart charge transfer prevails, as indicated by the first ionization potentials of the metals, carbon and silicon. The respective values are C ( $-11.26 \text{ eV}$ ), Si ( $-8.15 \text{ eV}$ ), Cu ( $-7.73 \text{ eV}$ ), Ti ( $-6.82 \text{ eV}$ ) and Pd ( $-8.34 \text{ eV}$ ). The formation of Cu-C and Ti-Cu bonds would involve charge transfer from the metal to carbon; with Pd-Si, probably not. In each case, however, charge transfer to C would be likelier than to Si. Therefore, as the size and bonding state of the metal-oxygen couples combined into the concept of ion polarizabilities (46) (see Fig. 29), one can see that the most likely cation dopants for rutile are (in a decreasing order of predicted performance):  $\text{Cu}^{2+} > \text{Zn}^{2+} > \text{Mn}^{2+} > \text{Fe}^{2+} > \text{Co}^{2+} > \text{Ni}^{2+}$ . In terms of polarizability, James and Catlow (47) already predicted that substitutional divalent cations would stabilize the CS planes best in rutile. The literature data indicate, however, that other aliovalent cations of +3 charge states could also fulfill a similar role, albeit not as efficiently. For example, stuffing the lattice with too much  $\text{Fe}^{3+}$  could alter the desirable tetragonal crystal structure of the Magnéli phase rutiles into the hard, brittle and abrasive pseudobrookite ( $\text{FeTi}_2\text{O}_5$ ) (39,48) or the ilmenite ( $\text{FeTiO}_3$ ) (49) perovskites. This is an important point, because

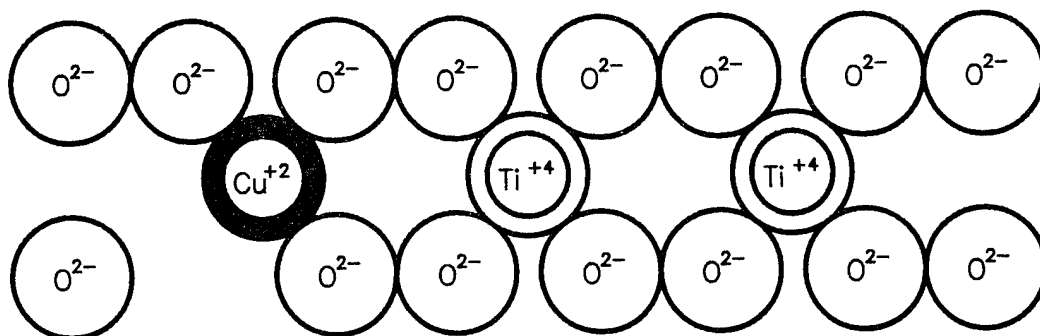


Figure 28. Schematic representation of oxygen vacancy formation in TiO<sub>2.00</sub> by doping with the aliovalent Cu<sup>2+</sup> cation.

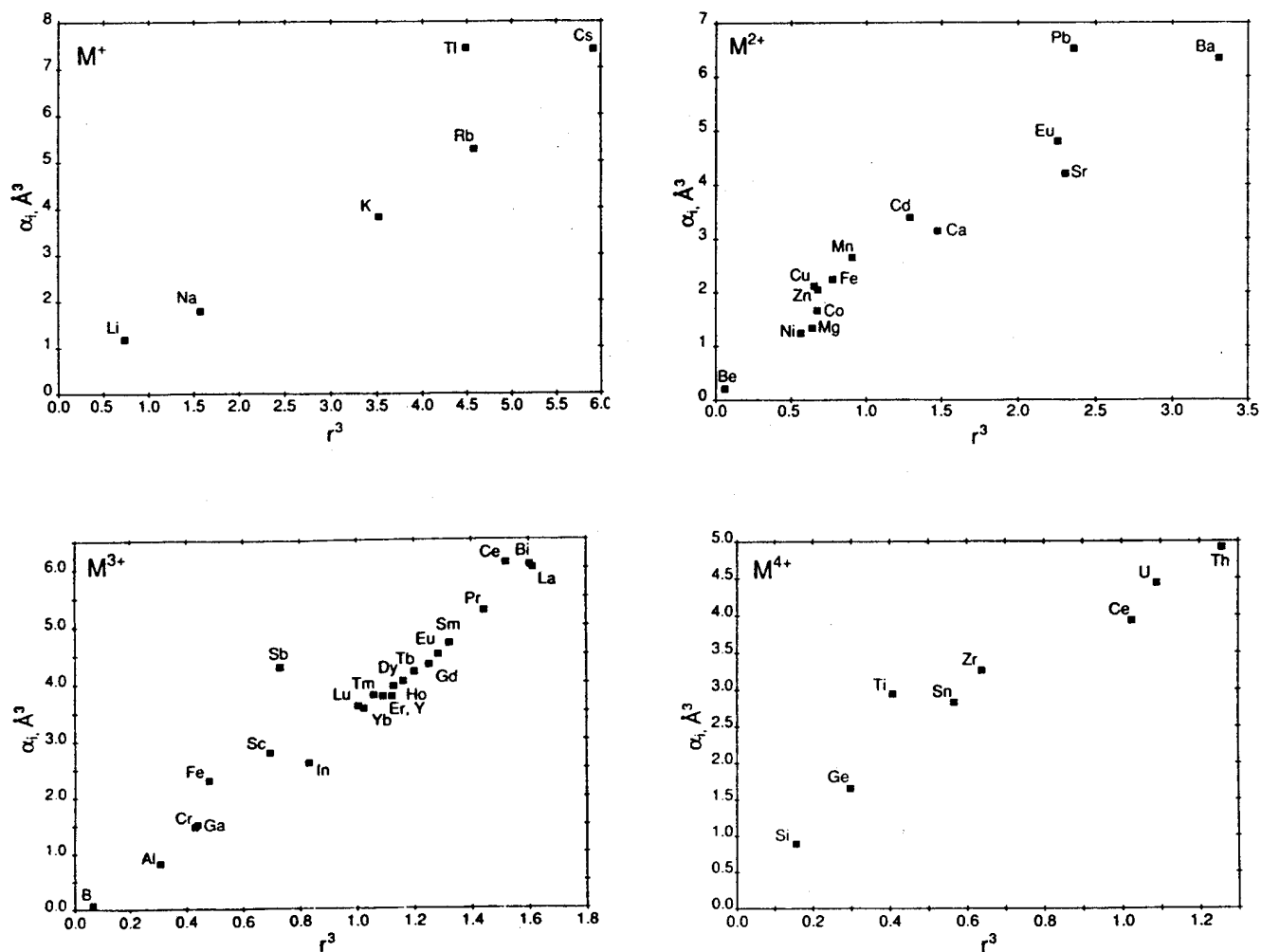


Figure 29. Dielectric polarizabilities of  $M^{2+}$ ,  $M^{3+}$  and  $M^{4+}$  cations vs. (crystal radius); from (46).

to molecularly engineer a  $(\text{Ti} + \text{Cu})\text{O}_{1.70}$  lubricious oxide, 0.3 moles of  $\text{Cu}^{2+}$  (contained in some likely vehicle such as  $\text{CuO}$ ) would have to be added substitutionally to 0.7 moles of  $\text{TiO}_{2-x}$  to generate the desired compound. In case of the 0.3 moles of  $\text{Fe}^{3+}$  added as  $\text{Fe}_2\text{O}_3$ , the new compound would have to equilibrate at an oxygen content of  $\text{Ti}_{0.7}\text{Fe}_{0.6}\text{O}_{1.70}$ . The cation content here adds up to more than one atomic weight per molecular weight of the mixed oxide. This means that the rutile lattice may not be able to tolerate being "stuffed" with so much iron oxide, possibly leading to undesirable crystal structure changes. It could also mean that the titanium-iron "bronze" phases [a term often referred to in the cases of mixed oxide Magnéli phases (50)] may be separated by pockets of unreacted iron oxide.

There is enough information in the literature to further assist in the selection of likely and poor dopants. The  $\text{Al}^{3+}$  is a highly efficient acceptor and, by virtue of its small size, it can readily diffuse into the rutile lattice and promote the annihilation of the  $\text{Ti}^{3+}$  building blocks essential for the formation of the Magnéli phases ( $\text{Ti}^{3+} - e = \text{Ti}^{4+}$ ) (43). Doping with aluminum ions may help rutile as a semiprecious stone from turning dark but is disastrous to doped rutile electrodes, because of the loss of conduction electrons. Chromium and nickel were shown to be poor promoters of the anatase-to-rutile transformation. Their poor performance may be related to their preference for undistorted octahedral sites (41). Copper, on the other hand, prefers octahedral sites and has a strong tendency toward tetrahedral distortion because of the Jahn-Teller splitting. The Jahn-Teller splitting refers to the condition in which the crystal lattice is distorted from the cubic to the tetragonal configuration as a consequence of having some  $3d$  orbitals of fewer electrons than other orbitals. This condition results in an electrostatic imbalance that has the effect of repelling some oxygen anions more than others. As the overall result, these anions are pushed further away, creating a change from the cubic to the tetragonal symmetry. This ability renders copper oxide the essential ingredient in the high temperature superconductive oxides. It appears that copper readily enters a strained crystal structure and is stabilized at defect planes. Its variable valency from +1 to +2 may also play a part in accommodating the lattice strain.

Based on these data, formulation studies were started with model compounds representing "good" ( $\text{Cu}^{2+}$  as  $\text{CuO}$ ), "possible" ( $\text{Fe}^{3+}$  as  $\text{Fe}_2\text{O}_3$ ) and "poor" ( $\text{Co}^{2+}$  as  $\text{CoO}$ ,  $\text{Ni}^{2+}$  as  $\text{NiO}$ ) dopants for rutile. Although other cations (e.g.,  $\text{Ga}^{3+}$ ,  $\text{Zn}^{2+}$ ,  $\text{Mn}^{2+}$ ) could have been candidates as well, not enough data were in the literature to justify their immediate consideration. The probability of being successful with copper was further strengthened by previous work with rutile-supported copper catalysts, where increased electrical conductivity was observed after reduction of the copper-rutile system (51,52). This increase was attributed to the partial electron transfer  $\text{Cu}^0 + \text{Ti}^{4+} \longrightarrow \text{Cu}^{\delta+} + \text{Ti}^{3+}$  and simultaneous intercalation of copper to form bronzes (52), similar to other well-known bronzes of vanadium and titanium normally used for electrode (53) and catalyst (54,55) applications. Iron was already shown to generate CS planes. Nickel (56) and cobalt (57,58) both tend to form titanate perovskites instead of Magnéli phase bronzes.

## **4.2 A Simple Preparation Method for Cation-Doped Rutile**

There is a wide variety of likely doping techniques for rutile. One might employ alkoxide precursors (59) similar to the preparation of superconductive oxides (60), coprecipitation of colloidal (61) or nanophase (62,63,64) oxide particles or one could prepare the starting powders via polymeric precursors (65). Then, the ceramic molds can be fabricated by the tried-and-true method of mechanically mixing the oxides and/or carbonates followed by ball milling before and after calcining and, finally, hot-pressing the dried powder mix (41,42,43). Ideally, the particle size of both the titania and the dopant oxides should be as small and similar as possible to shorten the equidistant cation diffusion paths into (preferably) substitutional sites in the rutile lattice. Shorter diffusion distances require lower hot-pressing and heat-treatment temperatures and shorter treatment times at temperature.

The simplest and least expensive preparation method consists of ball milling the various doping oxides with anatase powders, hot-pressing the milled mix under temperatures high enough to convert anatase to rutile and, at the same time, to thermally diffuse the dopant cations into the partially reduced rutile lattice. This part of the work was performed by CERCOM, Inc. (Vista, CA) under the direction of Dr. Andre Ezis, Hughes P.O. No. M9-332581-KKA. CERCOM undertook the job based on a Hughes Proprietary technical letter dated 13 August 1991 and signed a Non-Disclosure Agreement with Hughes Aircraft Company on 30 November 1991 enabling the subcontract. Details of the Hughes-recommended preparation procedure are also described in (66).

The most important criterion of successful doping is the development of chemically induced Magnéli phases in the hot-pressed and cured (heat-treated) samples. The effectiveness of the preparation procedure(s) can only be determined by X-ray diffraction (XRD) and the proper interpretation of the complex diffractograms by specialized experts in the field. Dr. Robert L. Clarke (Dextra Assoc., Orinda CA) performed this part of the research under Hughes P.O. S9-333846-SAA, with the cooperation of Dr. Vaughan White of The New Zealand Institute for Industrial Research and Development, Industrial Research Ltd. (Lower Hutt, New Zealand). Their participation was also made possible by signing the Non-Disclosure Agreement.

The combined analytical techniques were designed to (a) determine the best fabrication steps as well as the type and amount of dopants necessary to tailor rutiles into specific Magnéli phase ranges, and (b) select the most representative candidate(s), whose SEM tribometry would correlate chemical composition and the associated crystal structure with friction and wear properties. This approach was selected to circumvent blind tribometry of samples, which may have remained as a physical mix of dopant and titanium oxides.

#### 4.2.1 Doping with CuO

The basic procedure (see APPENDIX A) consisted of wet ball milling a 50:50 mix of CuO (<45  $\mu\text{m}$  avg. particle size, the smallest available) and anatase (0.5  $\mu\text{m}$  avg. particle size) powder master blend for 24 hours using non-contaminating (non-reactive) milling media. This step was followed by drying, further dry-milling for 30 minutes and sieving the powder mix through a 5-mesh screen. The master blend was then similarly ball-milled wet with the balance of anatase to yield a *theoretical* blend of  $(\text{Ti} + \text{Cu})\text{O}_{1.80}$ . The final blend was also dried, dry-milled for 30 minutes and sieved through ASTM 5- and 30-mesh screens (6.35 and 0.59 mm, respectively).

The resulting powder mix was hot-pressed (HP) between graphite platens at 1200°C, under 2500 psi pressure for 0.5 hour, in a rapid-induction-heated HP oven capable of 2000°C+ temperature that can be reached within seconds. The mold (No. 971-3) was then slow-cooled to 800°C and then to room temperature. Pure anatase powder (the baseline) was similarly processed into a slightly reduced rutile mold (No. 917-4).

Both molds were of high structural integrity. The anatase-turned rutile baseline lost only 7.1% weight, while the doped blend lost a large amount (34%) of weight. The latter did contain 15 to 20  $\mu\text{m}$  pores and specularly reflecting inclusions. The presence of the voids indicated the formation of volatiles during the pressing process.

A piece of the No. 971-3 doped mold was heat-treated in air per the following cycle: (a) heat to 1100°C in 2 hours, (b) hold at 1100°C for 20 hours, and (c) shut-off the furnace and slow-cool to room temperature. The test piece had a delaminated appearance after heat-treatment. It seemed to suffer from outgassing and/or the release of residual stresses. Since only 0.4% additional weight was lost, the primary damage mode may have been the latter. As a consequence, even without the benefit of any additional analytical work, a decision was made to alter the preparation process to include a more conducive HP and heat-treatment environment. The pressing temperature was reduced to 1100°C and the heat-treatment atmosphere was changed from air to an Ar + 3% H<sub>2</sub> gas mixture. These changes were incorporated to exclude the effects of any residual oxygen from the annealing atmosphere and enhance the *in situ* reduction of rutile for more efficient dopant diffusion within the mold.

The alternate (improved) method consisted of the following steps:

1. Ball mill as before to a theoretical blend of  $(\text{Ti} + \text{Cu})\text{O}_{1.80}$  and hot-press at 1100°C for 6 hours (instead of at 1200°C for 0.5 hours).

2. Heat-treat (anneal) a small piece of the mold in Ar + H<sub>2</sub> at 1100°C for 48+ hours (over the weekend).
3. Heat-treat another small piece of the mold in air at 1100°C for 48+ hours (same length of time as before) to see any differences in appearance and/or degradation.
4. Perform XRD and XPS/ESCA on the samples to determine the efficacy of the processes.

The XRD analyses from IR Ltd. were routed through Dextra Associates for additional evaluation (APPENDIX B). The results are condensed in Table 2:

1. The pressed anatase baseline exhibited XRD peaks characteristic to rutile, with only traces of Magnéli phases, as expected.
2. Although pressing between the graphite platens at 1100°C, combined with the increased time in the hot press (from ~0.5 hour to 6 hours) did produce a mold of good structural integrity, there was no reaction between the rutile and CuO.
3. Heat-treatment in the 3% hydrogen-containing argon environment for ~48 hours at 1100°C caused the formation of a Magnéli phase compound similar in XRD pattern to a titanium-vanadium bronze with the stoichiometry of V<sub>3</sub>Ti<sub>6</sub>O<sub>17</sub> (Fig. 30). This material is equivalent to a Ti<sub>9</sub>O<sub>17</sub> (TiO<sub>1.89</sub>) compound. If all the copper ions entered the lattice substitutionally, the stoichiometry should have been TiO<sub>1.80</sub>-like. Either some of the dopant oxide volatilized from the material, or it diffused to the surface of the mold during pressing which, in turn, was machined off by the customary "clean-up" procedure to remove the thin, inhomogeneous skin from the mold.
4. Heat-treatment in air under the same time-temperature conditions was not conducive to dopant-induced Magnéli phase formation.

The samples described in Table 2 were also analyzed in a Perkin-Elmer (Physical Electronics) PHI-5500 XPS(ESCA)/SAM spectrometer and by SEM/EDX using a Cambridge Stereoscan 250, Mk.3, at Hughes Aircraft Company (APPENDIX C):

1. The pressed doped mixture exhibited a 4-band surface skin structure, with a total approximate width of 2 mm. A ceramurgical cross section of the mold was tested by SEM/EDX, followed by XPS/SAM. The data indicated heavy segregation of copper on the as-molded surface, with progressive depletion of the dopant toward the middle of the



Table 2. Results of the first successful heat-treatment study.

Sample Number	Description	XRD Results	Implications
#988-2 (as-pressed); BN 54/4	titania (rutile)	rutile with some minor reduction peaks	XRD is sensitive enough to pick up very minor changes in stoichiometry
#988-3 (as-pressed); BN 54/2	rutile hot-pressed with CuO at 1100°C, for 6 hours, to obtain theoretical (Ti+Cu)O <sub>1.80</sub> .	no reaction; rutile identified; minor reduction peaks	no significant change in structure
#998-3 (argon heat- treated); SN99; BN 54/1	rutile with CuO, pressed as above + heat-treated in hydrogen- containing argon at 1100°C over weekend	Only small amount of rutile survived. New compound formed: V <sub>3</sub> Ti <sub>6</sub> O <sub>17</sub> -like Ti-Cu bronze is suspected	Ti <sub>9</sub> O <sub>17</sub> -like Magnèli phase; a CuO-doped analog may have been made

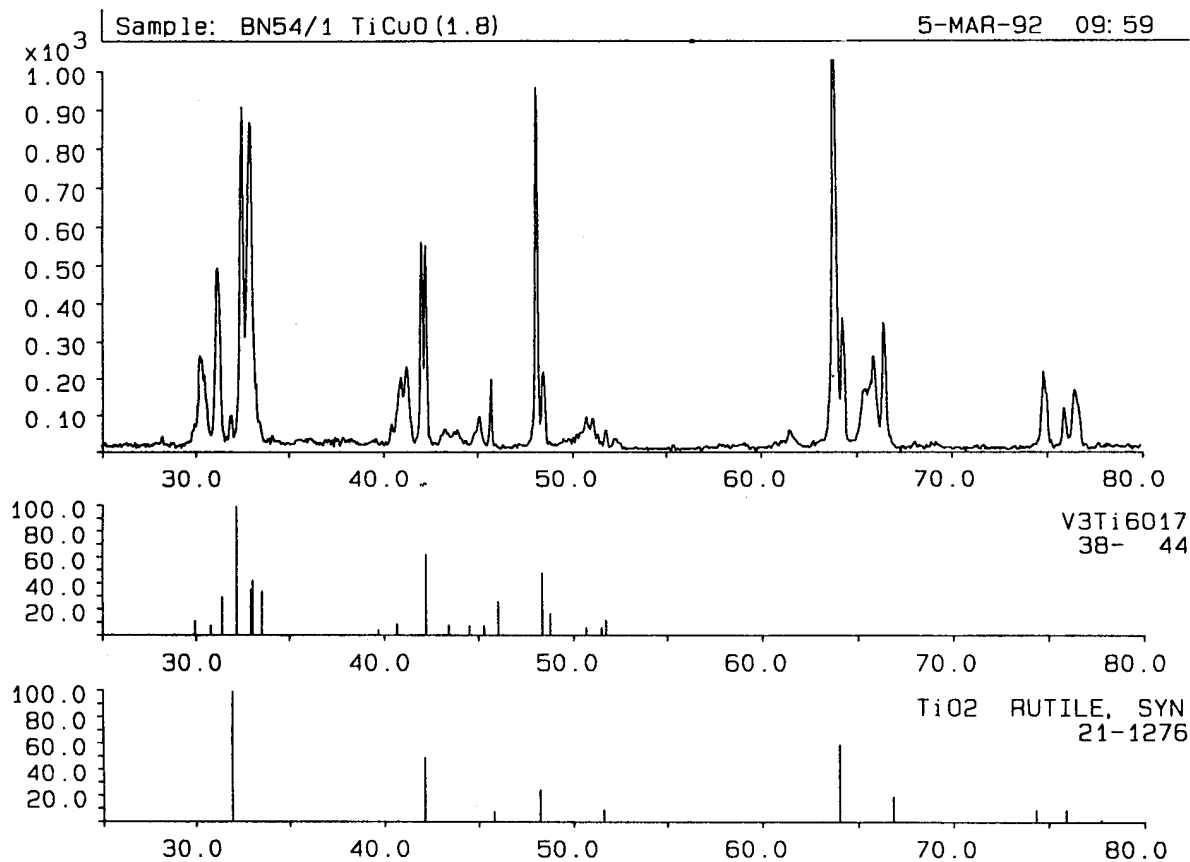


Figure 30. IR, Ltd. X-ray diffractogram of CuO-pressed, polycrystalline rutile  $[(Ti + Cu)O]_{1.80}$  theoretical blend, hot-pressed + annealed] compared to the diffractograms of  $V_3Ti_6O_{17}$  and pure rutile (also see Table II for sample identification).

mold. The gold color probably originated from a Cu + Cu<sub>2</sub>O mixture. Following an opposite trend, the porosity was the greatest in the middle of the mold, with progressive reduction in the size and the number (frequency) of the pores toward the surface. The major elements seen in the bulk were carbon, oxygen, titanium and only ~1 atomic percent of copper. Titanium was seen in both the +3 and +4 charge states. There was some Na and K contamination also.

2. The air-heat-treated blend showed a greater amount (~4 to 6 at.%) of residual copper within the bulk. On sputtering, the carbon content decreased quickly.
3. The blend heat-treated in the Ar + H<sub>2</sub> gas mixture showed great similarities with the as-pressed rutile (undoped) baseline. Potassium was not seen in this sample and sodium was at a lower concentration. Copper was present in low 1.2 to 1.3 at.% concentration, with less carbon than in the baseline material.

The overall data indicated that a significant part of the copper dopant was lost by surface diffusion-enhanced evaporation. Since the volume self-diffusion of copper has a lower activation energy (46 kcal/mol) than that of oxygen in rutile (60 to 70 kcal/mol) (67), and the gold-colored Cu<sub>2</sub>O is known to volatilize at high temperatures (that is why copper gaskets used in baked, ultrahigh vacuum chambers must be made from oxygen-free, high conductivity copper), the migration and volatilization hypothesis is reasonable. As shown later in this report, the appearance of some of the used SEM tribometer specimens fabricated from the doped mixes, after testing in vacuum and in P<sub>ox</sub>, reinforced the accuracy of this hypothesis.

What seemed to be puzzling is the fact that in titanium-vanadium bronze electrodes or catalysts vanadium enters the rutile substitutionally, in the V<sup>4+</sup> form, with its excess 3d<sup>1</sup> electron available for conduction (68). This is the same type of donor-doping as one obtains with niobium ions (43,69). An isovalent cation dopant should not be able to expel oxygen from the rutile lattice, unless they can exhibit multivalency. Vanadium oxides do exist with compositions between V<sub>2</sub>O<sub>3</sub> and VO<sub>2</sub>, forming from slabs of rutile-like structure, sharing faces. These Magnèli phases also show transitions from the semiconducting to the metallic state (70). In addition to vanadium possibly being present in the 3+ charge state in the solid solution of the mixed oxide, the negatively charged oxygen vacancies that form during calcining could be loosely bound to the V<sup>4+</sup> occupying a substitutional site. The same has been observed with such vacancies bound to the substitutional Nb<sup>4+</sup> ions (69). If these oxygen vacancies are more-less stable at the substitutional sites, then the Magnèli phases are also stabilized.

The formation of a titanium-copper ( $\text{TiO}_{1.89}$ -like) bronze compound was confirmed by 4-point electrical contact measurements performed by Dr. Rob Clarke (Dextra Assoc.), see APPENDIX D. It is shown in Figs 1 and 2 that the oxygen stoichiometry and the electrical behavior of the rutile Magnèli phases are closely related. With the Ar +  $\text{H}_2$  heat-treated sample, the results of six separate volume resistivity measurements were 0.056, 0.050, 0.058, 0.055 and 0.054  $\Omega\cdot\text{cm}$ , with an average value of 0.054  $\Omega\cdot\text{cm}$ . The corresponding conductivity (the reciprocal of resistivity) is equal to  $1/0.054 = 18.519$  mho. If one plots  $\log_{10} 18.519 = 1.27$  against the oxygen content of rutile (see Fig. 31), the stoichiometry of  $\text{TiO}_{1.89-1.90}$  is indicated. The electrical conductivity measurements closely match the XRD-estimated oxygen stoichiometry.

Both the as-pressed rutile baseline and the as-pressed and unreacted  $\text{CuO}$  + rutile blend exhibited infinite resistivities (i.e., zero conductivity). An insufficient amount of electrically conductive Magnèli phases always results in the absence of significant electrical activity. Along the same lines, all insulating ceramic oxides are white due to the absence of conduction electrons on the surface. These charge carriers absorb in the red, turning the color of the electrically conductive (by electrons) ceramics blue-black (43,71). This is also the reason why all high  $T_C$  superconductive oxides are blue-black, and why the now-obsolete titania-based, spacecraft thermal control coatings turned dark due to color center formation on exposure to vacuum, the hot sun and solar wind (72,73).

The successful generation of the Magnèli phases by doping prompted a second hot-pressing and heat-treatment study at CERCOM, as depicted in Table 3. The objectives were: (a) press the  $(\text{Ti} + \text{Cu})\text{O}_{1.80}$  at a lower ( $900^\circ\text{C}$ ) temperature and heat-treat in Ar +  $\text{H}_2$  both at  $900^\circ\text{C}$  and  $1100^\circ\text{C}$ , (b) press the  $(\text{Ti} + \text{Cu})\text{O}_{1.80}$  at the higher ( $1100^\circ\text{C}$ ) temperature and heat-treat in Ar +  $\text{H}_2$  both at  $900^\circ\text{C}$  and  $1100^\circ\text{C}$  (one of these samples would represent the repeatability of the original, successful preparation effort), and for the first time, (c) try a  $(\text{Ti} + \text{Cu})\text{O}_{1.70}$  *theoretical* blend for the first time, pressed at  $900^\circ\text{C}$  and heat-treated at both temperatures.

The examination of the molds indicated that only the  $1100^\circ\text{C}$ -pressed samples cured at both temperatures had the same, relatively flaw-free appearance as before. The white-gray discoloration and the blistering of the other samples indicated a strong possibility of oxygen contamination (by a leak or heavy internal outgassing in the furnace around the afflicted samples) or another reaction anomaly. XRD did show the formation of Magnèli phases, but these phases were associated with reduced rutile and not with any doping-induced versions (APPENDIX E). It was especially disappointing that the  $1100^\circ\text{C}$ -pressed,  $1100^\circ\text{C}$ -heat-treated mix did not repeatedly react into the anticipated titanium-copper bronze compound.

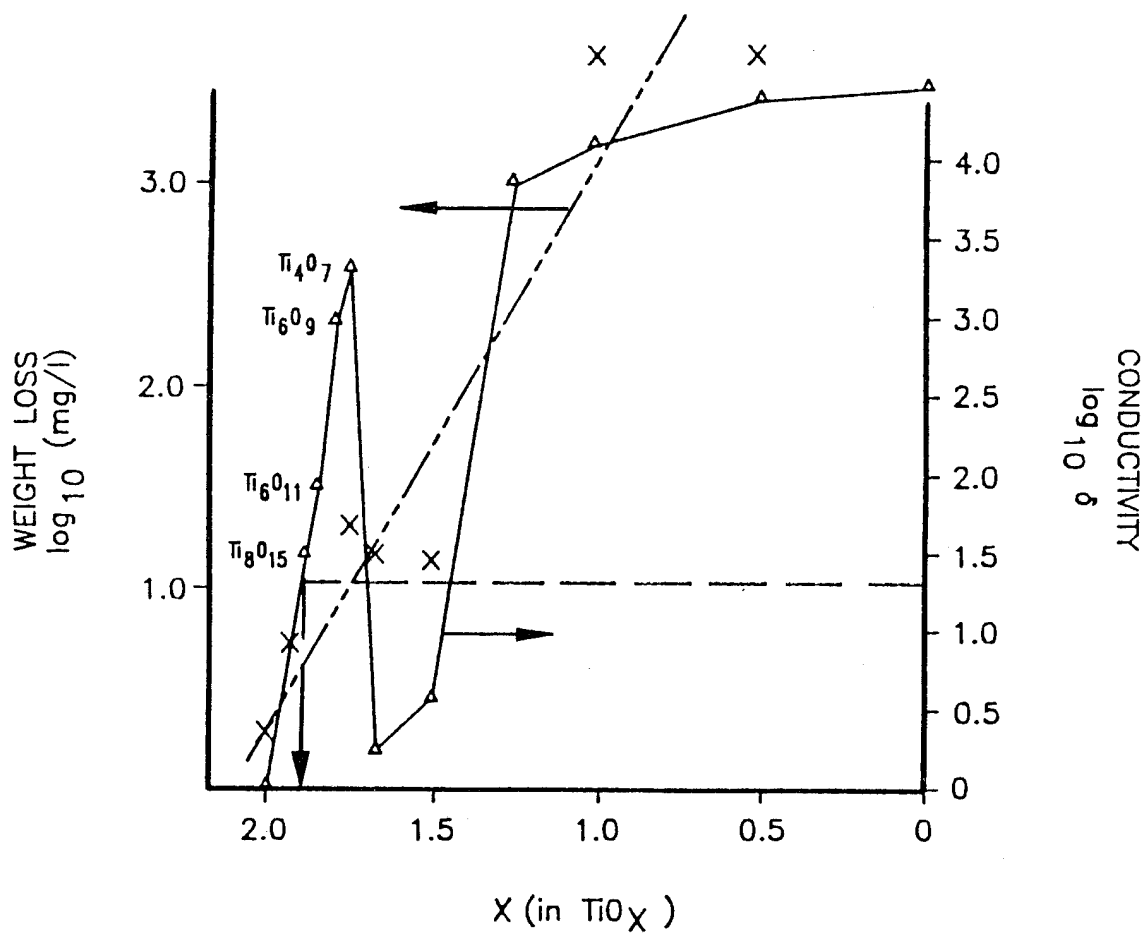


Figure 31. Electrical conductivity-indicated stoichiometry of CuO-doped rutile  $[(\text{Ti} + \text{Cu})\text{O}_{1.80}]$  theoretical blend, hot-pressed annealed; (also see Table 2 for sample identification).

Table 3. Results of the second heat-treatment study to further elucidate pressing and curing temperatures.

Sample No.	Description	Sample Appearance
988-1 (1100°C HP run)	(Ti+Cu)O <sub>1.80</sub> theoretical; Heat-treated at 900°C for 48 hours.	Uniform, dark blue color, no copper beads; 0.12% weight loss.
	(Ti+Cu)O <sub>1.80</sub> theoretical; Heat-treated at 1100°C for 48 hours.	Uniform, dark blue color; some copper beads on the surface; 1.7% weight loss.
1009-1 (900°C HP run)	(Ti+Cu)O <sub>1.80</sub> theoretical; Heat-treated at 900°C for 48 hours.	Red skin on surface; delamination close to the surface; 3.78% weight loss.
	(Ti+Cu)O <sub>1.80</sub> theoretical; Heat-treated at 1100°C for 48 hours.	Numerous copper beads on surface; heavy blistering and some white-gray discoloration; 5.28% weight loss.
1009-2 (900°C HP run)	(Ti+Cu)O <sub>1.70</sub> theoretical; Heat-treated at 900°C for 48 hours.	Red skin on one face; delamination close to the surface; 5.81% weight loss.
	(Ti+Cu)O <sub>1.70</sub> theoretical; Heat-treated at 1100°C for 48 hours.	Numerous copper beads on surface; heavy blistering and some white-gray discoloration; 7.60% weight loss.

A review of the heat-treatment procedure revealed that CERCOM used a cold-walled, walk-in oven for the process. Before the small sample pieces could be treated, CERCOM technologists had to wait until a full furnace load was collected for a similar heat-treatment run of other types of samples and production hardware. Note that weekend-long baking of a variety of ceramics at 900°C or 1100°C temperatures in the reducing argon + hydrogen environment is quite common. CERCOM could not guarantee that the first heat-treated piece (which reacted into a bronze) was placed into the same furnace grid position and had the same neighbors as the second (unreacted) one. Since large walk-in ovens do not have the same thorough temperature mapping and atmospheric control as small table-top lab furnaces, the temperature and atmospheric environmental differences the two samples experienced may have caused the poor repeatability.

The lack of control over the oven gas chemistry during heat-treatment could have contributed to the disparate results. Initially, it was believed that an Ar + 3% H<sub>2</sub> environment totally free of any oxygen content would be needed for annealing at 1100°C. Oxygen-depleted lattices (titania or copper oxide) have a more open structure than fully stoichiometric ones, helping the diffusion of dopant cations to substitutional sites. Yet, the oxygen pressure vs. temperature phase diagrams of the Cu-O system in Fig. 32 (74,75) indicate that at 1100°C CuO is reduced to metallic copper in only trace amounts of oxygen. The effects of excess oxygen escaping from the progressively reduced rutile (and CuO) notwithstanding, the copper beads observed on the surface of the annealed samples were indicative of this transformation. The data in Fig. 32 also show that for copper to remain in the +2 charge state (i.e., as CuO) at 1100°C,  $P_{Ox}$  should be near one atmosphere. For copper to be in the +1 state (i.e., as Cu<sub>2</sub>O),  $P_{Ox}$  may be lowered to near 10<sup>-5</sup> atmosphere. The facts that (a) we were not successful forming the titanium-copper bronze by heat-treating in air, but succeeded doing that in a reducing atmosphere, and (b) a great deal of the dopant disappeared during annealing, point to the presence of ionic copper in the +1 charge state. The greater ability of Cu<sup>1+</sup> to expel oxygen from the rutile lattice than Cu<sup>+2</sup> might explain the formation of the titanium-copper TiO<sub>1.89</sub>-like bronze in spite of a significant loss of the dopant during the pressing and heat-treatment processes.

The data in Fig. 33, taken from (76), further confirm the severe reduction of CuO during hot-pressing and the weekend-long heat-treatments. If the blends were annealed in vacuum instead of a reducing atmosphere at near atmospheric pressure, CuO would have been completely reduced to Cu<sub>2</sub>O and Cu<sub>2</sub>O to metallic copper in about an hour, at temperatures as low as 550°C. If, by that time, the dopant cation did not find a substitutional site in the rutile lattice, then the likelihood of it becoming Cu<sup>0</sup> metal is there. However, conduction electrons are lost as the neutral species are being generated, thus the white-gray discoloration of some of the heat-treated pieces. Some reduction may have already occurred during hot-pressing not only because of the long, 6-hour process, but also because of using graphite

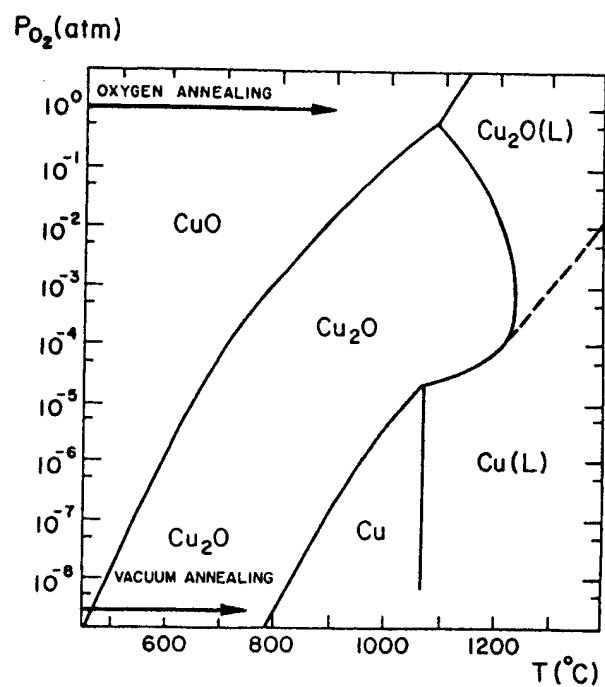
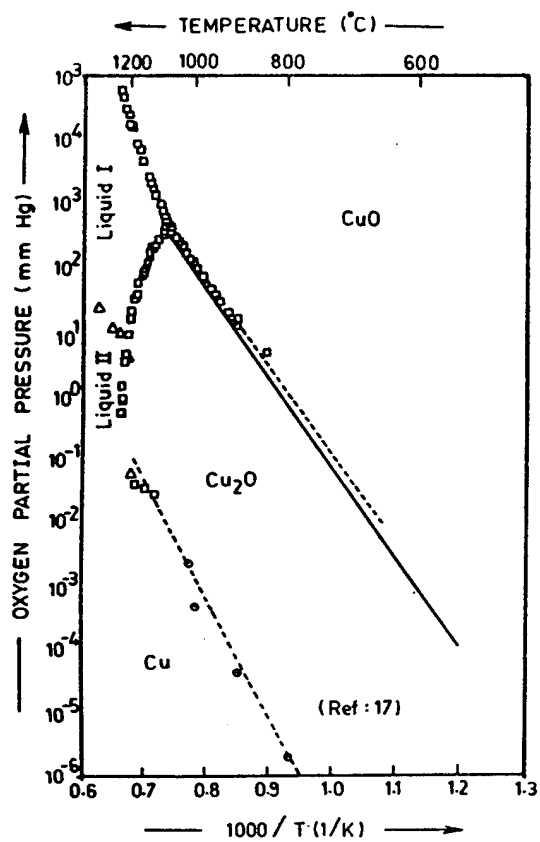


Figure 32. Copper-oxygen phase diagrams from Ref. 74 (left) and Ref. 75 (right).



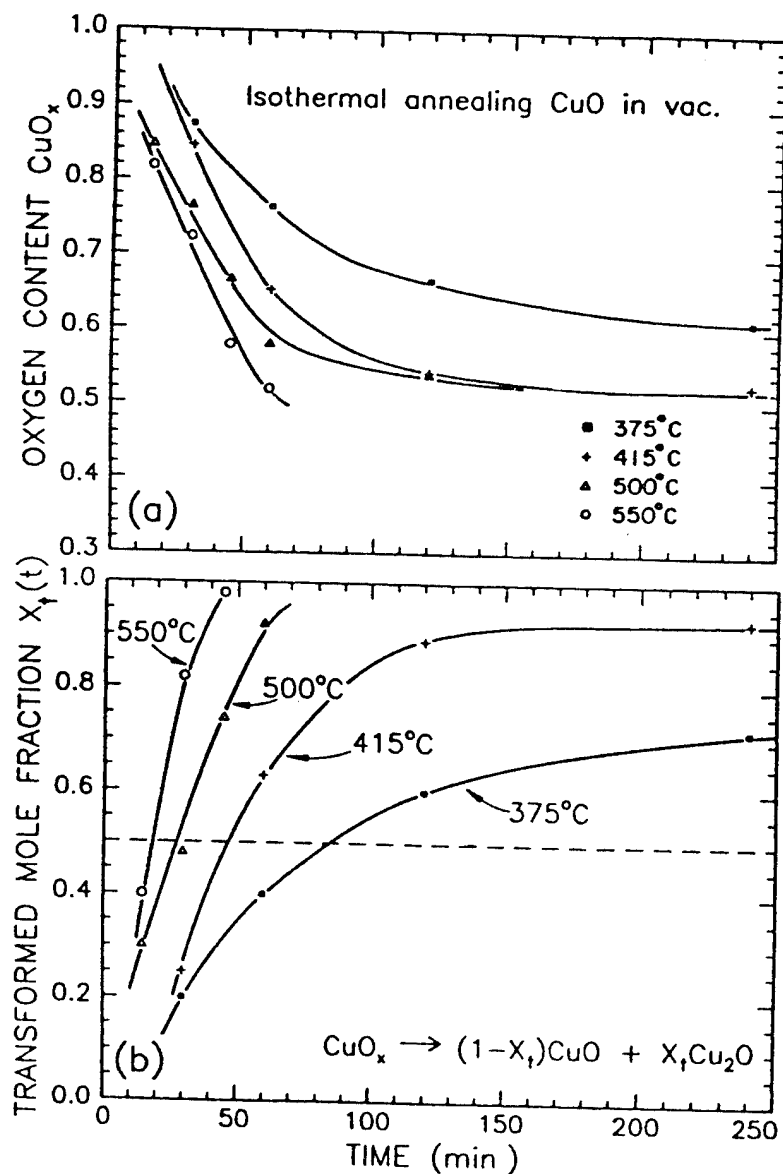


Figure 33. The results of isothermal annealing CuO in  $2 \times 10^{-7}$  torr vacuum: (a) oxygen content of copper oxide thin films vs. time of isothermal annealing from 375° to 555°C and (b) the transformed mole fraction of the  $\text{Cu}_2\text{O}$  phase vs. annealing times corresponding to (a); from (76).

pressing platens. The presence of graphite assured a reducing atmosphere around the molds even though the starting hot-pressing atmosphere was room air. It helped reduce the rutile matrix for ease of cation diffusion, but it also helped in the rapid reduction of CuO (77).

Thermal diffusion acting to replace  $\text{Ti}^{4+}$  with substitutional, aliovalent cations appears to be an inefficient process without additional safeguards. While the scope of the present study did not include the refinement of this simple molecular engineering technique, there is now some indication of how to optimize the process. The use of nanophase  $\text{TiO}_2$  and CuO (or  $\text{Cu}_2\text{O}$ ) coprecipitated in stoichiometric or overstoichiometric mixtures, followed by lower temperature but longer heat-treatment in controlled  $P_{\text{Ox}}$  would certainly represent an improvement. However, the temperature of the treatment must be high enough to induce the anatase-to-rutile transformation.

Model compounds could also be prepared by molecular beam epitaxy (MBE). One would still have to depend on the inherent formation of the Magnéli phases as a function some energy input (heating, irradiation, severe shock, etc.), because even MBE could not select the desired CS plane lattice sites in a controlled manner. Perhaps MBE on an alternatively heated and cooled substrates (rapid laser heating and quenching) may be more suitable for molecularly engineering doped lubricious oxides.

#### 4.2.2 Doping with $\text{Fe}_2\text{O}_3$ , $\text{CoO}$ and $\text{NiO}$

Experimental molds were also prepared at CERCOM with the same anatase powder blended with  $\text{Fe}_2\text{O}_3$ ,  $\text{NiO}$  and  $\text{CoO}$  to an ideal stoichiometry of  $(\text{Ti} + \text{Dopant Cation})\text{O}_{1.80}$ . The modified preparation method of  $1100^\circ\text{C}$  HP and heat-treat which worked best with the CuO the first time around was retained.

The XRD data (APPENDIX F) indicated that neither the cobalt nor the nickel entered the rutile lattice to form significant amounts of reacted Magnéli phases. Small quantities of titanates were found in the samples, as expected. Iron showed some promise as a dopant. The  $(\text{Ti} + \text{Fe})_3\text{O}_5$  component in the rutile matrix indicated the possibility of the desired reaction. IR Ltd. was particularly interested in this compound in terms of further Mössbauer spectroscopy to determine the nearest-neighbor environment around the iron substitutionals.

As a final round, samples of all of the  $1100^\circ\text{C}$ -pressed/ $1100^\circ\text{C}$  heat-treated samples were annealed further at  $1300^\circ\text{C}$ , for 48+ hours in the conventional, reducing atmosphere. The aim was to determine the effects of an even higher temperature on the reactivity of each dopant, in the absence of atmospheric oxygen. The data indicated a pervasive absence of Magnéli phases attributed to the action of cobalt or nickel. The Magnéli phases that were observed are presumed to have been generated by heating in the  $\text{Ar} + \text{H}_2$  atmosphere only. Interestingly, the  $1300^\circ\text{C}$  annealing temperature destroyed the titanium-

copper bronze structure that did form at 1100°C. At 1300°C, the major phase in the iron-blended sample was  $\text{Fe}_2\text{TiO}_5$  with some unusual changes (shifts) in the XRD peaks previously seen after the 1100°C preparation procedure. IR Ltd. showed interest in performing Mössbauer spectroscopy on this sample also to determine the valence state and site symmetry of iron.

The overall results with the copper, iron, cobalt and nickel oxide dopants were in accord with the predictions. However, the reliability of the present preparation process is not good enough to offer an unqualified correlation with the preranked behavior.

#### **4.3 Variable Temperature SEM Tribometry of CuO-doped Rutile**

The samples described in Table 2 comprised the base materials from which SEM tribopins and flats were fabricated: (a) the undoped rutile baseline referred to hereafter as *rutile*, (b) the unreacted  $\text{TiO}_2$  + CuO blend (the *mix*), and (c) the doped and reacted rutile similar to a titanium-vanadium bronze equivalent to a Magnéli phase of  $\text{TiO}_{1.89}$  (the *bronze*). The main objective of the SEM tribometry was to correlate the chemistry and crystal structure of these model compounds with their tribological properties, in light of the predictions made in Figs. 1 and 8. Ideally, the dopant should expel just the right amount of oxygen by chemical means even before the surfaces come in contact, during the preparation of a lubricious oxide. The stoichiometry of rutile is thus confined *á priori* to a narrow, desired range. The selected range should (ideally) be retained in any environment.

A given range should depend on what the tribologist intends to do: (a) as predicted in Figs. 1 and 8, for a low-wearing brake material, an electrical contact or a surface-charge-bleeding audio/video tape guide, the stoichiometry of the electrically conductive, high COF  $\text{TiO}_{1.80}$  is desired, (b) for a self-lubricating, low friction material where an electrical insulator is needed the low COF  $\text{TiO}_{1.70}$  would be more suitable, and (c) for use in high temperature air, the  $\text{TiO}_{1.70}$  would be preferred over the  $\text{TiO}_{1.95}$  version, because the more oxygen-rich compound is still so full of oxygen that no conceivable chemical stabilization method could prevent additional loss of anions inevitably occurring during heating in vacuum or at very low  $P_{\text{O}_2}$ . Regaining oxygen in high temperature air (or in LOX) should not be a problem for any of the materials already reacted into a *bronze*, if the theoretical concept of doping worked exactly as conceived.

Since the actual stoichiometry of the rubbed triboflat surface cannot be measured *in situ* and there is no reliable way to estimate it as a test progresses, it is worth repeating that the measured friction trends are only qualitative. Confirming the trend predicted in Figs. 1 and 8 is both necessary and sufficient for the purposes of the program. Any *bronze* which exhibits the least change in COF and MAX.COF as well as the corresponding  $\tau_s$  as a function of temperature and test atmosphere is the most promising lubricious

oxide. The absolute magnitude of the COF, MAX.COF and  $\tau_s$  is also important, but not nearly as much as *unchanging* values of COF under *changing* extreme environmental conditions.

#### 4.3.1 Friction Behavior in Vacuum

The three different types of samples in Table 2 (the *rutile*, the *mix* and the *bronze*) were subjected to SEM tribometry in vacuum ( $\sim 1 \times 10^{-5}$  torr).

The COF values of *rutile* are presented in Fig. 34. This material is designated as  $\text{TiO}_{2-x}$ (HP) in the illustration. Fig. 8 is reproduced here again to help in the interpretation of the data. As shown in Fig. 34, the first 300 oscillatory cycles were completed in lab-ambient air ( $\sim 50\%$  R.H.). Then, the test assembly was pumped down and sliding was resumed by starting a temperature upramp. The rapid temperature increase was accompanied by an equally sudden COF increase, as predicted by the solid-arrowed direction in the included sister figure. Continued heating at  $\sim 1000^\circ\text{C}$  removes progressively greater amounts of oxygen from the rubbed triboflat surface and drives the COF function over a maximum. Keeping the operating triboflat at the highest test temperature brings COF down quickly to a steady-state condition. There, the electrochemical potential gradient, which retards the escape of additional amounts of oxygen from the rutile lattice, is counterbalanced by the oxygen-removing ability of heating in vacuum. The large COF peak that develops on heating is extremely undesirable for a thermally stable lubricious oxide slated for vacuum applications.

During the ensuing temperature downramp, the small amounts of residual moisture and oxygen in the test atmosphere resorb very slowly onto the sliding surfaces. The tribological response of the Magnèli phases is now following the upward direction on the negative slope of the  $\tau_s$  vs. stoichiometry function. The values increase back to the high  $\tau_s$  (and COF) peak at  $\text{TiO}_{1.80}$  (see the broken-arrowed direction below). Interestingly, the highest COF values coincide both during the thermal upramp and downramp portions of the test.

Admitting atmospheric air into the vacuum chamber at 1800 cycles lowers COF from the  $\text{TiO}_{1.80}$  maximum, as indicated by the continuation of the broken-arrowed direction cascading down the positive slope of the Fig. 8 function. The equilibrium COF after 1800 cycles, in air, is higher than the equivalent values at the onset of sliding (also in air). This increase is attributed to the enlarged wear scar and a bigger real-area-of-contact ( $A_r$ ) at the end of the test. Sliding always begins with a typical Hertzian contact area and stress established by the 0.49 N normal load. At the termination of each test, this relatively small contact zone increases to a much larger wear scar, whose size depends on the wear of the specimens in the particular contact combination. In the well-known equation of  $F_k = \tau_s \cdot A_r$  the  $\tau_s$  may be the same both at the beginning and the end of the experiment, but  $A_r$  may have easily doubled or tripled

# $\text{TiO}_{2-x}(\text{HP})$

LUB002-1

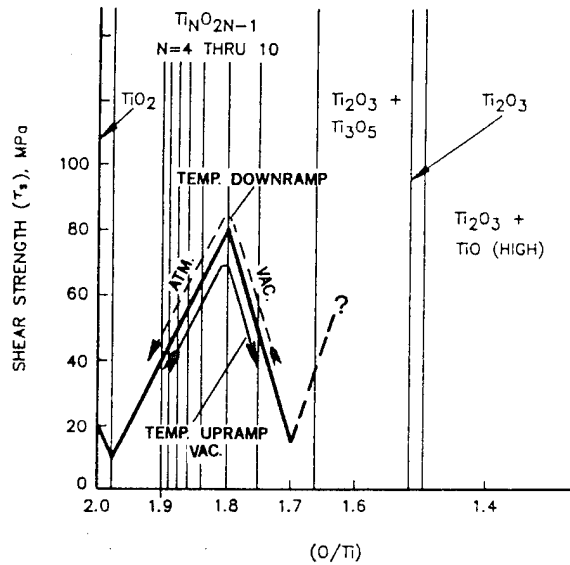
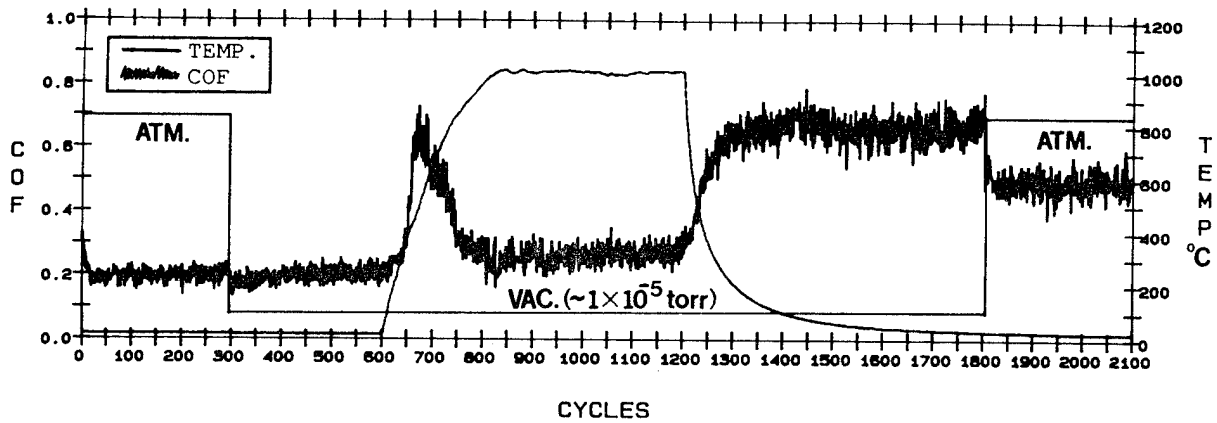


Figure 34. SEM tribometer-measured average coefficients of kinetic friction (COF) of hot-pressed, undoped rutile (slightly reduced during the hot-pressing process) sliding against itself, in vacuum. Figure 8 is reproduced for ease of data interpretation.

in time. This phenomenon is exactly the same as the friction force ( $F_k$ ) increase between a progressively more worn-in and smoother memory disc and its head (78).

The same arguments apply to the COF curve of the *mix* [designated as  $\text{TiCuO}_{2-x}(\text{HP})$ ] shown in Fig. 35. As seen in the same figure, the initial COF values, both in air and in vacuum, are lower than that of *rutile*. Even more importantly, the COF increase on thermal upramp is less than in the case of the baseline. This smaller increase would have been anticipated only if the *mix* reacted into the *bronze*, i.e., if the reaction had already expelled a portion of the oxygen from the rutile lattice. That would have meant a reduction in the size of the COF increase peak, but it would have also been accompanied by a higher initial COF value before that peak. Instead, the initial COF (both in air and in vacuum) was unexpectedly low here. The unusually low COF was gratifying, but could not be explained by the current model. As shown later in this report, this COF reduction was precipitated by the unreacted  $\text{Cu}_2\text{O}$  more-or-less accumulating on the sliding surface.

On thermal downramp, the COF increase was slower and the maximum COF value attained was lower than in the case of the baseline *rutile*. At the same time, as the lab atmosphere was introduced into the chamber at 1800 cycles, the COF reduction was significantly larger than that of the baseline. Even in its unreacted form, the copper oxide(s) may have favorably influenced (i.e., reduced) the level of COF. The phenomenon of preferential copper oxide accumulation on the sliding surfaces will be a recurring theme in this report.

COF data on the *bronze* are also given on the bottom of Fig. 35 [the  $\text{TiCuO}_{2-x}(\text{HP}+\text{ANN.})$ ]. The COF peak on heating was even lower than in the case of the *mix* in the middle and far lower than with the *rutile* baseline at the top of the illustration. As pointed out before, the best tribological footprint of the *bronze*-forming reaction is the significant reduction in the magnitude of this friction peak.

The sudden reduction of COF at room temperature, right after pump-down, was unexpected. This low vacuum friction was preceded by significantly higher friction in air. The large drop in COF may signify the sensitivity of the doping-induced Magnèli phases and, possibly, the exposed dopant atoms (ions) themselves to atmospheric moisture. Hydrogen bonding-induced COF increases are common with substrates that can chemisorb water. As discussed before, the exposed Lewis acid sites at the Magnèli phase arrays emerging on the surface are inherently sensitive to moisture. Apparently, the phases produced by cation-doping are even more reactive. There is ample evidence in the literature that the high  $T_c$  superconductive oxide analogs to lubricious oxides are equally sensitive to moisture adsorption (79 through 85). The  $\zeta$  potential-calculated electronegativity of  $\text{CuO}$ , as related to the adsorption of hydronium ions, is almost exactly the same as that of the  $\text{YBaCuO}$  (1-2-3) compound. Therefore, this supposition explaining the moisture effect is reasonable.

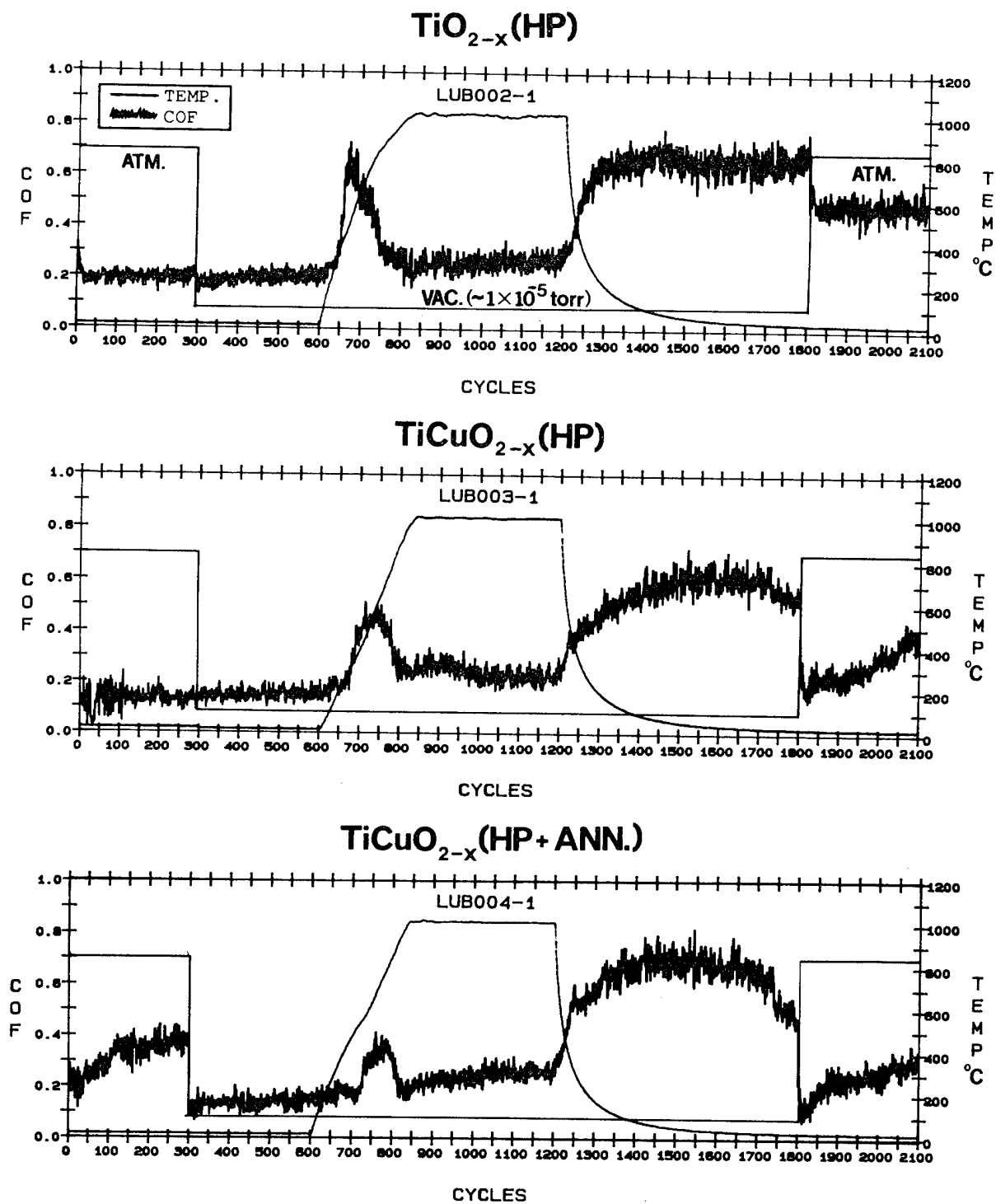


Figure 35. SEM tribometer COF results of undoped and CuO-doped rutile samples sliding against themselves in vacuum, presented together to allow comparison of COF behavior under identical test conditions.

As the temperature was downramped, the second COF maximum reached on cooling (at around 1500 cycles) was higher than previously measured with the *rutile* baseline. The theoretical predictions forecast no change in the respective COF maxima, because a brand new, never-before-used piece of *bronze* doped to a  $\text{TiO}_{1.89}$ -like stoichiometry should not be any more stable against additional oxygen loss than a piece of *rutile* baseline reduced to the same stoichiometry during the SEM tribometric heating process. If the maximum, tribometric heating-induced oxygen depletion did reach the  $\text{TiO}_{1.70}$  level at 1200 cycles, then the thermal downramp-caused slow resorption of the oxygenated species should be able to bring the COF values back up the negative slope of the  $\tau_s$  function. As before, the initial segment of the broken-arrowed direction in Fig. 8 should be followed, to the maximum value predicted at  $\text{TiO}_{1.80}$ . Again, it is suspected that the presence of the exposed copper ions and/or defect planes associated with the copper oxides themselves are responsible for this deviation.

Due to the high significance of the *bronze* tribotest on the bottom of Fig. 35, this test was repeated with brand new specimens. The data in Fig. 36 indicate good repeatability. The small doublet peak on thermal upramp remained just as small as before. This finding was all-important. According to predictions, these peaks have to be smaller than those associated with the *mix* and, especially, with the *rutile* baseline. Doublet instead of singlet COF increase peaks on heating was observed once before (see Fig. 17). The cause of the doublet cannot be fully explained at this time. One likely reason might be the possible, and unpredictably random, spalling of the newly developed tribosurface layer discussed previously in 3.2.4.

The series of COF charts in Fig. 37 are the MAX.COF-equivalents of those shown previously in Fig. 35. The MAX.COF values are at least double the COF magnitudes at any given points of the experiments. At the same time, the frictional variations ("hash") are consistently higher across the board. There is no discernible change, however, in the relative shape and trend of the respective friction curves. It is especially important to note that there is no change in (a) the relative size ranking of the temperature upramp COF peaks, and (b) the atmospheric moisture-sensitivity of the *bronze*.

#### 4.3.2 Friction Behavior in Partial Pressures of Oxygen

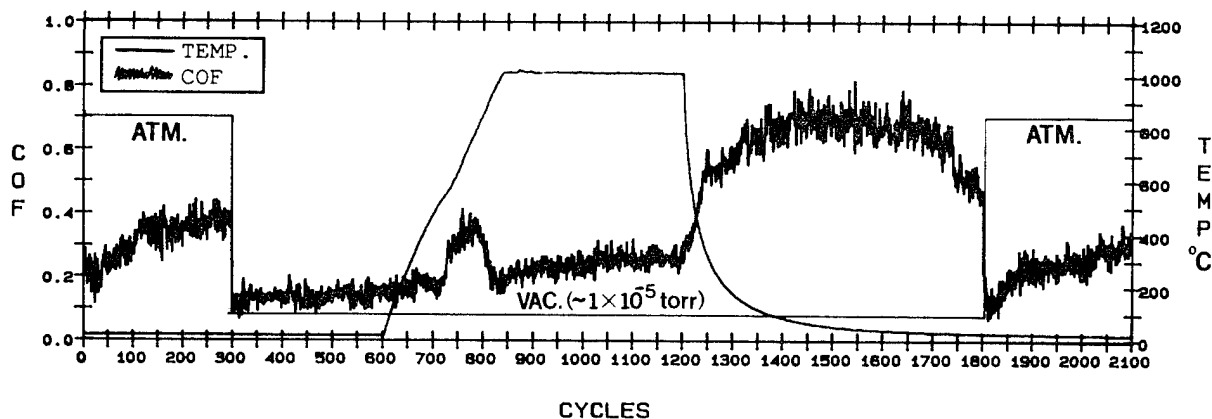
An identical series of SEM tribometer experiments was performed with new sets of *rutile*, *mix* and *bronze* specimens, in  $P_{\text{O}_2}$ .

The data on *rutile* in Fig. 38 are in accordance with the prediction that the rapid increase in COF on heating will occur at a higher temperature than in vacuum. Since the lidded subchamber level of evacuation is only as good as the one provided by the mechanical vacuum pump (estimated as  $\sim 1 \times 10^{-2}$  to  $1 \times 10^{-3}$  torr), there is a much larger number of water and oxygen molecules above the rubbed triboflat



# $\text{TiCuO}_{2-x}$ (HP+ANN.)

LUB004-1



LUB007-1

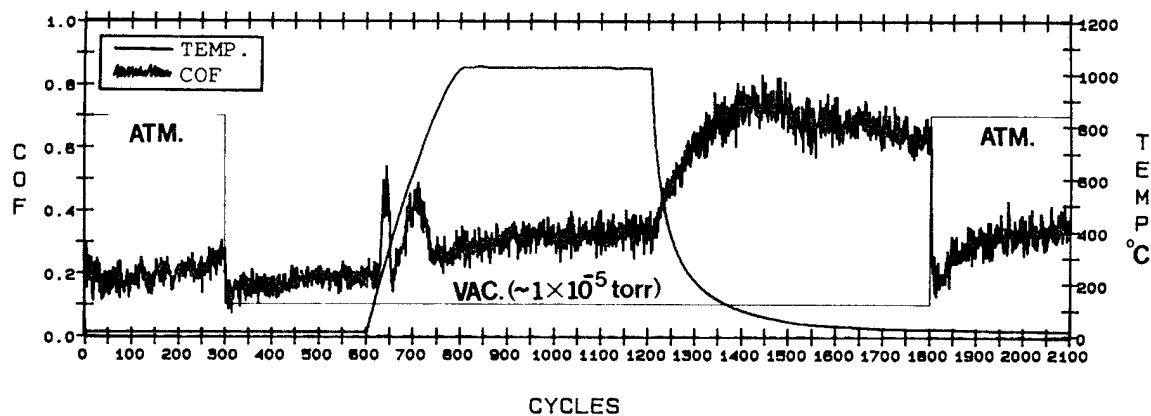


Figure 36. Duplicate SEM tribometer COF results of CuO-doped rutile samples  $[(\text{Ti} + \text{Cu})\text{O}_{1.80}]$  theoretical blend, hot-pressed + annealed sliding against themselves in vacuum (two new sets of specimens).

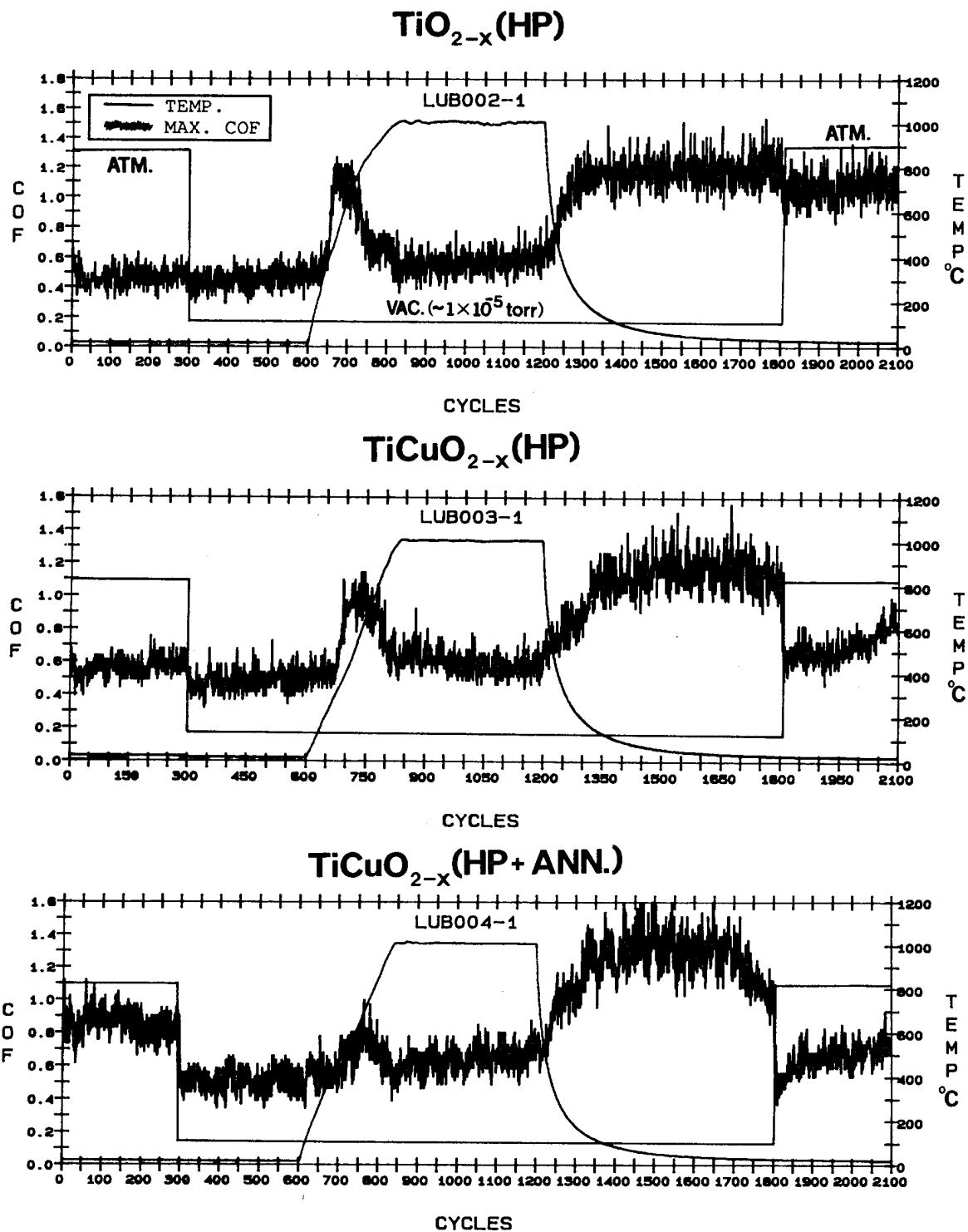


Figure 37. MAX. COF results associated with the tests described in Fig. 35 to allow comparison of COF (average kinetic friction) with MAX. COF (maximum break-away or static friction) behavior of the same counterfaces as a function of temperature, in vacuum.

# $\text{TiO}_{2-x}(\text{HP})$

LUB006-1

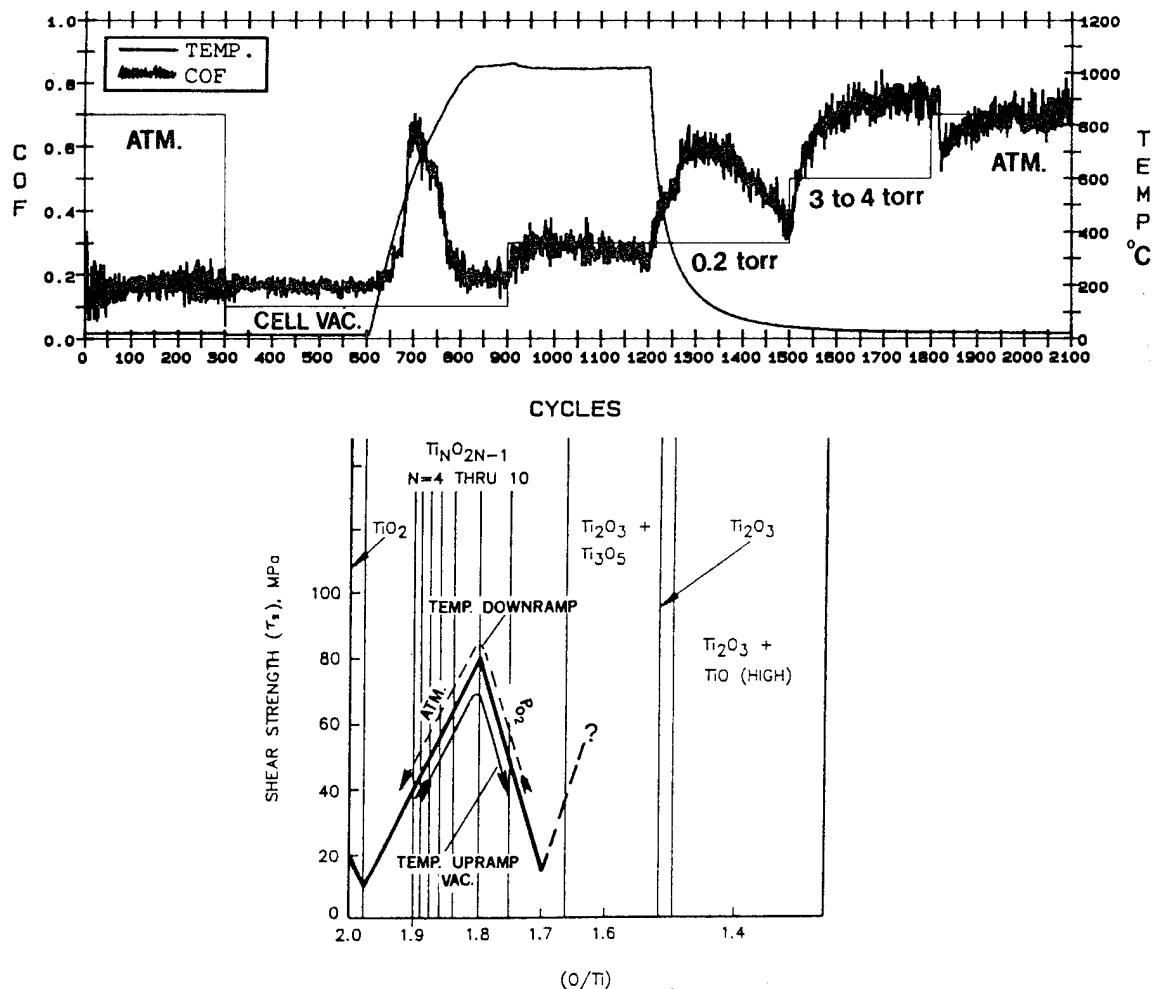


Figure 38. SEM tribometer-measured average coefficient of kinetic friction (COF) of hot-pressed, undoped rutile (slightly reduced during the hot-pressing process) sliding against itself in various partial pressures of oxygen ( $P_{\text{Ox}}$ ). Figure 8 is reproduced for ease of data interpretation.

than in  $\sim 1 \times 10^{-5}$  torr vacuum. The half-height of the COF increase occurs at  $\sim 500^\circ\text{C}$  here, while in Fig. 34 the equivalent temperature is only  $\sim 400^\circ\text{C}$ . The high slope of the rapid increases and the respective decreases on cooling is the same in both cases.

It is important to remember that the decrease in COF on continued heating at  $\sim 1000^\circ\text{C}$  is the footprint of  $\tau_s$  reduction, as the oxygen content becomes less than  $\text{TiO}_{1.80}$  (the second segment of the solid-arrowed direction). At  $\sim 1 \times 10^{-5}$  torr, the minimum COF achieved at continued heating depends on the equilibrium surface stoichiometry attained at that particular (high) temperature and (low) partial pressures of the residual gases. Keeping the temperature constant but raising the partial pressure of oxygen above the tribospecimens upsets this equilibrium and drives the COF function higher on the negative  $\tau_s$  slope. The COF grows closer to the maximum at  $\text{TiO}_{1.80}$ . The same phenomenon was observed and discussed before in 3.2.4.

In the same vein, if the  $P_{\text{O}_2}$  were kept constant but the temperature lowered, the equilibrium could be disturbed once more. The increased sorption of oxygen onto the rubbed surfaces further brings COF up on the negative slope. The values should become closer yet to the predicted maximum at  $\text{TiO}_{1.80}$ .

The COF did increase on cooling in 0.2 torr. The rising COF did not reach another equilibrium at  $\sim 1370$  cycles, however. It did not, because the equilibrium stoichiometry of the surface may have become disturbed by another factor: the in-diffusion of excess surface oxygen into the lattice, commencing at  $\sim 1370$  cycles.

As shown previously in Fig. 5 and discussed in 3.2.4, on thermal downramp, the subsurface and the bulk suddenly becomes more oxygen-deficient than the surface. In the low  $P_{\text{O}_2}$  environment, the pull of the internal electrochemical potential gradient (the need for more oxygen by the depleted lattice) becomes greater than the rate of oxygen resupply to the surface. Therefore, on further cooling the specimens in 0.2 torr, the COF should proceed downward if the in-diffusion of oxygen became greater than its rate of sorption onto the surface. A proof of this argument can be tested by stopping and reversing the downward trend of COF by admitting substantially higher partial pressures of  $\text{O}_2$  into the subchamber.

This gradual COF reduction from the short-lived maximum at  $\sim 1370$  cycles was indeed reversed immediately by increasing the  $P_{\text{O}_2}$  into the 3 to 4 torr range. Note that any further temperature reduction during this maneuver was negligible. The surface and the immediate subsurface suddenly became enriched with oxygen and the electrochemical potential gradient between the most oxygen-rich and oxygen-poor regions lessened substantially. As a consequence, the COF near room temperature was free to equilibrate undisturbed starting at  $\sim 1700$  cycles, near the ultimate value expected at  $\text{TiO}_{1.80}$ . The new equilibrium held steady; it was allowed to develop for over 100 cycles before atmospheric air was

admitted into the chamber. Compare this steady-state COF with the preceding, changing values around ~1370 cycles.

The *rutile* baseline data, along with those of the *mix* and the *bronze* are presented together in Fig. 39. The *rutile* and the *mix* COF curves are very similar with one major discrepancy: admitting 0.2 torr of oxygen at 1000°C did not increase, but reduced the COF. The unreacted dopant atoms exposed on the surface may have influenced the COF response differently from the predicted trend. As discussed more thoroughly in the next subsection (4.3.3), copper did diffuse preferentially to the surface of the triboflat in  $P_{O_2}$ . The other important observations with the *mix* COF are (a) the size of the thermal upramp peak is smaller than that of the the baseline, and (b) there is no change in COF on pumpdown, but a large change in COF on admitting air into the chamber at the end of the test (the moisture sensitivity issue). The findings here are in line with those of the equivalent vacuum tests in Fig. 35 (Test No. LUB003-1). The shape of the second *mix* test's COF curve agrees well with the first one, showing good repeatability (Fig. 40).

The *bronze* results on the bottom of Fig. 39 confirmed the same sample-to-sample trend shown previously in Fig. 35. The COF peak on heating was smaller than that of the *mix* and far lower than that of the *rutile* baseline. The friction-stabilizing effect of the Magnéli phases manifested itself the same way here as in the case of the vacuum tests. The greater sensitivity of *bronze* to moisture was also reconfirmed. The variations in the *bronze* COF magnitudes are less, both on gas bleed-in and thermal downramp, than with the *rutile* baseline. It can be seen that the shape of the COF function of the *rutile* and the doped *rutile bronze* are more similar to each other than to the *mix* curve. The visibly different frictional variations of the *mix* indicate that the sliding surfaces underwent some sort of change. The rubbing interface acts differently from those of the *rutile* and the *bronze*.

The MAX.COF curves in Fig. 41 are associated with the COF functions in Fig. 39. The difference in the much higher MAX.COF vs. the lower COF magnitudes is greater here than the similar disparity previously observed with the vacuum tests. The progressively reduced heights of the thermal upramp MAX.COF peaks from the *rutile* to the *bronze* match the reduction observed with the COF upramp peaks. An interesting artifact of the MAX.COF curves is the unusually stable (but high) friction of the *bronze* under gas bleed-in and thermal downramp conditions. The MAX.COF of the *bronze* test (LUB008-1) is very high (near 1.1), but steadier than in the case of the *rutile* baseline (LUB006-1). Again, as before in Fig. 39, the appearance of the *rutile* and the *bronze*'s friction curves were more similar to each other than to the *mix* curve.

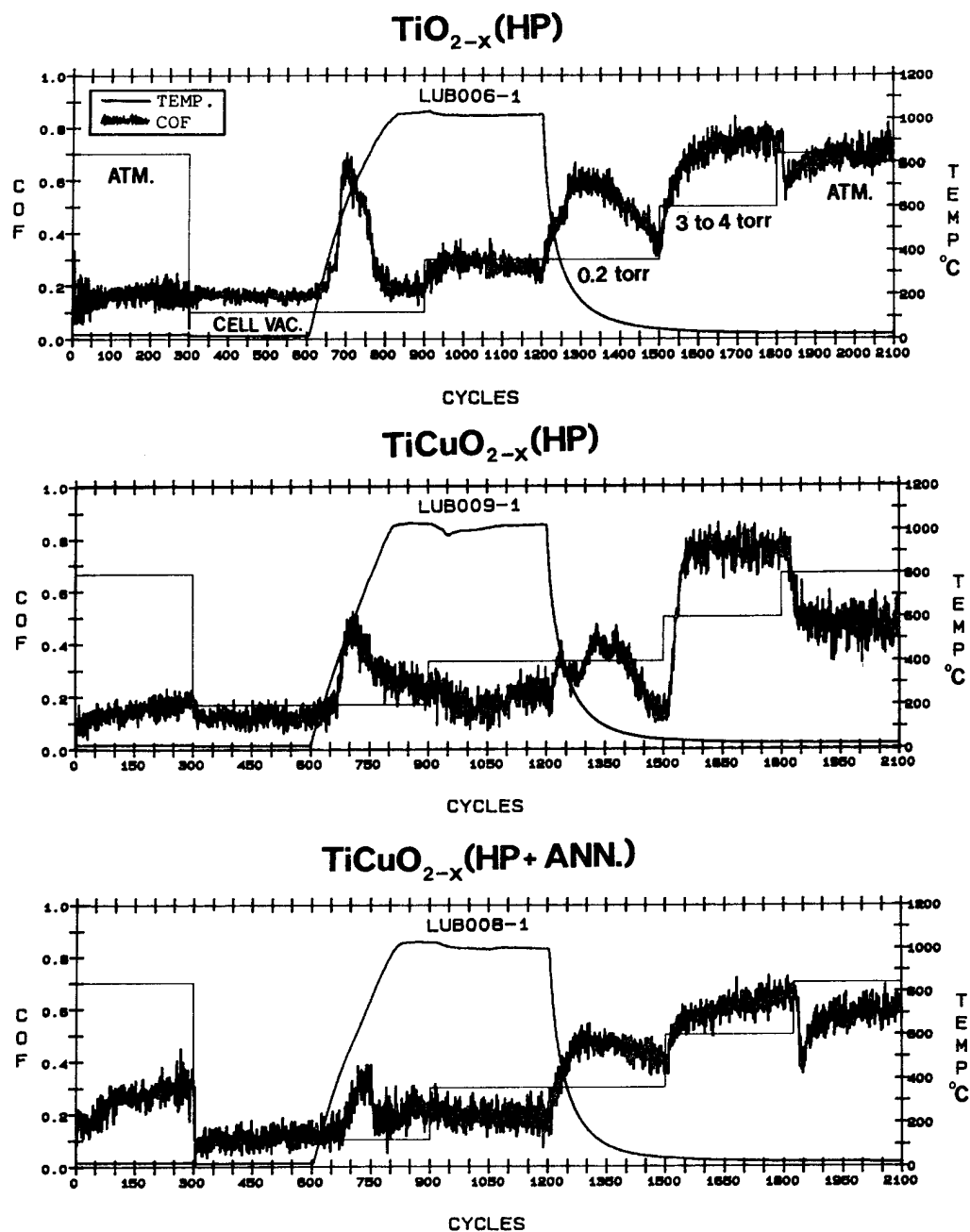
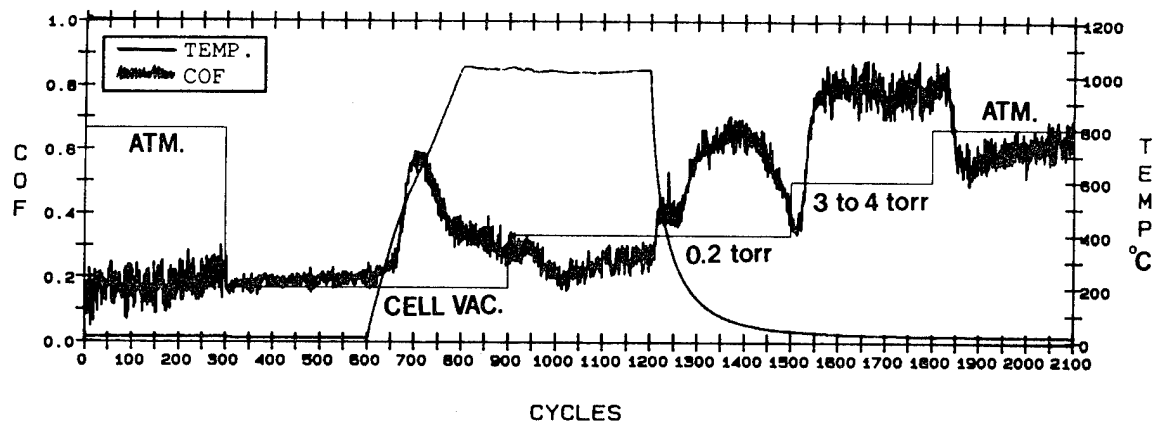


Figure 39. SEM tribometer COF results of undoped and CuO-doped rutile samples sliding against themselves in P<sub>OX</sub>, presented together to allow comparison of COF behavior under identical test conditions.

# $\text{TiCuO}_{2-x}(\text{HP})$

LUB005-1



LUB009-1

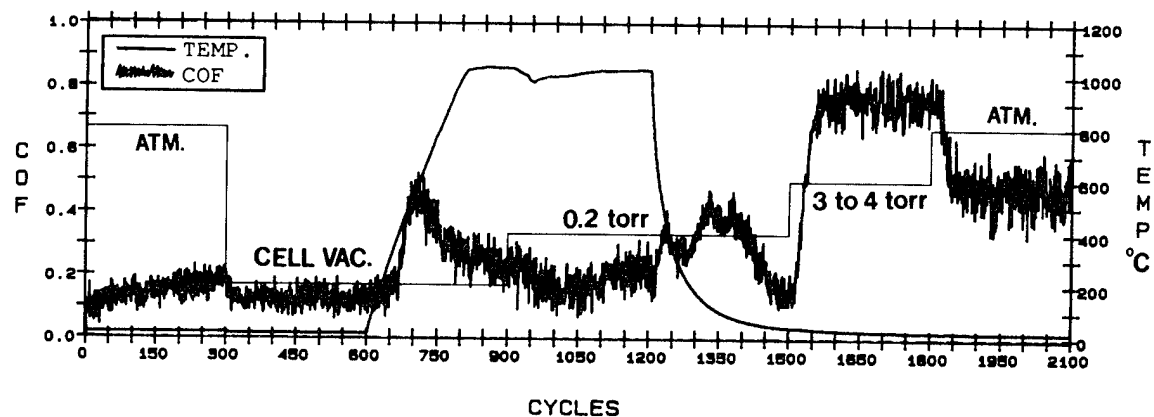


Figure 40. Duplicate SEM tribometer COF results of CuO-doped rutile samples  $[(\text{Ti} + \text{Cu})\text{O}]_{1.80}$  theoretical blend, hot-pressed] sliding against themselves in  $\text{P}_{\text{OX}}$  (two new sets of specimens).

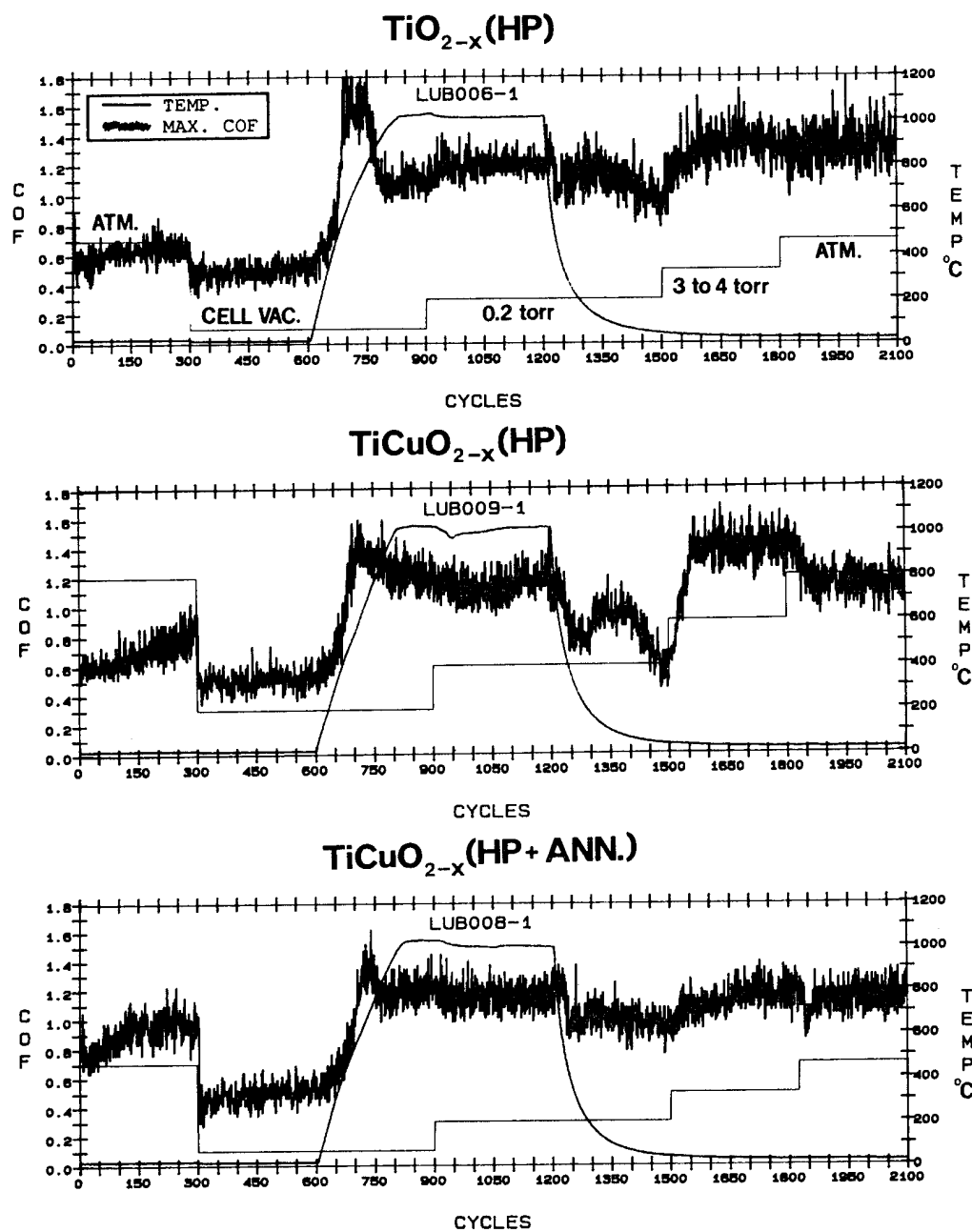


Figure 41. MAX. COF results associated with the tests described in Fig. 39, to allow comparison of COF (average kinetic friction) with MAX. COF (maximum break-away or static friction) behavior of the same counterfaces as a function of temperature, in  $P_{\text{OX}}$ .



Since the juxtaposition of all three vacuum tests and all three  $P_{ox}$  COF curves in Figs. 35 and 39, as well as the respective MAX.COF curves in Figs. 37 and 41 seemed handy for comprehensive evaluation of the data, the same methodology is followed by presenting improved versions of these figures in two, all-encompassing illustrations. To further enhance the observations of the similarities and differences in material behavior, the high "hash" of the respective friction curves was smoothed by a computer program in Figs. 42 and 43. A subroutine of the RS/1<sup>®</sup> data analysis software is capable of smoothing the scatter by locally weighed regression of successive groups of 20 ea. COF or MAX.COF data points (for a description of the LOWESS method, see Ref. 86).

One basic goal of the present research program is to produce a model compound, which exhibits less COF and MAX.COF variations during SEM tribometry than those of the undoped *rutile*. The advantages of the *bronze* lie in the progressively smaller thermal upramp peaks (marked with arrows in Figs. 42 and 43) from the *rutile* to the *bronze*, along with the progressively increasing temperatures needed to induce the onset of the peaks. Peaks of diminishing size are strong evidence of the copper-induced Magnèli phases being able to stabilize friction at roughly the same level in any environment.

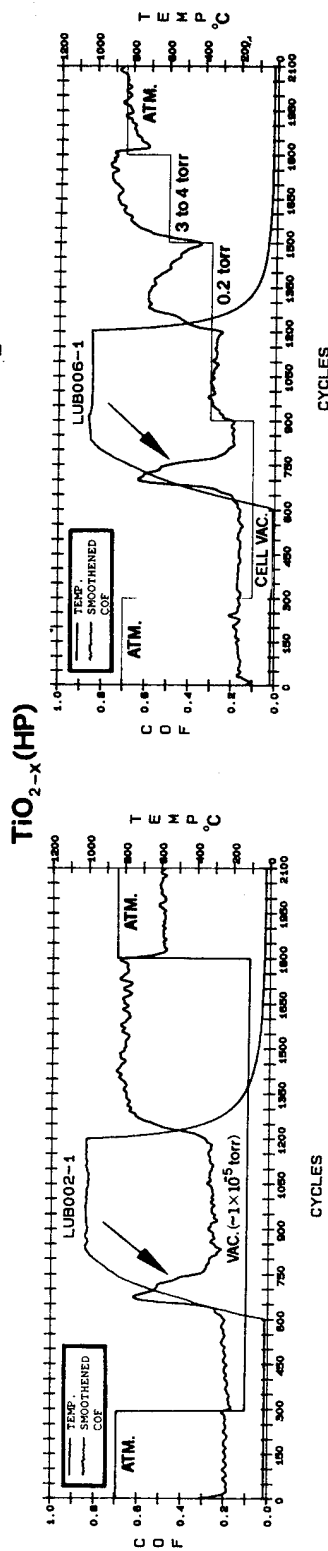
The thermal upramp peak would disappear (flatten) completely only if the stoichiometry would be stabilized near  $TiO_{1.70}$ . Furthermore, it would also mean that oxygen enrichment of the atmosphere at any temperature or cooling the specimens at any given  $P_{ox}$  should have no effect on increasing COF or MAX.COF. The sliding surfaces would refuse to chemisorb oxygen, because the entire specimen body had been chemically pre-reduced to a stable and highly oxygen-deficient state. Ideally, such doping-induced pre-stabilization translates into flatter friction curves, both on heating and cooling, in any atmospheric environment. If both the size and the variations of the COF/MAX.COF could be reduced simultaneously, then true molecular engineering of a lubricious oxide would be accomplished.

The average thermal upramp values of COF of the *bronze* samples are within the 0.1 to 0.2 range, in any of the test environments. This narrow range is low in terms of the customary friction coefficients one usually observes with any solid lubricant at high temperatures, especially in air or in LOX. The corresponding MAX.COF are, however, unexpectedly high.

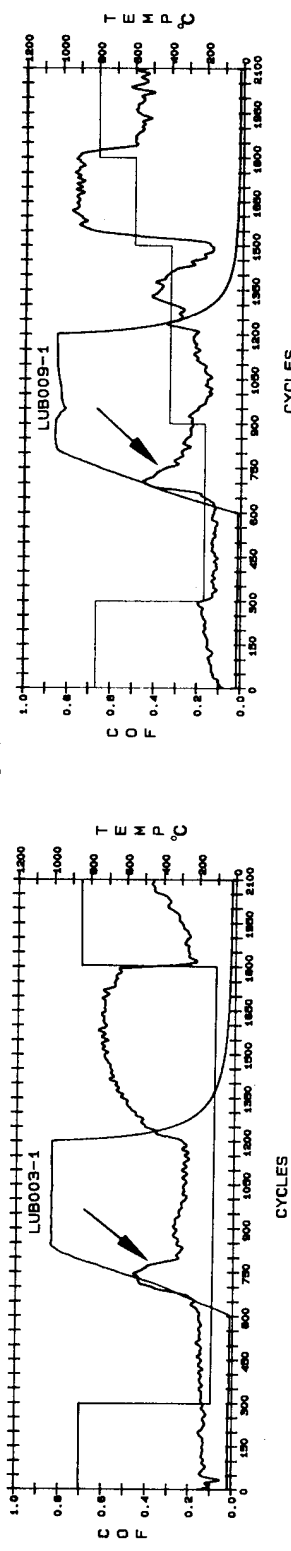
It is not known whether or not the high MAX.COF is caused by the strong attractive interaction of the dangling titanium bonds (the  $Ti^{3+}$  Lewis acid sites) between the contacting *bronze* surfaces. This point may be clarified by scanning tunnelling microscopy (87) or, better yet, by atomic force microscopy at various levels of doping. If MAX.COF were controlled by the number and the distribution of the active sites at the sliding interface, then the magnitude of the friction should come down on oxygen resaturation of the surface. These dangling bonds could not have been responsible for any COF or MAX.COF increases during cooling in vacuum. On thermal downramp, the residual oxygenated species

ATM.-VAC.-ATM.

ATM.-P<sub>O<sub>2</sub></sub>-ATM.



$\text{TiCuO}_{2-x}(\text{HP})$



$\text{TiCuO}_{2-x}(\text{HP} + \text{ANN.})$

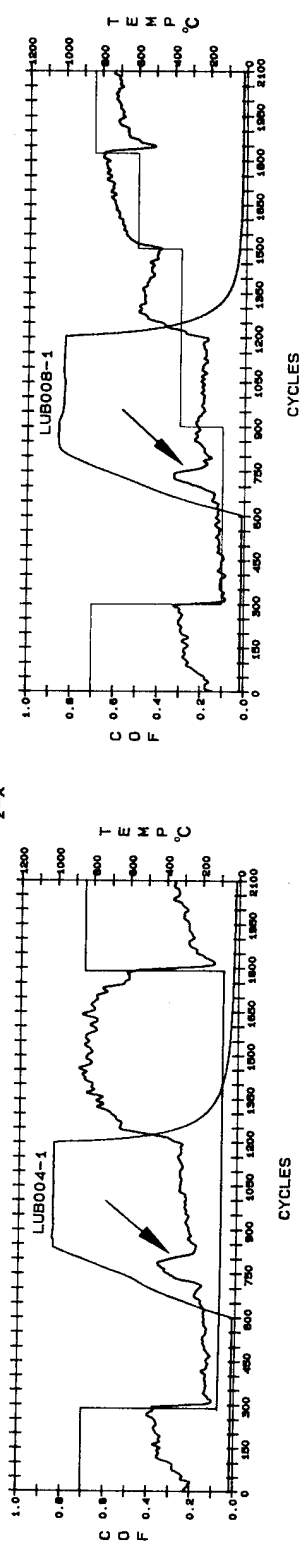
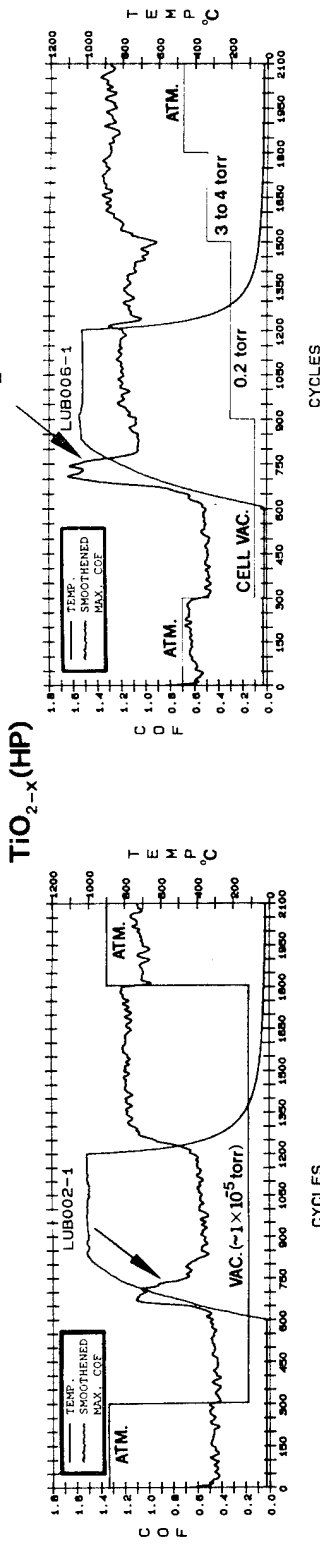


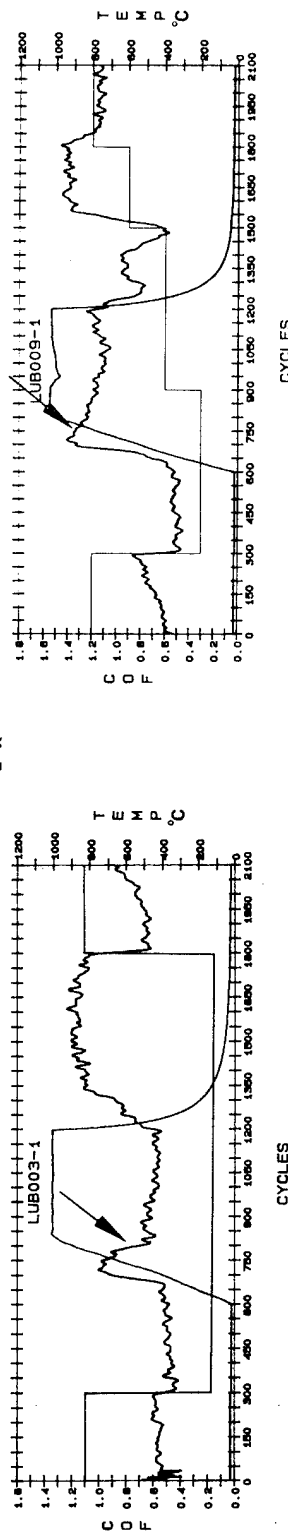
Figure 42. Regression-smoothed COF functions from Figures 35 and 37 to allow COF comparison of all typical and equivalent tests on undoped and doped rutile, as a function of test temperature and atmospheric environment.

ATM.-VAC.-ATM.

ATM.-P<sub>O<sub>2</sub></sub>-ATM.



**TiCuO<sub>2-x</sub>(HP)**



**TiCuO<sub>2-x</sub>(HP+ANN.)**

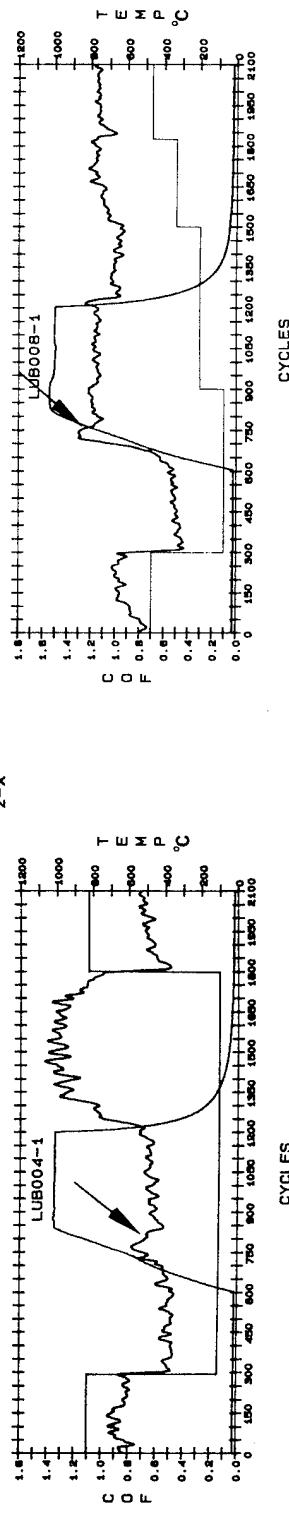


Figure 43. Regression-smoothed MAX. COF functions from Figures 39 and 41, to allow MAX. COF comparison of all typical and equivalent tests on undoped and doped rutile, as a function of test temperature and atmospheric environment.

in the SEM column are resorbing onto the rutile surface to annihilate the dangling bonds the same way as (albeit slower than) pure oxygen sorbing from the various  $P_{Ox}$  atmospheres. Therefore, the basic cause of the high MAX.COF values lies elsewhere and needs further investigation.

#### 4.3.3 Wear Behavior in Vacuum and Partial Pressures of Oxygen

The pin tip wear scars and the associated wear tracks on the mating flats of all tests were photographed in the SEM after the experiments. The low magnification secondary electron (SE) images are presented in Fig. 44. The overview of the photos indicate that (a) the wear scars of the vacuum tests seem to be somewhat larger than the  $P_{Ox}$  tests, (b) the scars associated with the  $P_{Ox}$  tests charge less under the electron beam than the vacuum equivalents, (c) the surface of the *mix* and the *bronze* specimens are visibly rougher than the *rutile*'s, and (d) the *rutile* pin of the  $P_{Ox}$  test exhibited recrystallized surface artifacts, possibly indicating surface contamination. EDX of the pin tip did not, however, indicate any other elemental signatures than those of titanium and oxygen (Fig. 45).

The backscattered electron (BSE) images of the pin tips tested in vacuum (and originally depicted in the SE photomicrographs in Fig. 44) are given in Fig. 46. The rougher and more porous nature of the *mix* and the *bronze* are brought out with even greater clarity. The high magnification SEM photomicrographs of the same samples, taken on unused areas of both the pin and the flat, clearly indicate that the increased roughness was caused by excessive grain growth (Fig. 47). Similar photographs of two sets of the *bronze* samples in Fig. 48 show remarkably uniform appearance of the rough crystal structures and the equally rough conditions of the as-machined surfaces. These samples resemble the appearance of the purposely reduced rutile surfaces previously shown in Figs. 24 through 27, although those undoped samples exhibited a lesser degree of grain growth.

It is well-known that there is grain coarsening during solid state sintering of ceramics at high temperatures (88,89). Titanium dioxide is no exception to this rule (90 through 93). In addition to the conventional, thermally induced and time-dependent grain growth phenomenon, there is abnormal grain growth of titania due to the presence of cation dopants, especially where the starting powder is anatase (94). In the present case, grain growth occurred in the presence of copper ions even where the copper did not enter the rutile lattice (see the SEM photomicrograph of the *mix* in the middle of Fig. 47). Since the *mix* was hot-pressed exactly the same way as the *rutile* baseline (i.e., both samples were exposed to the 1100°C HP temperatures for 6 hours only while the *bronze* saw an additional 48+ hours at the same temperature), the grain growth of the *mix* is related to cation contamination.

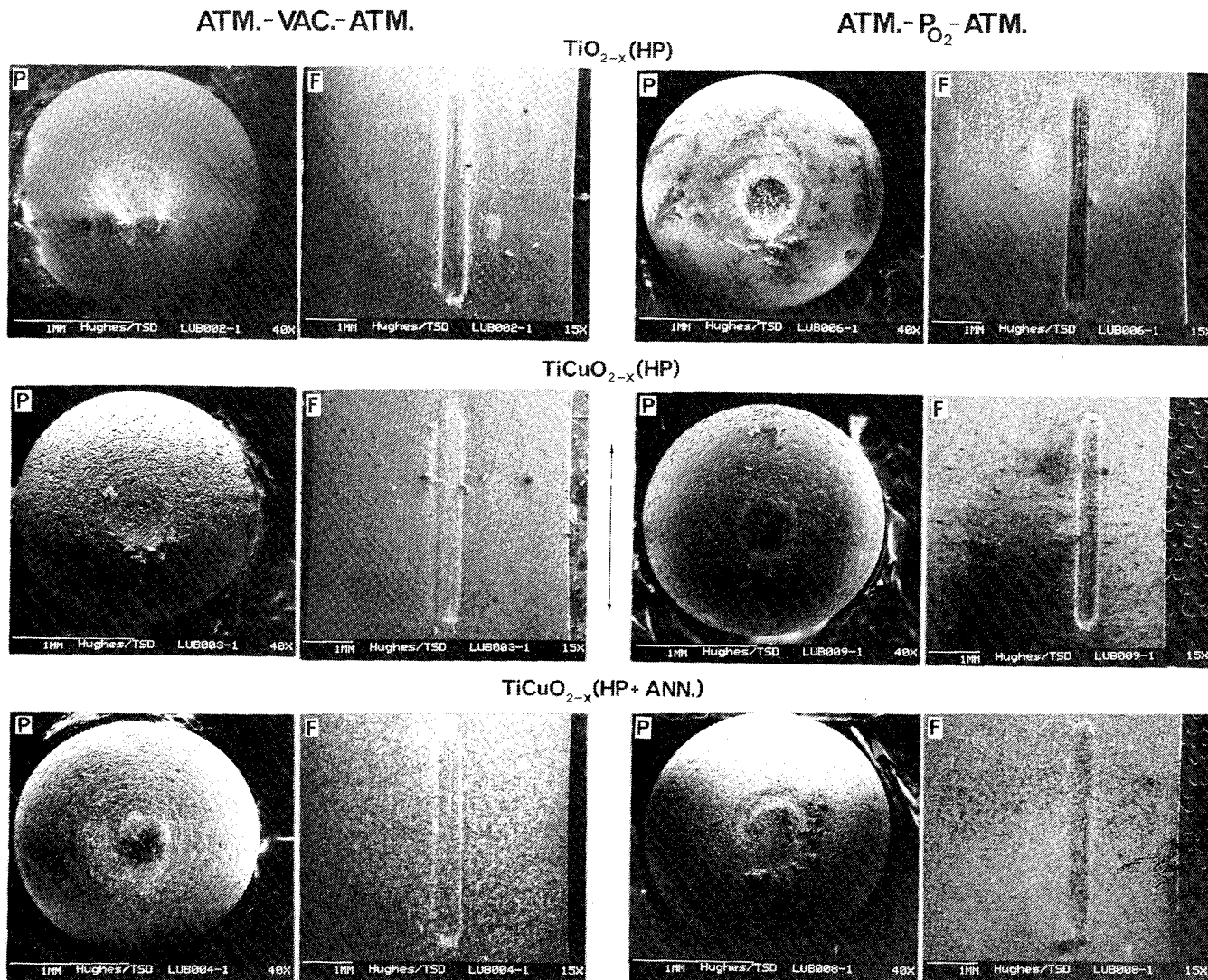
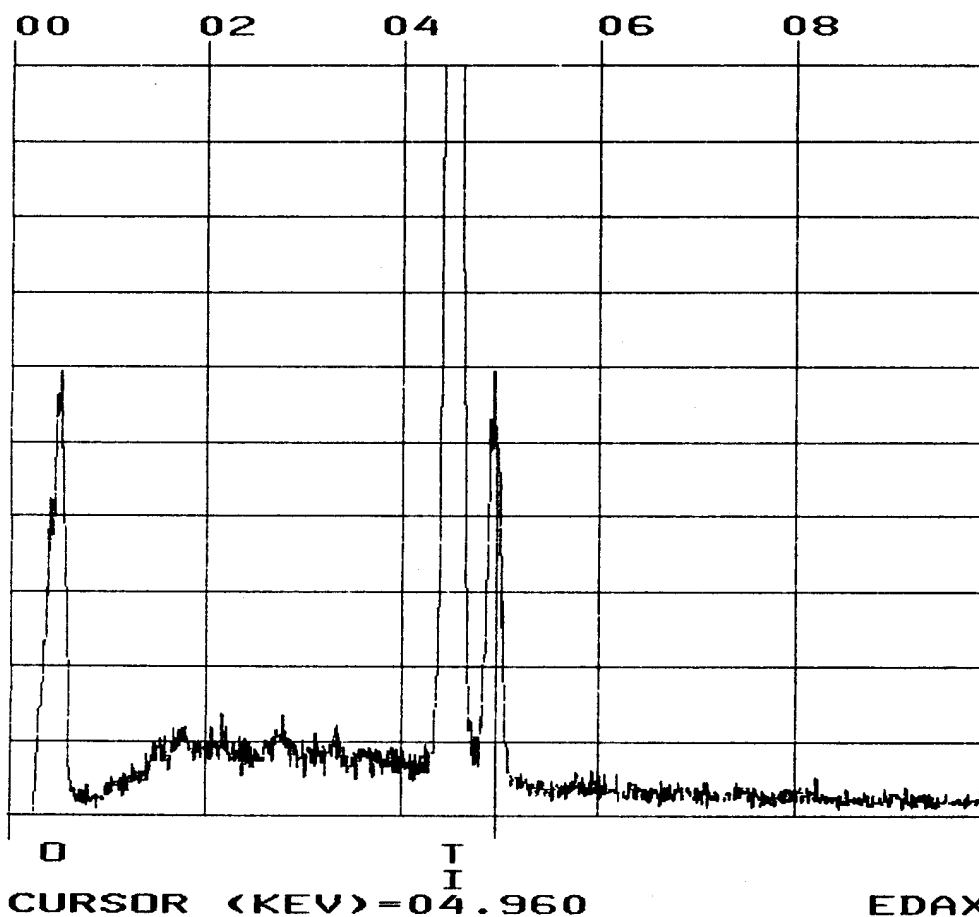


Figure 44. Low magnification SEM photomicrographs of pin (P) tip and flat (F) wear scars associated with all the vacuum tribotests described in Figs. 42 and 43, showing generally lower wear rates in  $\text{P}_{\text{O}_2}$ . Double-headed arrow indicates direction of oscillatory sliding.

-OCT-92 13:12:38  
RATE: CPS TIME 27LSEC  
00-20KEV:10EV/CH PRST: OFF  
A: B:  
FS= 506 MEM: A FS= 50



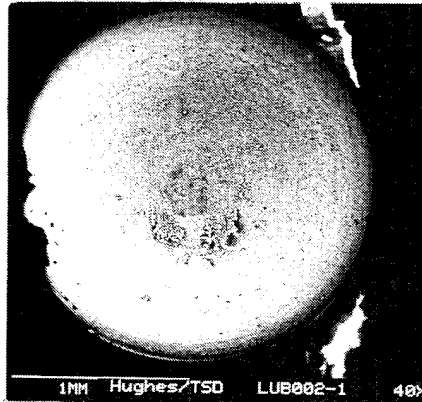
LUB006-1: ALL AREAS  
(TI PEAK=2022)  
1000X 20KV

HUGHES/TSD

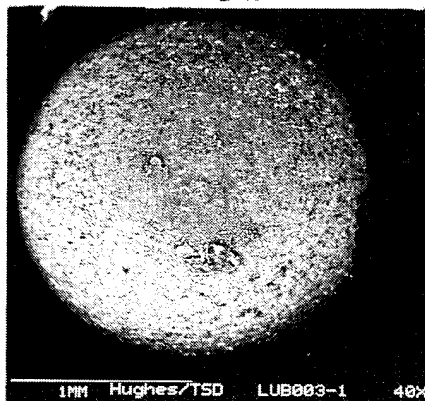
Figure 45. Energy dispersive X-ray spectrum (EDS) of the undoped rutile pin tested in P<sub>ox</sub>.

ATM.-VAC.-ATM.

$\text{TiO}_{2-x}(\text{HP})$



$\text{TiCuO}_{2-x}(\text{HP})$



$\text{TiCuO}_{2-x}(\text{HP} + \text{ANN.})$

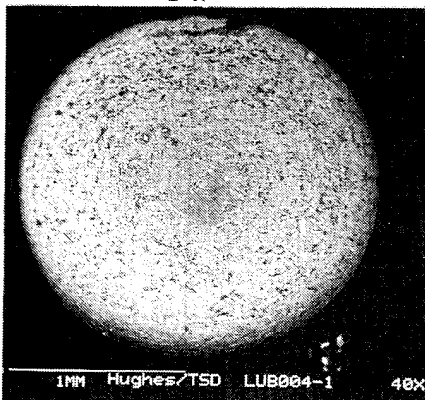
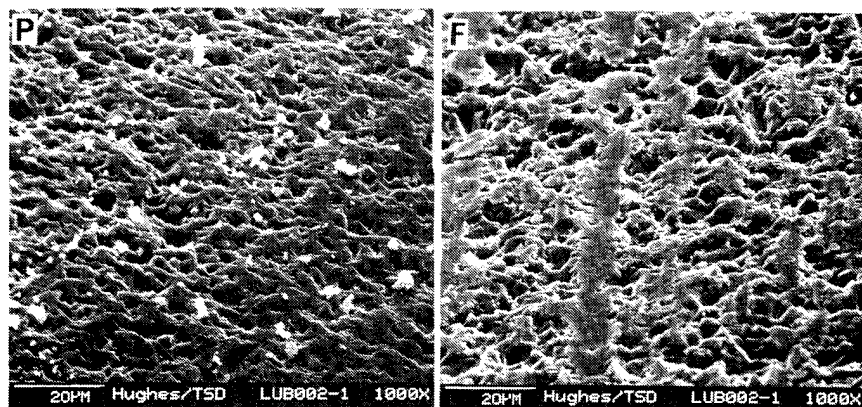


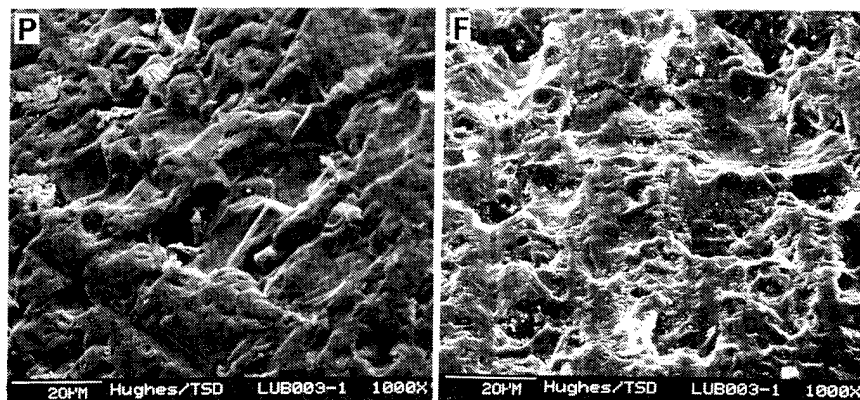
Figure 46. Low magnification SEM photomicrographs (backscattered electron images) of pin tip wear scars associated with vacuum tribotests, showing rougher surface structure that developed on CuO-doping. Double-headed arrow indicates direction of oscillatory sliding.

ATM.-VAC.-ATM.

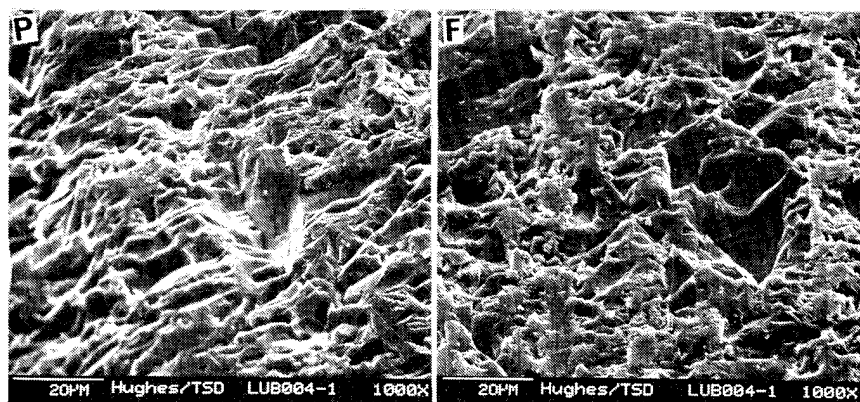
$\text{TiO}_{2-x}(\text{HP})$



$\text{TiCuO}_{2-x}(\text{HP})$



$\text{TiCuO}_{2-x}(\text{HP} + \text{ANN.})$



60°

50°

Figure 47. High magnification SEM photomicrographs of unused pin (P) tip and flat (F) portions of vacuum-tribotested specimen surfaces (also see Figs. 35 and 37), showing grain growth due to CuO-doping.



$\text{TiCuO}_{2-x}(\text{HP} + \text{ANN.}) \bullet \text{ATM.} - \text{VAC.} - \text{ATM.}$

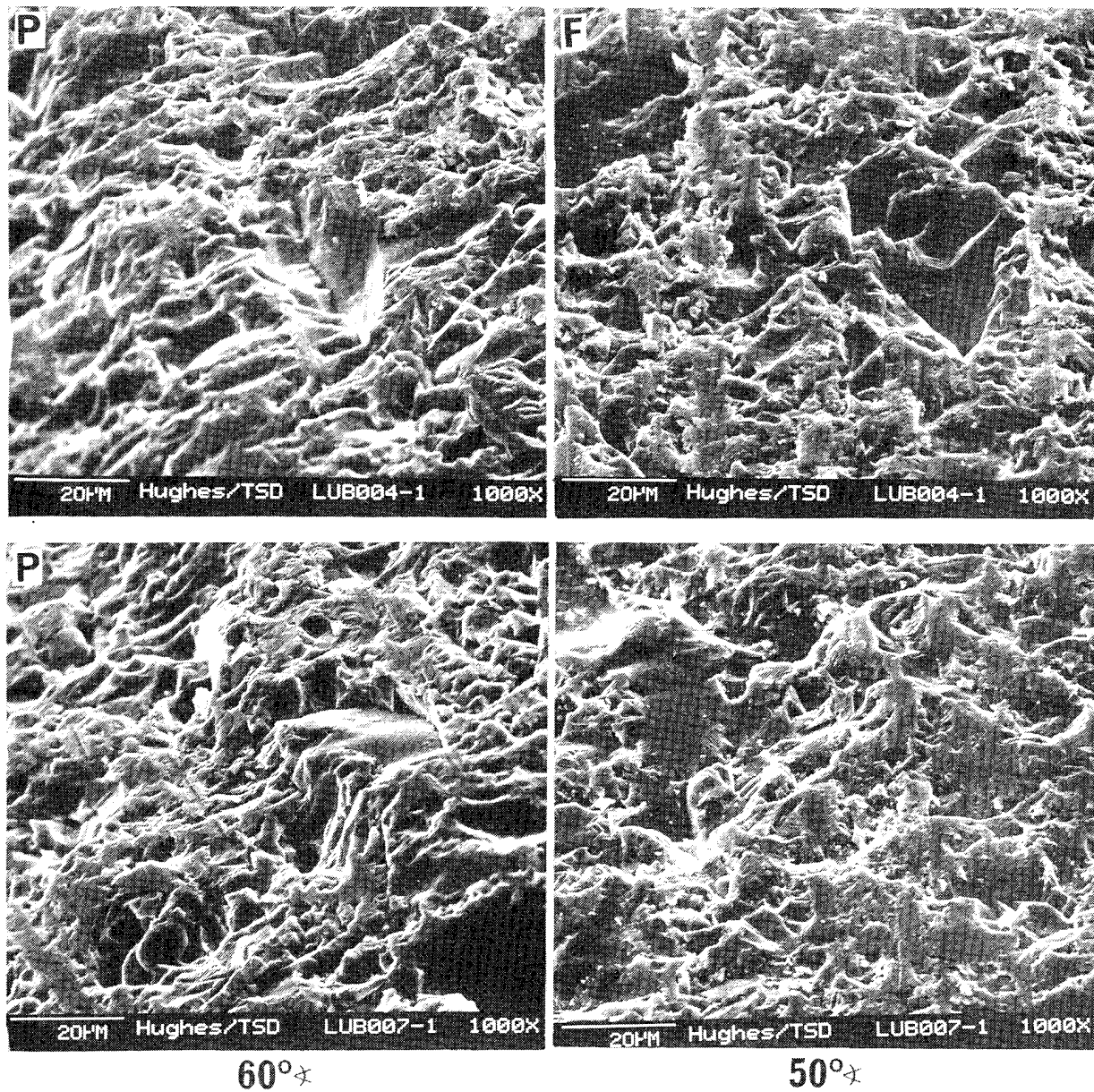


Figure 48. High magnification SEM photomicrographs of unused pin (P) tip and flat (F) portions of duplicate-vacuum-tribotested specimen surface sets (also see Fig. 36), showing consistency of grain growth due to CuO-doping.

It is the unusual grain growth of the *mix* and the *bronze* which influenced the real-area-of-contact ( $A_r$ ) and the respective friction values. The  $A_r$  changed from the smaller but more numerous microareas of the *rutile* tribocontacts to the larger, but fewer contact zones of the other two types of samples (Figs. 49 and 50). Although the respective  $A_r$  values cannot be estimated accurately from the scar photomicrographs in Fig. 49, the high magnification photos in this illustration agree qualitatively with the results deduced from Fig. 44 in that the scars associated with the  $P_{ox}$  tests are smaller. The scars of the *mix* and the *bronze*  $P_{ox}$  specimens charge less under the  $e$ -beam. The reduced surface charging, combined with the copper-discoloration of the respective flats (but not the pin tips) after the tests, indicated the preferential accumulation of a conductive layer on the surface of the flats.

The unused areas on the mating pin and flat of the  $P_{ox}$  test were also examined by SEM photomicrography. The separated substance accumulated on the surface of the (hotter) flat only (Fig. 51). This is an important finding: most of the temperature- and environment-induced tribological changes pertaining to the influence of doping depends mostly on the chemical and physical state of the least-worn triboflat. Additional SEM photomicrography and EDX of the other flats in Figs. 52 through 54, combined with the copper color of the separated cubic microcrystallites, revealed that it was cuprous oxide ( $Cu_2O$ ) that preferentially accumulated on the  $P_{ox}$ -tested *mix* and the *bronze* flats. The accumulation on the  $P_{ox}$  specimens was far greater than on the vacuum-tested ones and this accumulation was enhanced in the wear track (Figs. 55 and 56). The high magnification SEM photomicrographs of the worn pin tips in Fig. 57 confirm the results in Fig. 49 in that the  $Cu_2O$ -containing tips representing the  $P_{ox}$  tests exhibited the least surface charging (i.e., the highest electrical conductivity of the wear scars).

To understand and interpret the charging phenomenon and the associated tribological effects, the physical and chemical properties of the  $Cu_2O$  must be examined. The lattice of the cuprous oxide is close to ionic. It has a cubic (cuprite) structure with a lattice constant  $a_0 = 4.2696 \text{ \AA}$ . Every unit cell contains two molecules, with the oxygens forming a body-centered cube. Each oxygen is surrounded by a tetrahedron of four nearest-neighbor copper ions, while each copper is sandwiched between two oxygens at an equal distance of  $1.85 \text{ \AA}$  (94,95). The facts that the heat of formation of  $Cu_2O$  ( $-43.00 \text{ kcal/mol}$ ) is more negative than that of  $CuO$  ( $-38.50 \text{ kcal/mol}$ ) (96), and  $Cu_2O$  is more volatile than  $CuO$ , preferential accumulation of the former on the heated triboflat surfaces is expected. This copper-colored suboxide is a well-known metal-deficient,  $p$ -type (donor) semiconductor useful in solar cell applications. The volume resistivity of these oxide films can vary from  $60$  to  $10^6 \text{ } \Omega\text{-cm}$  (74). Since the resistivity of stoichiometric or very slightly substoichiometric rutile is infinite and that of the  $CuO$ -doped *bronze* is less than  $1 \text{ } \Omega\text{-cm}$  (APPENDIX D), the reduced surface charging of the  $P_{ox}$  *mix* pin tips is attributed to the transfer of the conductive  $Cu_2O$  from the flat to the pin. Although the pin tips of the *bronze* are inherently conductive, the accumulated  $Cu_2O$  still appears to control the surface charging.

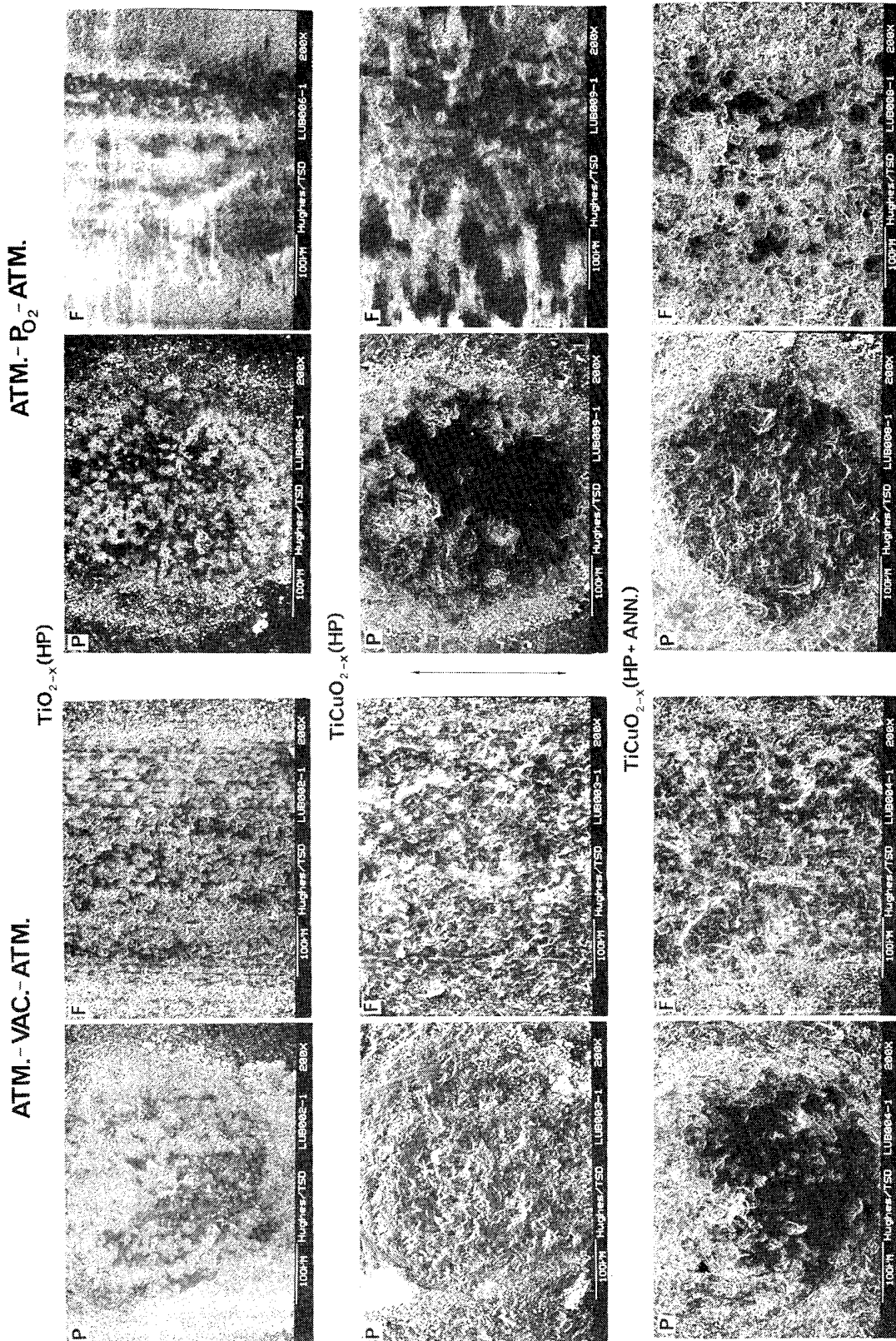


Figure 49. High magnification SEM photomicrograph equivalents of Fig. 44 pin tip and flat wear scars tested in vacuum. Tip scars include entire areas of apparent contact; flat scar photos taken full-width at midstroke. Double-headed arrow indicates direction of oscillatory sliding.

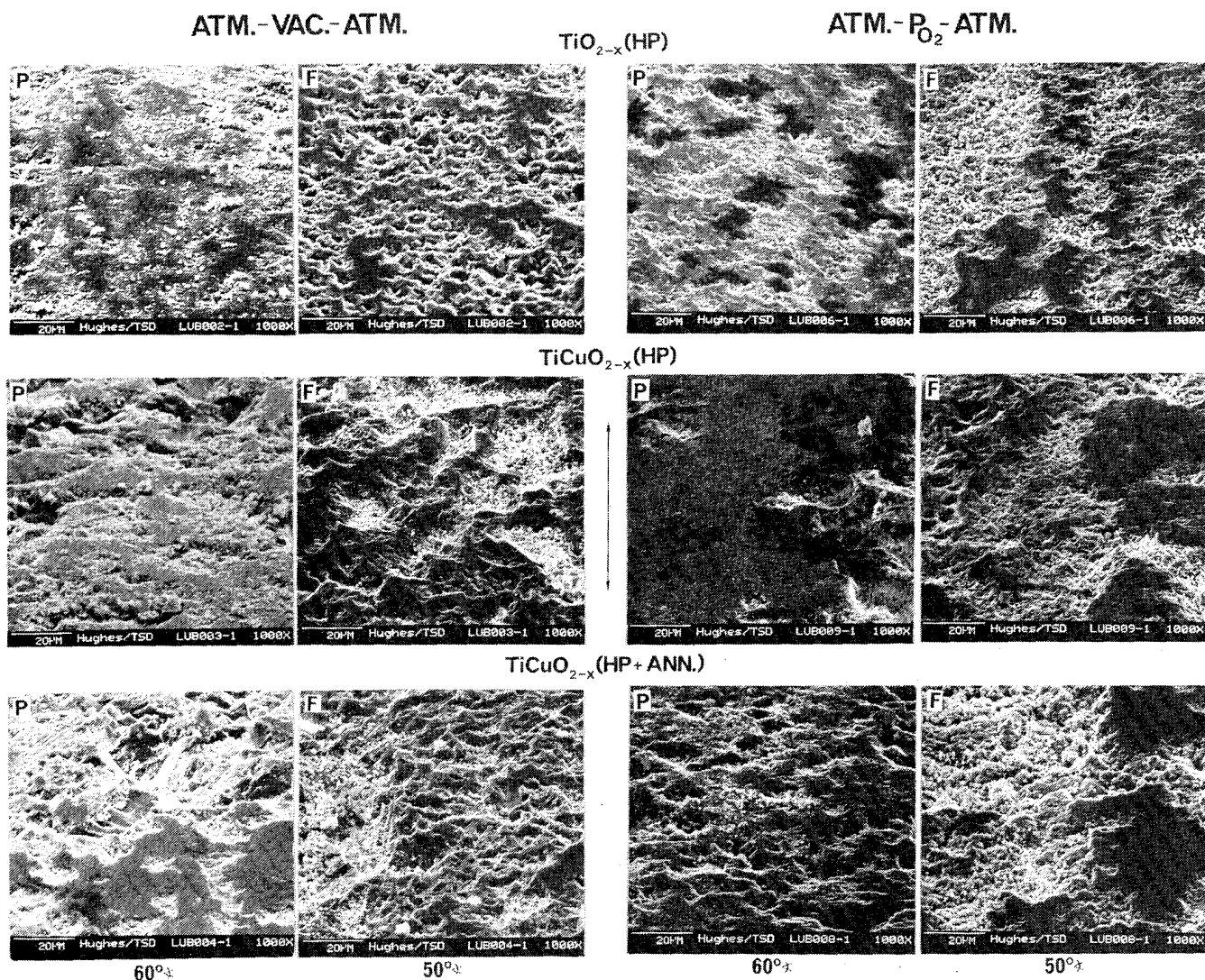


Figure 50. Shallow angle, high magnification SEM photomicrographs of typical areas of pin (P) tip and flat (F) wear scars tested in vacuum from Fig. 49, showing smaller real areas of contact ( $A_r$ ) on the flats' wear path due to CuO-doping-caused grain growth. Double-headed arrow indicates direction of oscillatory sliding.



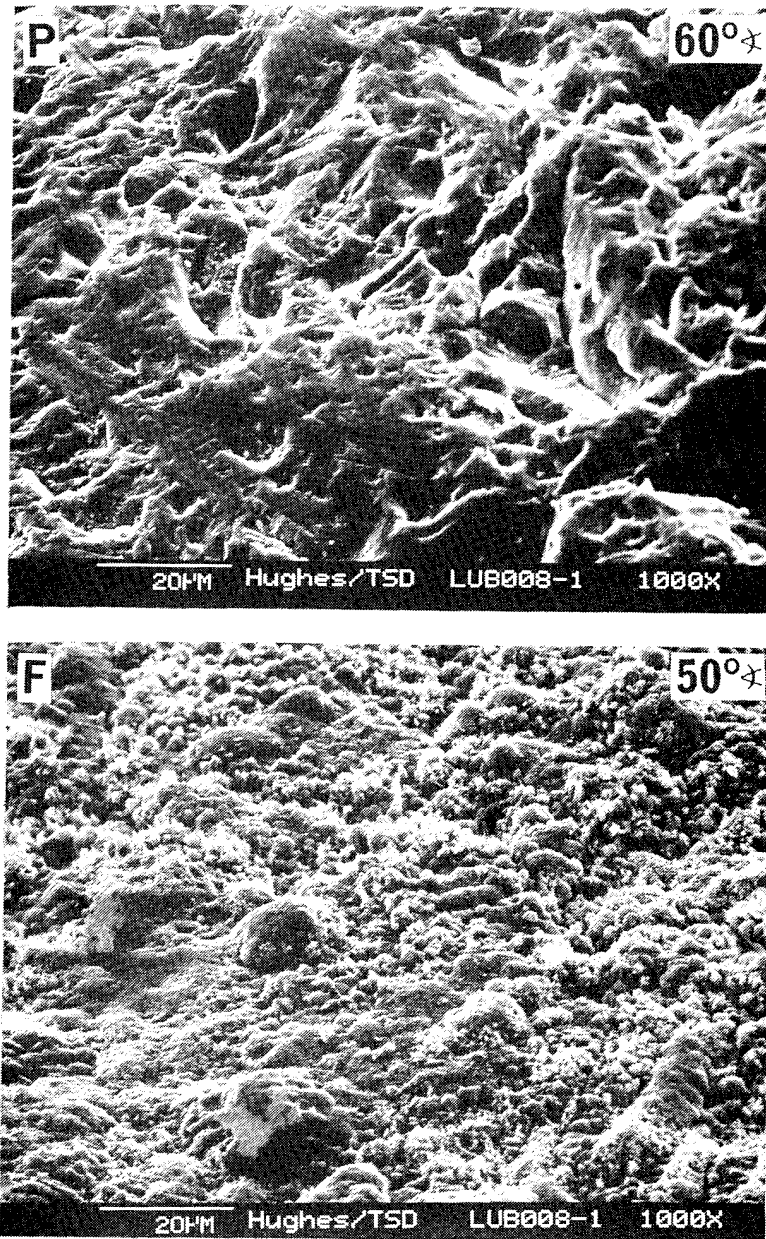
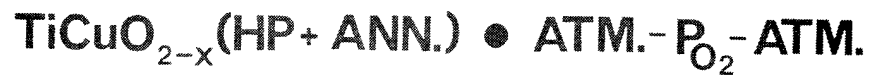
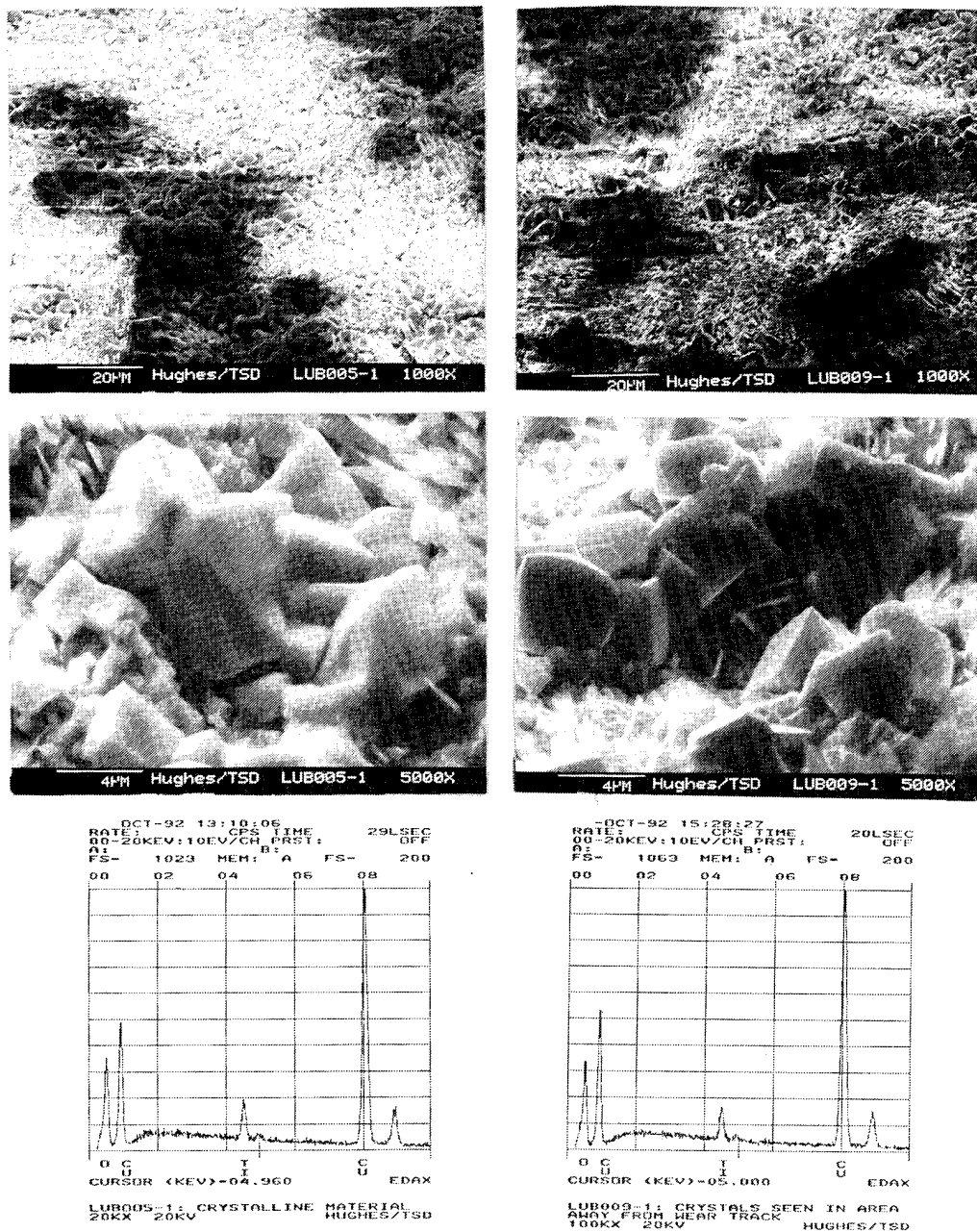


Figure 51. Shallow angle, high magnification SEM photomicrographs of typical, unused portions of the heat-treated Ti-Cu-bronze pin (P) tip and flat (F) tested in  $\text{P}_{\text{O}_2}$ , showing heavy surface accumulation of  $\text{Cu}_2\text{O}$  on the heated flat (F) but no accumulation on the unheated pin (P).

# $\text{TiCuO}_{2-x}(\text{HP})$



## $\text{ATM.-P}_{\text{O}_2}\text{-ATM.}$

Figure 52. High magnification SEM photomicrographs of unworn areas of duplicate CuO-doped rutile flats  $[(\text{Ti} + \text{Cu})\text{O}_{1.80}]$  theoretical blend, hot-pressed], with accompanying EDS spectra at ultrahigh magnifications showing accumulation of the cubic  $\text{Cu}_2\text{O}$  during  $\text{P}_{\text{Ox}}$  tribotests.

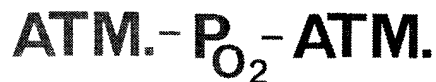
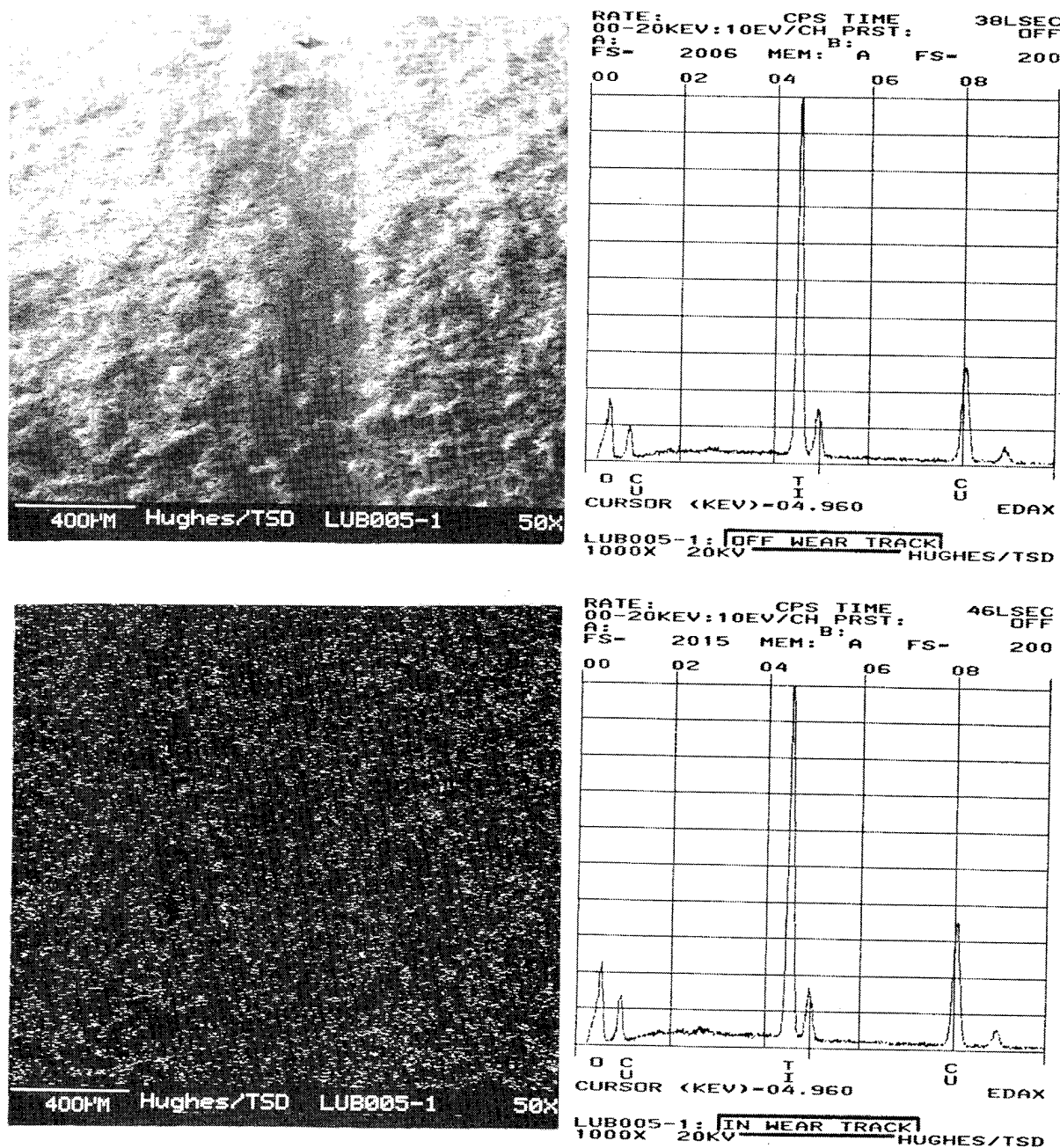
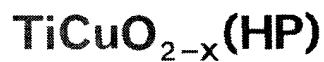


Figure 53. Low magnification SEM photomicrographs and high magnification EDS spectra of areas in and out of the flat's wear scar of one of the two  $\text{P}_{\text{O}_x}$  tests shown in Fig. 52. Slight accumulation of the smeared  $\text{Cu}_2\text{O}$  in the wear track is indicated.

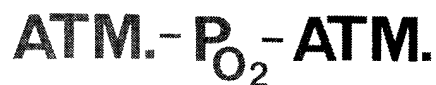
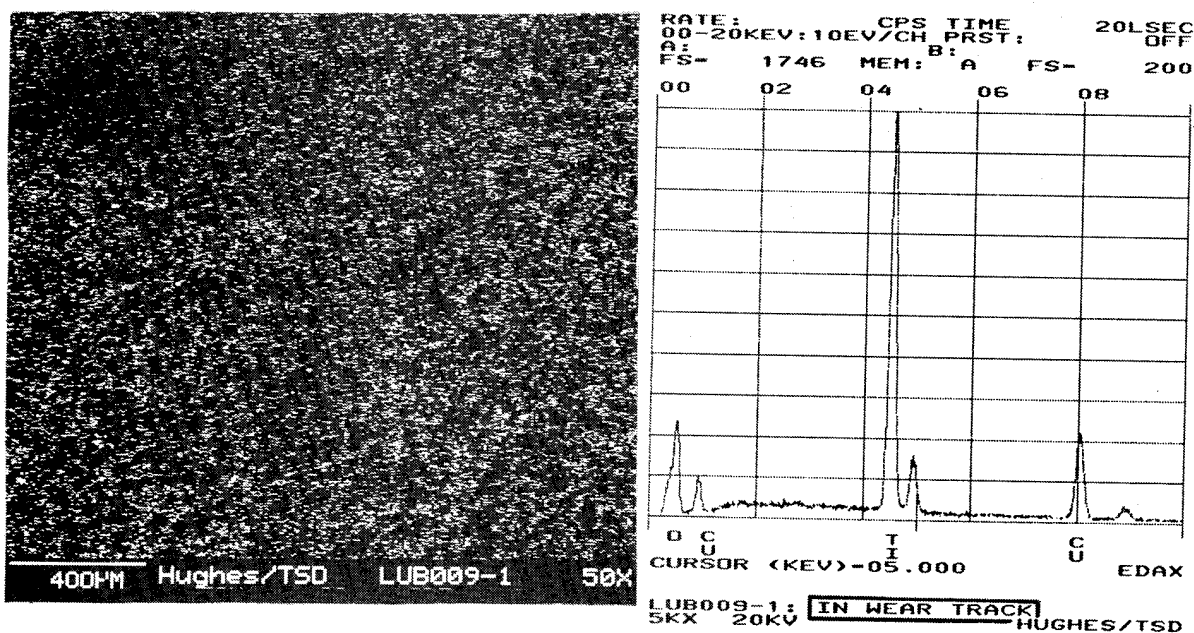
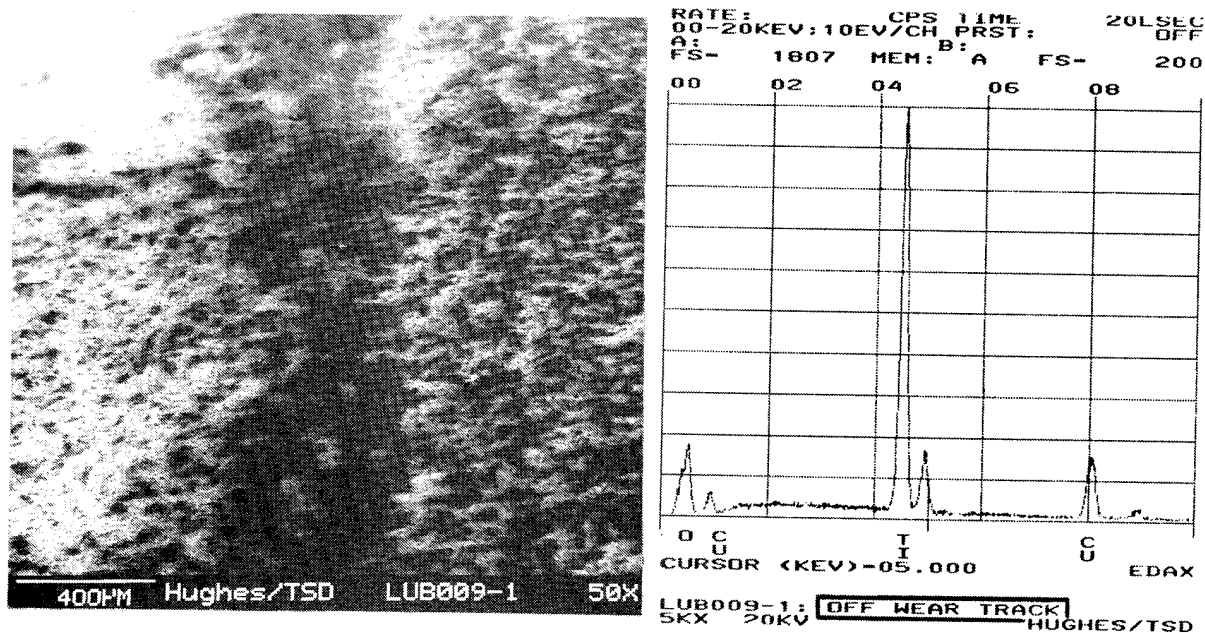
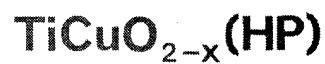
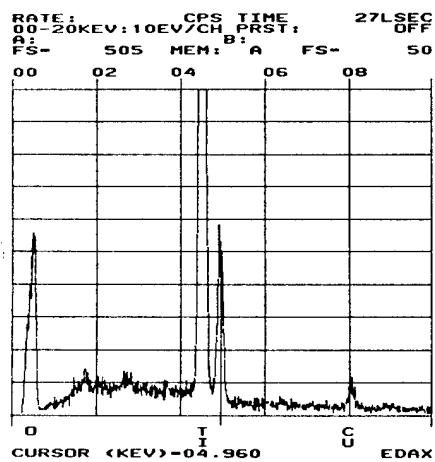


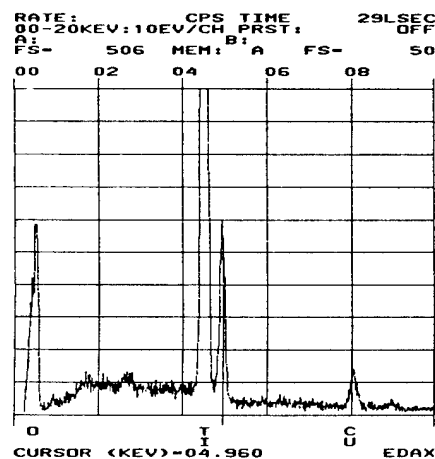
Figure 54. Low magnification SEM photomicrographs and high magnification EDS spectra of areas in and out of the flat's wear track of the second of the two  $\text{P}_{\text{O}_x}$  tests shown in Fig. 52. Slight accumulation of the smeared  $\text{Cu}_2\text{O}$  in the wear tracks is indicated.



# $\text{TiCuO}_{2-x}(\text{HP})$

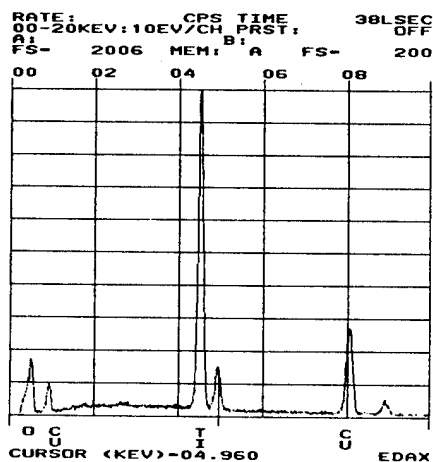


LUB003-1: OFF NEAR TRACK  
(TI PEAK-2021)  
1000X 20KV HUGHES/TSD

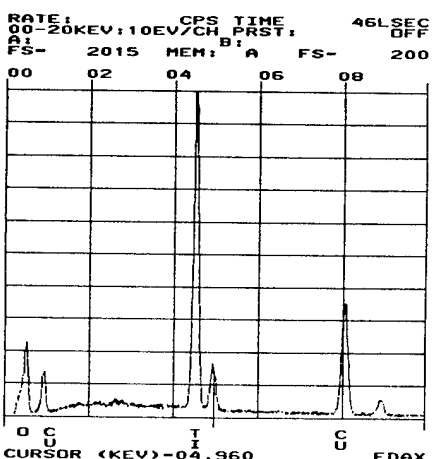


LUB003-1: IN WEAR TRACK  
(TI PEAK-2023)  
1000X 20KV HUGHES/TSD

**ATM.-VAC.-ATM.**

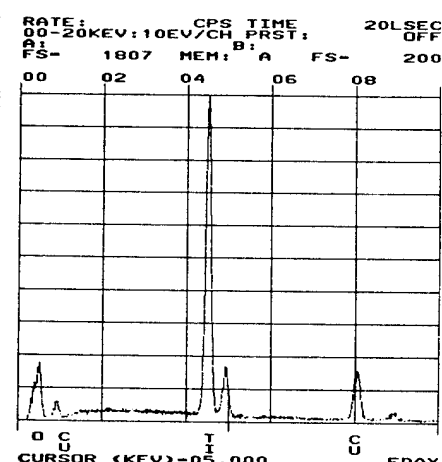


LUB005-1: OFF NEAR TRACK  
1000X 20KV HUGHES/TSD

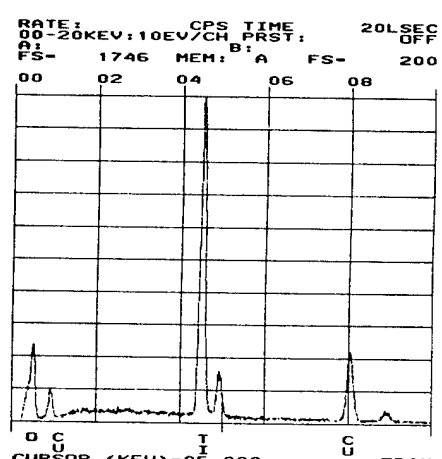


LUB005-1: IN WEAR TRACK  
1000X 20KV HUGHES/TSD

**ATM.-P<sub>O2</sub>-ATM.**



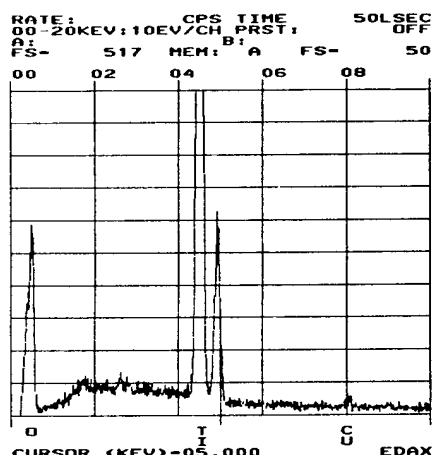
LUB009-1: OFF NEAR TRACK  
5KX 20KV HUGHES/TSD



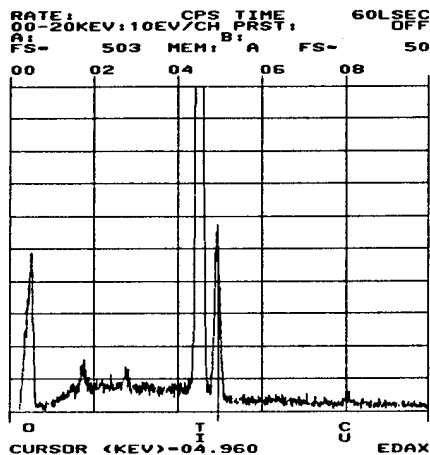
LUB009-1: IN WEAR TRACK  
5KX 20KV HUGHES/TSD

Figure 55. Comparison of in-wear-track, high magnification, EDS spectra of vacuum- and P<sub>Ox</sub>-tested flats fabricated from CuO-doped rutile [(Ti + Cu)O<sub>1.80</sub> theoretical blend, hot-pressed], showing preferential accumulation of Cu<sub>2</sub>O in P<sub>Ox</sub>.

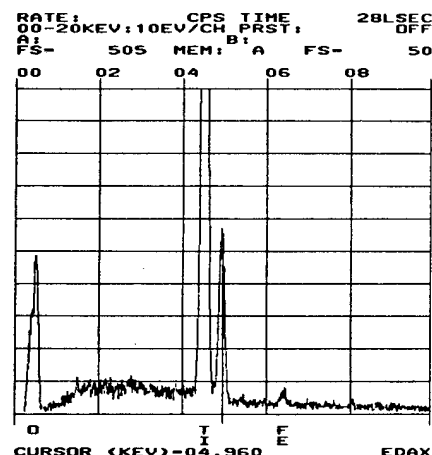
# $\text{TiCuO}_{2-x}(\text{HP} + \text{ANN.})$



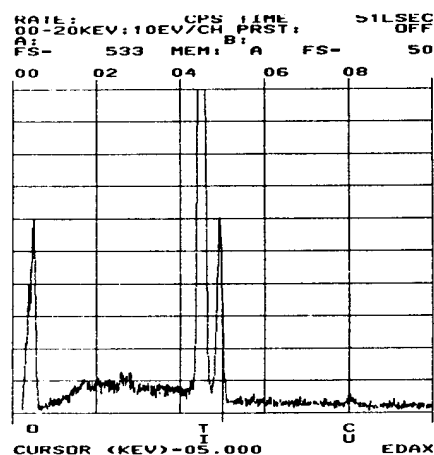
LUB004-1: OFF WEAR TRACK  
(TI PEAK-2068)  
1000X 20KV HUGHES/TSD



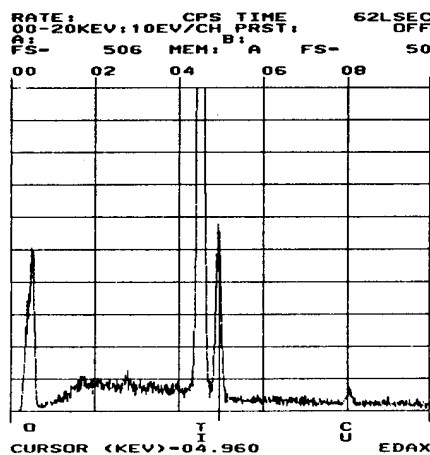
LUB007-1: OFF WEAR TRACK  
(TI PEAK-2010)  
1000X 20KV HUGHES/TSD



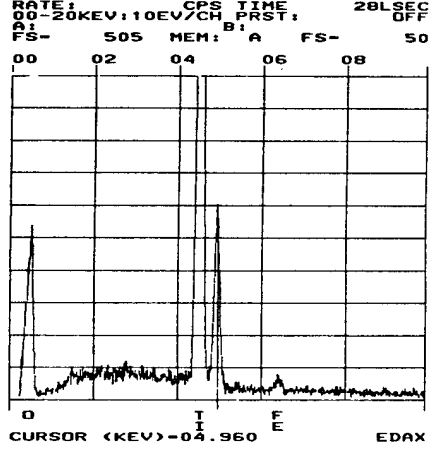
LUB008-1: OFF WEAR TRACK  
(TI PEAK-2021)  
1000X 20KV HUGHES/TSD



LUB004-1: IN WEAR TRACK  
(TI PEAK-2130)  
1000X 20KV HUGHES/TSD



LUB007-1: IN WEAR TRACK  
(TI PEAK-2025)  
1000X 20KV HUGHES/TSD



LUB008-1: IN WEAR TRACK  
(TI PEAK-2021)  
1000X 20KV HUGHES/TSD

ATM.-VAC.-ATM.

ATM.- $\text{P}_{\text{O}_2}$ -ATM.

Figure 56. Comparison of in-and-out-of-wear-track, high magnification EDS spectra of vacuum- and  $\text{P}_{\text{O}_2}$ -tested flats fabricated from the heat-treated Ti-Cu-bronze, showing minimal (if any) copper compound accumulation in either environment. Source of trace iron contamination of  $\text{P}_{\text{O}_2}$ -tested sample is unknown.

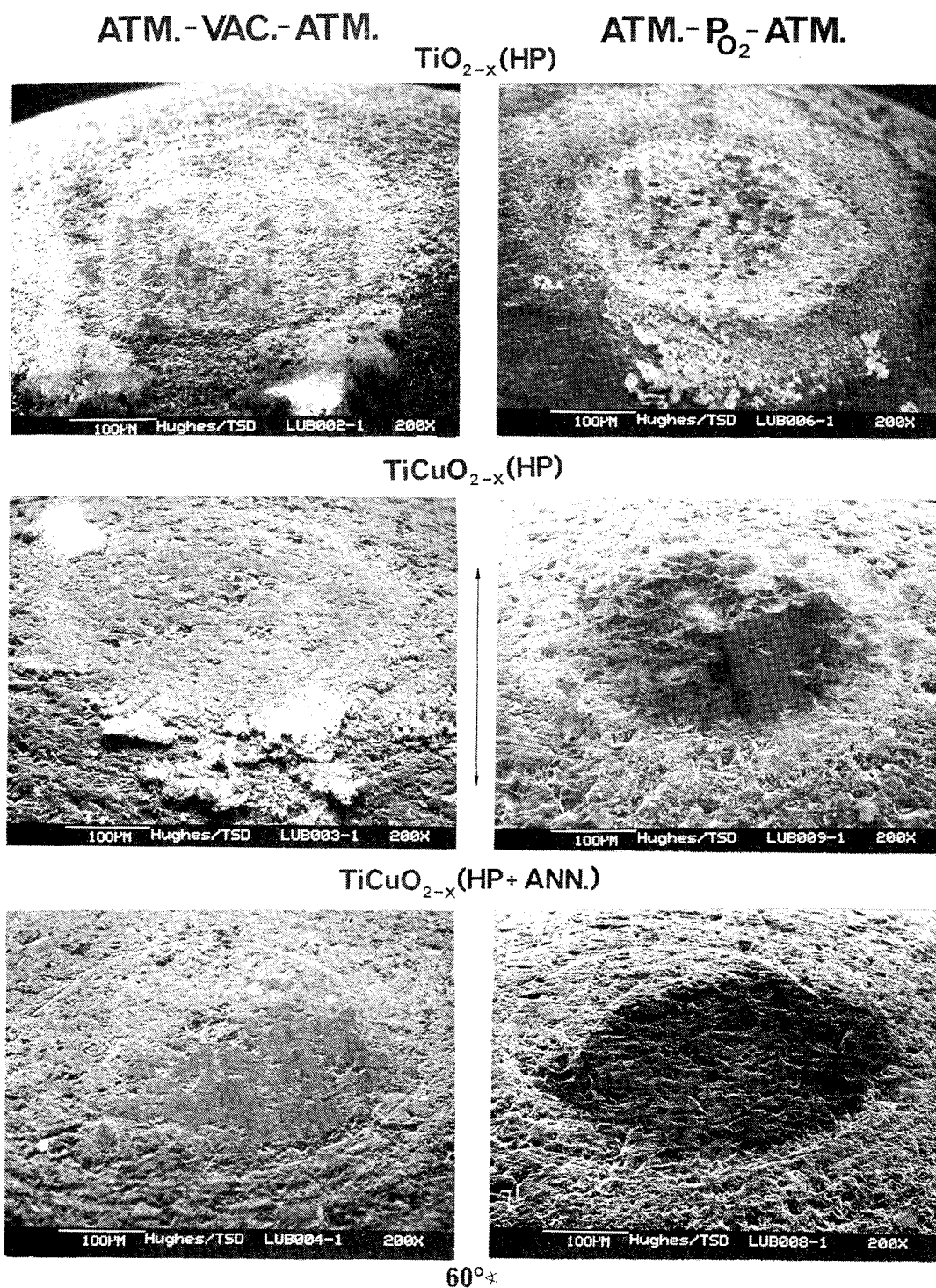


Figure 57. Shallow angle, high magnification photomicrographs of all worn pin tips, showing reduced charging of the wear scars associated with CuO-doped rutile tested in  $\text{P}_{\text{O}_x}$  only. Double-headed arrow indicates direction of sliding.

These findings, combined with the progressively reduced heights of the thermal upramp COF increase peaks show the following:

1. Enrichment of the tribosurface in ionic copper species enhances COF reduction, either in the form of  $\text{Cu}_2\text{O}$  or as copper-enriched Magnèli phases. In either case, cuprous oxide does not appear to be a tribologically undesirable contaminant.
2. It cannot be discounted that the copper species accumulated on the *mix*'s surface reacted with the rutile lattice during the SEM tribotests to form tribocatalytically generated Magnèli phases. The reduced size of the *mix* COF increase peaks did not depend on the preferential accumulation of the  $\text{Cu}_2\text{O}$ , because COF reduction occurred during the vacuum *mix* test as well, where no copper diffusion to the surface was observed.
3. The large grains exposed on the rubbing surfaces of the *mix* and *bronze* specimens created large coalesced plateaus of  $A_F$ . These plateaus are surrounded by the "valleys", where the preferentially diffused  $\text{Cu}_2\text{O}$  was still untouched. These undisturbed portions became replenished by  $\text{Cu}_2\text{O}$  and other copper-containing debris wearing off the rubbed plateaus. Only a thin layer of the sliding-depleted  $\text{Cu}_2\text{O}$  and the indigeneous doped Magnèli phases comminuted by the tribological action remained on the plateaus to influence the size and shape of the characteristic COF traces. Cuprous oxide had to have some influence on the COF, however. The  $P_{\text{OX}}$  *mix* and *bronze* tips could charge less under the *e*-beam only because  $\text{Cu}_2\text{O}$  could transfer there from the flats. The cooler pins could not generate their own surface-diffused oxides.

The illustrations from Figs. 58 through 65 are presented to show good repeatability in the appearance of the used specimens originating from duplicate experiments. The photomicrographs in Fig. 61 also show good alignment of the pin tip against the flat. Note the close proximity of the wear scars to the center of the concentric rings: these rings were caused by the machining process and indicate the geometric center of the pin tips.

Recall that the appearance of the initially unexpected and puzzling downward trend in COF at 0.2 torr  $P_{\text{OX}}$ , on thermal downramp, was attributed to either the diffusion phenomenon discussed above or to some sudden spallation of the surface (see related discussions in 3.2.4 and 4.3.2). The wear-related hypothesis option is similar to the explanation offered for the appearance of the doublet peaks in Figs. 17 and 36. As previously discussed, one way to resolve the competing diffusional gradient vs. spallation hypotheses is to observe differences in the wear rates of the vacuum vs.  $P_{\text{OX}}$  tests.

$\text{TiCuO}_{2-x}$  (HP+ ANN.) • ATM.-VAC.-ATM.

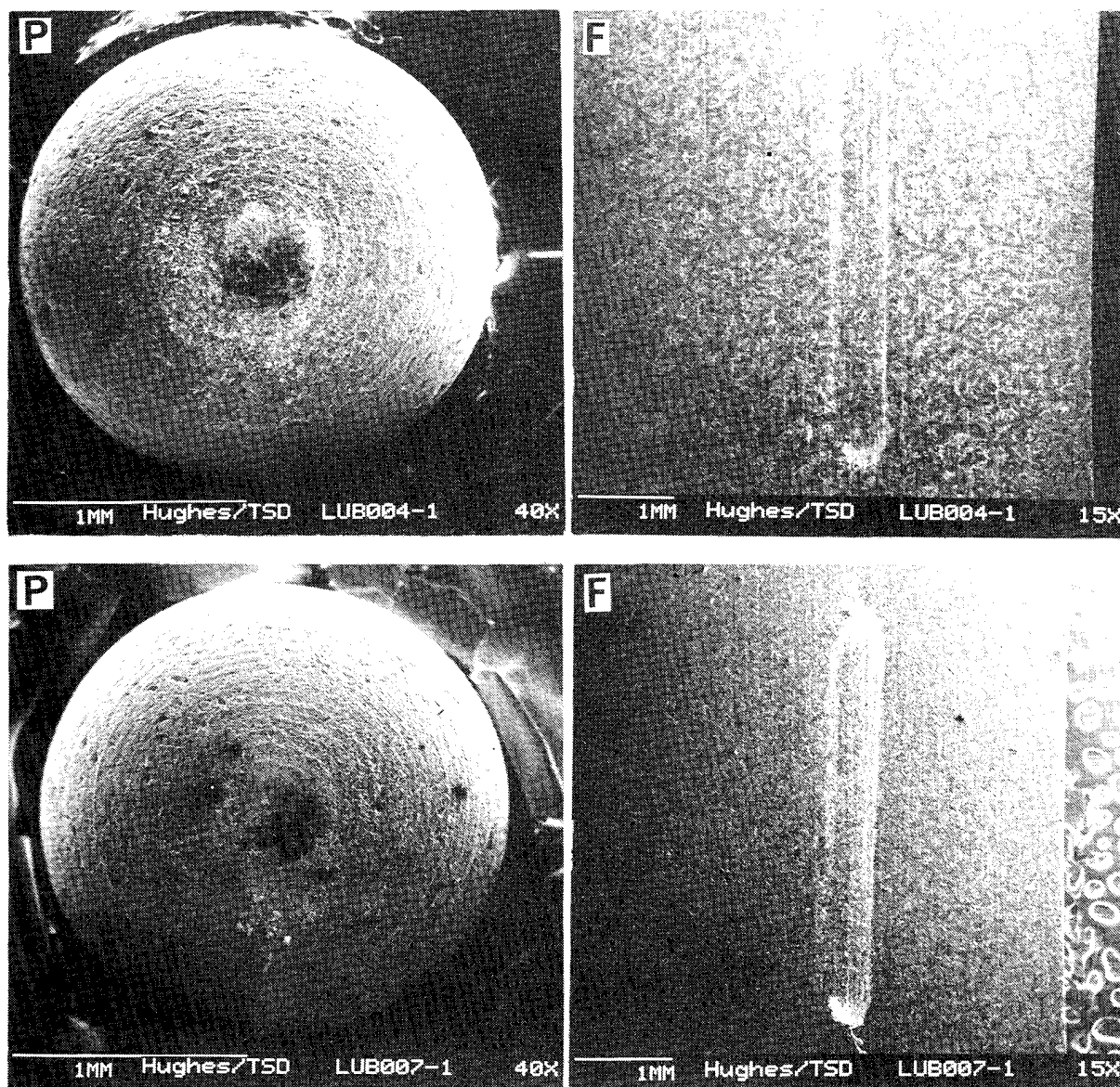


Figure 58. Low magnification SEM photomicrographs of duplicate vacuum tribotest pin (P)/ flat (F) wear scars associated with the tests described in Fig. 36, showing repeatable wear scar appearance. Double-headed arrow indicates direction of sliding.

$\text{TiCuO}_{2-x}$  (HP+ ANN.) • ATM.-VAC.-ATM.

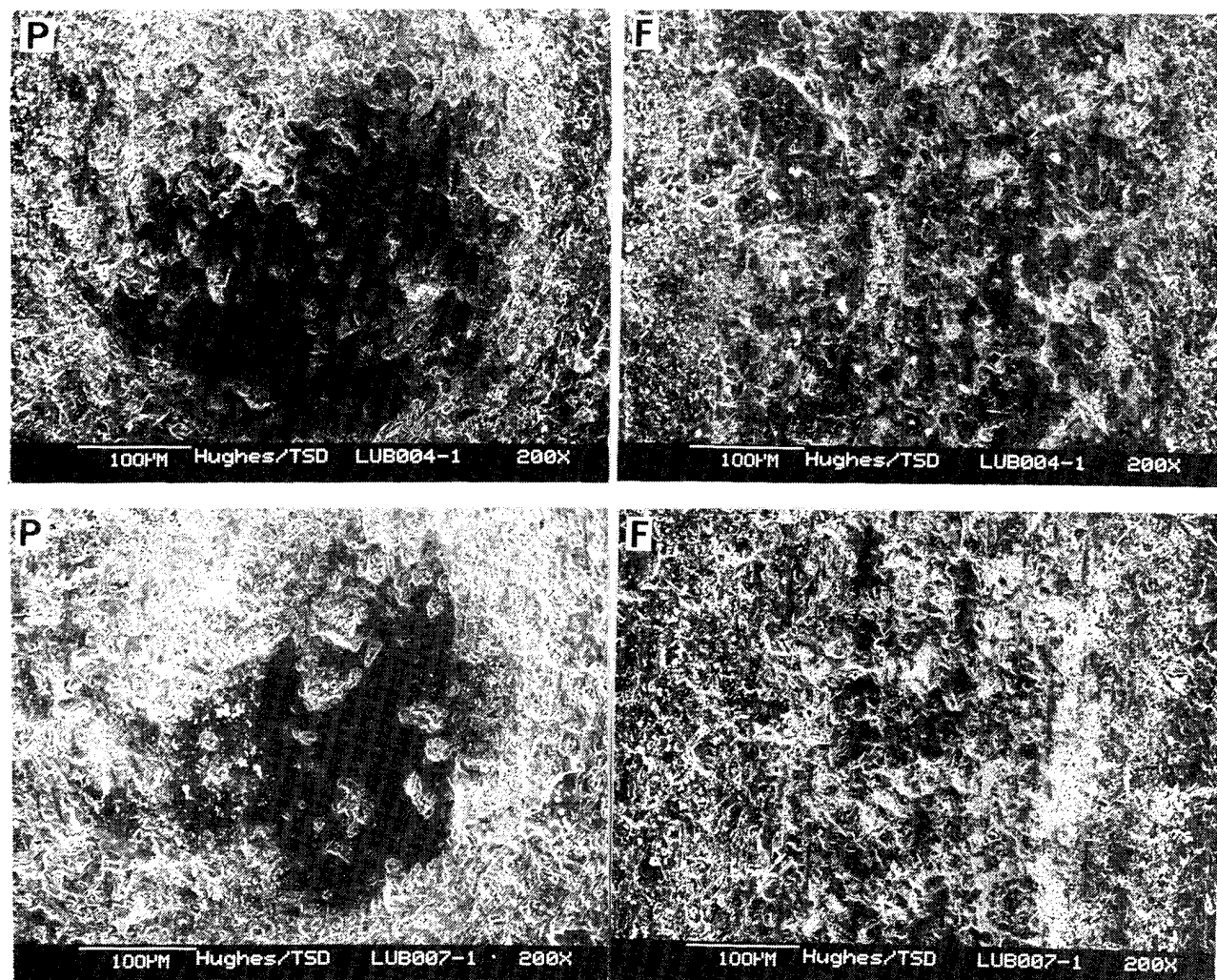


Figure 59. High magnification SEM photomicrograph equivalents of Fig. 56 [(P) = pin scar, (F) = flat wear track]. Double-headed arrow indicates direction of siding.



$\text{TiCuO}_{2-x}$  (HP+ ANN.) • ATM.-VAC.-ATM.

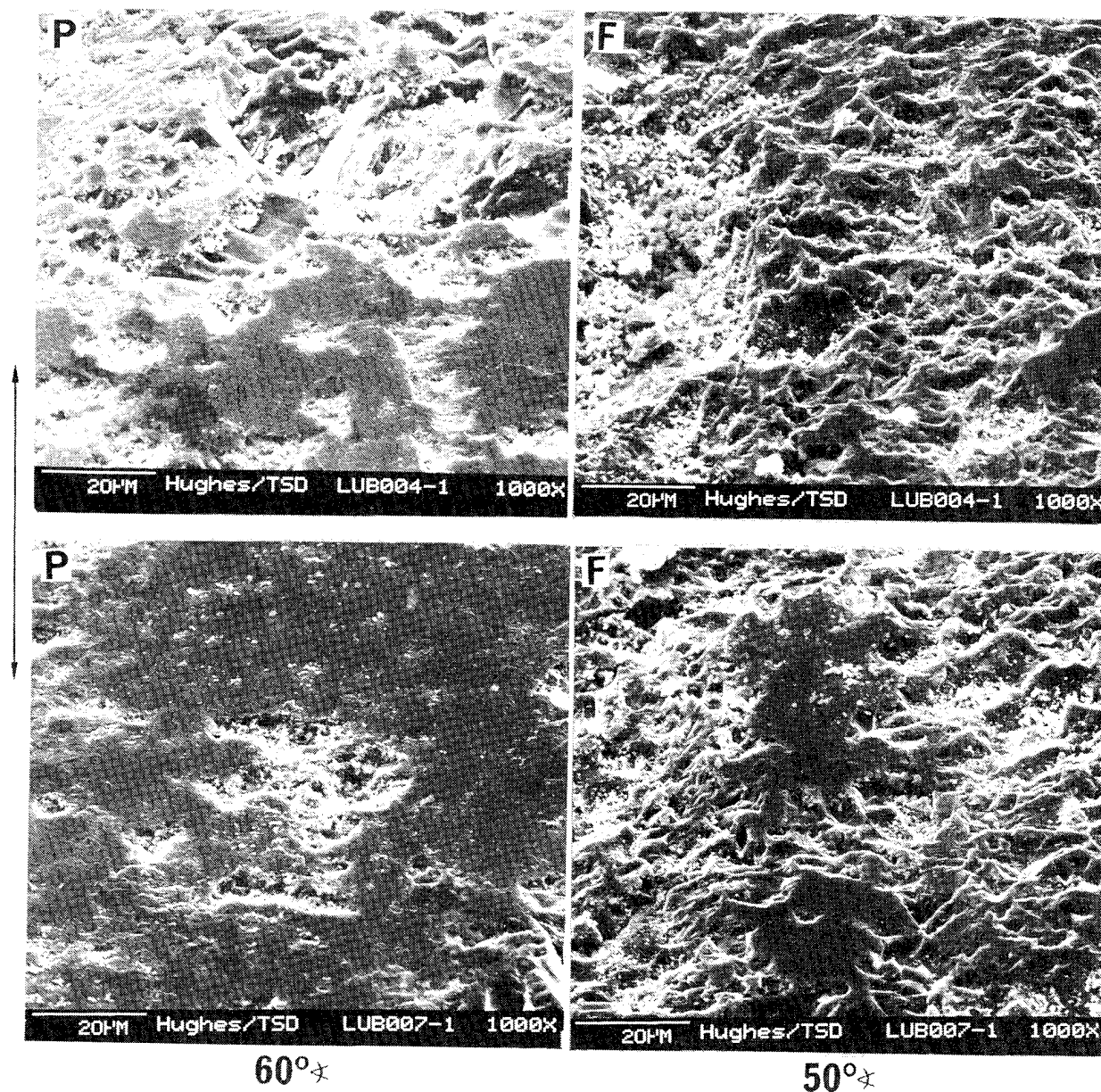


Figure 60. Shallow angle, SEM photomicrographs of Fig. 59 pin (P)/flat (F) wear scars at even higher magnification. Double headed arrow indicates direction of sliding.

$\text{TiCuO}_{2-x}(\text{HP} + \text{ANN.}) \bullet \text{ATM.} - \text{VAC.} - \text{ATM.}$

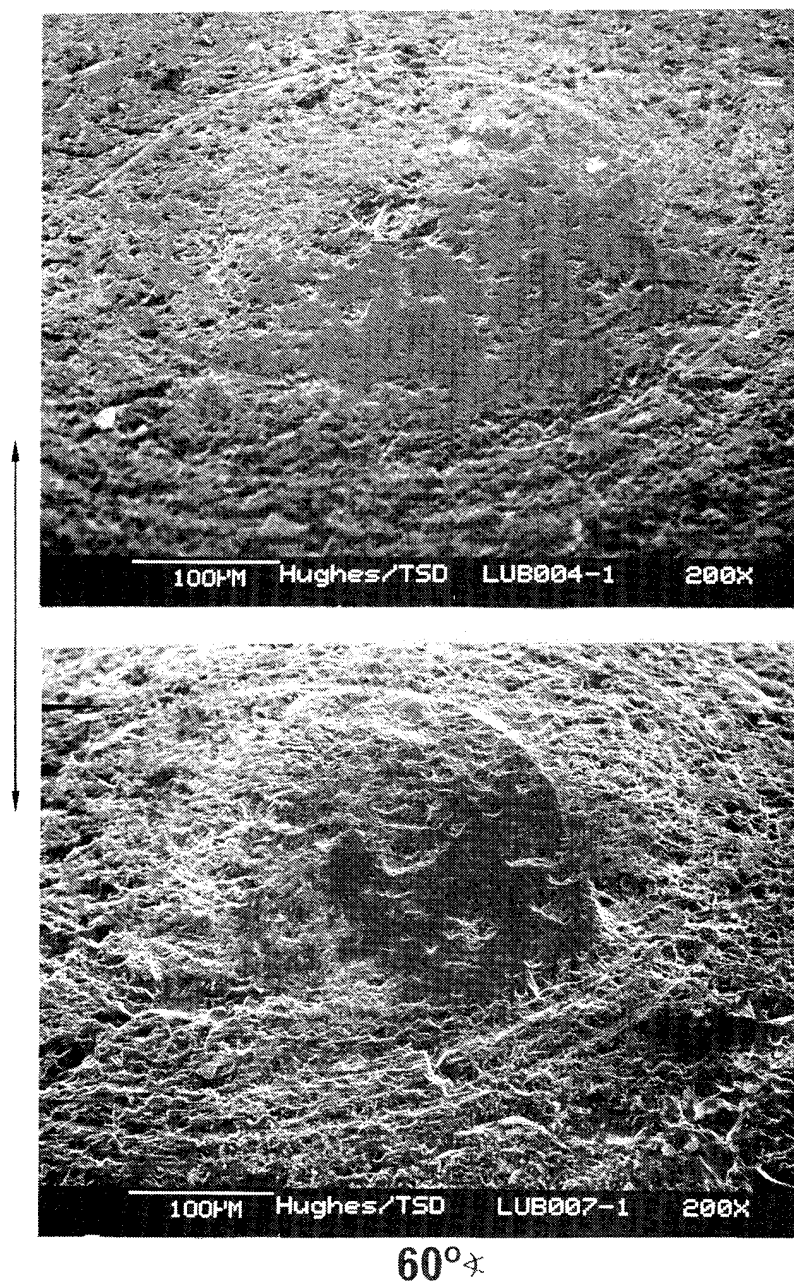


Figure 61. Shallow angle, high magnification SEM photomicrographs of pin wear scars (also see Fig. 58), showing repeatable alignment and appearance of the scars. Double-headed arrow indicates direction of sliding.



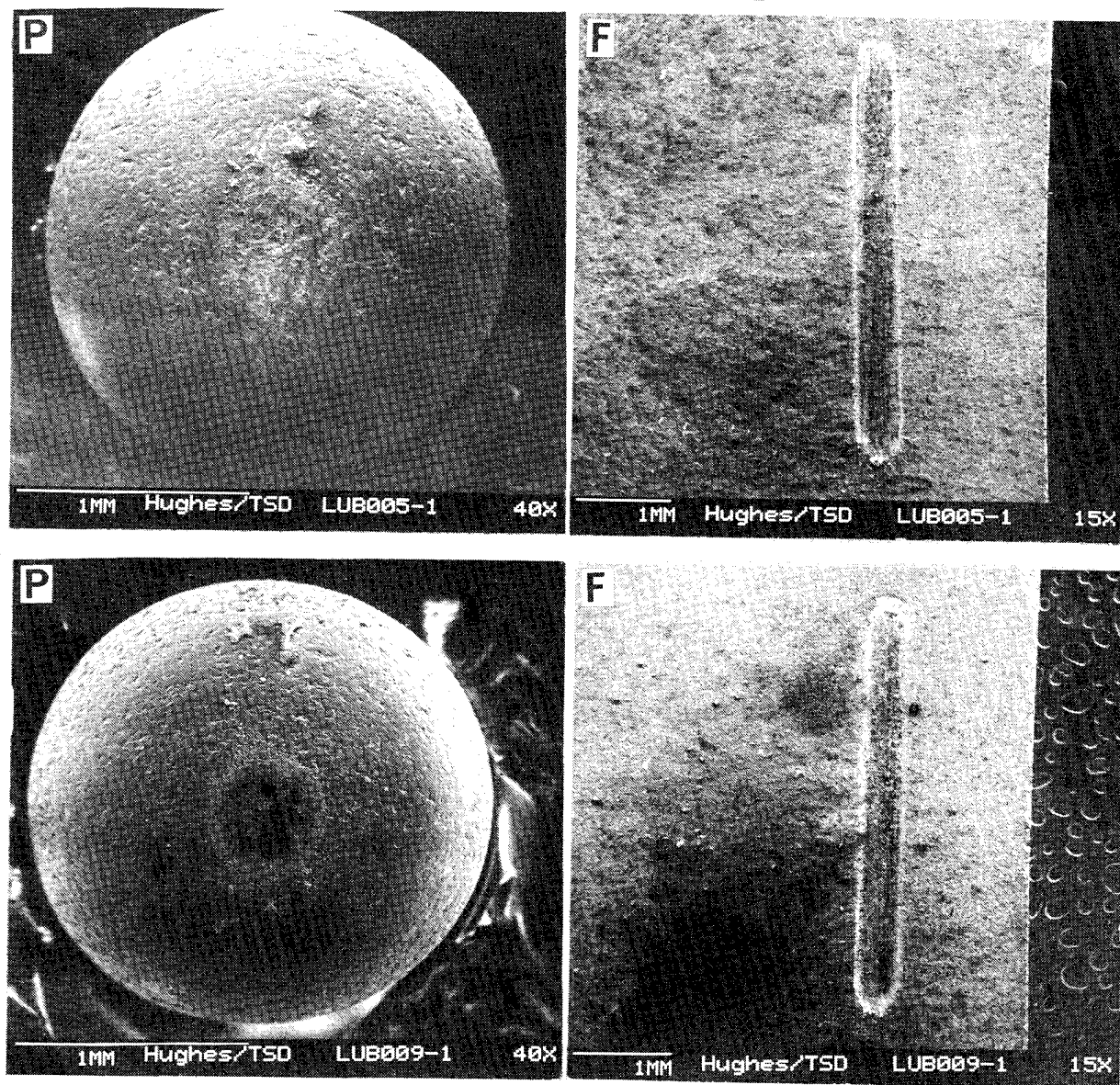


Figure 62. Low magnification SEM photomicrographs of duplicate  $\text{P}_{\text{Ox}}$  tribotest pin (P)/ flat (F) wear scars associated with the tests described in Fig. 40 showing repeatable scar appearance. Double-headed arrow indicates direction of sliding.

$\text{TiCuO}_{2-x}(\text{HP}) \bullet \text{ATM.} - \text{P}_{\text{O}_2} - \text{ATM.}$

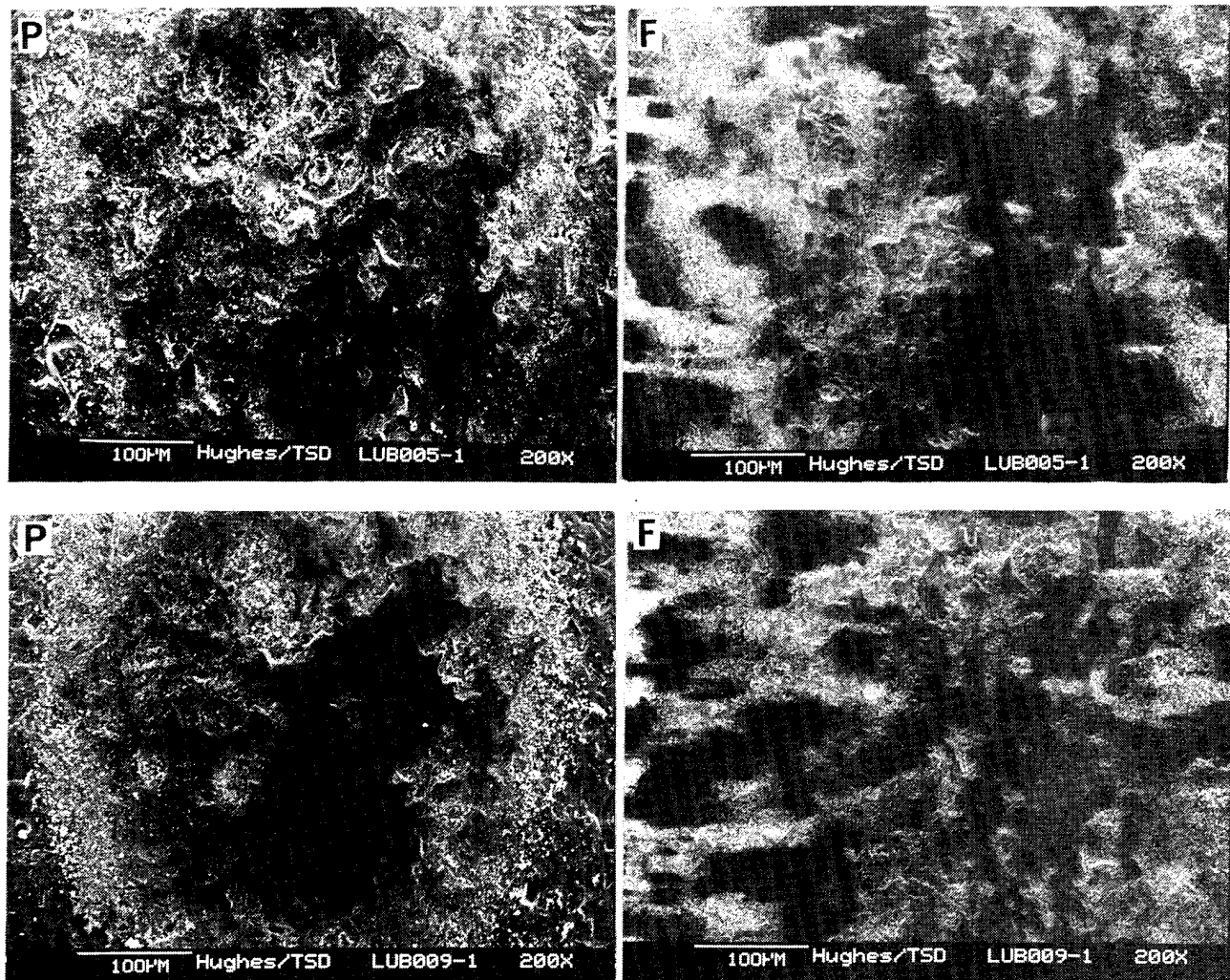


Figure 63. High magnification SEM photomicrograph equivalents of Fig. 62 [(P) = pin scar; (F) = flat wear track]. Double-headed arrow indicates direction of sliding.

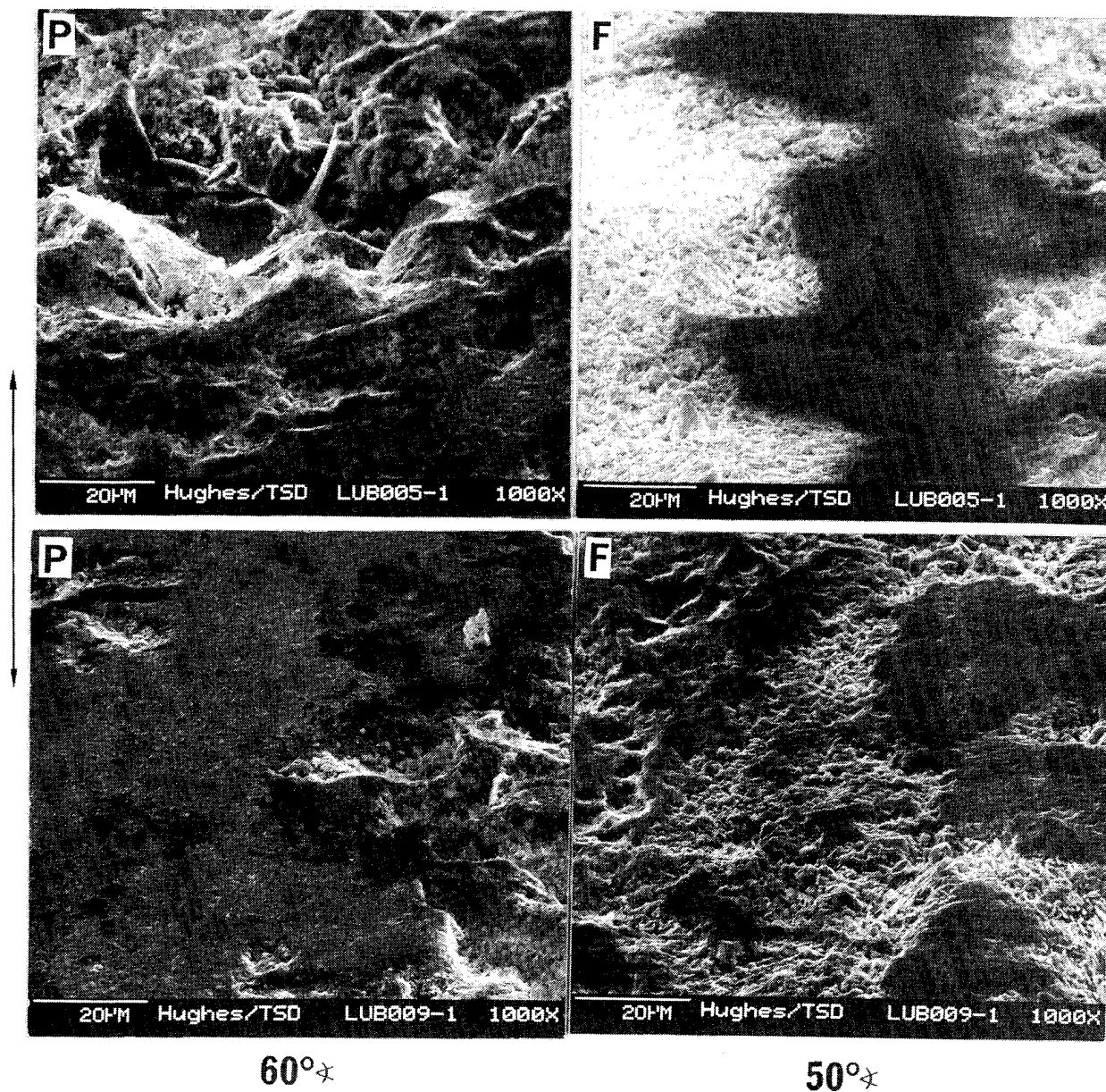


Figure 64. Shallow angle, high magnification SEM photomicrographs of Fig. 63 pin (P)/ flat (F) wear scars at even higher magnification. Double-headed arrow indicates direction of sliding.

$\text{TiCuO}_{2-x}(\text{HP}) \bullet \text{ATM.} - \text{P}_{\text{O}_2} - \text{ATM.}$

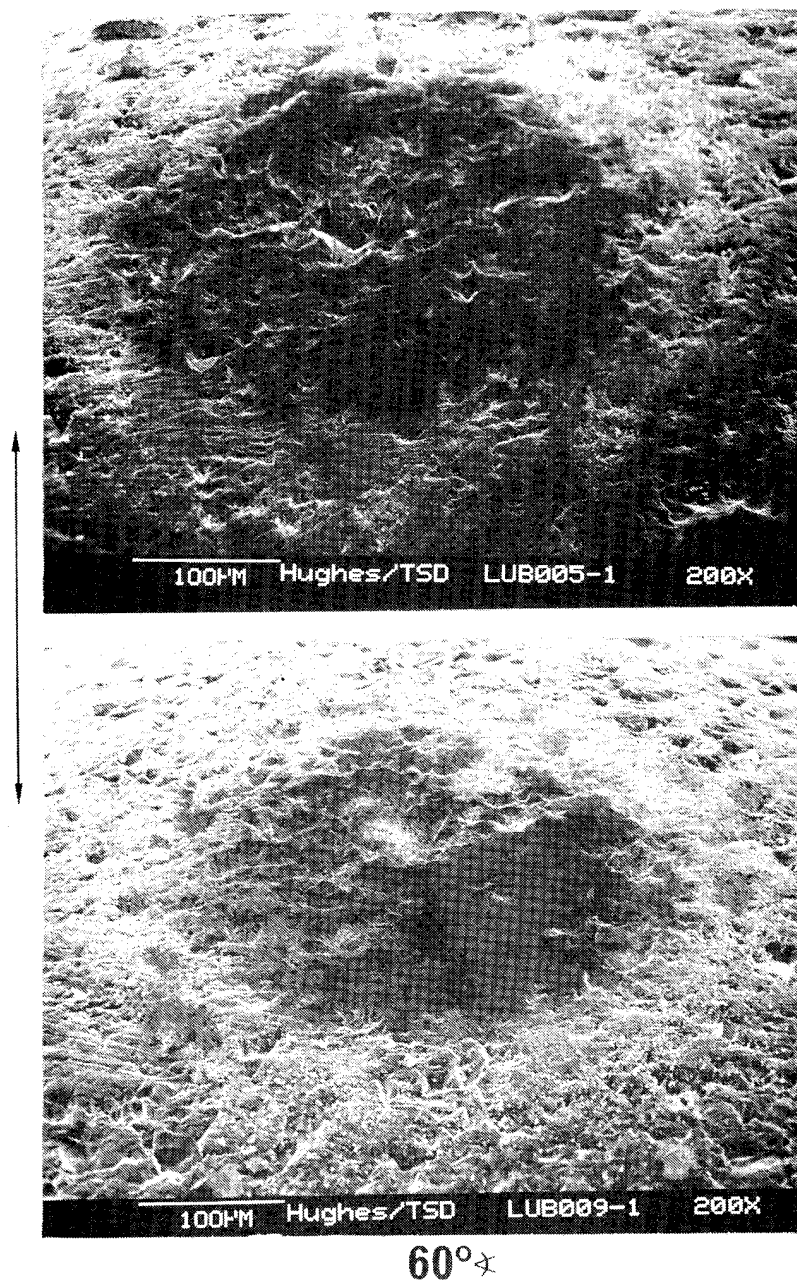


Figure 65. Shallow angle, high magnification SEM photomicrographs of pin wear scars (also see Fig. 62), showing repeatable alignment of the scars. Double-headed arrow indicates direction of sliding.

If excessive spalling did occur in  $P_{Ox}$ , then the normalized wear rates should be significantly higher than those rates associated with the significantly shorter vacuum tests. Accordingly, spalling-induced increases in wear rate due to surface stresses which might develop from sudden stoichiometric (and  $\tau_s$ ) changes at the sliding interface would not occur in vacuum. This method of arbitrating the relative merits of the competing hypotheses is especially intriguing, because all the  $P_{Ox}$  tests in Figs. 39 and 40 show the same characteristic COF changes between 1200 and 1800 cycles. If the time-normalized wear rates of the equivalent samples tested in vacuum and in  $P_{Ox}$  showed consistent disparity, the data would fit the spallation hypothesis. Since this disparity did not manifest itself, the diffusion hypothesis is accepted.

#### **4.4 Tester 2A Tribometry of Undoped and CuO-doped Rutile**

Tester 2A is a unique, wide temperature range tribometer designed and constructed during Part I of the Tribological Fundamentals Program for engineering-scale, lab-bench-type friction and wear experiments. It was developed to test the sliding friction and wear characteristics of various bare and solid lubricated ceramic and other high temperature bearing material combinations under a wide spectrum of environmental conditions. Its unique feature is the ability to determine the tribological behavior of high rolling contact fatigue (RCF) resistance ceramics (normally tested under oil-lubricated conditions, at R.T.) in the sliding mode, especially in high temperature air, using the same RCF rod specimen. The details of this apparatus were described previously in (12,97).

As shown in the schematics in Fig. 66, a vertically spinning RCF rod (Fig. 67) is squeezed, in a nutcracker fashion, by two rubshoes (Fig. 68) of line contact configuration. The rubshoes are pressed against the rod through rigid moment arm/pressure bar combinations pivoted around their own triaxial transducers (Fig. 69). The two six-degrees-of-freedom force gages are capable of measuring the normal load, the friction force and any misalignment loads simultaneously. The steady-state loads are applied through adjustable tension springs. Wear may be determined *in-situ* by proximity gages measuring the wear-induced incursion of the rubshoes towards the rod and by measuring the rubshoe wear scars after the test under a travelling microscope or from photomicrographs.

The tribocontacts are heated by a water-cooled quartz lamp to  $\sim 850^\circ\text{C}$  (see Fig. 69). The actual temperature of the sliding interfaces depends on the emissivity of the respective rubbing surfaces. The lamp is equipped with an elliptical reflector to heat the rod/rubshoes contact region only. This concentration of heat, combined with the reduction of heat transfer away from the sliding zone by special low thermal conductivity ceramic specimen holders, reduces the size of the specimen furnace to  $\sim 500\text{ cm}^3$ . A metal safety cover on the top of the heated region contains an eye-safe observation window and, on the side, an orifice for the IR beam of the pyrometer. The beam further passes through an inner-

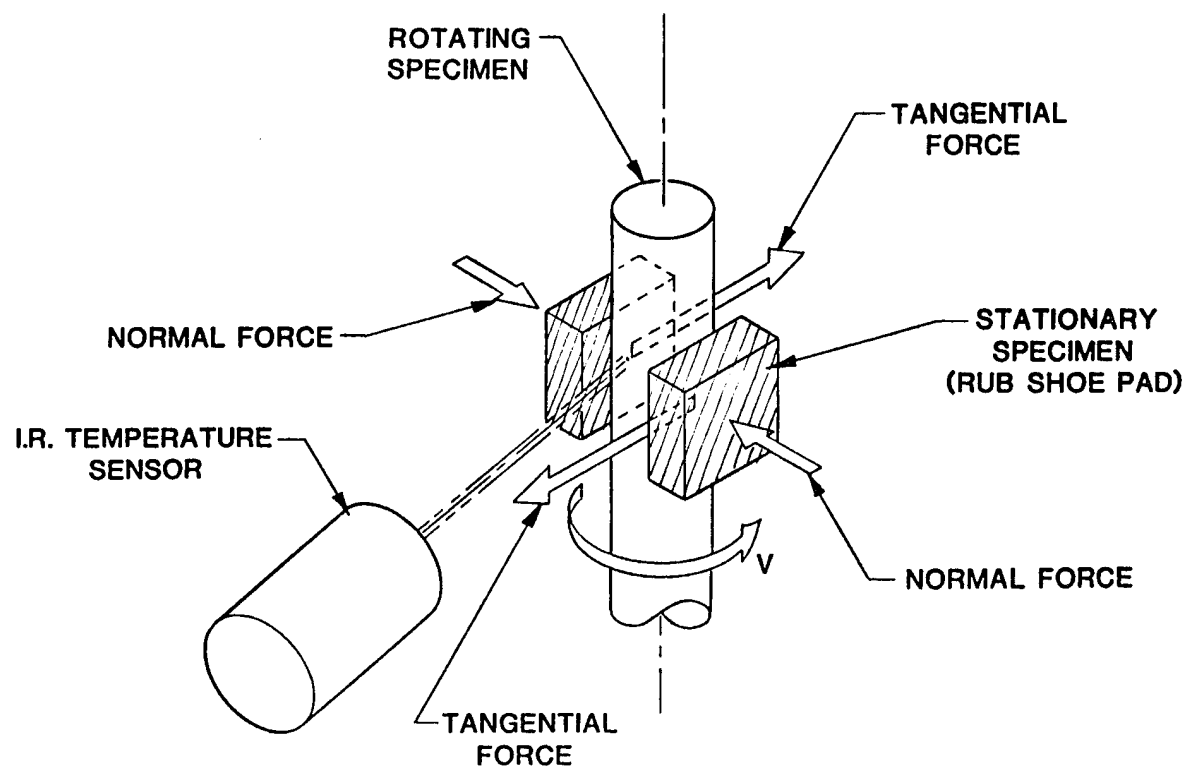


Figure 66. Schematic of the Hughes Tester 2A high temperature tribometer.

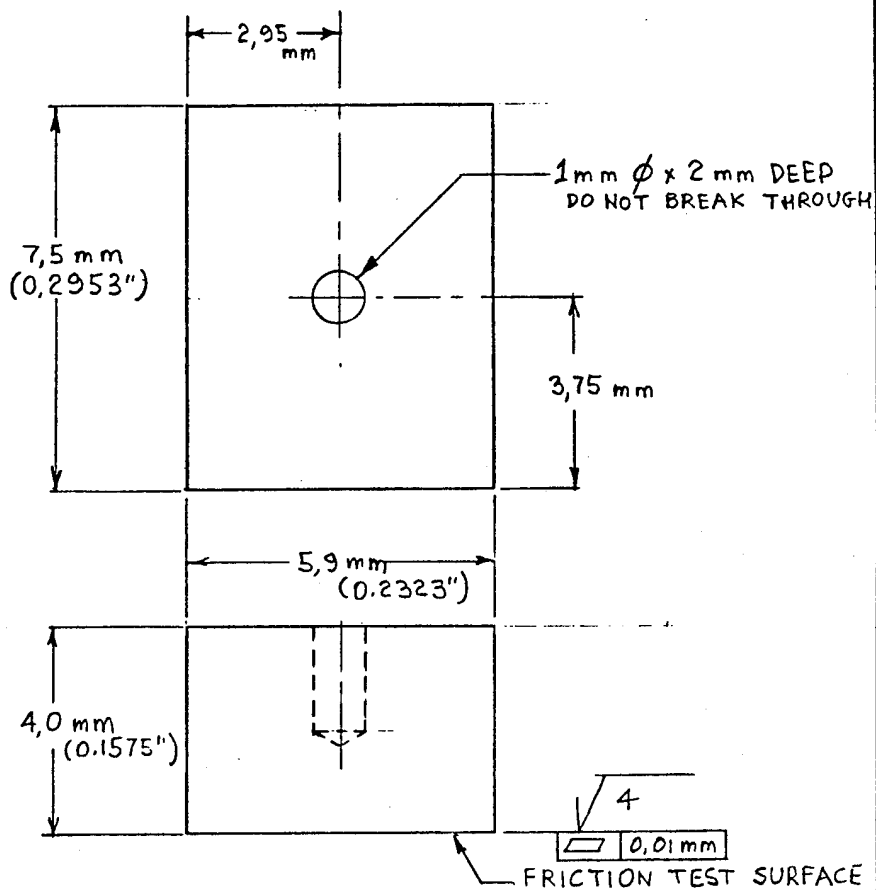


REVISION																		
LTR	DESCRIPTION	DATE	APPROVED															
		<table border="1" style="width: 100%; border-collapse: collapse;"> <thead> <tr> <th style="width: 20%;">PART DASH NO.</th> <th style="width: 30%;">DIAMETER "D"</th> <th style="width: 50%;">LENGTH "L"</th> </tr> </thead> <tbody> <tr> <td>-1</td> <td>.3750</td> <td>3.50</td> </tr> <tr> <td>-2</td> <td>.3750</td> <td>3.00</td> </tr> <tr> <td>-3</td> <td>.3600</td> <td>3.50</td> </tr> <tr> <td>-4</td> <td>.3600</td> <td>3.00</td> </tr> </tbody> </table>		PART DASH NO.	DIAMETER "D"	LENGTH "L"	-1	.3750	3.50	-2	.3750	3.00	-3	.3600	3.50	-4	.3600	3.00
PART DASH NO.	DIAMETER "D"	LENGTH "L"																
-1	.3750	3.50																
-2	.3750	3.00																
-3	.3600	3.50																
-4	.3600	3.00																
<p>DIMENSIONS IN INCHES. (1 IN = 25.4 mm)</p> <p><b>ROTATING TEST SPECIMEN - RCF ROD</b></p> <table border="1" style="width: 100%; border-collapse: collapse;"> <tr> <td colspan="2" style="width: 40%;">HUGHES AIRCRAFT COMPANY EL SEGUNDO, CALIFORNIA</td> <td colspan="2" style="width: 60%;">CONTRACT: TRIBOLOGICAL FUNDAMENTALS</td> </tr> <tr> <td style="width: 30%;">DR LEO FIDERER, 20 AUG. '86</td> <td style="width: 10%;">SIZE A</td> <td style="width: 20%;">FSCM NO 82577</td> <td style="width: 40%;">DWG NO RCF</td> </tr> <tr> <td>TEL (213) 616-4826</td> <td>SCALE</td> <td>1/16"</td> <td>SHEET</td> </tr> </table>				HUGHES AIRCRAFT COMPANY EL SEGUNDO, CALIFORNIA		CONTRACT: TRIBOLOGICAL FUNDAMENTALS		DR LEO FIDERER, 20 AUG. '86	SIZE A	FSCM NO 82577	DWG NO RCF	TEL (213) 616-4826	SCALE	1/16"	SHEET			
HUGHES AIRCRAFT COMPANY EL SEGUNDO, CALIFORNIA		CONTRACT: TRIBOLOGICAL FUNDAMENTALS																
DR LEO FIDERER, 20 AUG. '86	SIZE A	FSCM NO 82577	DWG NO RCF															
TEL (213) 616-4826	SCALE	1/16"	SHEET															

FORM NO. 11062-1-CS OCT80

Figure 67. Hughes-modified engineering drawing of the NTN-Bower rolling contact fatigue (RCF) rod for Tester 2A use.

SP 519166



PURPOSE TRIBOLOGICAL FUNDAMENTALS PROGRAM					TITLE FLAT RUBSHOE (MODIFIED)		
MATL & SPEC AS PER PURCHASE ORDER SPECIFICATION					SCALE 10/1	TOLERANCES ANGULAR $\pm$	LINEAR $\pm$ 0,1 mm
ORIGINATOR LEO FIDERER	APPR <i>mq</i>	DATE APRIL 23 1987	BLDG E1	ROOM (M/S) B2323C (D145)	PHONE (213) 616-4826	HUGHES AIRCRAFT COMPANY	SKETCH PAD SP 519166

437 CS APR 85

Figure 68. Engineering drawing of the Tester 2A (modified) rubshoe.



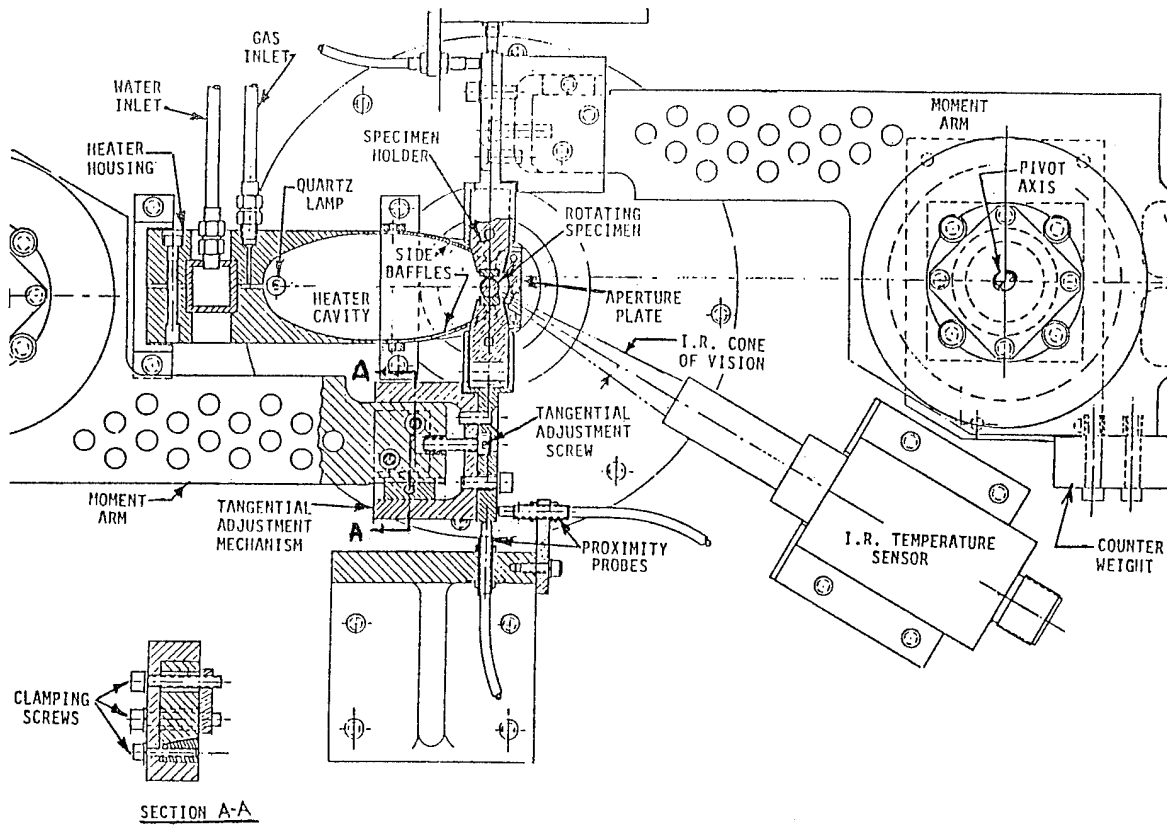


Figure 69. Detailed schematic of the Hughes Tester 2A high temperature tribometer.

aperture heat shield. There are gas cooling passages through the spindle, exhausting the warmed-up gas around the sliding specimens. This feature permits the use of filtered laboratory air or inert gas-purged test atmospheres without excessive cooling of the specimen region.

The A/D board, as well as the data logging (Labtech Notebook<sup>®</sup>) and analysis (RS/1<sup>®</sup>) software are the same ones used with the SEM tribometer. The overall view of the Tester 2A, with the desktop computer system attached, is shown in Fig. 70.

Rutile rubshoes vs.  $\alpha$ -SiC rod combinations were tested previously during Part I of the program, employing commercially available titania and  $\alpha$ -SiC samples. Statistical analysis of the results of two tests (4 rubshoes vs. rod contacts) indicated good repeatability: the standard deviation in rutile rubshoe wear was within ~9% of the arithmetic mean, while that of the  $\tau_s$  values fell within ~5% of the mean (12).

Using the test parameters described in Table 4, example results taken from (12) with Kyocera T-972 titania rubshoes running against Carborundum Hexoloy-SA80T silicon carbide RCF rod are reproduced here in Fig. 71. Since the IR pyrometer was operating at the emissivity setting of 1.0 and the emissivities of both titania and  $\alpha$ -SiC are close to 0.85 (12), the measured temperature of ~700°C in air was higher than 850°C. Note that the temperature profile of the thermal upramp followed by a thermal downramp was similar to the one employed during SEM tribometry. The data in Fig. 71 indicate that the magnitude and the hash of COF are higher at the lower specimen temperatures and lower at the higher specimen temperatures. On heating, the COF goes through a maximum and tends toward a minimum. This happens in spite of the fact that both  $A_{app}$  and  $A_r$  are both growing due to the increasing size of the wear scars. Similar to the results obtained with the SEM tribometer, the  $\tau_s$  and COF of rutile were first increased then decreased at the elevated temperatures. Switching back and forth between an air and an argon environment did not make any difference in either the hash width or the COF magnitude.

The photographs of the used rubshoes associated with the test described in Fig. 71 are also reproduced here from (12), in Fig. 72. This illustration serves as the wear baseline for the Tester 2A experiments planned for *rutile*, *mix* and *bronze* rubshoes. The additional data in Fig. 72 are especially useful indicating that the  $\tau_s$  calculated per the apparent area of contact is at least one to two orders-of-magnitude lower than the surface shear strength predicted by Fig. 1. This probably means that the real area of contact is one or two orders of magnitude smaller than the apparent (projected) contact area.

A similar test methodology was employed to examine the tribological behavior of *rutile*, *mix* and *bronze* rubshoes sliding against the silicon carbide triboceramic found best during Part I of the program: the sinter-HIP ESK  $\alpha$ -SiC. Interest centered around the engineering tribobehavior of these doped rutile materials in high temperature air against silicon carbide, with special attention to the effects of any

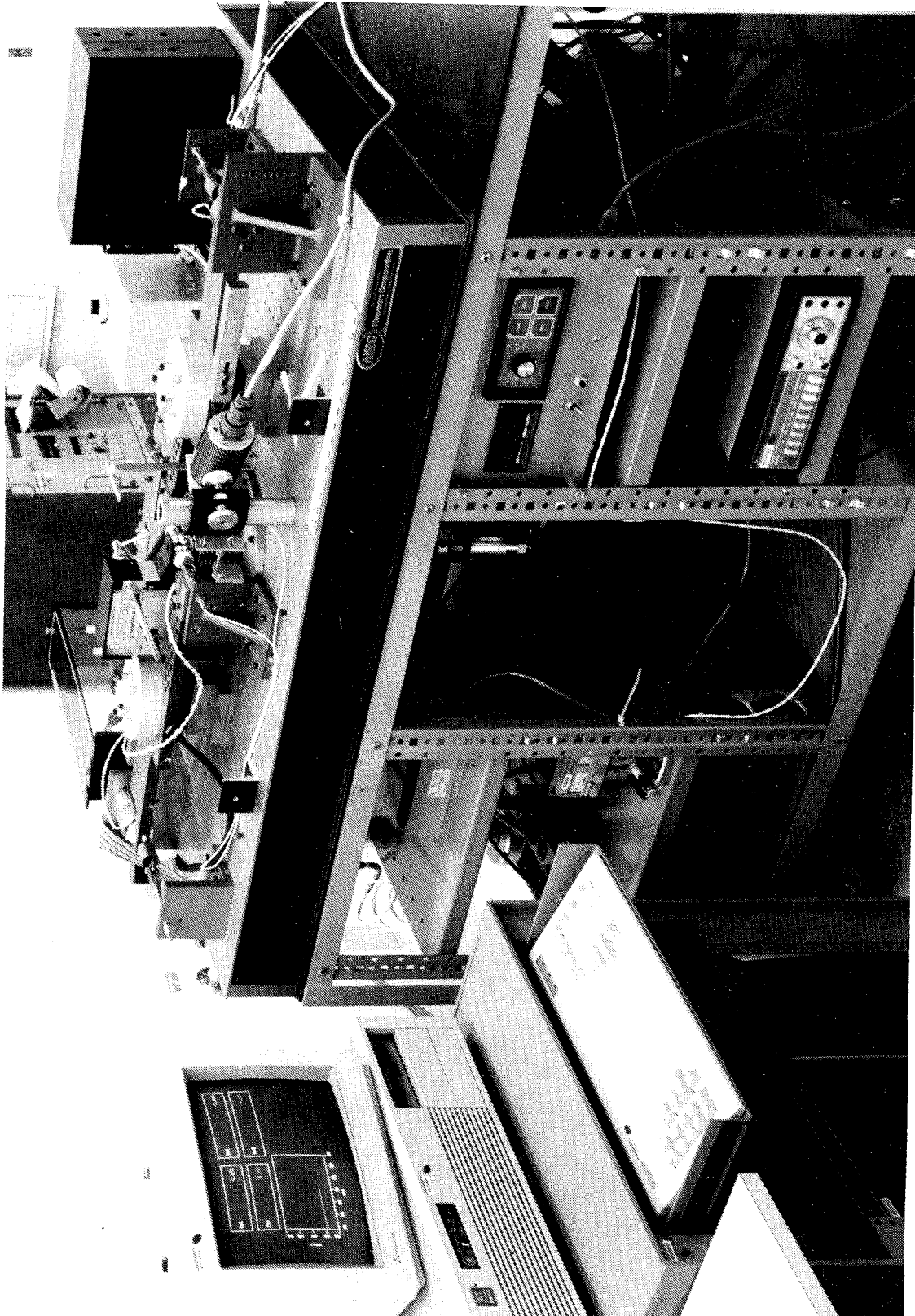
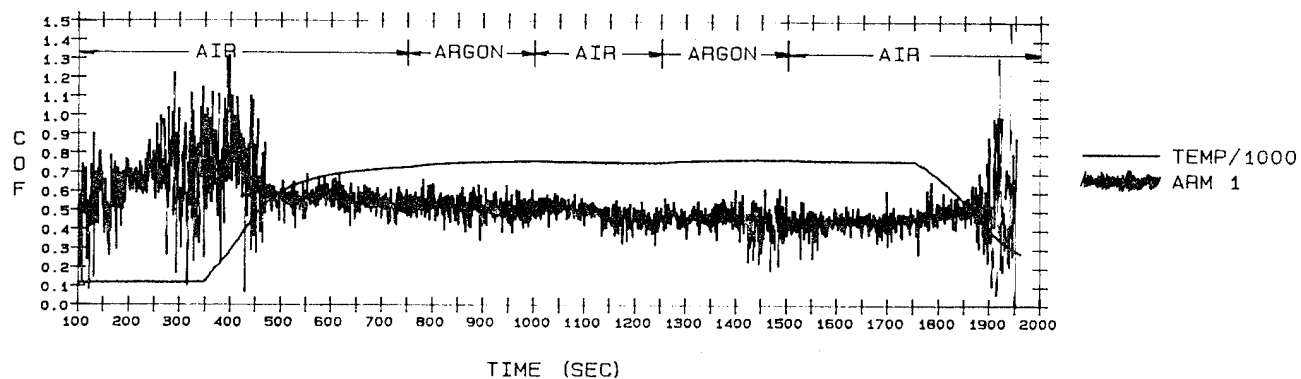


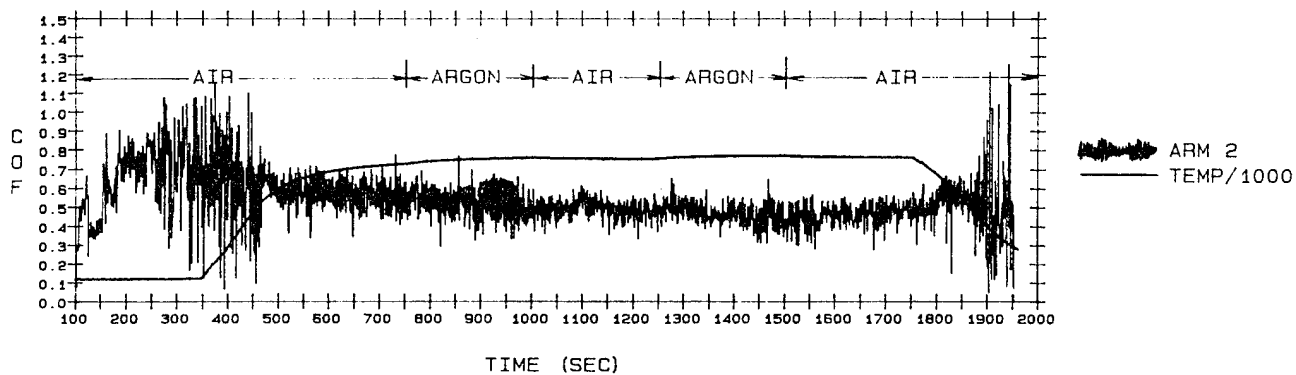
Figure 70. Photograph of the Tester 2A with dedicated computer for data logging and analysis.

Table 4. Test conditions for Tester 2A experiments.

Test Parameters	Magnitude
Normal Load (Steady-State)	1.36 kgf = 13.34N (3.0 lbs)
Speed: <ul style="list-style-type: none"> <li>during loading</li> <li>steady-state</li> </ul>	~400 rpm = 0.20 m/s (.66 fps) 700 rpm = 0.35 m/s (1.16 fps)
Duration: <ul style="list-style-type: none"> <li>time</li> <li>sliding distance</li> </ul>	20 - 30 min 420 - 630 m (1378 to 2067 ft)
Data Sampling Rates: <ul style="list-style-type: none"> <li>Wear</li> <li>Load</li> <li>Friction Force</li> <li>Rubshoe Temperature</li> <li>Pyrometer Temperature Output</li> <li>Heater Temperature</li> <li>Bearing Temperature</li> <li>Proximity Probes Power</li> <li>L.C. Power</li> </ul>	1 Hz 1 Hz 1 Hz 1 Hz 1 Hz 0.5 Hz 0.5 Hz 0.5 Hz 0.5 Hz
Test Atmosphere	Dry, Filtered Air
Test Temperatures	R. T. (No Heat Added) or ~850°C (Pyrometer Temperature)



RUTF\_3, 4: 13.3 N (3 lbs), 700 rpm  
 SOHIO HEXOLAY SA SiC ROD/KYOCERA FLAT  
 AIR/ARGON

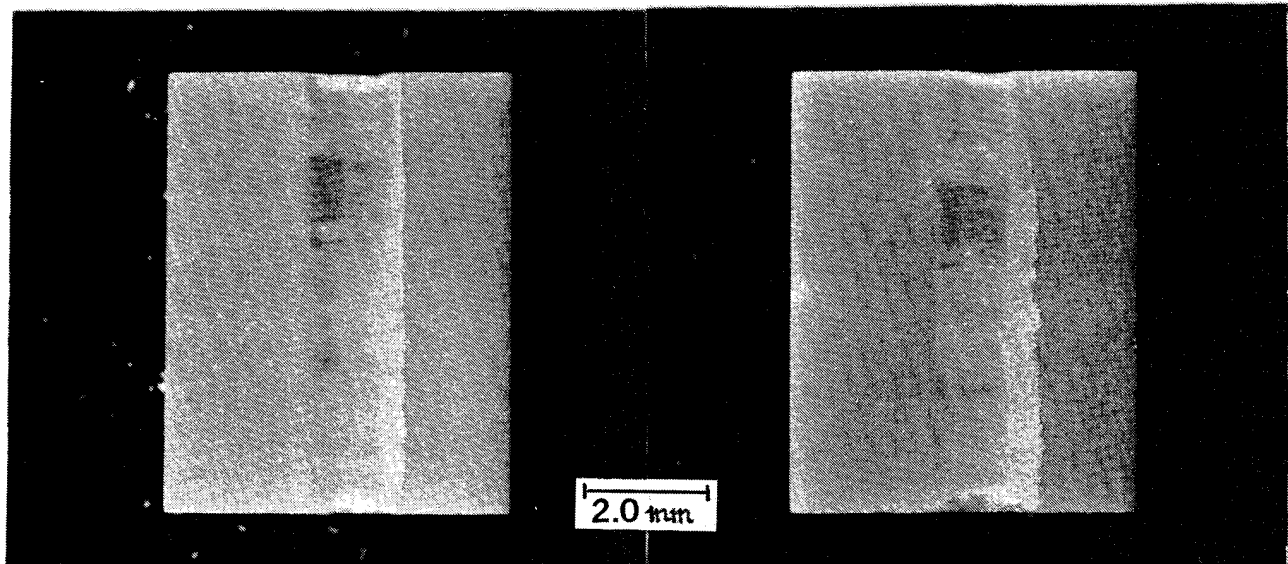


RUTF\_3, 4: 13.3 N (3 lbs), 700 rpm  
 SOHIO HEXOLAY SA SiC ROD/KYOCERA FLAT  
 AIR/ARGON

Figure 71. Tester 2A friction traces of Kyocera rutile rubshoes tested against an  $\alpha$ -SiC RCF rod, under standard test conditions (see Table 4 ); from (12).

ARM NO.1

ARM NO.2



$$A_{\text{apparent}} = 1.5 \text{ mm} \times 7.4 \text{ mm}$$

$$\tau = \frac{(0.48)(1.36 \text{ kg})}{11.1 \text{ mm}^2} = 0.06 \text{ kg} / \text{mm}^2$$

$$\underline{\underline{\tau = 0.6 \text{ MPa} ; \quad \underline{\underline{\dot{V} = 6 \times 10^{-14} \text{ m}^3 / \text{N} \cdot \text{m}}}}}$$

$$A_{\text{apparent}} = 1.0 \text{ mm} \times 7.5 \text{ mm}$$

$$\tau = \frac{(0.48)(1.36 \text{ kg})}{7.5 \text{ mm}^2} = 0.09 \text{ kg} / \text{mm}^2$$

$$\underline{\underline{\tau = 0.9 \text{ MPa} ; \quad \underline{\underline{\dot{V} = 5.57 \times 10^{-14} \text{ m}^3 / \text{N} \cdot \text{m}}}}}$$

RUTF\_3, 4: 13.3 N (3 lbs), 700 rpm  
 SOHIO HEXOLY SA SiC ROD/KYOCERA FLAT  
 AIR/ARGON

Figure 72. Appearance of used Tester 2A Kyocera rutile rubshoes tested against an  $\alpha$ -SiC rod, under standard test conditions (see Table 4); from (12). Arrow was added to original figure to indicate the direction of counterface sliding.

preferentially migrated copper oxide to the sliding surfaces. Doped rutiles may replace and/or complement carbon and boron nitride coatings applied to the silicon carbide fibers reinforcing high fracture toughness ceramic-ceramic composites.

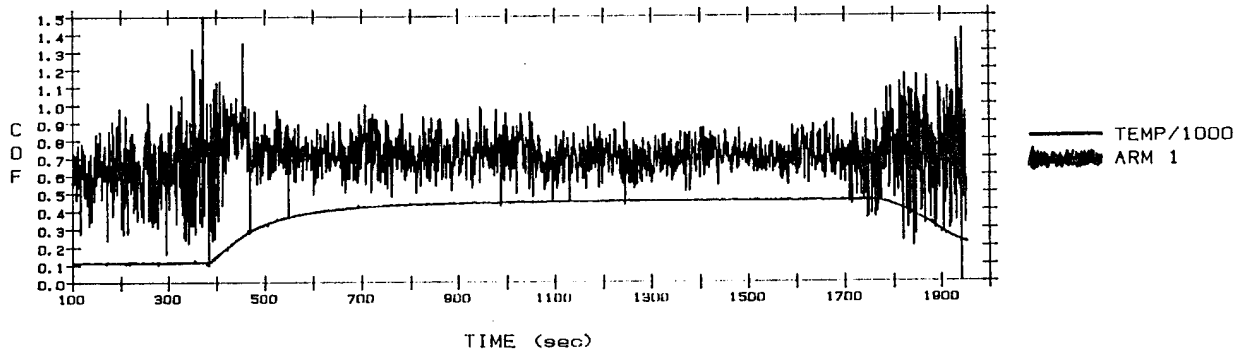
Considering the high partial pressure of oxygen in atmospheric air, the high test temperatures in the present case was expected to oxidize the  $\text{Cu}_2\text{O}$  to  $\text{CuO}$  (Fig. 32). The tribological response of  $\text{CuO}$  may be significantly different from the unoxidized Magnèli phases or those contaminated with  $\text{Cu}_2\text{O}$ . Another point of interest was the sensitivity of  $\text{Cu}^{2+}$  in  $\text{CuO}$  to atmospheric moisture (98), similar to the previously found reactivity of the Magnèli phases and  $\text{Cu}_2\text{O}$  with water.

The COF traces as a function of temperature for *rutile*, *mix* and *bronze* rubshoes, in air, are given in Figs. 73, 74 and 75, respectively. The used rubshoes associated with these tests are depicted with their worn and unworn areas in Figs. 76 and 77.

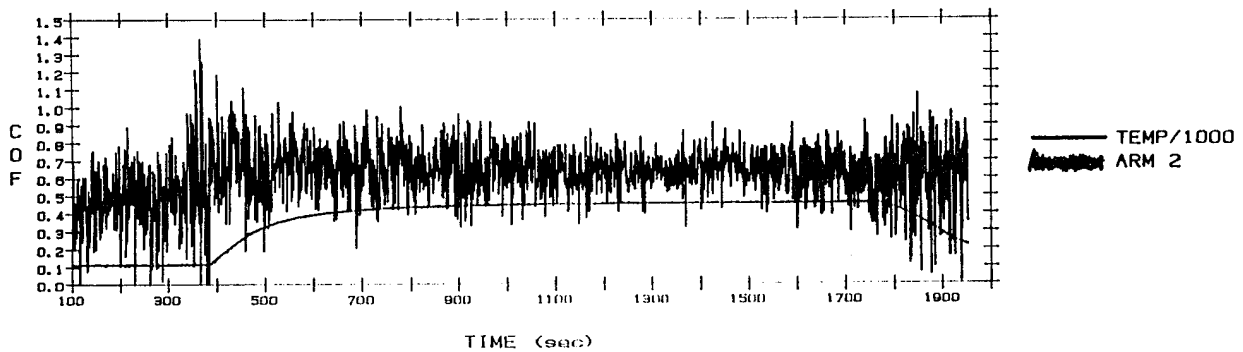
At first glance, the comparison of these friction curves and the previous baseline shown in Fig. 71 reveals certain similarities. However, closer examination also indicates significant differences:

1. Only the friction curve of *rutile* agrees with the baseline in terms of magnitude and an increase in frictional variations (hash) at the lower temperatures. The fact that the baseline in Fig. 72 was yellow-white and remained that color during and after the friction test, and that the current rubshoe specimens remained significantly darker during every one of the tests (see Fig. 76), may have influenced the emissivity of the specimens and the maximum temperature the lamp heater was able to impart to them. In spite of applying of the same maximum lamp power as before, the pyrometer indicated lower maximum temperatures in Figs. 73 through 75 than in Fig. 71. This may be attributed to the higher emissivity (*ergo* lower temperature) of the darker specimens shown in Fig. 76. The higher friction of the slightly substoichiometric *rutile* at the high temperatures in Fig. 73, compared with the lower overall friction of the stoichiometric equivalent in Fig. 71, may have been helped by this temperature difference.
2. The friction response of the *bronze* in Fig. 75 is less temperature-sensitive than that of the *rutile*. This finding is in accordance with the SEM tribometric results. However, the Tester 2A-produced variation in COF values is much less in high temperature air than the difference in COF measured by the SEM tribometer at significantly higher temperatures, both in vacuum and in  $\text{P}_{\text{Ox}}$ .

# $\text{TiO}_{2-x}(\text{HP})$



A988\_4 FRONT, 13.3N (3.0 lbf), 700 RPM  
 ESK ALPHA SILICON CARBIDE POST HIPPED ROD  
 AIR

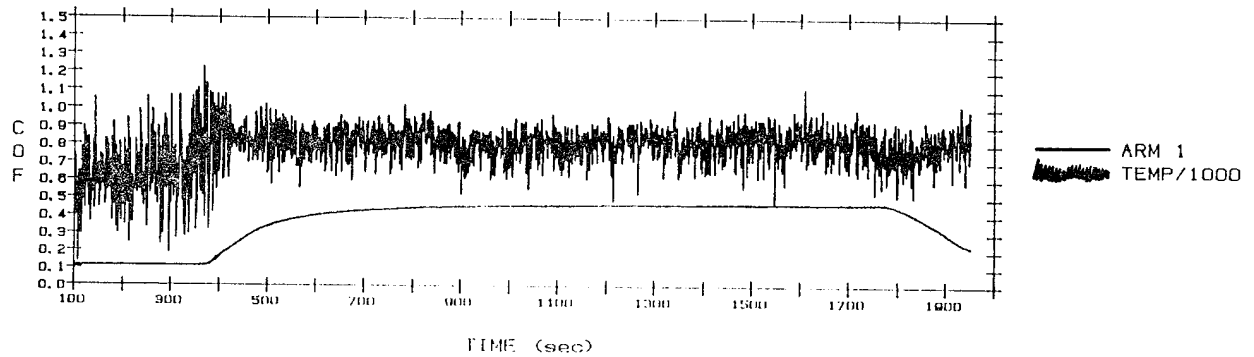


A988\_4 BACK, 13.3N (3.0 lbf), 700 RPM  
 ESK ALPHA SILICON CARBIDE POST HIPPED ROD  
 AIR

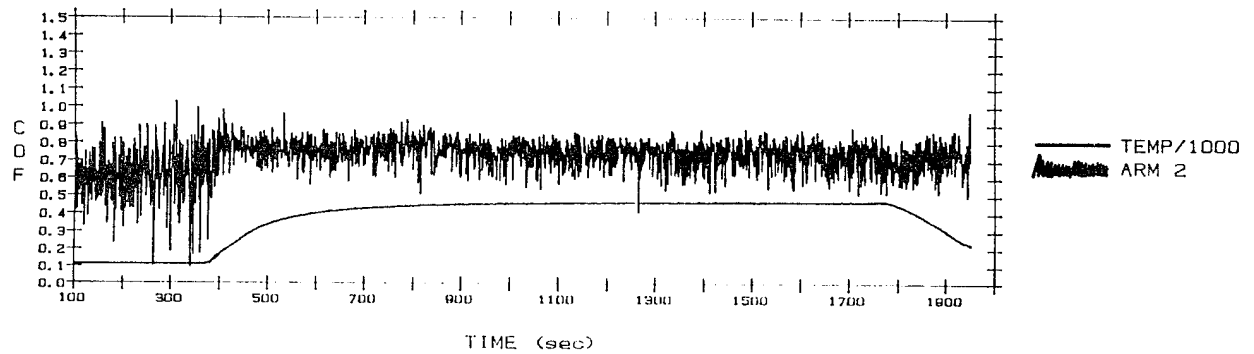
Figure 73. Tester 2A friction traces of *rutile* rubshoes tested against an  $\alpha$ -SiC RCF rod, under standard test conditions (see Table 4).



# $\text{TiCuO}_{2-x}(\text{HP})$



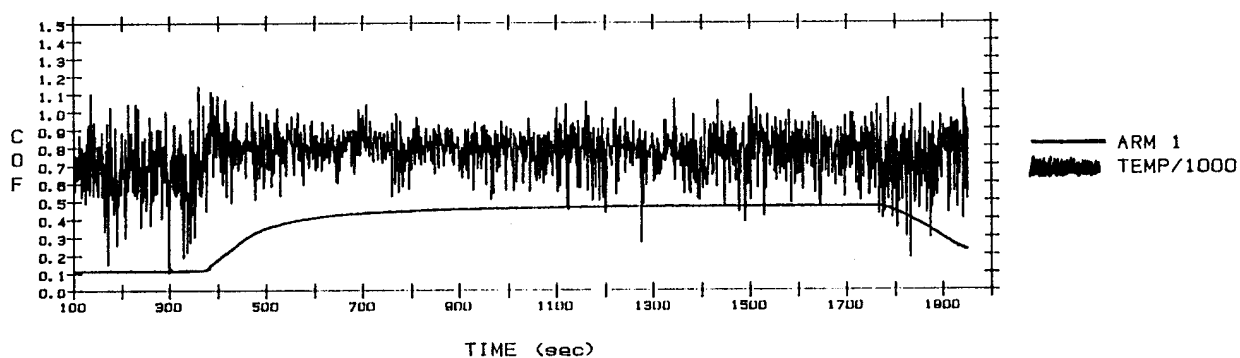
A988\_1 FRONT, 13.3 N (3.0 lbf), 700 RPM  
ESK ALPHA SILICON CARBIDE POST HIPPED ROD  
AIR



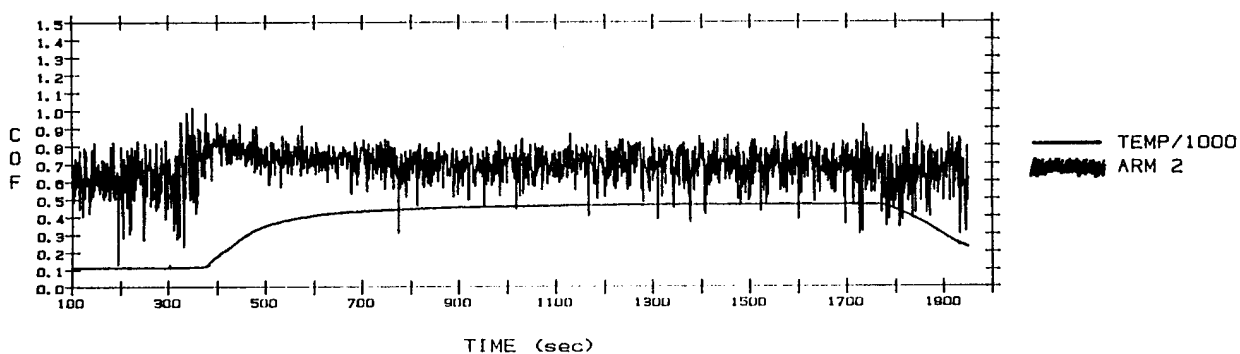
A988\_1 BACK, 13.3 N (3.0 lbf), 700 RPM  
ESK ALPHA SILICON CARBIDE POST HIPPED ROD  
AIR

Figure 74. Tester 2A friction traces of *mix* rubshoes tested against an  $\alpha$ -SiC RCF rod, under standard test conditions (see Table 4).

# $\text{TiCuO}_{2-x}(\text{HP} + \text{ANN.})$



A988\_3 FRONT. 13.3 N (3.0 lbe). 700 RPM  
ESK ALPHA SILICON CARBIDE POST HIPPED ROD  
AIR



A988\_3 BACK. 13.3 N (3.0 lbe). 700 RPM  
ESK ALPHA SILICON CARBIDE POST HIPPED ROD  
AIR

Figure 75. Tester 2A friction traces of *bronze* rubshoes tested against an  $\alpha$ -SiC RCF rod, under standard test conditions (see Table 4).

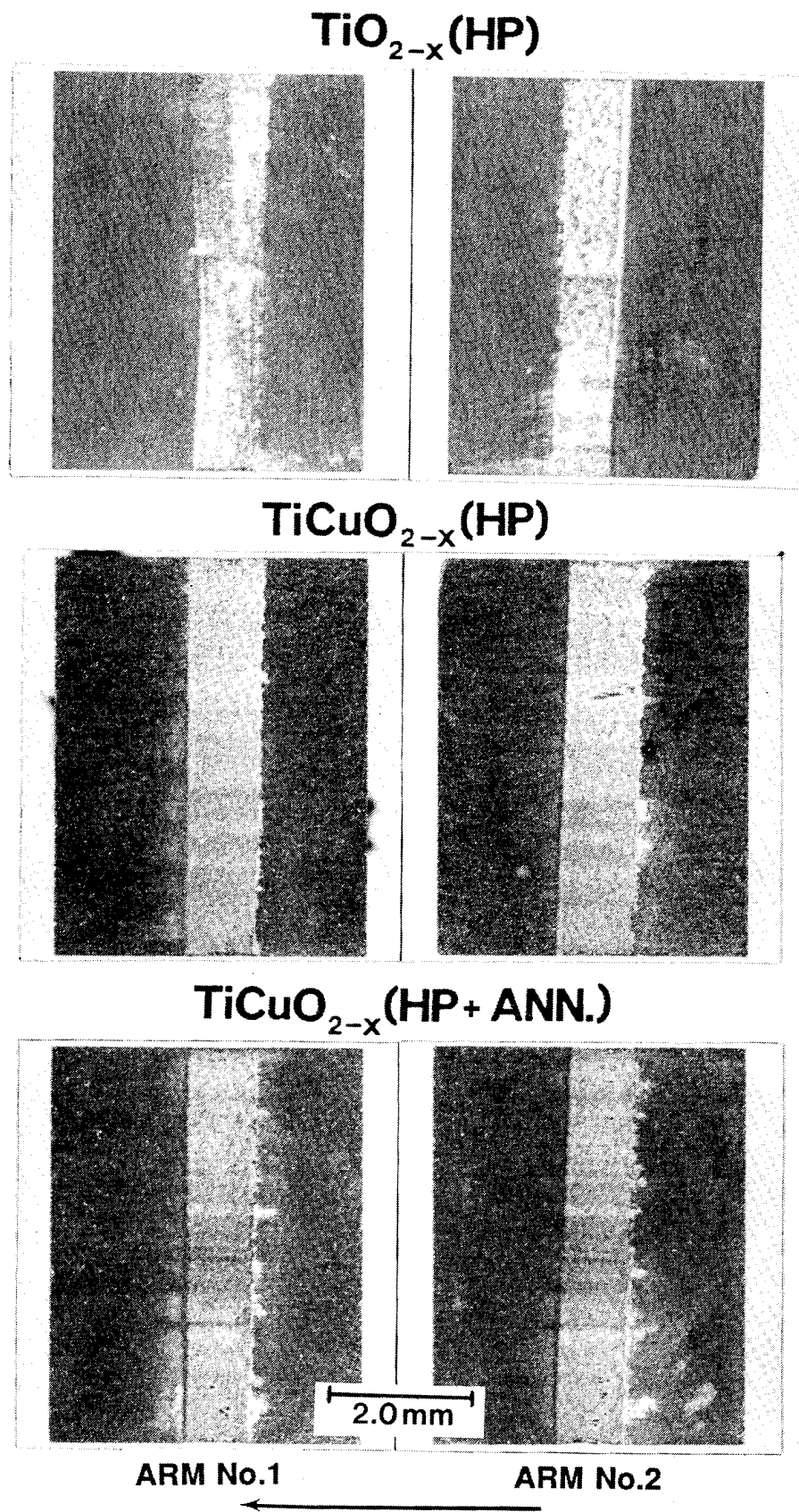


Figure 76. Low magnification optical photomicrographs of used Tester 2A *rutile*, *mix*, and *bronze* rubshoes associated with the test described in Figures 73, 74 and 75 (7.9x mag.). Arrow indicates the direction of counterface sliding.

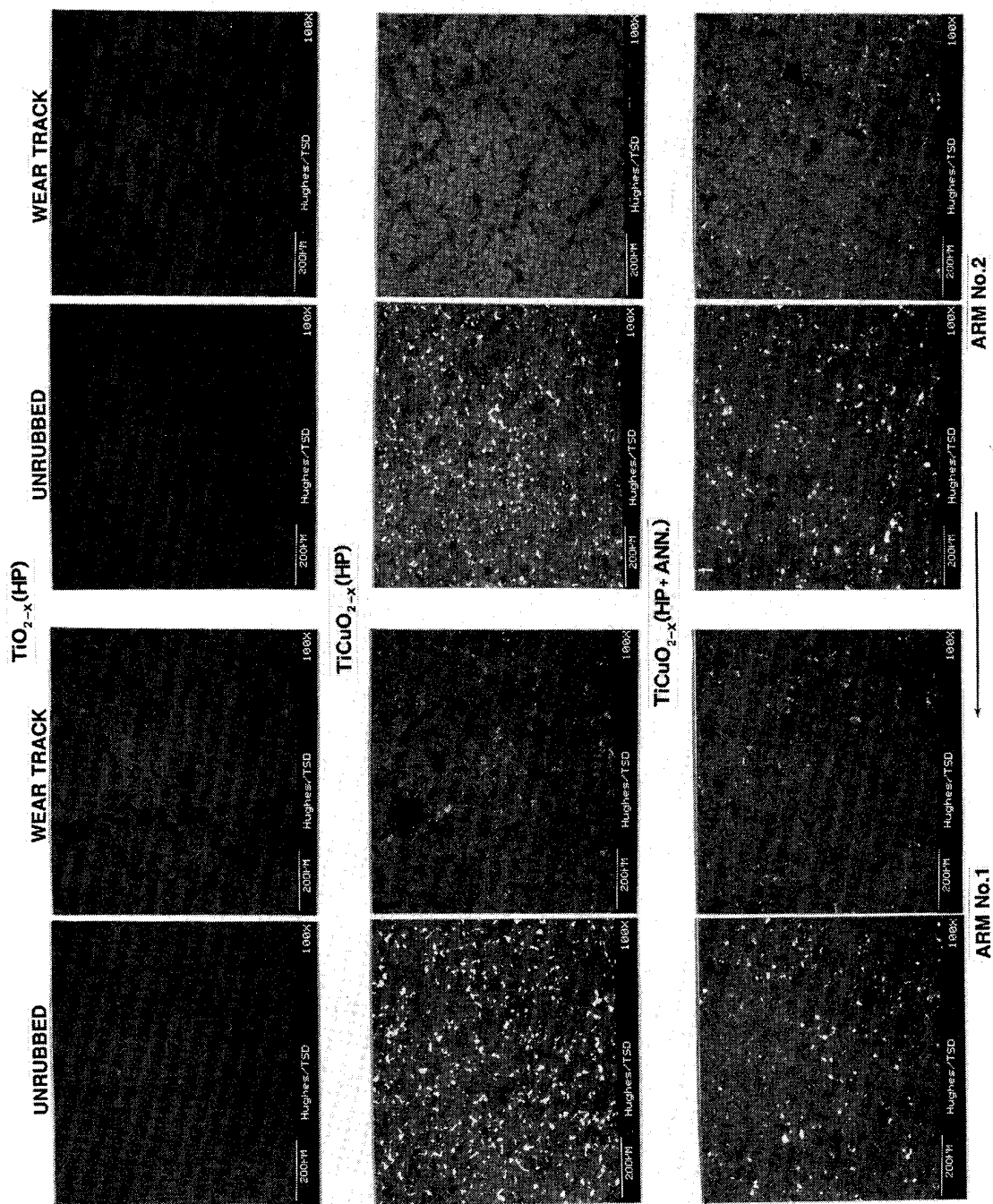


Figure 77. Typically representative SEM photomicrographs of the used rub shoes shown in Figure 76, taken in and out of the wear tracks.

3. The *mix* exhibited the smoothest sliding behavior. The magnitude of the COF did not differ significantly from the other samples and no effects attributed to moisture sensitivity were observed.

Judging from the wear scar widths in Fig. 76, the *mix* wore somewhat more than the other two samples, whose wear was nearly equivalent. These results are reliable, considering the excellent alignment of the scars and good repeatability of their sizes. There seems to be no significant difference between the wear rate of the commercially available Kyocera (stoichiometric) rutile in Fig. 72 and the present samples in Fig. 76. This may have been influenced by the nature of the alumina dopant in the Kyocera material. Aluminum ions (as previously explained herein) harden the lattice without generating Magnéli phases.

The SEM photomicrographs in Fig. 77 help shed some light on the basic cause of the minor, but observable friction and wear behavior difference between the two doped materials: the *mix* and the *bronze*. There are different accumulation tendencies of the copper-containing constituents (copper oxide and Cu metal precipitate-inclusions) on the respective rubshoe surfaces. As observed before with the SEM tribometer flats and pins, the CuO-doped *mix* and *bronze* rubshoes exhibit different quantities of the EDS-confirmed, copper-containing precipitates on the heated, but yet-unrubbed surface. The sliding action smears the rutile-type constituents over the inclusions. Thus, the COF is controlled more by the rutile-type constituents of the rubshoes than the surface-smeared metallic copper and the copper oxides. There seems to be little difference between the extent of surface smearing on the part of the undoped *rutile* and the smearing tendencies of the rutile-type parts of the *mix* and the *bronze*.

From the engineering standpoint, neither the *bronze*, nor its rutile-based precursors are practical lubricious oxides for use in high temperature air; the COF is still too high. The apparently low  $\tau_s$  of the rubshoes notwithstanding (see calculations in Fig. 72 and the equivalent wear scar sizes in Fig. 76), one should obtain COF values of  $0.10 \pm 0.05$  for any good solid lubricant material. Even in high temperature air, the friction should not be higher than 0.2 to 0.3 under the engineering loads and contact configuration applied by the Tester 2A specimen contact. The elevated but more even friction of the *bronze* (and perhaps even the *mix*) may render these doped oxides as viable candidates for ceramic brake materials (or powder additives in brakeshoes) at temperatures ranging from room ambient to  $\sim 850^\circ\text{C}$ .

## 5.0 CONCLUSIONS AND RECOMMENDED FUTURE WORK

The rutile polymorph of polycrystalline  $\text{TiO}_{2-x}$  was utilized for a molecular engineering study, whereby undoped and cation-doped rutile were examined analytically and tribometrically to determine the accuracy of a hypothesis pertaining to stoichiometric and shear strength stabilization of rutile by chemical means.

The results confirmed the predicted, oxygen-vacancy-controlled creation of high and low lattice (strain) energy Magnèli phases in undoped rutile, exhibiting higher and lower surface shear strength and friction, respectively. The  $\text{TiO}_{1.70}$  appears particularly promising as a low friction lubricious oxide, in contrast with the high friction  $\text{TiO}_{1.80}$  counterpart. Unfortunately, the high sensitivity of any narrow stoichiometric region to temperature and the partial pressure of oxygen of the surrounding atmosphere causes purposely reduced rutile to be thermo- and tribo-oxidatively unstable. This instability renders undoped rutile unsuitable as a practical lubricious oxide useful for extreme environmental applications.

Achieving stoichiometric and shear strength stability was attempted by doping polycrystalline rutile with selected cations similar in size and polarizability to the  $\text{Ti}^{4+}$ , but with lower valencies. Doping with these aliovalent cations was predicted to cause chemical expulsion of oxygen from the rutile lattice to maintain charge balance and to generate the specific crystallographic shear planes constituting the various Magnèli phases. Copper, iron, cobalt and nickel ions were tried as dopants, listed in order of diminishing capacity. As predicted, copper (in the original form of  $\text{CuO}$ , which provided the  $\text{Cu}^{2+}/\text{Cu}^{1+}$  ions during hot-pressing and annealing in a reducing atmosphere) was shown best to date, using this relatively simple preparation technique. The attempt to make the  $(\text{Ti}+\text{Cu})\text{O}_{1.80}$  model compound resulted in a nonstoichiometric reaction, where only a portion of the copper ions entered the lattice to form Magnèli phases. The rest of the dopant either evaporated, remained partially behind as  $\text{Cu}_2\text{O}$  on the surface or was left completely reduced as metallic copper. The reacted compound itself is a new, never-before-reported titanium-copper *bronze*, which exhibited an X-ray diffractogram closely resembling the Magnèli phases of the well-known  $\text{V}_3\text{Ti}_6\text{O}_{17}$  (M/O ratio = 1.89). In addition, the doped material had the electrical conductivity of polycrystalline rutile reduced to  $\text{TiO}_{1.89}$ .

SEM tribometric and engineering-type friction and wear bench tests at temperatures up to  $1000^\circ\text{C}$ , in various partial pressures of oxygen, indicated that the copper doped, rutile-structured *bronze* exhibited the predicted reduction in the characteristic (and highly undesirable) frictional increase that occurs as the oxygen stoichiometry of pure rutile is changed gradually from  $\text{TiO}_{2.00}$  to  $\text{TiO}_{1.80}$  (the highest friction Magnèli phase). However, these tribotests also indicated that neither the *bronze* nor its undoped and reduced precursors are practical lubricious oxides, because their coefficients of kinetic friction are still too high (0.6 to 0.7). Nevertheless, the elevated but relatively stable friction coefficients

of the *bronze* at all of the test temperatures and atmospheric environments may enable the use of this material as ceramic brakes or powder additives in automotive brakeshoes, for a variety of wide temperature range applications.

Since partial doping reduced the undesirable frictional increase on progressive removal of oxygen from the rutile lattice, full doping to a titanium *bronze* equivalent to the lowest friction Magnèli phase beyond  $\text{TiO}_{1.80}$  (i.e.,  $\text{TiO}_{1.70}$ ) could conceivably keep friction low and even both in reducing and oxidizing atmospheres, at any temperature. If full doping to  $\text{TiO}_{1.70}$  would be possible, it would be an especially advantageous method of formulating a stable lubricious rutile.

In a strong oxidizing environment (e.g., in LOX), the much more mildly (and more easily) reduced, low friction  $\text{TiO}_{1.93-1.98}$  compound may already serve well, since its stoichiometry cannot be changed any further in LOX. Turbopump engineers would welcome the availability of a thermo-oxidatively stable, low friction and wear bearing or gear lubricant impervious to LOX to extend pump life and improve performance.

The simple hot-pressing and heat-treatment method used during the present program does not appear to be the most advantageous for preparing cation-doped rutile. It is also unlikely that the doping of other transition metal oxides that do form Magnèli phases of predictably varying shear strengths can be achieved by simple hot-pressing commercially available rutile with the appropriate, commercially available metal oxides. Other preparation methods, some directed toward fabricating monolithic parts and some directed toward thin films, may be more desirable. Examples of these methods are coprecipitation of nanophase oxides followed by heat-treatment in moderate temperatures (i.e., under  $1000^\circ\text{C}$ ) for bearing material blanks or wet-chemical doping, reactive cosputtering, and molecular beam epitaxy for depositing thin films. Low cost application of thin, low shear strength films onto ceramic fibers reinforcing high fracture toughness ceramic-ceramic composites would be especially useful. For example, pure rutile does not react with the oxidized  $\text{SiO}_2$  "skin" that develops on  $\alpha$ -SiC fibers in high temperature air until  $1550^\circ\text{C}$ . If the dopant(s) can be shown similarly unreactive, lubricious *bronze* layers could outperform the presently employed carbon and h-BN fiber coatings as fracture toughness-enhancing debond agents. Unfortunately, these more conventional coating materials are thermo-oxidatively unstable above  $450^\circ\text{C}$  and  $900^\circ\text{C}$ , respectively.

The advanced doping techniques may be able to insert not only copper, but other likely cations (e.g.,  $\text{Zn}^{2+}$  or  $\text{Mn}^{2+}$ ) into the rutile lattice as well. Other transition metal oxides that form Magnèli phases of predictably manipulatable shear strengths could also serve as possible candidates for further cation doping studies.

## 6.0 REFERENCES

1. P. R. Viars, "The Impact of IHPTET on the Engine/Aircraft System," paper presented at the AIAA/AHS/ASEE Aircraft Design, System and Operation Conf., July 31- Aug. 2, 1989, Seattle, WA, AIAA Paper No. 89-2137.
2. "Advanced Turbine Technology Application Program, (ATTAP)," (USDOE Assistant Secretary for Conservation and Renewable Energy, Wash. D. C., Office of Transportation Systems), Report No. DOE/CE-0257, Apr. 1989.
3. H. E. Helms, et al, "AGT (Advanced Gas Turbine) Technology Project," Final Report, Report No. NASA CR-182127, Detroit Diesel Allison, Indianapolis, IN, Aug. 1988.
4. C. Faulkner, and F. Ferita, "ALS Turbomachinery Technology," paper presented at the Aerospace Technology Conf. and Expo., Long Beach, CA, Oct. 1-4, 1990, SAE Paper 901882.
5. G. R. Sundberg, "Advanced Launch System (ALS) Actuation and Power Systems Impact Operability and Cost," IEEE AES Magazine, 5, pp. 20-23 (1990).
6. R. M. Hoodless, Jr., J. C. Monk, and H. A. Cikanek, "National Launch System Space Transportation Main Engine," paper presented at the 42nd. Cong. of the Int. Astronautics Federation, Oct. 5-11, 1991, Montreal, Canada, AIAA Paper No. IAF-91-259.
7. R. D. Paster, and G. J. Hallinan, "SSME and Beyond: Future Earth-to-Orbit Propulsion in the U.S.A.," paper presented at the 41st. Cong. of the Int. Astronautical Federation, Oct. 6-12, 1990, Dresden, GDR, AIAA Paper No. IAF-90-237.
8. J. R. Stone, L. M. Shaw, and C. A. Aukerman, "Plans for the Development of Cryogenic Engines for Space Exploration," paper presented at the AIAA/NASA/OAI Conf. on Advanced SEI Technologies, Sept. 4-6, 1991, Cleveland, OH, AIAA Paper No. 91-3438.
9. B. Reed and S. Schneider, "Hydrogen/Oxygen Auxiliary Propulsion Technology," paper presented at the AIAA/NASA/OAI Conf. on Advanced SEI Technologies, Sept. 4-6, 1991, Cleveland, OH, AIAA Paper No. 91-3440.
10. M. Buffo, "Technical Comparison of Seven Nation's Space Plane Programs," paper presented at the AIAA Space Programs and Technologies Conf., Sept. 25-28, 1990, Huntsville, AL, AIAA Paper No. 90-3674.
11. J. Thomas, and W. Powell, "The NASP Program: A Status Report," paper presented at the AIAA Space Programs and Technologies Conf., March 24-27, 1992, Huntsville, AL, AIAA Paper No. 92-1417.
12. M. N. Gardos, "Determination of the Tribological Fundamentals of Solid Lubricated Ceramics, Volume 1: Summary," WRDC-TR-90-4096, Hughes Aircraft Company, El Segundo, CA, November 1990.
13. M. N. Gardos, "The Effect of Anion Vacancies on the Tribological Properties of Rutile ( $\text{TiO}_{2-x}$ )," Tribology Trans., 31, pp. 427-436 (1988); also see discussions on this paper, Tribology Trans., 32, pp. 30-31 (1989).
14. M. N. Gardos, H.-S. Hong, and W. O. Winer, "The Effect of Anion Vacancies on the Tribological Properties of Rutile ( $\text{TiO}_{2-x}$ ), Part II: Experimental Evidence," Tribology Trans., 32, pp. 209-220 (1990).



## **REFERENCES (Con't)**

15. M. N. Gardos, "The Tribooxidative Behavior of Rutile-Forming Substrates," Mat. Res. Soc. Symp. Proc. Vol. 140, New Materials Approaches to Tribology: Theory and Applications, Eds. L. E. Pope, L. L. Fehrenbacher, and W. O. Winer, pp. 325-338 (1989).
16. P.C.S. Hayfield, "Electrode Material, Electrode and Electrochemical Cell," U.S. Patent No. 4,422,913; Dec. 27, 1983.
17. R. L. Clarke, and S. K. Harnsberger, "New Electrically Conductive Ceramic -- A Fundamental Advance in Electrode Technology," Amer. Laboratory (News Ed.), June 1988.
18. C. DellaCorte, and D. L. Deadmore, "Vickers Indentation Hardness of Stoichiometric and Reduced Single Crystal TiO<sub>2</sub> (Rutile) from 25 to 800°C," NASA TM-105959, Apr. 1993.
19. R. V. Sirivardane, and J. P. Wightman, "Interaction of Hydrogen Chloride and Water with Oxide Surfaces, III. Titanium Dioxide," J. Coll. Interface Sci., 94, pp. 502-513 (1983).
20. J. A. Eastman, Y. X. Liao, A. Narayanasamy, and R. W. Siegel, "Processing and Properties of Nanophase Oxides," Mat. Res. Soc. Symp. Vol. 155, pp. 255-266 (1989).
21. K. H. G. Ashbee, and R. E. Smallman, "The Plastic Deformation of Titanium Dioxide Single Crystals," Proc. Roy. Soc. A, 274, pp. 195-205 (1962).
22. O. W. Johnson, et al, "High Temperature Deformation of Rutile," AFML-TDR-64-114, U. of Utah, Salt Lake City, UT, Contract No. AF33 (616)-6832, Project No. 7320, Task No. 735001 (April 1964).
23. R. C. DeVries, R. Roy, and E. F. Osborn, "The System TiO<sub>2</sub>-SiO<sub>2</sub>," Trans. Brit. Ceram. Soc., 53, p. 525-540 (1954).
24. M. F. Best, and R. A. Condrate, Sr., "A Raman Study of TiO<sub>2</sub>-SiO<sub>2</sub> Glasses Prepared by Sol-Gel Processes," J. Mat. Sci., 4, p. 994-998 (1985).
25. C.U.I. Odenbrand, J.G.M. Brandin, and G. Busca, "Surface Acidity of Silica-Titania Mixed Oxides," J. Catalysis, 135, p. 505-517 (1992).
26. H. Sankur, and W. Gunning, "Crystallization and Diffusion in Composite TiO<sub>2</sub>-SiO<sub>2</sub> Thin Films," J. Appl. Phys., 66, p. 4747-4751 (1989).
27. H. Sankur, and W. Gunning, "Sorbed Water and Intrinsic Stress in Composite TiO<sub>2</sub>-SiO<sub>2</sub> Films," J. Appl. Phys. 66, p. 807-812 (1989).
28. A. A. Galuska, J. C. Uht, P. M. Adams, and J. M. Coggi, "Ion Mixing of Ti and TiO<sub>y</sub> Films on SiO<sub>x</sub>," J. Vac. Sci. Technol., A6, p. 2403-2409 (1988).
29. J. J. Brennan, "Interfacial Characteristics of Glass-Ceramic Matrix/SiC Fiber Composites," J. de Physique, Coll. C5, 10(49), pp. C5-791-809 (1988).
30. M. J. Mayo, R. W. Siegel, A. Narayanasam, and W D. Nix, "Mechanical Properties of Nanophase TiO<sub>2</sub> as Determined by Nanoindentation," J. Mater. Res., 5, pp. 1073-1082 (1990).
31. R. S. Averback, H. Hahn, H. J. Höfler, J. L. Logas and T. C. Shen, "Kinetic and Thermodynamic Properties of Nanocrystalline Materials," Mat. Res. Soc. Symp. Proc. Vol. 153, pp. 3-12 (1989).
32. "Kyocera Fine Ceramics," Kyoto Ceramic Co., Ltd., Technical Bulletin No. CAT/3T7804 TD.

## **REFERENCES (Con't)**

33. M. N. Gardos, "Continuing Development of Solid Lubricants Technology by Molecular Engineering of Lubricious Oxides and Fluorides," Volume 1, Technical/Management Proposal, Ref. No. F6896/EDSG P061137, Hughes Aircraft Co., El Segundo, CA, April 1990.
34. L. A. Bursill, "An Electron Microscope Study of the FeO-Fe<sub>2</sub>O<sub>3</sub>-TiO<sub>2</sub> System and of the Nature of Ion-Doped Rutile," J. Solid State Chem. 10, 72-94 (1974).
35. L. A. Bursill, I. E. Grey, and D. J. Lloyd, "High-Temperature Rutile-Derived Crystallographic Shear Structures. I. (020)<sub>r</sub> CS Structures," J. Solid State Chem., 16, pp. 331-347 (1976).
36. L. A. Bursill, and G. G. Stone, "Determination of the Displacement Vector at (210) Boundaries in Gallia-Doped Rutile," Philos. Mag., 32(6), pp. 1151-1158 (1975).
37. M. Guermazi, P. Thevenard, J. P. Dupin, and C.H.S. Dupuy, "Effects of Implantation in Rutile with Metallic Ions," Radiation Effects, 49, 61-64 (1980).
38. M. Guermazi, P. Thevenard, and C. Dupuy, "Compound Synthesis in TiO<sub>2</sub> Implanted with Rubidium," Radiation Effects, 64, 197 (1982).
39. M. Guermazi, P. Thevenard, and M. G. Blanchin, "Chemical Twinning Induced by Chemical Implantation in TiO<sub>2</sub>," Radiation Effects, 91, 125-137 (1985).
40. R. D. Shannon, "Phase Transformation Studies in TiO<sub>2</sub> Supporting Different Defect Mechanisms in Vacuum-Reduced and Hydrogen-Reduced Rutile," J. Appl. Phys., 35, 3414-3416 (1964).
41. K.J.D. MacKenzie, "7.-The Calcination of Titania: IV. The Effect of Additives on the Anatase-Rutile Transformation," J. Brit. Cer. Soc., 74, 29-34 (1975).
42. *ibid*, "V. Kinetics and Mechanisms of the Anatase-Rutile Transformation in the Presence of Additives," p. 77-84.
43. M.F. Yan, and W.W. Rhodes, "Effects of Cation Contaminants in Conductive TiO<sub>2</sub> Ceramics," J. Appl. Phys., 53, 8809-8818 (1982).
44. M.-H. Whangbo and E. Canadell, "Analogies between the Concepts of Molecular Chemistry and Solid-State Physics concerning Structural Instabilities. Electronic Origin of the Structural Modulations in Layered Transition Metal Dichalcogenides," J. Am. Chem. Soc., 114, pp. 9587-9600 (1992).
45. M. N. Gardos, "Tribology and Wear Behavior of Diamond," Chapter 12 in Synthetic Diamond: Emerging CVD Science and Technology, John Wiley & Sons, N.Y., NY, Jan. 1994.
46. R. D. Shannon, "Dielectric Polarizabilities of Ions in Oxides and Fluorides," J. Appl. Phys., 73, pp. 348-366 (1993).
47. R. James, and C.R.A. Catlow, "The Energetics of Shear Plane Formation in Reduced TiO<sub>2</sub>," J. Phys. (Paris), 38, pp. C7-32 - 35.
48. A. Perez, "Ion Implantation Effects in Crystalline Inorganic Insulators," Nucl. Instrum. & Methods Phys. Res., B1, pp. 621-627 (1984).
49. P. F. McDonald, A. Parasiris, R. K. Pandey, B. L. Gries, and W. P. Kirk, "Paramagnetic Resonance and Susceptibility of Ilmenite, FeTiO<sub>3</sub> Crystal," J. Appl. Phys., 69, pp. 1104-1106 (1991).

## REFERENCES (Con't)

50. J. McHardy, and P. Stonehart, "Electrochemistry of Transition Metal Oxide Bronzes and Related Compounds," Int. Rev. Sci., Phys. Chem. Ser. 2, Vol. 6: Electrochemistry, J. O'M. Bockers ed., Butterworths, London, 1976.
51. P. A. Sermon, K. Rollins, P. N. Reyes, S. A. Lawrence, M.A.M. Lawrence and M. J. Davies, "Nature of Oxide-supported Copper (II) Ions and Copper Derived from Copper (II) Chloride," J. Chem. Soc., Faraday Trans., 83, pp. 1347-1353 (1987).
52. M. d. Arco, A. Cuballero, P. Malet, and V. Rives, "Effect of Consecutive and Alternative Oxidation and Reduction Treatments on the Interactions between Titania (Anatase and Rutile) and Copper," J. Catalysis; 113, pp. 120-128 (1988).
53. Z. Takehara, T. Nishimura, and I. Makino, "Activation of  $\text{TiO}_2$  and  $\text{MnO}_2$  by Vanadium Doping as Cathodes in Nonaqueous Lithium Cells," in New Materials and Processes, Volume 3, JEC Press, Inc., Cleveland, OH, 1985, pp. 259-263.
54. T. Ono, Y. Nakagawa, H. Miyata, and Y. Kubokawa, "Catalytic Activity of  $\text{MoO}_3$  and  $\text{V}_2\text{O}_5$  Highly Dispersed on  $\text{TiO}_2$  for Oxidation Reactions," Bull. Chem. Soc. Jpn., 57, pp. 1205-1210 (1984).
55. G. T. Went, L.-J. Leu, and A. T. Bell, "Quantitative Structural Analysis of Dispersed Vanadia Species in  $\text{TiO}_2$  (Anatase) Supported  $\text{V}_2\text{O}_5$ ," J. Catalysis, 134, pp. 479-491 (1992).
56. A. Muan, "Equilibrium Relations in the System  $\text{NiO-TiO}_2$  in the Temperature Range  $1300^\circ$  to  $1750^\circ\text{C}$ ," J. Am. Ceram. Soc., 75(6), pp. 1357-1360 (1992).
57. G. Yamaguchi, and T. Tokuda, "Some Aspects of Solid State Reactions between Oxides," Bull. Chem. Soc. Jpn., 40, pp. 843-851 (1967).
58. S.-W. Ho, J. M. Cruz, M. Houalla, and D. M. Hercules, "The Structure and Activity of Titania Supported Cobalt Catalysts," J. Catalysis, 135, pp. 173-185 (1992).
59. J. L. Look, and C. F. Zukoski, "Alkoxide-Derived Titania Particles: Use of Electrolytes to Control Size and Agglomeration Levels," J. Am. Ceram. Soc., 75, pp. 1587-1595 (1992).
60. S. Katayama, and M. Sekine, "Bi-Sr-Ca-Cu-O Superconductive Films Fabricated Using Metal Alkoxides," J. Mater. Res., 6, pp. 36-41 (1991).
61. T. Sugimoto, "Preparation and Characterization of Monodispersed Colloidal Particles," MRS Bull., XIV, pp. 23-27 (1989).
62. R. W. Siegel, and J. A. Eastman, "Synthesis, Characterization and Properties of Nanophase Ceramics," Mat. Res. Soc. Symp. Proc. Vol. 132, pp. 3-14 (1989).
63. J. A. Eastman, Y. X. Liao, A. Narayanasamy, and R. W. Siegel, "Processing and Properties of Nanophase Oxides," Mat. Res. Soc. Proc. Vol. 155, pp. 255-266 (1989).
64. R. W. Siegel, "Cluster-Assembled Nanophase Materials," Annu. Rev. Mater. Sci., 21, pp. 559-578 (1991).
65. P. A. Lessing, "Mixed-Cation Oxide Powders via Polymeric Precursors," Ceram. Bull., 68, pp. 1002-1007 (1989).
66. M. N. Gardos, Hughes Technical Journal No. 5495, pp. 20-25, 31 July 1991; pp. 26-36, 05 May 1992; pp. 37-53, 19 May 1992, pp. 54-58, 30 July 1992.

## **REFERENCES (Con't)**

67. H. M. O'Bryan, Jr., and G. Parravano, "On the Sintering of Single Crystal Rutile," *Mat. Sci. Eng.*, 1, pp. 177-182 (1966).
68. M. Musci, M. Notaro, F. Curcio, C. Casale, and G. DeMichele, "Laser Synthesis of Vanadium-Titanium Oxide Catalysts," *J. Mater. Res.* 7, pp. 2846-2852 (1992).
69. K. Kobayashi, M. Takata, Y. Fujimura, and S. Okamoto, "Investigation of Trapping States in a Nb-Doped Rutile by Admittance Spectroscopy," *J. Appl. Phys.*, 60, pp. 4191-4196 (1986).
70. A. Wold, and K. Dwight, "Preparation and Characterization of Several Conduction Transition Metal Oxides," ONR Contract No. N000 14-86-K-0234, R&T No. 4134005, Technical Report No. 21, Brown University (Dept. of Chemistry), Providence, RI, 24 May 1989.
71. R. W. Rice, "Comment on 'Black Color in Partially Stabilized Zirconia'," *J. Am. Ceram. Soc.*, 74, pp. 1745-46 (1991); also see J. Soria, and J. S. Moya, "Reply to Comment on Black Color in Partially Stabilized Zirconia," *J. Amer. Ceram. Soc.*, pp. 1747-1748 (1991).
72. "Surveyor III Parts and Materials/Evaluation of Lunar Effects", P70-54, Hughes Aircraft Company, Culver City, CA, 22 January 1971.
73. T. E. Tsai, E. J. Friebele, and D. L. Griscom, "Radiation-Induced Defect Centers in Glass Ceramics," *J. Appl. Phys.*, 65, pp. 507-513 (1989).
74. S. B. Ogale, P. G. Bilurkar, N. Mate, S. M. Kanetkar, N. Parikh and B. Patnaik, "Deposition of Copper Oxide Thin Films on Different Substrates by Pulsed Excimer Laser Ablation," *J. Appl. Phys.*, 72, pp. 3765-3769 (1992).
75. J. Li, G. Vizkelethy, P. Revesz, J. W. Mayer and K. N. Tu, "Oxidation and Reduction of Copper Oxide Thin Films," *J. Appl. Phys.*, 69, pp. 1020-1029 (1991).
76. J. Li, J. W. Mayer and K. N. Tu, "Nucleation and Growth of  $\text{Cu}_2\text{O}$  in the Reduction of  $\text{CuO}$  Thin Films," *Phys. Rev. B.*, 45, pp. 5683-5686 (1992).
77. J. Li, G. Vizkelethy, P. Revesz, J. W. Meyer, L. J. Matienzo, F. Emmi, C. Ortega and J. Siejka, "Influence of Carbon on the Enhanced Oxygen Loss in Copper Oxide Films," *Appl. Phys. Lett.*, 58, pp. 1344-1346 (1991).
78. R. Koka, T. Pitchford, M. Jesh, and D. Edbert, "Studies on Head/Disc Contact Area Increase During Contact Start/Stop and Continuous Drag Testing of Thin Film Discs," *Tribology Trans.*, pp. 1-10 (1993).
79. M. F. Yan, R. L. Barns, H. M. O'Bryan, Jr., P. K. Gallagher, R. C. Sherwood, and S. Jin, "Water Interaction with the Superconducting  $\text{YBa}_2\text{Cu}_3\text{O}_7$  Phase," *Appl. Phys. Lett.*, 51, pp. 532-534 (1987).
80. I. Nakada, S. Sato, Y. Oda and T. Kohara, "Two Crystal Phases in the Superconducting Ba-Y-Cu-O System and Their Reactivity to Water," *Jap. J. Appl. Phys.*, 26, pp. L697-L698 (1987).
81. C.-A. Chang, "Reduced Moisture-Induced Degradation of  $\text{YBaCuO}$  Superconducting Films by Silver and High Deposition Temperatures," *Appl. Phys. Lett.*, 53, pp. 1113-1115 (1988).

## REFERENCES (Con't)

82. M. W. Ruckman, D. H. Chen, A. R. Moodenbaugh, S. M. Heald, S. L. Qiu, C. L. Lin, M. Strongin, D. Nichols, and J. E. Crow, "Modification of  $\text{YBa}_2\text{Cu}_3\text{O}_{(7-x)}$  Ceramics by Adsorbed Water and Other Gases," paper presented at the 4th Northeast Regional Meeting on Processing and Application of High  $T_c$  Superconductors, New Brunswick, NJ, 9 May 1988, prepared in cooperation with Temple Univ., Philadelphia, PA, DE88-011518/BNL-41304, CONF-880519-2 (N88-28140).
83. A. J. Drehman, M. W. Dumais, J. A. Horrigan, G.-C. Wang, and Y. F. Liew, "Near-Surface Stoichiometry of High Temperature Superconducting  $\text{YBaCuO}$  Thin Films," *J. Mater. Res.*, 5, pp. 1392-1396 (1990).
84. P. Svoboda, P. Vasek, O. Smrkova, D. Sykorová, P. Plecháček and M. Nevřiva, "Aging Effects in Ceramic High- $T_c$  Superconductors," *Solid State Commun.*, 75, pp. 331-334 (1990).
85. A. Q. Wang, and T. R. Hart, "Measurement of  $\zeta$  Potential from the Adsorption of Hydronium Ions ( $\text{H}^+$ ,  $\text{OH}^-$ )," *Appl. Phys. Lett.*, 60, pp. 1750-1752 (1992).
86. J. M. Chambers, W. S. Cleaveland, B. Kleiner, and P. A. Tukey, Graphical Methods for Data Analysis, Wadsworth Int. Group and Duxbury Press, 1983.
87. G. S. Rohrer, V. E. Henrich, and D. A. Bonnell, "Structure of the Reduced  $\text{TiO}_2$  (110) Surface Determined by Scanning Tunneling Microscopy," *Science*, 250, pp. 1239-1241 (1990).
88. N. J. Shaw, "Densification and Coarsening during Solid State Sintering of Ceramics: A Review of the Models II. Grain Growth," *Powder Metall.*, 21(5), pp. 31-33 (1989).
89. R. S. Berry, J. Bernholc, and P. Salamon, "Disappearance of Grain Boundaries in Sintering," *Appl. Phys. Lett.*, 58, pp. 595-597 (1991).
90. L. H. Edelson, "The Role of Particle Substructure on the Sintering of Monosized Titania," M.S. Thesis, Lawrence Berkeley Laboratory, U. of Calif. Berkeley, CA, Dec. 1986.
91. H. Hahn, J. Logas, and R. S. Averbach, "Sintering Characteristics of Nanocrystalline  $\text{TiO}_2$ ," *J. Mater. Res.*, 5, pp. 609-613 (1990).
92. W. Wagner, R. S. Averbach, H. Hahn, W. Petry, and A. Wiedenmann, "Sintering Characteristics of Nanocrystalline  $\text{TiO}_2$  - A Study Combining Small Angle Neutron Scattering and Nitrogen Absorption - BET," *J. Mater. Res.*, 6, pp. 2193-2198 (1991).
93. K.-N. P. Kumar, K. Keizer, A. J. Burggraf, T. Okubo, H. Nagamoto, and S. Morooka, "Densification of Nanostructured Titania Assisted by a Phase Transformation," *Nature*, 358, pp. 48-51 (1992).
94. A. P. Reyes, E. T. Ahrens, R. H. Heffner, P. C. Hammel, and J. D. Thomson, "Cuprous Oxide Nanometer for High-Pressure Magnetic Resonance Experiments," *Rev. Sci. Instrum.*, 63, pp. 3120-3122 (1992).
95. Handbook of Chemistry and Physics 64th. Ed. CRC Press, Boca Raton, FL, 1983-1984.
96. Chemical Engineers' Handbook, 4th Ed., McGraw-Hill, New York, 1979.
97. L. Fiderer, "Unique Friction and Wear Tester for Fundamental Tribology Research," in Selection and Use of Wear Tests for Ceramics, ASTM STP 1010, Eds. C.S. Yust, and R. G. Bayer, pp. 24-42 (1988).

### **REFERENCES (Con't)**

98. H. Reiche, W. W. Dunn, and A. J. Bard, "Heterogeneous Photocatalytic and Photosynthetic Deposition of Copper on  $\text{TiO}_2$  and  $\text{WO}_3$  Powders," *J. Phys. Chem.*, 83, pp. 2248-2251 (1979).

**APPENDIX A** - "Summary of Lubricious Oxide Development,  
Job# 915050," Preliminary and Summary Reports,  
CERCOM Inc., Vista, CA, 24 December 1991. and  
04 June 1992.

June 4, 1992

Job #: 915050

Customer: Hughes

Subject: Summary of Lubricious Oxide Development

The Magneli phase, in the form of oxygen-deficient rutile ( $\text{TiO}_{2-x}$ ), exhibits characteristically low and high shear strength. The program is to develop the non-stoichiometric rutile based compound using di-valent and tri-valent cations, such as  $\text{Cu}^{+2}$ ,  $\text{Ni}^{+2}$ ,  $\text{Co}^{+2}$  and  $\text{Fe}^{+3}$ . The powders were formulated to fabricate the high friction  $\text{TiO}_{1.8}$ .

#### PROCESSING

Powders were milled using isopropyl alcohol in neoprene-lined jar with zirconia grinding media. Master blend, containing 50 w/o of  $\text{TiO}_2$  and 50 w/o of doping oxide, were first milled for 24 hours. The master blend was further milled with the balanced  $\text{TiO}_2$  for final composition. After drying and dry milling, the powders were screened through 5 and 30 mesh. The dry powders were loaded into graphite die and hot pressed at  $1100^\circ\text{C}$  under 3000 psi. Some samples also went through further annealing at  $1100^\circ\text{C}$  in air or argon for 48 hours. This program had 4 hot press runs to date. The results are summarize based on the hot press sequence.

#### RESULTS

##### First Hot Press, Run #971

Two  $\text{TiO}_2$  and two  $\text{TiCuO}_x$  were hot-pressed at  $1200^\circ\text{C}$  under 2500 psi. No deformation was observed at  $1200^\circ\text{C}$  and the billets exhibited high density. It was concluded that the material can be hot pressed at lower temperature. The effect of tooling was also studied in this run. One  $\text{TiO}_2$  and one  $\text{TiCuO}_x$  were hot pressed against molybdenum foils. The other set was pressed against graphite foils. Results showed that molybdenum would react with  $\text{TiO}_2$  and  $\text{TiCuO}_x$  and exhibited some reaction zones. Graphite foils were then decided for the future hot pressing.

One  $\text{TiCuO}_x$  sample was annealed in air for 20 hours. Delamination was observed after the annealing. SEM/EDX indicated that high Cu content was found on the delaminated surface.



#### Second Hot Press, Run #988

Two  $\text{TiO}_2$  and two  $\text{TiCuO}_x$  were hot pressed at  $1100^\circ\text{C}$  under 3000 psi. Some gold reaction zones were observed on the edges in  $\text{TiCuO}_x$ . XRD, performed by DSIR, indicated that the as-pressed  $\text{TiO}_2$  had rutile structure. As-pressed  $\text{TiCuO}_x$  contained rutile and copper metal.

Samples of  $\text{TiCuO}_x$  were annealed at  $1100^\circ\text{C}$  for 48 hours in air and in argon, respectively. Delamination and bloating were observed in the air-annealed sample. XRD indicated that this sample had rutile and copper titanate structures. On the other hand, the argon-annealed sample maintained its structural integrity. The annealed sample appeared blue in color. Copper metal droplets were also observed. This argon-annealed sample contained Magneli phase, and had low electrical resistivity, about  $0.046 \Omega\text{-cm}$ . Low resistivity is one of the characteristics for Magneli.

#### Third Hot Press, Run #992

$\text{TiO}_x$ ,  $\text{TiCoO}_x$ ,  $\text{TiNiO}_x$  and  $\text{TiFeO}_x$  were hot pressed at  $1100^\circ\text{C}$  under 3000 psi. Cracks were seen on  $\text{TiFeO}_x$ . The other billets showed good structural integrity. Air and argon annealings were also performed. According to DSIR's XRD analysis, rutile was the major component in all samples. There was some difference in appearance, which was attributed to the concentration of the minor phase. The air annealing did not change the structure too much. However, the argon annealing tended to reduce the doping oxides to their metal state.

As-pressed  $\text{TiCoO}_x$  contained small amount of  $\text{TiCoO}_{1.8}$ . The amount of  $\text{TiCoO}_{1.8}$  was increased slightly after air annealing. Argon annealed sample contained cubic and hexagonal cobalt metal.

As-pressed  $\text{TiNiO}_x$  exhibited a gray to gold color change. XRD indicated the concentration of minor phase,  $\text{NiTiO}_3$ , determined the color of the appearance. Air-annealed sample showed gold appearance with a grey core. XRD showed the presence of  $\text{NiTiO}_3$  in gold body and detected nickel metal in the grey core. The argon-annealed sample showed uniform grey color, and contained rutile and nickel metal.

$\text{FeTiO}_3$  and  $(\text{FeTi})_3\text{O}_5$  were detected in the as-pressed  $\text{TiFeO}_x$ . Air-annealed sample contained rutile and  $(\text{FeTi})_3\text{O}_5$ . The argon annealed sample had rutile,  $(\text{FeTi})_3\text{O}_5$  and iron metal.

#### Fourth Hot Press, Run #995

TiO<sub>2</sub> and TiCuO<sub>x</sub> were hot pressed in this run. The TiCuO<sub>x</sub>, from this run, exhibited some gold patterns, which was attributed to the inhomogeneous powder blending. Argon annealing was performed. Reaction between graphite foil and TiCuO<sub>x</sub> was observed. As-pressed and argon-annealed samples were sent to DSIR for analysis on April 27, 1992.

#### SUMMARY

Magneli phase was successfully fabricated using CuO doping and argon annealing. It appears that the powder processing and annealing are the two major processing issues. The CuO powders were 325 mesh, which corresponds to -45  $\mu$ m. Inhomogeneous dispersion can be expected when this powder was blended with sub-micron anatase TiO<sub>2</sub>. Furthermore, the heat treatment is required to promote the diffusion of doping cations into TiO<sub>2</sub> lattices. It is also shown that the atmosphere plays an important role in the annealing.

#### SPECIMEN FABRICATION

Three sets of SEM triboflats and tribopins were machined, from as-pressed TiO<sub>2</sub>, as pressed TiCuO<sub>x</sub> and argon-annealed TiCuO<sub>x</sub>, respectively. They were delivered to Hughes on June 4, 1992.

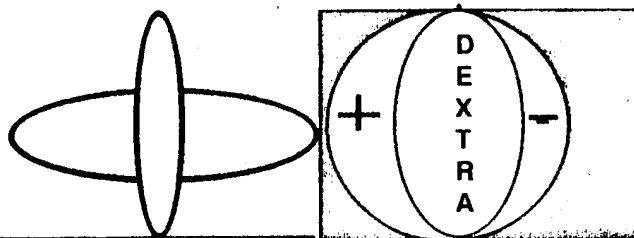
#### FURTHER WORK IN THIS PROGRAM

Additional 500 g of CuO was purchased. Powder process is in progress to formulate the TiO<sub>1.8</sub> as well as TiO<sub>1.7</sub>. Fifth hot press, at 900°C, and two subsequent annealing, at 900 and 1100°C, were also scheduled.

File: HUGHES-F

**APPENDIX B** - R. L. Clarke, Technical Letter to Hughes, HAC  
P.O.# S9-333846-SAA, Dextra Assoc., Orinda, CA,  
9 March 1992, with a Technical Addendum  
DSIR Chemistry, New Zealand, 6 March 1992.

# Dextra Associates



**ELECTROCHEMICAL AND RELATED TECHNOLOGY CONSULTANTS**

**PRINCIPAL CONSULTANT :**

**R.L. CLARKE D.M.S., C.CHEM., F.R.S.C., M.B.I.M.**

74 Muth Drive, Orinda CA 94563. Tel 510 254 2335 Fax 510 254 8451

March 9th 1992

Dr M. N. Gardos  
Materials Technology Laboratory  
Electro-Optical & Data Systems Group  
Bldg. E1 , MS F150. P.O.Box 902  
El Segundo, CA 90245

Dear Mike,

Enclosed are the results of the X ray diffraction analyses of the materials sent recently to DSIR in New Zealand.

One way to use the XRD results in their crude form is to make a transparency on the photocopier and lay the rutlie scan across the other samples. You will see right away that the argon sample is very different from the others. Sharp peaks mean the material is quite crystalline. Many peaks suggest the material is not in a preffered orientation, ie flat plates like playing cards.

The presence of free metallic copper in the air oxidised cases is surprising to me, but quite clearly there. The blackened crystals found in the air treated sample that when smashed reveal white titania? Does this suggest that reduction to Magneli at the surface had occured, are the copper salts a reducing agent or did you use copper metal?

The results form the analysts are reported below and the XRD scans are included.

I checked the samples with a four piont probe, the argon treated sample was the most conductive by a wide margin. About 0.046 ohms cm the other samples had very high resistivities. This might be a big clue.

Sample number	description	xrd result	implication
# 988-2 BN 54/4	titania	rutile titania with some minor reduction peaks	xrd is sensitive enough to pick up very minor changes in stoichiometry
#988-3 Copper doped titania BN 54/2	titania pressed with doped copper	no reaction, rutile identified, minor reduction peaks and copper metal identified some loss of oxygen from metal	no significant change in structure
#988-3 air heat treated S-N100 BN 54/3	rutile with copper dopant, heated in air	rutile predominating with Copper titanates	beads of copper found suggest rutile reduced on the surface. too much oxygen around to maintain Magneli
#988-3 Argon heat treated SN99 BN 54/1	rutile with copper dopant in argon with hydrogen. Reducing conditions	Only small amount of rutile survived. New compound formed suspect $\text{Cu}_3\text{Ti}_6\text{O}_{17}$ by analogy with the vanadium version which is known and has similar XRD.	$\text{Ti}_9\text{O}_{17}$ (copper +titanium) is a Magneli phase. The copper analogue may have been made.  Is it conductive? Is it a lubricous oxide?

The sample #988-3 air treated was examined under the microscope, two phases identified, a black powder that on crushing revealed a white powder. Rutile? Beads of copper appeared as the other phase. XRD identified  $\text{Cu}_2\text{TiO}_5$  and the 3/5 version. Rutile was the major phase present, compare the titania trace of sample #988-2 with #988-3.

The argon treated sample is completely different and shows a new or series of new compounds, well crystalline (good signal), quite unlike the rutile signal of #988-2.

The analysts recommend that the materials are examined in a scanning electron microscope with dedicated chemical analysis facility. The instrument will give semi-quantitative results for elements heavier than neon. That is, it will report on copper and titanium but not oxygen. They can examine the size, shape and crystalline aspect to determine if more than one compound had been formed and carry out point analysis to see if composition varied. The charges would be \$200 per sample including report.

Scanning electron microscope analysis is the first line of defense when there is a problem with interpretation of the XRD result.

The second possibility is that a new unknown compound has been formed( over 60,000 possibilities were matched against the diffraction pattern without success, from JCPDS International Center for Diffraction data file. The analysts want to study the crystal structure using a Rietveld refinement technique. It would be possible to determine the structure ( settle the problem about the relationship to Magneli phases).

Under a secrecy agreement they would like to work on this exciting (academic) problem with you and publish a joint paper, if you agree.

Please let me know how you want to proceed.

Looking at the diffraction patterns it seems quite obvious that the reaction under argon is considerably greater than in the other cases. Certainly significant new peaks have been created. It would be interesting to find out if the insertion of copper into the rutile structure has occurred, something has. The technique suggested by the analysts might be the quickest and smartest way to do it without disclosing what was actually done to prepare the sample until your patents have been filed.

The group in New Zealand have made XRD and crystallography their specialty. Dr Graeme Gainsford and Vaughan White are well known. their offer to elucidate the crystal structure of the new compound using powder diffraction is novel to me. Such studies usually require a single crystal which may be difficult to make.

Interesting stuff, isn't it?

Yours sincerely



Robert Clarke



NEW ZEALAND  
DEPARTMENT OF  
SCIENTIFIC AND  
INDUSTRIAL  
RESEARCH



**Urgent**

Date: 6 March 1992 Time : 1600

No. of Pages (inclusive) 8

Facsimile No.001 415 254 8451

Telephone +64(04)5666919

Facsimile +64(04)5694500

From: Vaughan White

Name: Rob Clarke

Department/Company: Dextra Associates

Dear Rob,

X-ray diffraction analyses of your samples have been run with the following results.

Sample:  $\text{TiO}_2$  #988-2

DSIR Code: BN54/4

The material is rutile with very small peaks around the base of the major peaks which have not been identified. They may be high suboxides or some other indication of slight reduction of the rutile. ( They are in the same general position as the  $\text{V}_3\text{Ti}_6\text{O}_{17}$  displayed with the Ar heat treat pattern. )

Sample:  $\text{TiCuO}_{1.8}$  #988-3 As Pressed

DSIR Code: BN54/2

The material is rutile with copper metal as a minor component. Very small peaks around the base of the major peaks have not been identified. They may be high suboxides or some other indication of slight reduction of the rutile.

Sample:  $\text{TiCuO}_{1.8}$  #988-3 Air heat treat SN-100

DSIR Code: BN54/3

The material is rutile with a small amount of  $\text{Cu}_2\text{TiO}_3$  and possibly a trace of  $\text{Cu}_3\text{TiO}_5$ . Copper metal is present as a trace component and other small peaks could not be assigned. Under low powered microscope there appear to be two phases present but the black particles crush to a white powder. Perhaps the white rutile is covered by a very thin black skin (of blackened rutile?). Beads of copper with a melted appearance are apparent under 40x magnification.

Sample:  $\text{TiCuO}_{1.8}$  #988-3 Ar heat treat SN99

DSIR Code: BN54/1

This sample contains small quantities of rutile and copper metal but consists primarily of a compound ( or compounds ) which is not documented among the 60,000 compounds in the data base issued by the JCPDS International Centre for Diffraction Data. The XRD pattern is displayed with the reference pattern for  $\text{V}_3\text{Ti}_6\text{O}_{17}$  which seems somewhat similar. This could mean that you have made  $\text{Cu}_3\text{Ti}_6\text{O}_{17}$  but this is by no means certain. This is all that we can do for the standard fee but we can pursue the investigation if you are prepared to authorise us to do this. There are two possibilities.

We can examine the material on a scanning electron microscope with a dedicated chemical analysis facility. The instrument available will give semi-quantitative results for elements heavier than neon. (ie. it will analyse Titanium and Copper but not Oxygen ) We would examine the shape and size of the crystals to determine whether there is more than one crystalline phase present, and carry out point analyses to check if the composition varies. Their overall composition can also be determined although this is fairly well established in this case. I have quoted the following charges for our standard qualitative XRD analyses:

US\$95.00/sample (includes local taxes) plus US\$30.00/batch administration and reporting fee

The additional charge for scanning electron microscope examination and analyses is US\$50 for the first sample with a discount for up to eight samples which is negotiable and varies with the job. The maximum charge likely for a batch of eight samples would be US\$300 and it would normally be much less than this. We turn to the scanning electron microscope and analysis facility first when we encounter difficulty with an X-ray diffraction analysis and we would appreciate it if you would authorise us to do this when necessary.

If this material is of sufficient interest to justify further work you may want us to look at a brown patch on the surface which is either copper or a copper compound. It is not representative of the whole and was avoided when the block was sampled for XRD but could be of interest as it may indicate that the copper is segregating during the synthesis.

The second possibility for further work on this sample centres on the likelihood that you have made a new compound and we are prepared to do this at no charge to yourself. As you are probably aware we do more with XRD than identify unknown materials. Our group has an interest in crystallography and our new manager, Dr Graeme Gainsford, has considerable expertise in this area. Using a Rietveld refinement technique it is possible to determine the crystal structure of a compound from the same powder pattern that we collect to identify the compound. It may be possible to apply this technique to your material and we are prepared to try this although it will take some time and may not succeed. The intention would be to publish the results in a joint paper and we would need your permission for this before we could proceed. The method of synthesis would also normally be included in such a publication. What do you say?

An invoice for US\$410 will follow shortly.

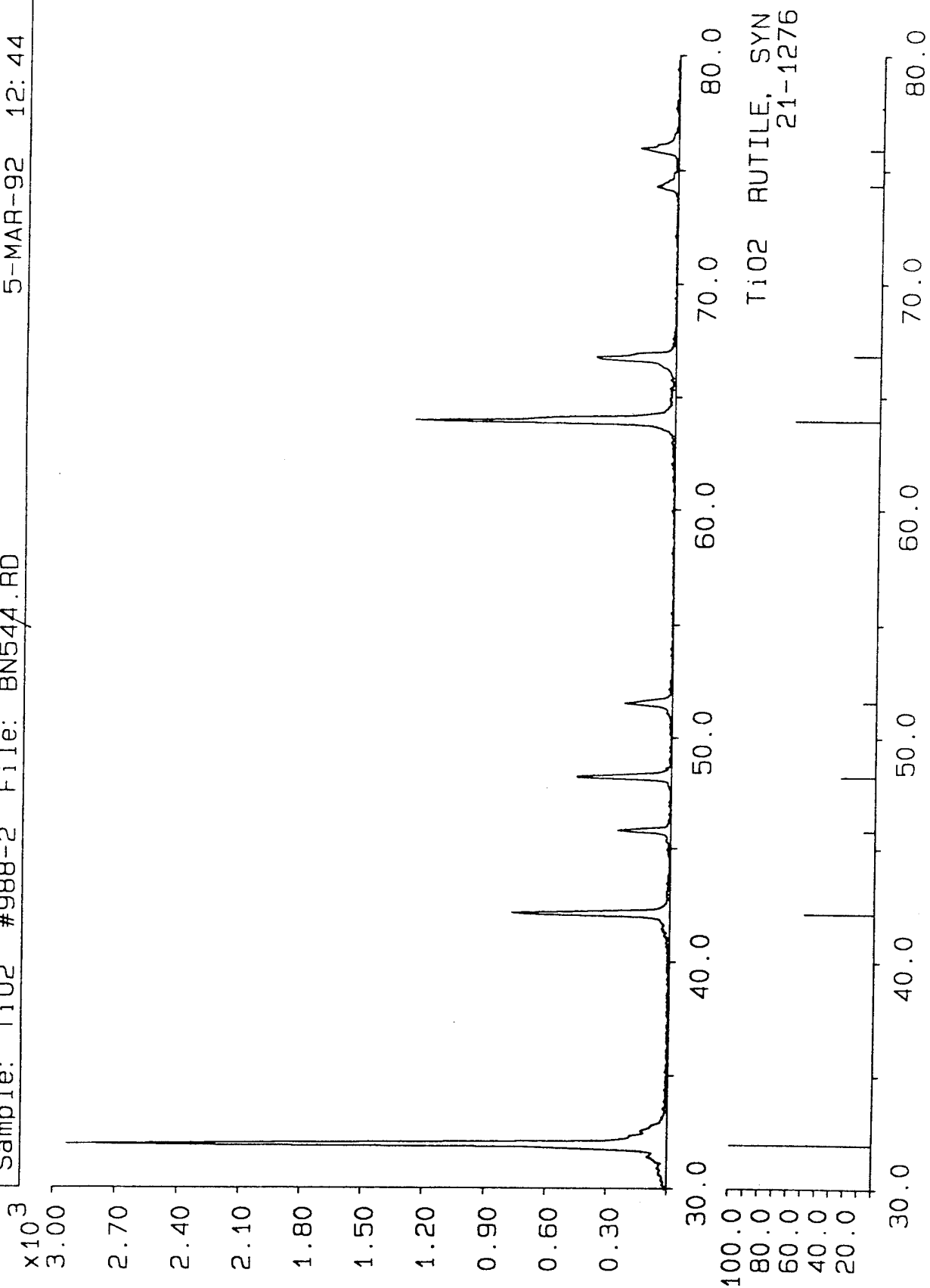
Best wishes



GV White

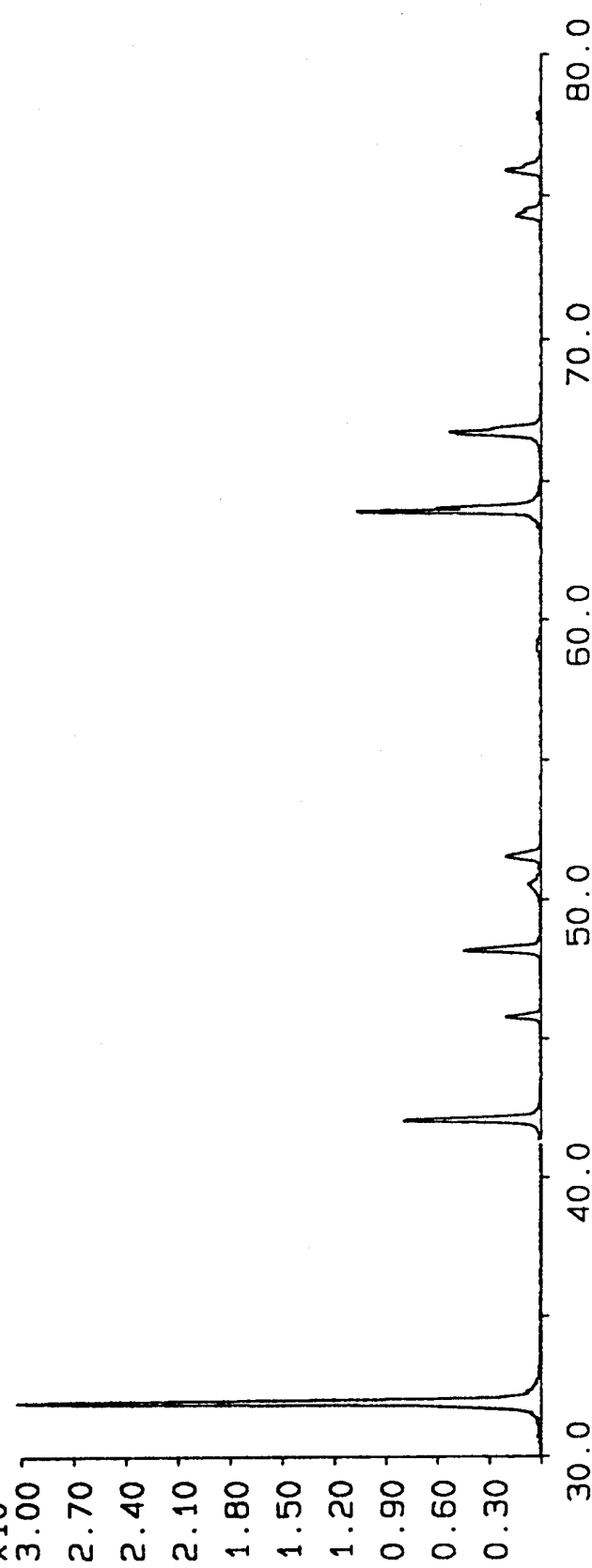


Sample: TiO2 #988-2 File: BN544.RD 5-MAR-92 12:44

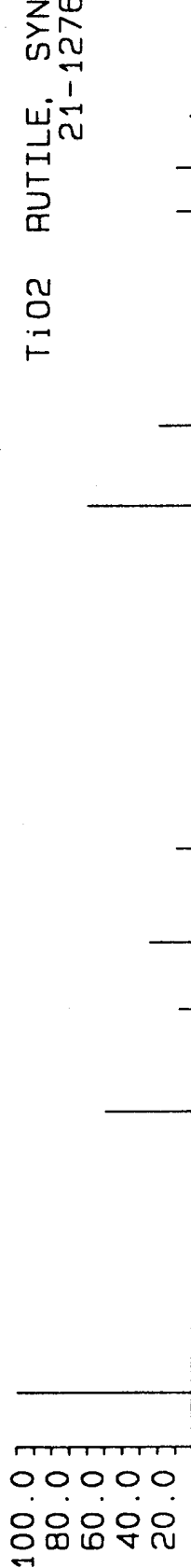


Sample: BN542 File: BN542.RD (11 988-3 as found) 5-MAR-92 09:48

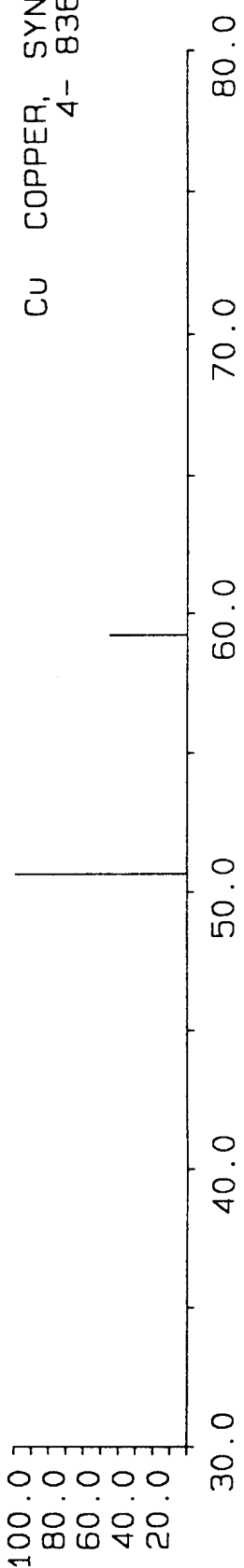
x10<sup>3</sup>

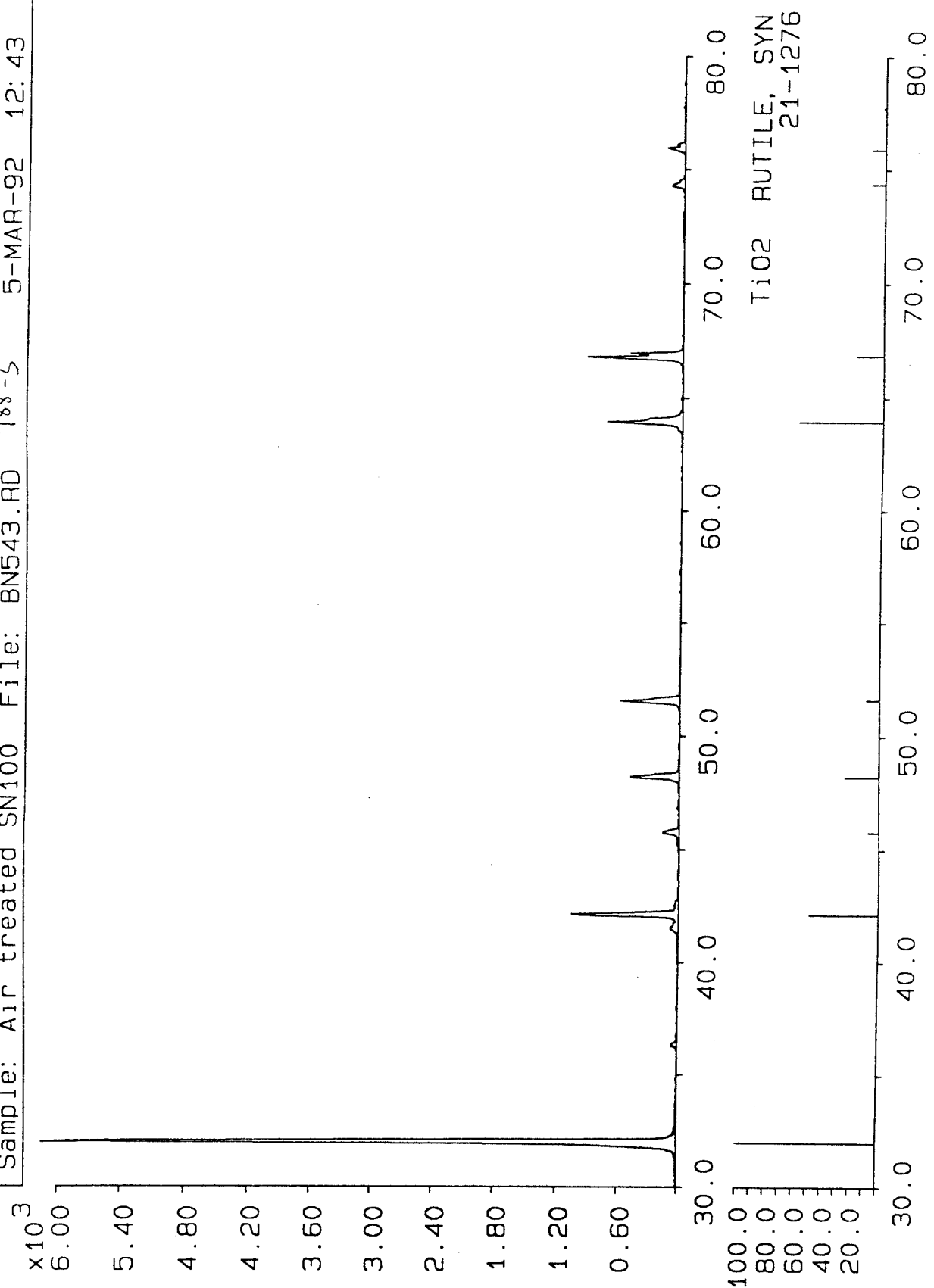


TiO2 RUTILE, SYN  
21-1276

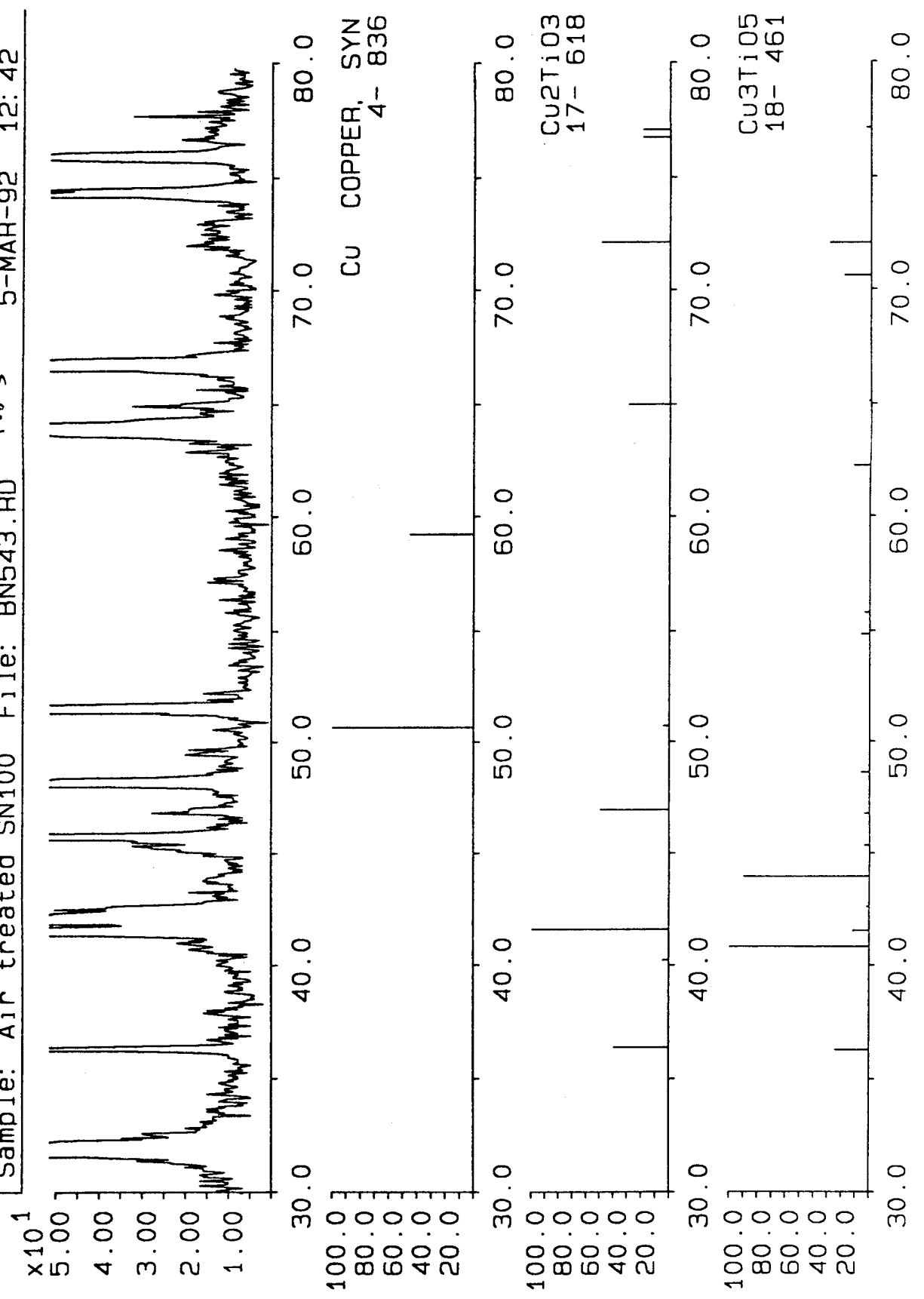


CU COPPER, SYN  
4- 836



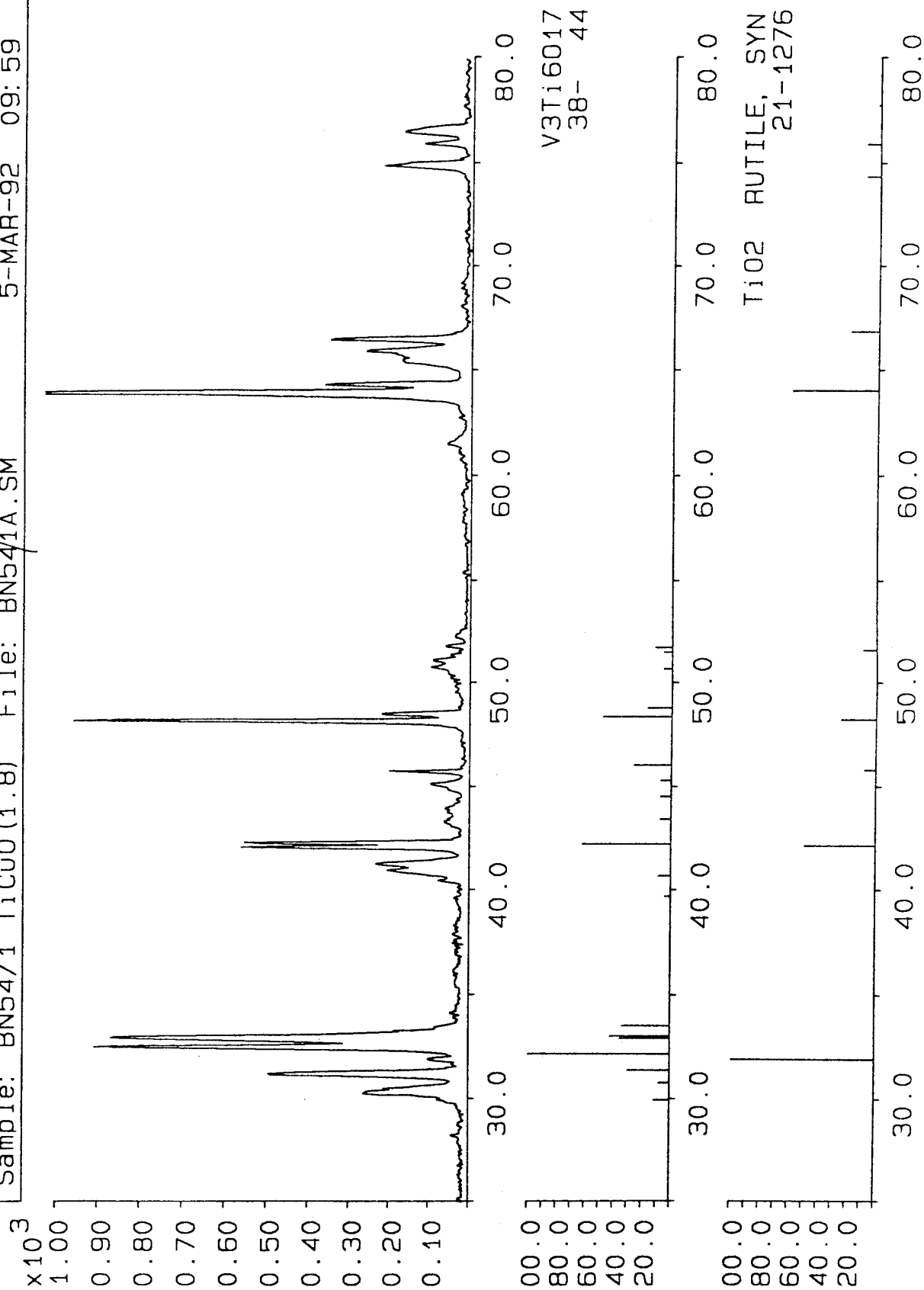


Sample: Air treated SN100 File: BN543.RD 988-3 5-MAR-92 12:42



Argon heat treated BN54/1 (988-3)

Sample: BN54/1 TiCuO(1.8) File: BN54/1A.SM 5-MAR-92 09:59



**APPENDIX C - D. A. Demeo, "Surface Analysis Examination  
of 988-3 Samples," Hughes Interdepartmental  
Correspondence No. 7621.10/09, 14 May 1992.**

# INTERDEPARTMENTAL CORRESPONDENCE

**HUGHES**

TO: M. N. Gardos

C: *Distribution*

DATE: 14 May 1992

REF: 7621.10/09

SUBJECT: Surface Analysis Examination  
of 988-3 SamplesFROM: D. A. Demeo  
ORG: 76-21-10BLDG: EO1 MAIL STA: F150  
LOC: EO PHONE: 66205

## SUMMARY

Three #988-3 samples, as pressed, air heat treated, and argon heat treated, were examined, using ESCA to determine the chemistry in a freshly fractured surface. In addition, the as-pressed material, which showed a banded structure in cross section, was examined in the SEM to determine the materials present in the various bands.

All three samples were basically titania,  $\text{TiO}_2$ , to which copper had been added. Heat, pressure, and then heat treatment under either oxidizing or reducing conditions were employed to incorporate copper into the normal rutile structure. X-ray diffraction, done elsewhere, showed structures which incorporated copper. Here, the object was to examine surfaces and, in the case of the metals, examine the oxidation states present. For the banded cross-section, there were obvious inhomogeneities which needed explanation.

Electron Spectroscopy for Chemical Analysis, or ESCA, is sometimes called x-ray photoelectron spectroscopy (XPS). As the name implies, the analysis is accomplished by bombarding the surface of the sample with x-rays and performing analysis of the kinetic energies of the electrons given up by the sample. Thus what might be called inner electron ionization potentials can be seen. Only electrons from very near the sample surface retain their original energies, so the technique is surface sensitive, and because the ionization potentials would be expected to vary depending on the other electrons around a nucleus, the technique is also valence sensitive.

## 988-3 As Pressed

The cross-sectioned sample is seen in Figure 1. Four distinct areas are seen; (A), a brown layer; (B) a black band; (C) a brown-black-white mixed layer; and (D) a dark area which persists through the thickness. The above letters will be used to designate the various layers. Initially we were going to take Auger spectra of the various layers, but they were insufficiently electrically

conductive. However, there was sufficient conductivity to see differences by scanning electron microscopy (SEM). The four bands, marked with the rasters of higher magnification photos, are seen in Figure 2 (40X). Later, it was found that backscattered electrons (BSE) gave additional contrast and detail to the areas, Figure 3 at 20X, so that additional SEM studies were performed.

Figures 4 and 5, at 200 and 2000X respectively, show area A. There are at least 2 phases present, the matrix represented in gray and the brighter phase. The less numerous darker areas appear to be voids. The gray area appears to be titanium dioxide, without copper, and the bright areas appear to be copper. EDX spectra of these areas are seen in Figures 6 and 7. An overall EDX spectrum shows all three elements, copper, oxygen, and titanium.

This is not the case in area B. This narrow band, seen in SEM in Figures 8 and 9, shows virtually no void or bright areas, and just a hint of grain structure, better seen in secondary electron (SE) mode than in BSE. The overall EDX spectrum, Figure 10, shows only  $\text{TiO}_2$ .

Area C shows many more void and bright areas. Large patches of the copper phase exist, and voids are numerous, as seen in the BSE photos, Figures 11 and 12. The heights of the copper peaks in this region were about 4X that seen in area A, normalizing on the most intense peak, that of titanium K-alpha.

Finally, area D shows both bright areas and voids in BSE photos, Figures 13 and 14. In this area, however, the voids appear more like crevices, and delineation between grains is more pronounced than in area B. Copper barely shows in the EDX spectrum, Figure 15. It is perhaps a factor of 3 or 4 lower than in A, and greater than an order of magnitude less than C. With some contrast between grains, however, there may be some indications of the incorporation of copper into the titanium dioxide.

ESCA spectra were run in the following manner: the samples were fractured to expose a surface across the thickness (approximately 0.2 inches) of the original block. The samples were introduced into vacuum and spectra run as fractured, at a sputter depth of approximately 10 Angstroms, where the surface carbon has hopefully been reduced without causing chemical changes from the argon ion sputtering, and finally at a depth of approximately 30 Angstroms. Survey spectra were run, followed by detailed spectra of carbon, oxygen, titanium, and oxygen. Here the intent was to use covalent carbon 1s as a standard, shifting it to 285.0 eV binding energy, and then using the same shift, which corrects for work functions and sample charging, to move the



detail spectra of the other elements to their "true" positions. Then an evaluation of the valence states of these elements could be made, based on others' data of binding energy vs. valence state.

The survey spectrum of the as-pressed sample is seen in Figure 16. In it are seen the spectra of the various elements present. Some "ghost" peaks are seen as well. These are caused by some aluminum radiation in the magnesium source, and show up as peaks shifted some 233 eV to lower binding energy from the positions of large, sharp peaks in the spectrum. The broader peaks labelled as an element plus 3 capital letters, such as O KVV, are Auger peaks which also are seen. The magnesium x-ray source was chosen to minimize interferences between the various ESCA and Auger peaks, which move, depending on the source used.

The major elements seen in the as-pressed sample were carbon, oxygen, and titanium, with only a trace of copper. Other trace elements seen were sodium and potassium. Detailed spectra of the major elements were run, along with copper. The results of all spectra are seen in Table I. Titanium is clearly oxide, with a binding energy of 459.0 eV. The "nominal" positions of metallic and oxidized titanium are 453.8 and 458.5 eV, respectively, but those are referenced to carbon at 284.6 eV; at a 285 eV reference, these become 454.2 and 458.9. Similarly, copper (2p<sub>3/2</sub>) was seen at 933.65 eV, Figure 17. Correcting to a 285 eV carbon reference, copper metal should be at 932.8 and oxide at 934.0 eV. On the other hand, there were no copper shake-up peaks in evidence. These peaks are typically seen for oxides, but not for the metallic state. Perhaps the best explanation is that copper is in an oxidized state, or positive valence, but is not fully cupric oxide.

Similar spectra were run after a nominal 10 Angstrom removal of material by argon ion sputtering. At this point carbon was seen to decrease somewhat, and titanium and copper increased. Generally some increase (0.3-0.4 eV) was seen in the detail spectra, and the titanium peaks began to split, so that two sets of peaks were needed to fit them. This is likely the result of a forced reduction by the argon ion beam, and not a property of the sample. The slight shift may have resulted from some carbide formation also because of the ion beam, as I increased the shift applied to all spectra slightly (0.2 eV), to move carbon to the correct position. However it was apparent that there was reduced titanium present. Compare Figures 18 (titanium with no sputtering) and 19 (after sputtering). These data are also summarized in Table I.

An additional 20 Angstroms (30 total) of material was removed, and the process repeated. Carbon was further reduced in intensity, and the ratio of reduced titanium

slightly increased (from about 80/20 ox/red to about 75/25).

An argon heat treated sample were analyzed similarly, with quite similar results. Potassium was not seen in this sample, and sodium was at lower concentration. Carbon decreased faster--there was less carbon at -10 Angstroms than at -30 for the first sample. The shifts seemed a little higher as well. Perhaps the covalent carbon reference was not quite as good. The results for the argon heat treated sample are seen in Table II.

Finally, an air heat treated sample was examined. The amounts of copper seen were higher by a quite noticeable amount in the survey spectra. Carbon decreased quickly, as in the case of the argon heat treated sample. Chemical shifts again appeared slightly higher, but probably due to less covalent carbon available as a reference. The spectra as received and at -10 Angstroms were entirely similar to the earlier samples. No spectra were run at -30 Angstroms. The results are summarized in Table III.

#### CONCLUSION

The sample examined by SEM/EDX appeared quite heterogeneous, with varying amounts of titanium oxide, copper, and voids in the various areas. The various colors of the different areas are not accounted for by this simplistic picture, however.

ESCA was used to analyze supposedly identical samples with varying heat treats. The percentage copper appeared to vary by about an order of magnitude, however. It is to be noted that there was little difference in chemical shift or in apparent chemistry of the various elements present. The shift differences seen are generally accounted for because of the use of the internal carbon as a binding energy reference. Carbide formation, as from the sputtering, may have confused the position of the truly covalent carbon. The fact that all of the binding energies appeared to rise slightly with sputtering gives evidence of this.

The copper seen in the fractured samples appears to be in an oxidized state. It is not, however, cupric oxide, which shows strong additional peaks, called shake-up peaks, in its ESCA spectrum.



D. A. Demeo  
Sr. Scientist

Table I

ESCA Data, Sample 988-3 As Pressed

Atomic Concentration

	C	O	Ti	Cu	Other
As Frac.	42	41	15	0.7 Na	0.5; K 0.9
-10	34	46	18	0.6 Na	0.5; K 1.0
-30	17	58	23	1.0 Na	0.5; K 0.8

Chemical Shifts

As Frac.	Ti	459.0
	O	530.3 (80%); 532.0 (20)
	Cu	933.65--no shake-up peaks
-10	Ti	459.4 (80); 457.7 (20)
	O	530.7 (85); 532.3 (15)
	Cu	933.9--no shake-up peaks
-30	Ti	459.4 (75); 457.5 (25)
	O	530.9 (85); 532.6 (15)
	Cu	933.9--no shake-up peaks

Table II

ESCA Data, Sample 988-3 Argon Heat Treated

Atomic Concentration

	C	O	Ti	Cu	Other
As Frac.	31	49	18	1.2	Na 0.2; N 0.7
-10	13	61	25	1.3	Na 0.04; N 0.1
-30	10	62	27	0.95	

Chemical Shifts

As Frac.	Ti	459.2; less than 10% @ 457.2
	O	530.5 (84); 532.2 (16)
	Cu	933.8--no shake-up peaks
-10	Ti	459.3 (65); 457.6 (35)
	O	530.8 (88); 532.6 (12)
	Cu	933.8--no shake-up peaks
-30	Ti	459.5 (58); 457.8 (42)
	O	530.95 (83); 532.5 (17)
	Cu	933.9--no shake-up peaks

Table III

ESCA Data, Sample 988-3 Air Heat Treated

Atomic Concentration

	C	O	Ti	Cu	Other
As Frac.	41	40	13	3.7	Na 2.0; Si 0.4
-10	16	56	21	6	Na 0.25

Chemical Shifts

As Frac.	Ti	459.3
	O	530.55 (75); 532.2 (20); 534.0 (6)
	Cu	934.2--no shake-up peaks
-10	Ti	459.4 (81); 457.7 (19)
	O	531.1 (80); 532.7 (16); 534.3 (4)
	Cu	934.3--no shake-up peaks

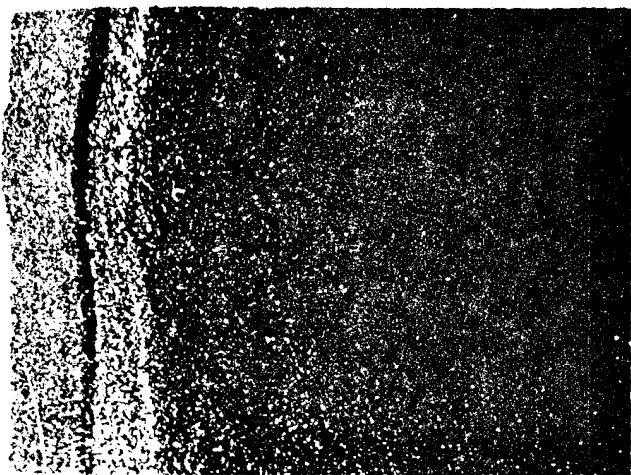


Figure 1. Optical photo of as-pressed sample showing colored bands, 8X.

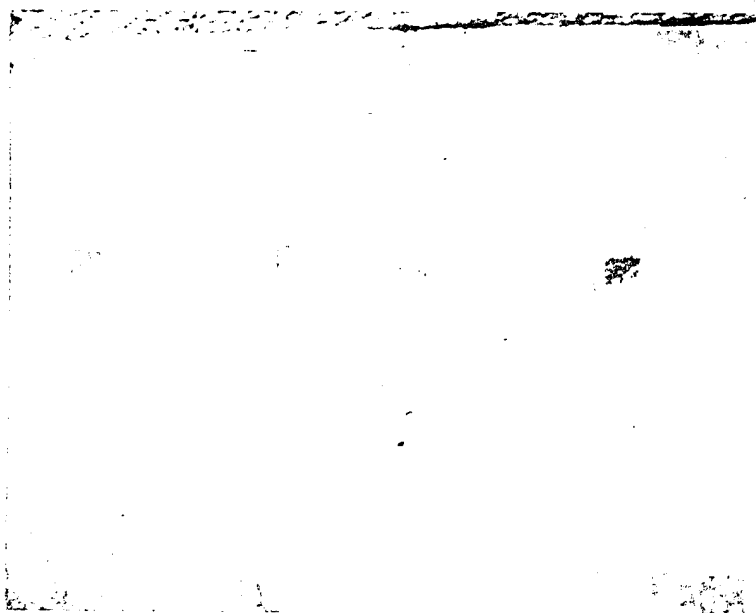


Figure 2. As-pressed sample seen in SEM, 40X. Small rectangles denote bands A-D discussed in text.



Figure 3. Same sample, now carbon coated for conductivity and seen in BSE mode, shows greater amount of contrast, 20X.

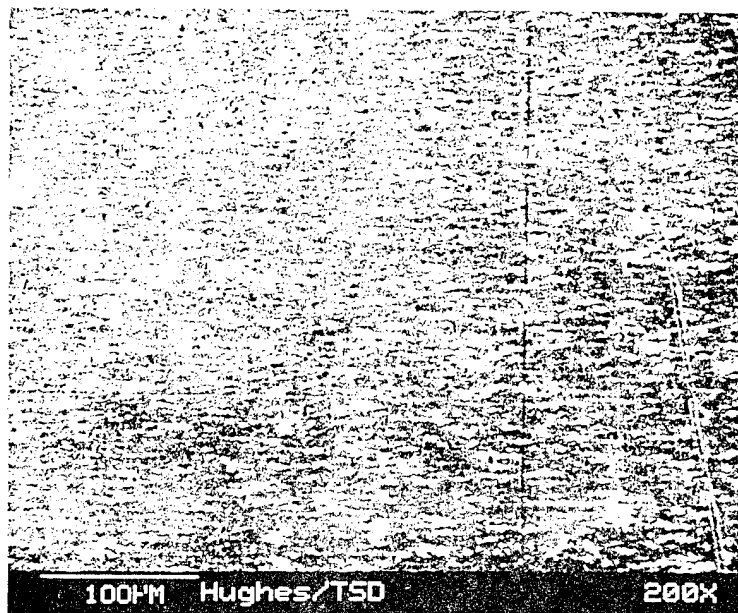


Figure 4. Area A, seen in BSE at 200X, shows finely dispersed (copper) particulates in (TiO<sub>2</sub>) matrix.

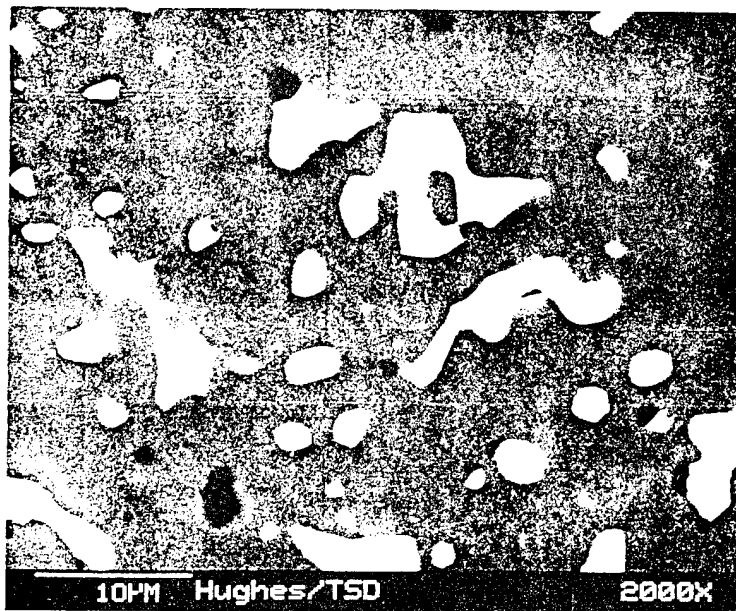


Figure 5. Area A, seen at higher magnification (2000X), shows fine dispersion of copper and population of tiny voids, which appear to have mostly rounded edges.

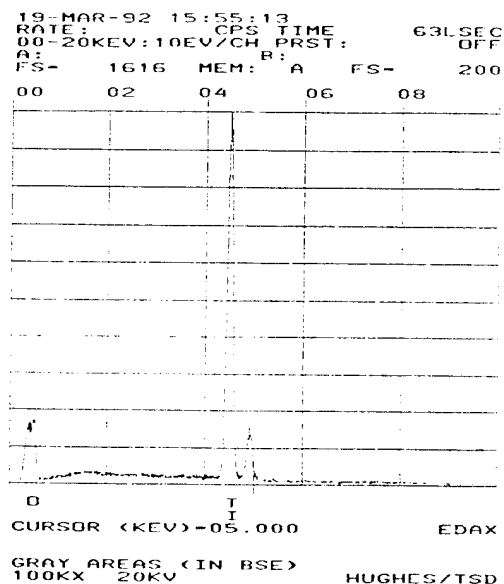


Figure 6. EDX spectrum (20 kV) of matrix area in area A and other areas. Titanium and oxygen are elements seen.

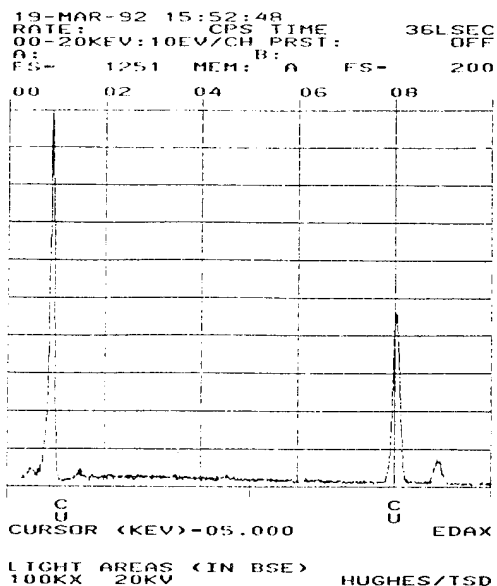


Figure 7. EDX spectrum (20 kV) of bright inclusion seen in as-pressed sample. Material appears to be copper, without oxygen or other elements.

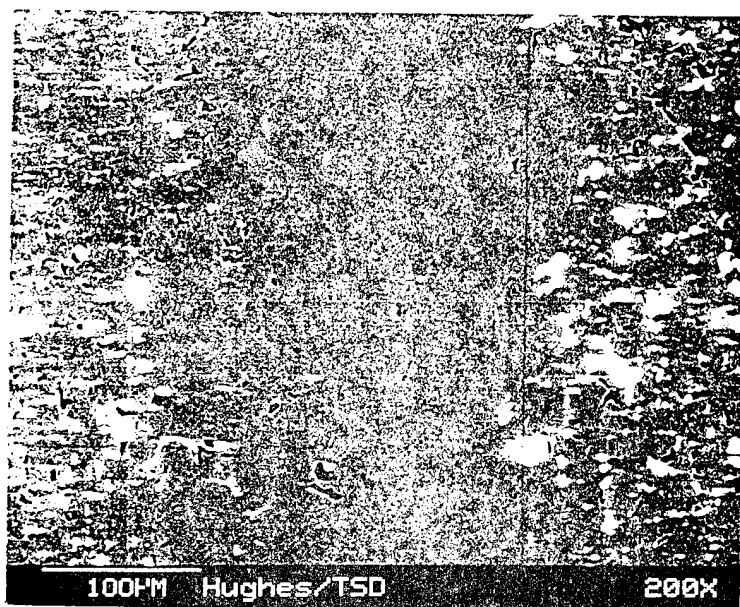


Figure 8. Area B, seen in BSE at 200X, seems to be rather uniform, without many bright inclusions or voids.



Figure 9. Detail of area B, SE mode at 2000X, shows some tiny bright areas and voids, but also shows slight contrast variations between grains.



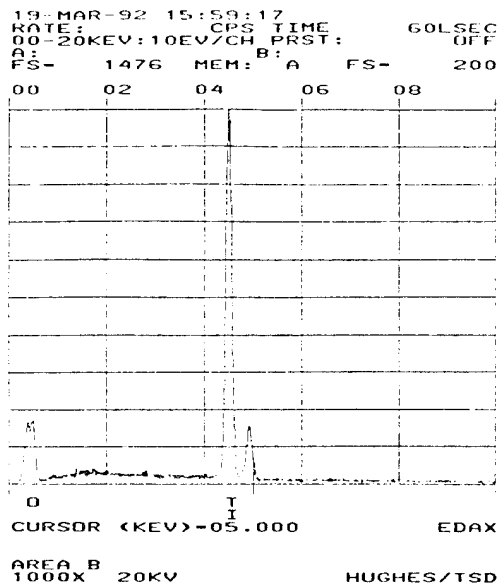


Figure 10. EDX spectrum of area B, taken at 20 kV, shows only titanium and oxygen. Copper from tiny inclusions is lost in noise level.

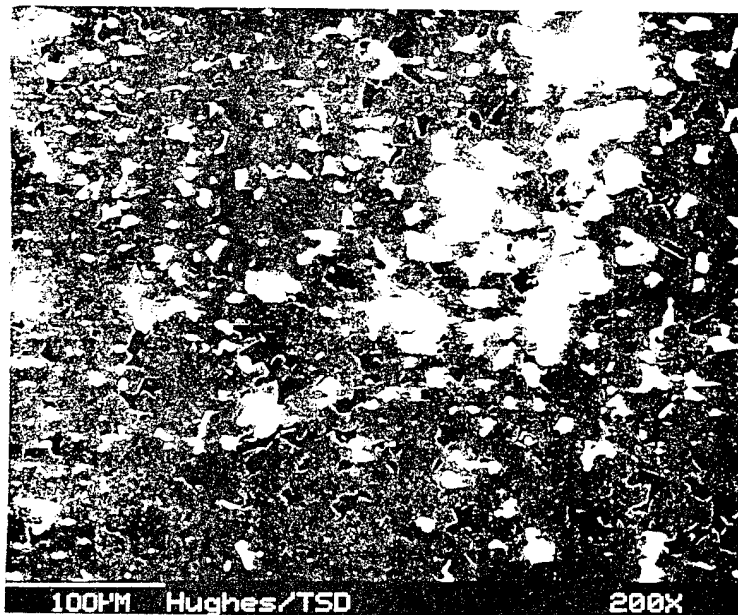
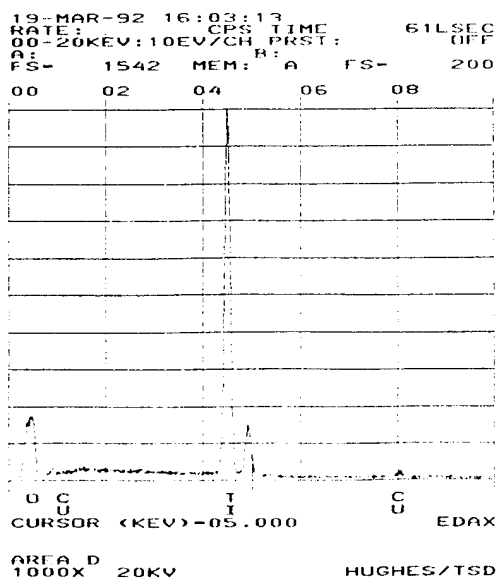
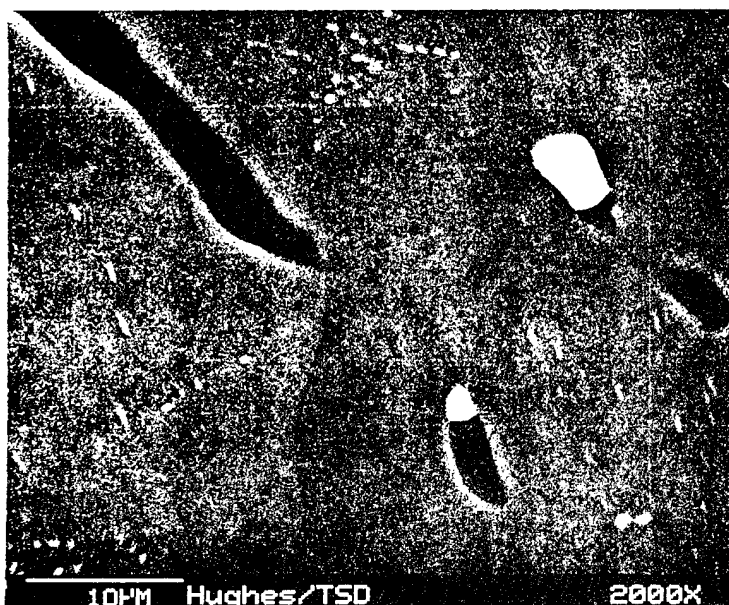
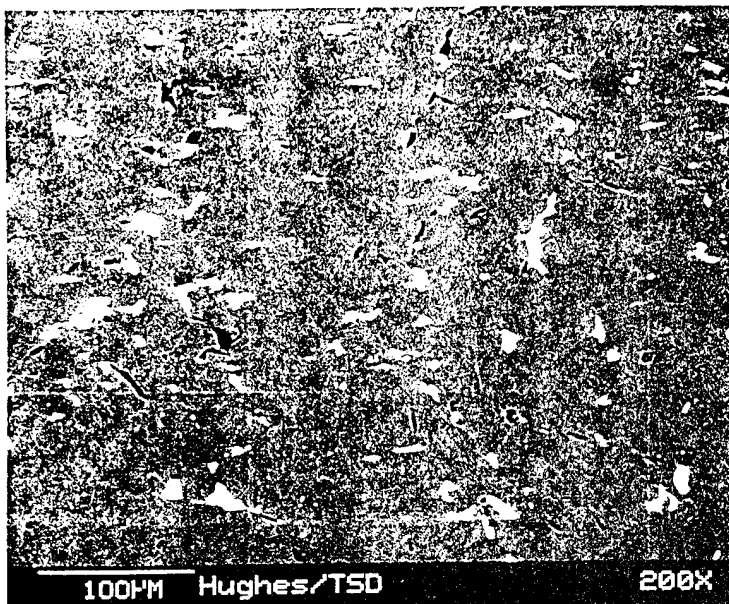


Figure 11. Area C, seen in backscatter mode at 200X, shows large (agglomerated?) inclusions, numerous voids.



Figure 12. Detail of area C, also BSE at 2000X, shows typical particle and void size for comparison with A and B.



ESCA SURVEY 3/20/92 ANGLE= 45 deg ACO TIME=31.19 min  
 FILE: TICU2 TICU01.8 #988-3 AS PRESSED  
 SCALE FACTOR= 5.715 k c/s, OFFSET= 1.176 k c/s PASS ENERGY= 89.450 eV mg 400 W

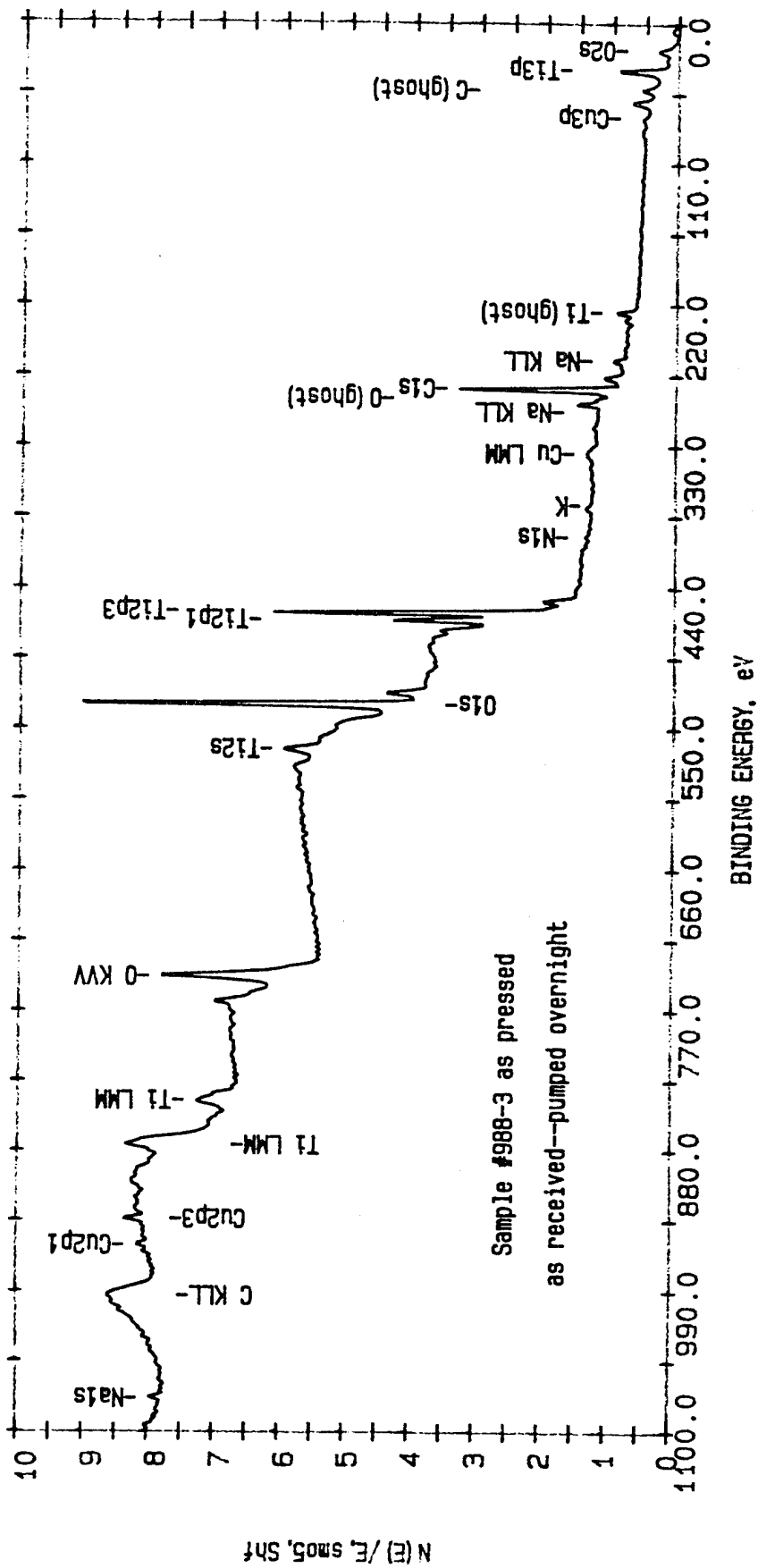


Figure 16. ESCA survey spectrum of freshly fractured sample 988-3 as pressed. Spectrum is "as fractured", that is, without any argon ion sputtering.

ESCA CURVE FIT 3/20/92 ANGLE= 45 deg ACQ TIME=73.21 min  
 FILE: Curve\_Fit TICU01.8 #988-3 AS PRESSED  
 SCALE FACTOR= 0.133 k c/s, OFFSET= 0.000 k c/s PASS ENERGY= 71.550 eV mg 400 W

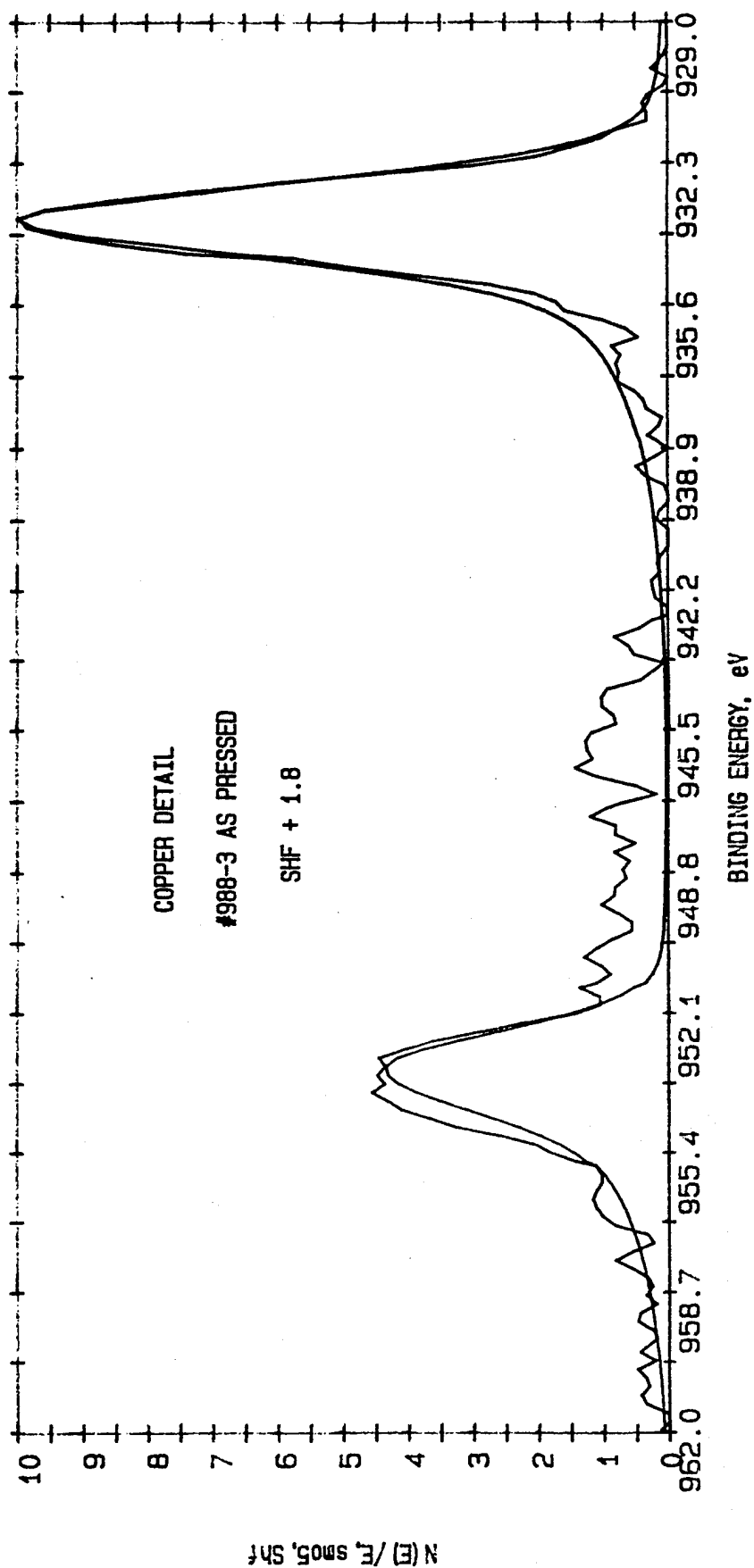


Figure 17. Copper detail ESCA spectrum, as pressed sample as fractured. No shake-up peaks, characteristic of copper oxide, are seen.

ESCA CURVE FIT 3/20/92 ANGLE= 45 deg ACQ TIME=11.02 min  
 FILE: Curve\_Fit TICU01.8 #988-3 AS PRESSED  
 SCALE FACTOR= 2.468 k c/s, OFFSET= 0.000 k c/s PASS ENERGY= 71.550 eV mg 400 W

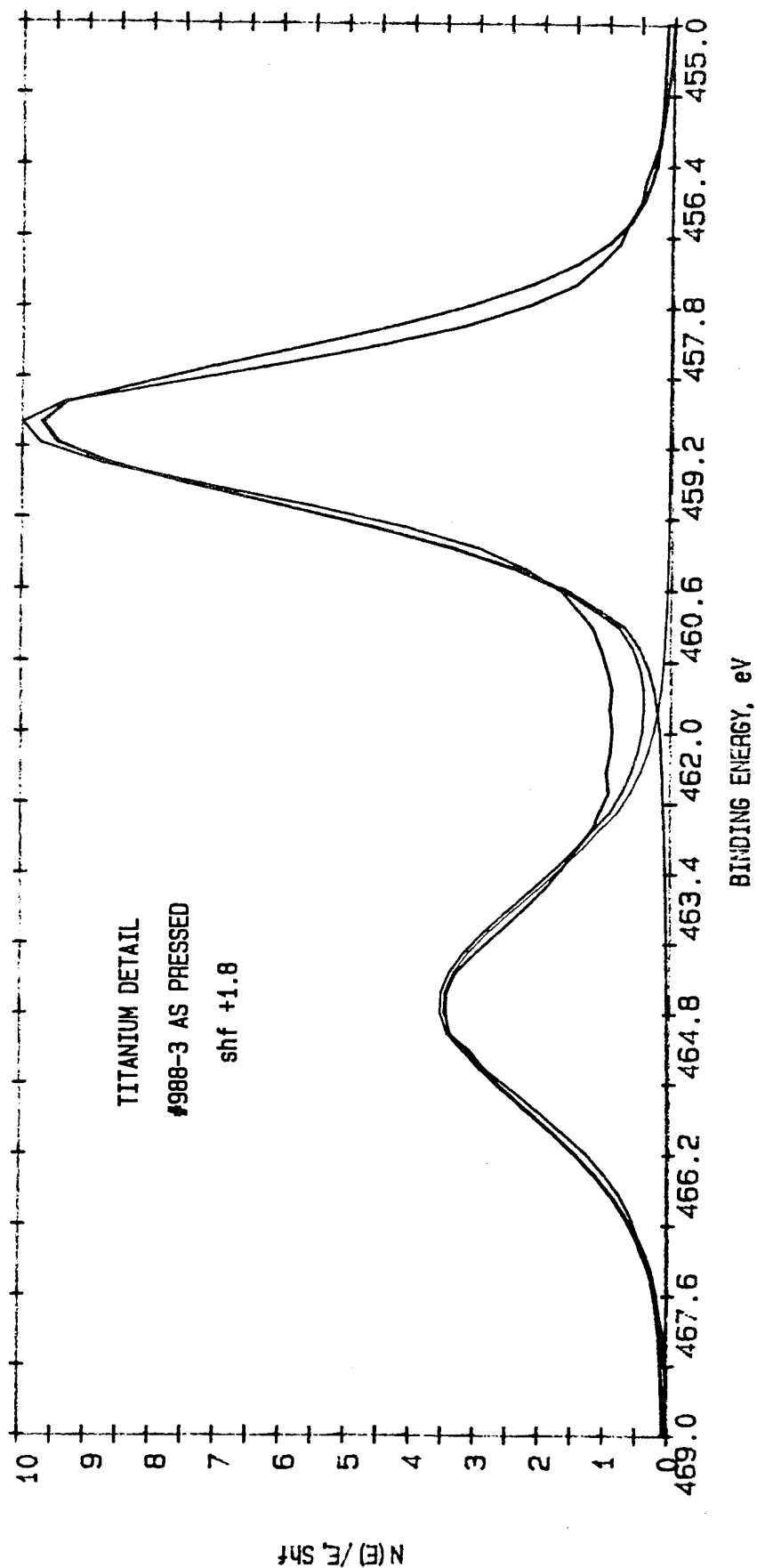


Figure 18. Detail ESCA spectrum for titanium, as pressed sample as fractured. A single pair of peaks with a 2:1 ratio was used for fitting.

ESCA CURVE FIT 3/20/92 ANGLE= 45 deg ACQ TIME=10.71 min  
 FILE: Curve\_Fit TICU01.8 #988-3 AS PRESSED  
 SCALE FACTOR= 3.814 k c/s, OFFSET= 0.000 k c/s PASS ENERGY= 71.550 eV mg 400 W

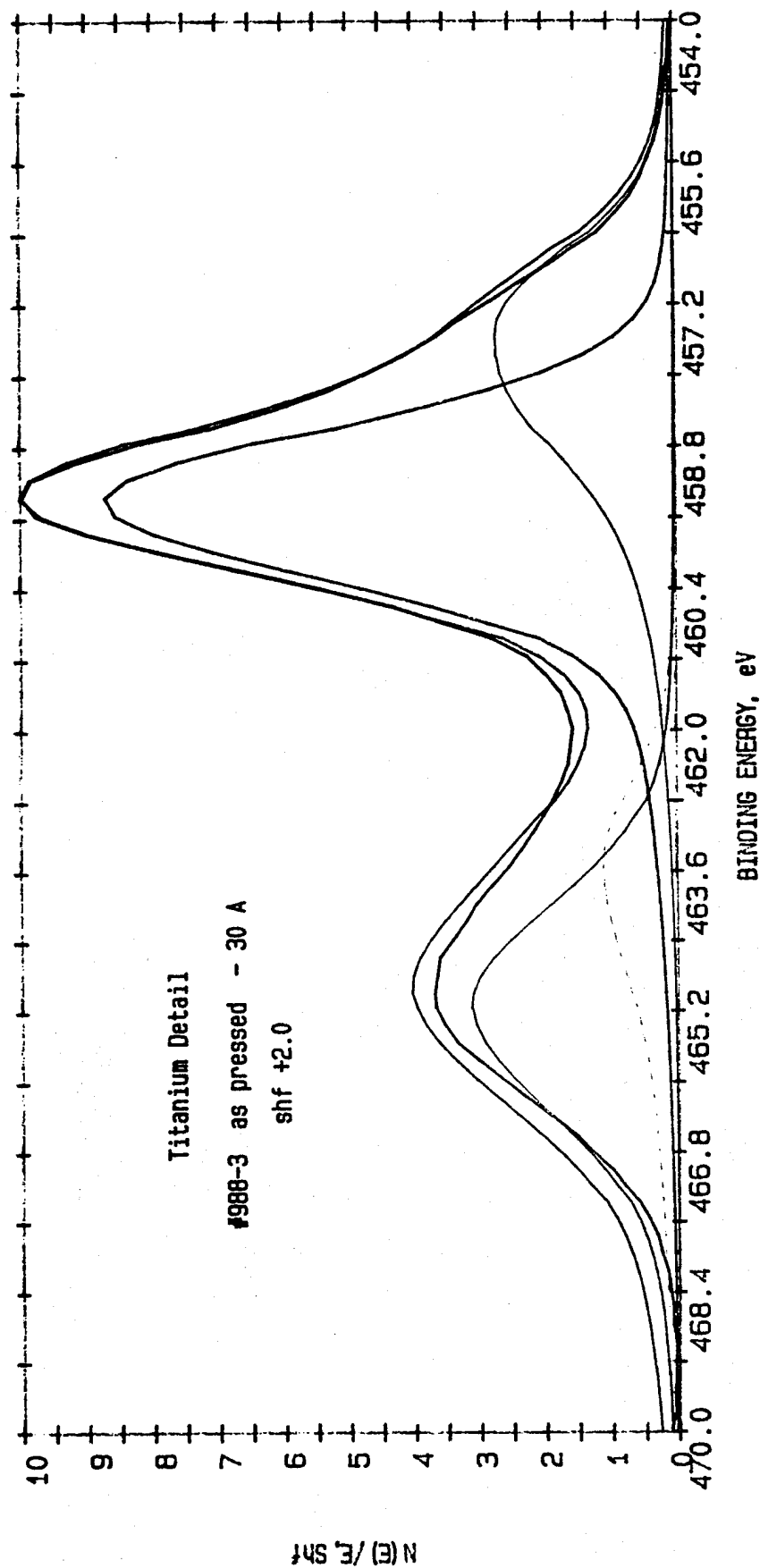


Figure 19. Detail titanium ESCA spectrum of same sample after sputtering. Low energy "tail", just barely evident before, has increased, so that two pairs of peaks, representing two different chemical states, are needed for fitting spectrum.

ESCA SURVEY 3/20/92 ANGLE= 45 deg ACQ TIME=31.19 min  
 FILE: TICU2 TICU01.8 #988-3 AS PRESSED  
 SCALE FACTOR= 5.715 k c/s, OFFSET= 1.176 k c/s PASS ENERGY= 89.450 eV mg 400 W

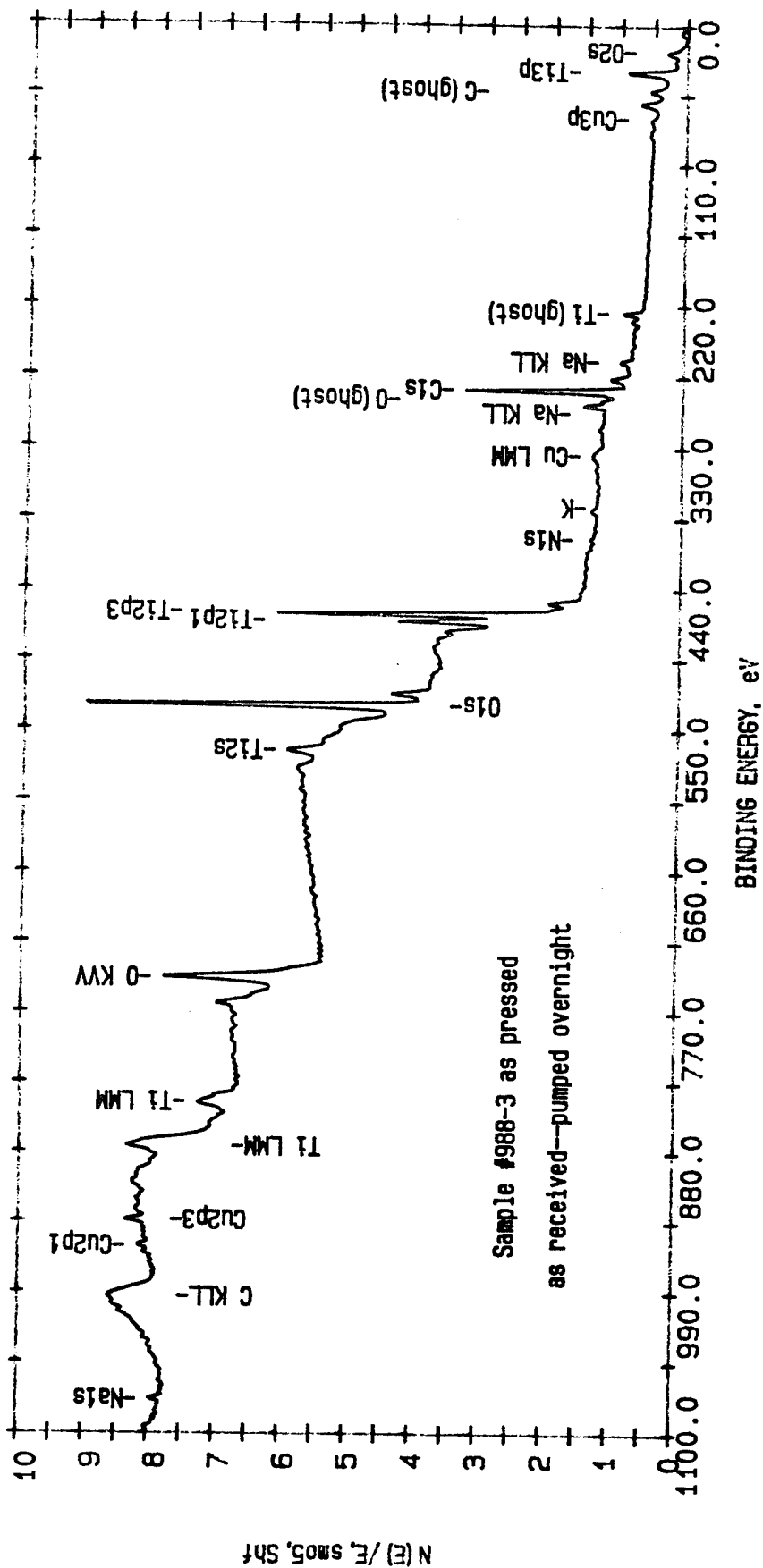


Figure 16. ESCA survey spectrum of freshly fractured sample 988-3 as pressed. Spectrum is "as fractured", that is, without any argon ion sputtering.

ESCA CURVE FIT 3/20/92 ANGLE= 45 deg ACQ TIME=73.21 min  
 FILE: Curve\_Fit TICU01.8 #988-3 AS PRESSED  
 SCALE FACTOR= 0.133 k c/s, OFFSET= 0.000 k c/s PASS ENERGY= 71.550 eV Mg 400 W

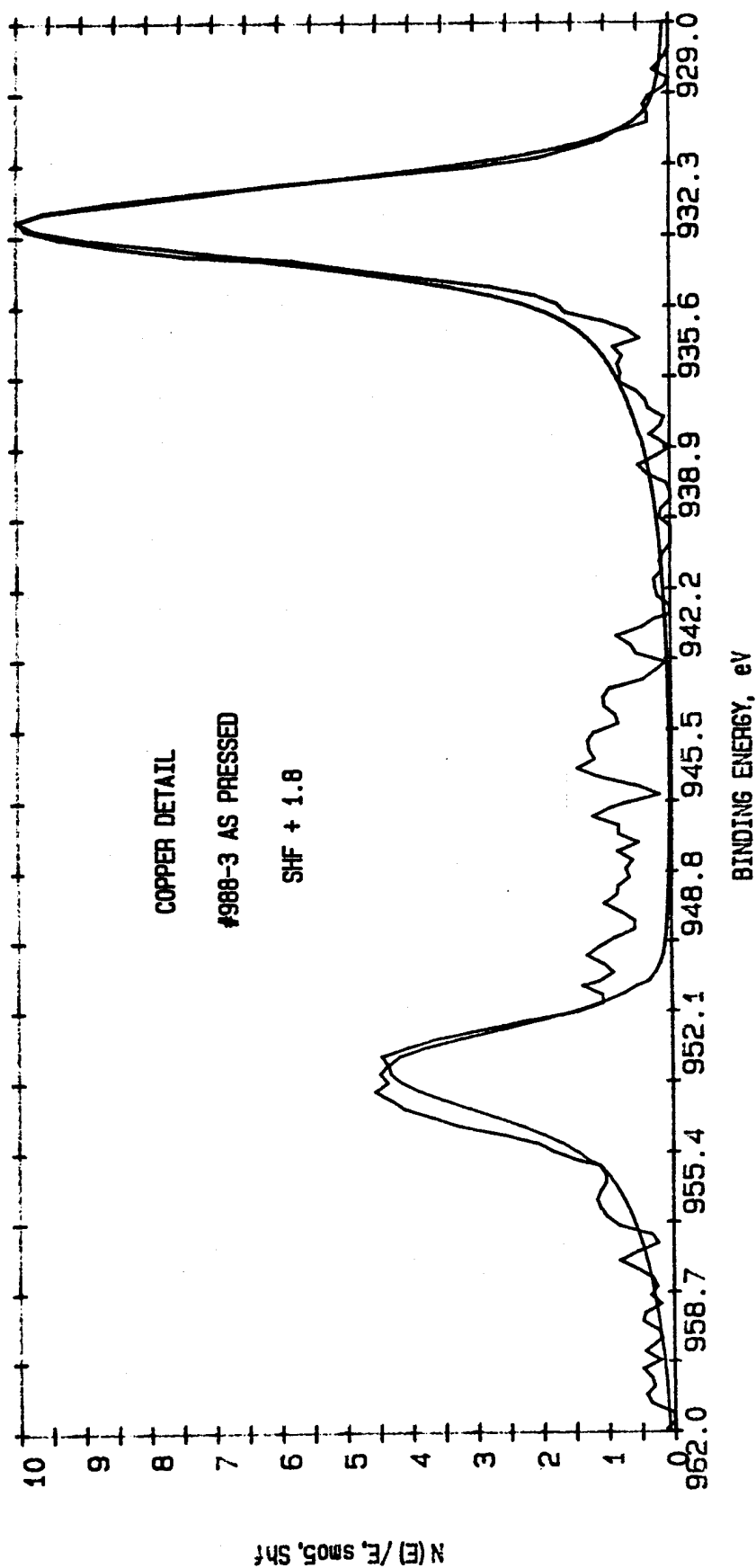


Figure 17. Copper detail ESCA spectrum, as pressed sample as fractured. No shake-up peaks, characteristic of copper oxide, are seen.



ESCA CURVE FIT 3/20/92 ANGLE= 45 deg ACQ TIME=11.02 min  
 FILE: Curve\_Fit TICU01.8 #988-3 AS PRESSED  
 SCALE FACTOR= 2.468 k c/s, OFFSET= 0.000 k c/s PASS ENERGY= 71.550 eV mg 400 W

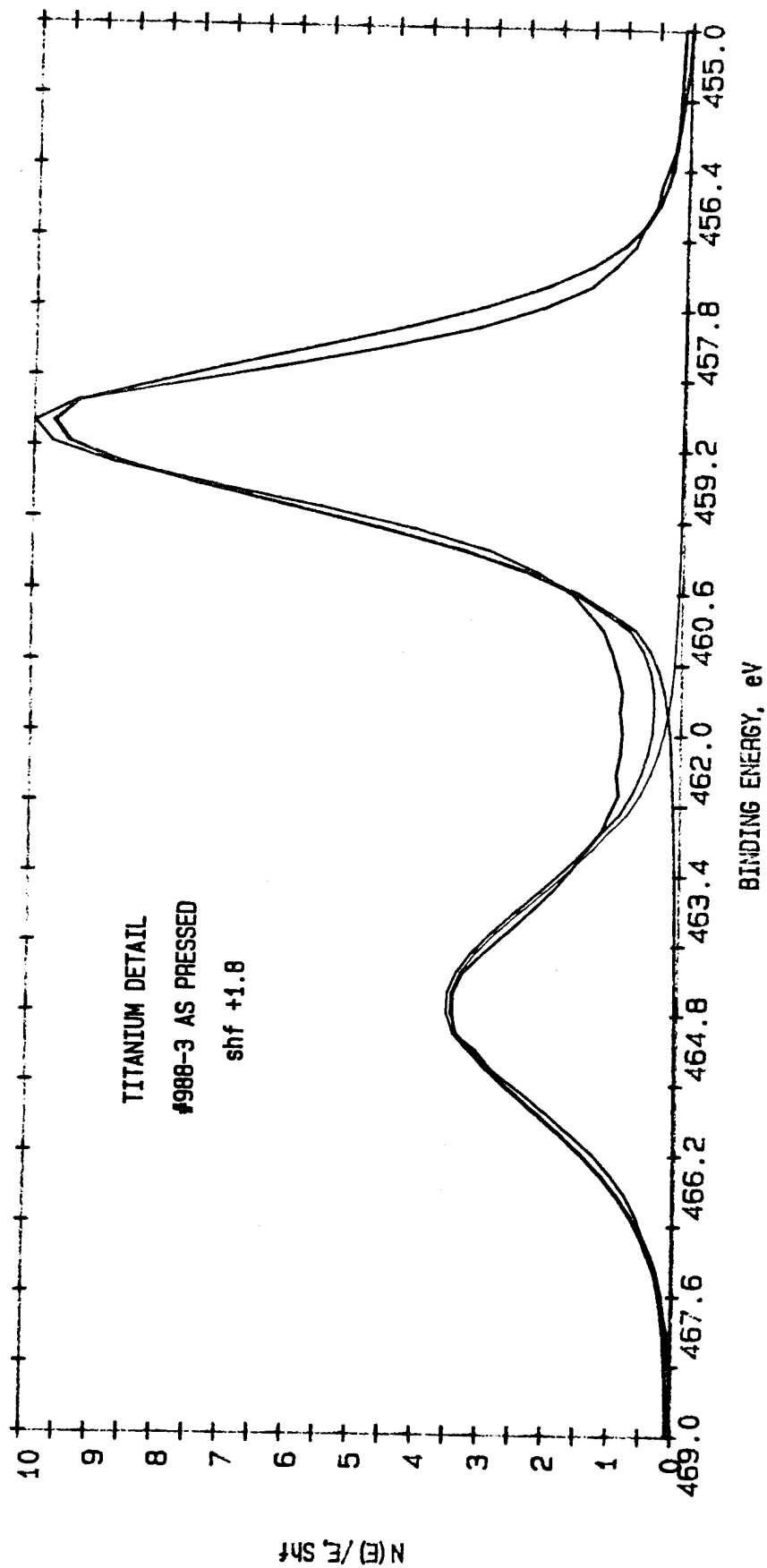


Figure 18. Detail ESCA spectrum for titanium, as pressed sample as fractured. A single pair of peaks with a 2:1 ratio was used for fitting.

ESCA CURVE FIT 3/20/92 ANGLE= 45 deg ACQ TIME=10.71 min  
 FILE: Curve\_Fit TICU01.8 #988-3 AS PRESSED  
 SCALE FACTOR= 3.814 k c/s, OFFSET= 0.000 k c/s PASS ENERGY= 71.550 eV mg 400 W

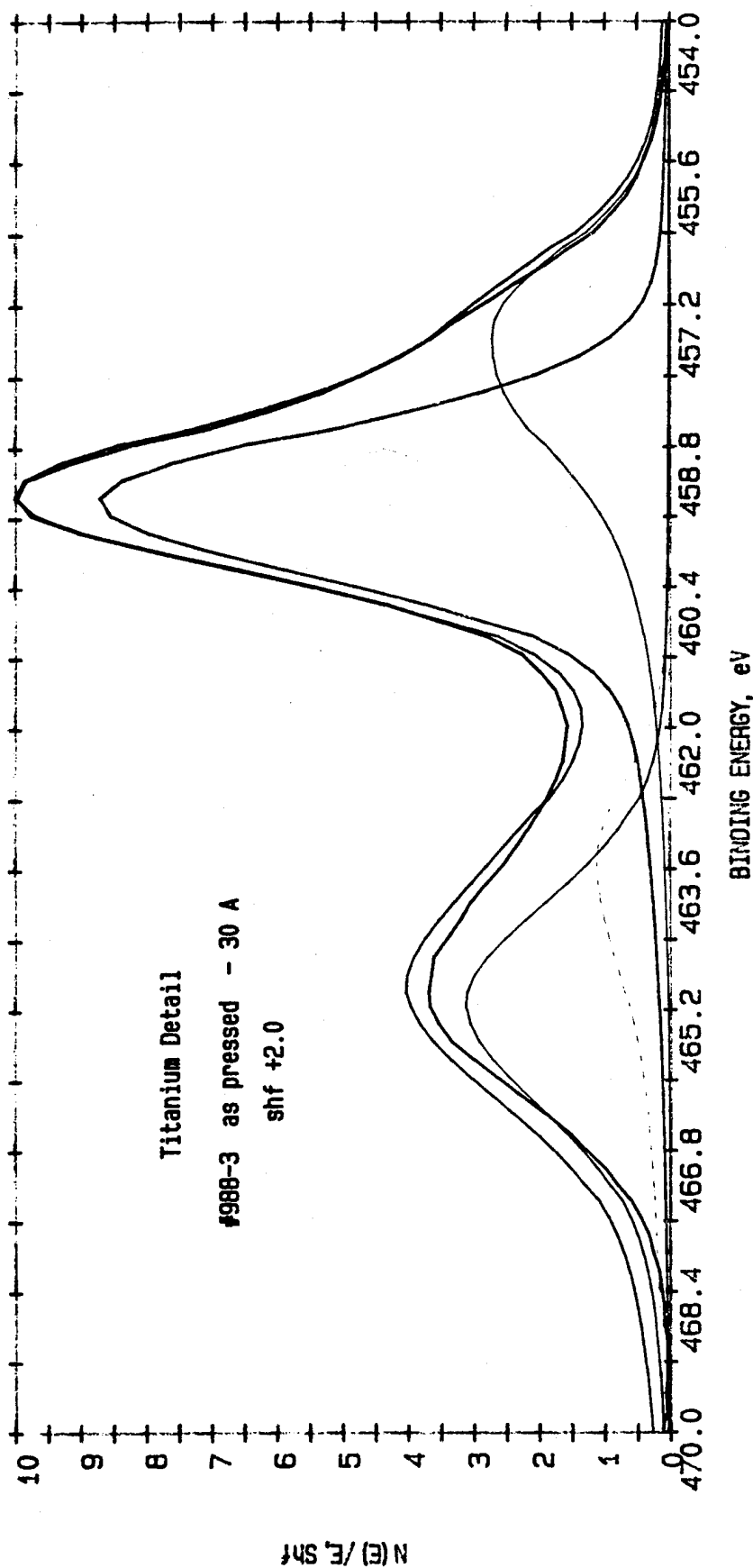


Figure 19. Detail titanium ESCA spectrum of same sample after sputtering. Low energy "tail", just barely evident before, has increased, so that two pairs of peaks, representing two different chemical states, are needed for fitting spectrum.

***APPENDIX D*** - R. L. Clarke, Technical Letter to Hughes HAC  
P.O.# S9-333846-SVX, Rev. A, Dextra Assoc.,  
Orinda, CA, 20 October 1992.

DEXTRA ASSOCIATES  
74 MUTH DRIVE  
ORINDA CA 94563  
TEL 510 254 7642 FAX 510 254 8451

UK ADDRESS: 6 DEW POND ROAD, FLITWICK BEDS MK45 1RT  
TEL/FAX 011 44 525 718 463

Dr. M.N. Gardos  
Hughes Aircraft Company  
Materials and Technology Laboratory  
Technology Support Division  
Electro-Optical & Data Systems Group  
Bldg E1 MS F150  
P.O.Box 902, El Segundo CA 90245

20/10/92

Dear Mike,

Herewith my write up on the experiments carried out on the samples 988-3,  $\text{Ti Cu O}_{1.8}$ , as pressed 988-2 which was titania and 988-3  $\text{Ti Cu O}_{1.8}$  which was heat treated in Argon. Note that 988-3 argon treated was electrically conductive having a resistivity at room temperature of the order of  $6 \times 10^{-2}$  Ohms cm.

The actual measurements by four point probe at room temperature were as follows:

argon treated	titania	as pressed	standard
BN 54-1	BN 54-2	BN 54-4	Ebonex™
0.056	infinite	infinite	0.006
0.050	..	..	0.006
0.049	..	..	0.004
0.058	..	..	0.0057
0.055	..	..	0.0061
0.0539	..	..	0.0058

These measurements vary as the four point probe is moved over the surface. We would expect a higher resistance for Magneli materials towards  $\text{Ti}_6\text{O}_{11}$  similar to BN54-1.

#### X-Ray Diffraction experiments

The x-ray diffraction studies were carried out using a Philips PW 1700 X-ray Powder Diffractometer using cobalt radiation. The scan was run with the beam moving through an arc from  $4-80^\circ 2\theta$  ( $2\theta$ ) at a speed of 0.025 degrees/second and a sampling interval of  $0.030^\circ 2\theta$  ( $2\theta$ ). The diffraction pattern was determined from the scintillations counted and transposed to a chart forming the patterns shown in figures 1-5 The JCPDS ICDD ( Joint Committee on Powder Diffraction Standards International Centre for Diffraction Data) inorganic database was searched up to and including set 39 using the Sandman routine in the Philips APD 1700 software. Small quantities of rutile

(titania) and copper metal were identified from this database but the main component was not.

Note the Sandman system is programmed to search and match up stored data with the sample to find a match. This is superior to the old method of matching up charts and trying to discount minor peaks due to background noise.

The XRD reference pattern for  $V_3Ti_6O_{17}$  seems somewhat similar. This could mean that  $Cu_3Ti_6O_{17}$  but this is by no means certain. The data does suggest a compound very similar to  $V_3Ti_6O_{17}$  but with a change in unit cell, probably because of a change in composition but this is speculation. A subsequent manual search up to set 41 was also unsuccessful but no attempt has been made to determine whether other cations are present.

I will send hard copies of the diffraction data by DHL along with the samples. Meanwhile I have asked (by telephone last night) for more work to try to identify further what you have made in sample BN 54/1 what you identify as 988-3 Argon heat treated SN-99, copper doped titania.

Vaughan White is very keen on carrying out more work on the sample to help understand the result and to support your work.

Note the new address and fax numbers for the changed DSIR.

The New Zealand Institute for Industrial Research and Development  
Gracefield Research Centre, Gracefield Road  
P.O. Box 31-310, Lower Hutt  
New Zealand      telephone 011 64 4 569 0185   fax 011 64 4 569 0117

I hope this helps. Let me know if you need any more.

Kind regards

Yours sincerely



Robert L. Clarke.

**APPENDIX E** - R. L. Clarke, Technical Letter to Hughes, HAC  
P.O.# S9-333846-SVX, Rev. A, Dextra Assoc.,  
Orinda, CA, 30 November 1992, with a Technical  
Addendum from DSIR Chemistry, New Zealand,  
16 November 1992.

REPORT OF THE XRD AND CONDUCTIVITY OF THE SIX SAMPLES RECEIVED DURING NOVEMBER 1992

I have tabulated the results from Cercom and Industrial Research (IR) together into a table. It seems from the results that weight loss corresponds to the formation of copper metal and Magneli phases. The XRD results contain so many Magneli phases in samples 1, 2 & 3 it is possible that the Cu Ti Oxides are present but masked. The weight loss numbers for the samples 5 & 6 would indicate that Magneli phases should be formed but the XRD does not confirm this.

SAMPLE	APPEARANCE after hot press	Appearance after heat treatment	XRD REPORT	Conductivity and comments
988-1, 1100 Hot Press. SN-164 1100 Heat Treat for 48 hrs A/Hydrogen. bulk Sample 12242a -1 by IR notification	Uniform dark blue	Small amount of Cu beads on surface. 1.7% weight loss See additional notes on XRD of various parts	Area not delaminated contained several Magneli phases, Ti5O9, Ti6O11, Ti8O17 major components, Cu metal and other oxide phases	Conductivity by 4 point probe at IR reported as 4460 S.m <sup>-1</sup> . Consistant with formation of Magneli phases. Resistivity by Dextra about 30 millohm cm
1009-1 900C Hot Press. SN-164 HT 1100 for 48 hrs. 12242b-2 by IR notification	Gray in center Pink white on surface	Many copper beads Sample blistered Weight loss 5.28%	Magneli phase titanium oxides. Ti 5 to Ti 8 XRD dominated by copper metal (caused bloating?)	Resistivity by Dextra about 20 millohm cm to 60 millohm cm
1009-2 900 HPress SN-164 1100 Heat treatment for 48 hrs. Sample 12242c -3 by IR notification	Gray in center Pink/white on surface	Many copper beads Sapmle blistered 7.6% weight loss	XRD pattern simillar to pattern above (12242b) but more Ti 5O9 (consistant with wieght loss)	Resistivity by Dextra about 10-80 millohm cm most conductive but also most variable
988-1 1100 HPress SN-172 900HT for 48 hrs. Sample 12242d -4 by IR notification	Uniform dark blue	No copper beads, sample uniform dark blue in color 0.12% wt loss (suggests no Magneli formed)	Sample mainly rutile titania and copper metal No copper titanium oxides found. some CuO	Conductivity by IR reported as 610 S.m <sup>-1</sup> Resistivity 200 millohm cm i.e least conductive Consistant with weight loss

Sample	Apperance after hot pressing	Appearance after Heat treatment	XRD report	Conductivity and comments
1009-1, 900 Hot Press. SN172 900 HT for 24 hrs. Sample 12242e -5 by IR notification	Gray in center, Pink/white on surface	a red skin on one face, delamination close to surface 3.78% wieght loss	Same XRD pattern as 12242d above i.e rutile titania with increasing amounts of copper metal	Conductivity by IR 3400 Sm <sup>-1</sup> Resistivity by Dextra measured at 30-35 milliohm cm
1009-2 900 Hot PressSN172 900 Heat treat 900 for 48 hrs. Sample 12242f -6 by IR notification	Gray in Center Pink/white on surface	Red skin on one face Delamination close to surface 5.81% wieght loss	Same XRD pattern as 12242d with increased copper metal	Conductivity by IR 2190 Sm <sup>-1</sup> Resistance by Dextra found to be 5 millohm cm more consistant with weight loss than XRD result
Sub samples of interesting sections of main samples	XRD	Comments		
Laminated layer of sample 12242a	mixture of Magneli phases not in same ratio as bulk and dominated by copper	Layer maybe close to carbon or graphite oven platten giving increased reduction	flake from laminate	graphite by XRD
Flakes of 12242e&f	same as bulk	if no Magneli phases are formed reduction in weight is due to copper metal losing oxygen?		

I plan to send samples of Ebonex to IR to calibrate against their results as some inconsistency has occurred in the differences in findings with respect to conductivity and resistivity. Do you want the samples 2 & 3 testing at IR?

Notice the lack of Magneli materials when heat treatment is 900C and yet there is a significant weight loss? The weight loss plus Magneli structures in the first three samples are compatible with the conductivity measurements. You know much more about what has gone on here, We may have missed the new copper titanium compounds as the presence of some mant Magneli phases makes interpretation of the back ground difficult.

Let me know if you want further tests done on these samples or do you prefer to have them sent back to you.



THE NEW ZEALAND INSTITUTE FOR INDUSTRIAL RESEARCH AND DEVELOPMENT  
FORMERLY PART OF DSIR

To: Mr R L Clarke  
Organisation: Atraverda Ltd  
Fax no.: 0044 525 840 667  
From: Vaughan White  
Date: 16 November 1992



Gracefield Research Centre  
Gracefield Road  
PO Box 31-310  
Lower Hutt  
New Zealand  
Phone: +64-4-569 0035  
Fax: +64-4-566 6004

No. of Pages (inclusive): 7

Your six sample slabs were received on 6 November. They were registered with job number 12242 and the following table identifies each individual sample:

12242A	1	TiCuO <sub>1.8</sub>	#988-1	1100°C HP	SN164	1100°C HT 48hrs Ar/H <sub>2</sub> bulk
12242B	2	TiCuO <sub>1.8</sub>	#1009-1	900°C HP	SN164	1100°C HT 48hrs Ar/H <sub>2</sub> bulk
12242C	3	TiCuO <sub>1.8</sub>	#1009-2	900°C HP	SN164	1100°C HT 48hrs Ar/H <sub>2</sub> bulk
12242D	4	TiCuO <sub>1.8</sub>	#988-1	1100°C HP	SN172	900°C HT 48hrs Ar/H <sub>2</sub> bulk
12242E	5	TiCuO <sub>1.8</sub>	#1009-1	900°C HP	SN172	900°C HT 48hrs Ar/H <sub>2</sub> bulk
12242F	6	TiCuO <sub>1.8</sub>	#1009-2	900°C HP	SN172	900°C HT 48hrs Ar/H <sub>2</sub> bulk

The samples were all examined under low power (40x) optical microscope and then analysed by X-ray Diffraction (XRD) for crystalline components. The XRD analyses were performed on small samples cut from the corner or edge of the sample slabs and ground to a fine powder. Features such as laminated areas were also sampled and analysed in the same manner. The major part of the slab was left intact in each case.

The conductivity was measured on samples 1,4,5, and 6 following the prescription of Van der Pauw (Philips Research Report 13, 1-9 (1958), in which two "resistances" must be determined using 4 contacts around the margins of a parallel faced slab, plus the thickness of the slab. From measurements made amongst 6 contacts around the margins of sample 1 it was estimated that conductivity was established within  $\pm 2\%$  by this method. (Dr M Presland)

## Results

Under the microscope copper beads were evident on all of the samples. Although some appeared redder than others the copper XRD peaks were not shifted as might be expected if an alloy with another metal was present and it was concluded that this was probably a surface colouring effect such as tarnishing and not worth further investigation.

## SAMPLE 1

A lamination was evident along one edge of sample 1 which when broken open yielded a shiny flake. Three XRD analyses were performed of parts of the slab.

12242A     1 corner cut from area which was not laminated  
12242G     flake from lamination of 12242A  
12242H     laminated layer of 12242A

### 12242A

The sample is a mixture of several major components. The major components are  $\text{Ti}_8\text{O}_{17}$ ,  $\text{Ti}_6\text{O}_{13}$  and  $\text{Ti}_5\text{O}_9$ . Minor amounts of other suboxides could be present but have not been identified. Copper metal is also a minor compound.

### 12242G

This flake is composed of graphite.

### 12242H

This sample is a mixture of the following suboxides,  $\text{Ti}_6\text{O}_{11}$ ,  $\text{Ti}_5\text{O}_9$ ,  $\text{Ti}_7\text{O}_{13}$  and  $\text{Ti}_8\text{O}_{15}$ . The components are not in the same proportions as 12242A. Copper metal seems to dominate the XRD pattern.

## SAMPLES 2 & 3

12242B	2	$\text{TiCuO}_{1.8}$	#1009-1	900°C HP	SN164	1100°C HT 48hrs	Ar/H <sub>2</sub> bulk
12242C	3	$\text{TiCuO}_{1.8}$	#1009-2	900°C HP	SN164	1100°C HT 48hrs	Ar/H <sub>2</sub> bulk

Samples B and C showed extensive bloating with copper beads.

### 12242B

The sample is a mixture of titanium suboxides but the XRD pattern is dominated by copper metal. The following oxides are present in major proportions:  $\text{Ti}_6\text{O}_{11}$ ,  $\text{Ti}_8\text{O}_{15}$ ,  $\text{Ti}_7\text{O}_{13}$  and  $\text{Ti}_5\text{O}_9$ . There are other minor unidentified phases present.

### 12242C

The XRD pattern shows this sample to be very similar to 12242<sup>8</sup> with more of the  $\text{Ti}_5\text{O}_9$  phase being present.

#### SAMPLE 4

12242D     4  $\text{TiCuO}_{1.8}$  #988-1 1100°C HP     SN172 900°C HT 48hrs Ar/H<sub>2</sub> bulk

#### 14424D

The sample is mainly rutile ( $\text{TiO}_2$ ) and copper metal. There are some minor unidentified peaks present. These peaks do not appear to be any other known suboxides or copper titanium oxides and are not same as the other unknown phases previously reported. (12217) One minor phase was tentatively identified as tenorite ( $\text{CuO}$ ).

#### SAMPLES 5 & 6

12242E     5  $\text{TiCuO}_{1.8}$  #1009-1 900°C HP     SN172 900°C HT 48hrs Ar/H<sub>2</sub> bulk  
12242J     flake of 12242E  
12242F     6  $\text{TiCuO}_{1.8}$  #1009-2 900°C HP     SN172 900°C HT 48hrs Ar/H<sub>2</sub> bulk  
12242K     laminated layer of 12242F

Samples 5 and 6 exhibited extensive surface lamination. A flake  $\approx 0.5\text{mm}$  thick was sampled from the surface of 5. A triangular crack pattern was evident at the edges of sample 6 and this was cut off and analyzed as K. A cavity was evident in the centre of 6 although there was only slight surface evidence of bloating.

These four samples 12242E, J, F and K have the same XRD pattern as <sup>SAMPLE 4</sup> 12242D with increasing amounts of copper metal in that order.

Please note that in the samples that contain a mixture of suboxides there are many peaks and therefore peaks from small quantities of copper titanium oxides and iron titanium oxides could be masked.

#### Conductivities

These were measured on the slabs remaining after the XRD samples were removed.

IRL Sample Code	Atraverda Code	Sample Thickness mm	Conductivity $\text{S.m}^{-1}$
12242A	1	3.14	4460
12242D	4	3.10	610
12242E	5	8.67	3400
12242F	6	8.59	2190

**APPENDIX F - R. L. Clarke, Technical Letter to Hughes, HAC  
P.O.# S9-333846-SVX, Rev. A Dextra Assoc.,  
Orinda, CA, 30 March 1992.**

## Dextra Associates

74 Muth Drive, Orinda, CA 94563  
Tel 510 254 7642 or 2335 Fax 510 254 8451

Dr. M. N. Gardos  
Hughes Aircraft Company  
Materials Technology Laboratory  
Electro-Optical & Data Systems Group  
Bldg E1, MS F150  
PO Box 902  
El Segundo, CA 90245

Reference: Purchase Order S9-333846-SXX

### Report on the second series of Carcom experiments to make metal stabilized Magnèli phase titanium sub oxides

Samples tested by XRD and microscopic examination at DSIR on the 27th March 1992. The findings on the following samples are as follows:

#992-2 as hot pressed	rutile
# 992 air high temp	rutile
# 992-2 argon High temp	rutile
# 992-3 as hot pressed	Ni Ti O <sub>3</sub>
# 992-3 air High Temperature	Ni Ti O <sub>3</sub> trace
# 992-3 argon high temp	Rutile throughout
#992-4 iron series as hot pressed	see report
# 992-4 iron as air treated	FeTi <sub>3</sub> O <sub>5</sub> as minor
# 922-4 iron argon treated	Fe Ti 3O <sub>5</sub> as major

Note: BN83/1 to BN83/9 inclusive are the sample numbers assigned to the samples and identify the XRD plots which will follow shortly. These are coming as hard copies rather than faxes and they will be on the same scale so overlays can be used in further analysis.

BN83/1 TiCo O<sub>1.8</sub> # 992-2 as hot pressed material.

The sample was an even grey color, when ground up it revealed a grey -green colored powder. The major component is rutile titanium oxide with a minor amount of cobalt titanium oxide, Ti Co O<sub>1.8</sub> which is a dark green colored compound.

BN83/2 Ti Co O<sub>1.8</sub> #992-2 air at high temperature SN111

The block varied in color and when ground gave a deeper green colored powder than the hot pressed material. XRD indicates the major component is rutile with a minor amount of cobalt titanium oxide present at a level greater than in the hot pressed sample above.

BN 83/3 TiCoO<sub>1.8</sub> High temperature treatment in argon

The block was an even grey color with a metallic skin on one end. the major component is rutile together with both cubic and hexagonal forms of cobalt metal. Both forms normally exist at room temperature.

BN83/4  $\text{TiNiO}_{1.8}$  # 992-3 as hot pressed

When split open the block was found to have a grey to gold color change across the smallest dimension. The block was sampled in two places, a grey fraction(sample 83/4A) and a gold fraction (sample BN83/4B)

Sample A-----Grey

The major component is rutile with a minor amount of free nickel metal and a trace of nickel titanium oxide(  $\text{NiTiO}_3$ ) a yellow compound.

Sample B-----Gold

The sample again has a typical rutile structure as the major fraction but with the nickel titanium oxide and nickel metal as minor components. The gold colored sample was richer in  $\text{NiTiO}_3$  than sample A.

BN83/5  $\text{TiNiO}_{1.8}$  #992-3 Air at high temperature SN111

The sample was mainly gold in color( sampled as BN83/5 with one end having a grey core(BN83/5B). A green and grey skin was observed at one end.

BN83/5 Body

The sample is composed of rutile as the major component and nickel titanium oxide as a minor component. No free nickel was observed.

BN83/5 B --Grey core

The major component is again rutile with free nickel as a minor component. A trace amount of nickel titanium oxide was observed.

BN 83/6  $\text{TiNiO}_{1.8}$  #992-3 argon at HT SN110

The block was grey throughout. The sample contained rutile as the major component and free nickel metal as a minor component.

BN83/ 7  $\text{TiFeO}_{1.8}$  # 992-4 as hot pressed

The block was grey in color and was ground down to a grey /brown powder.

The major component is rutile, with ilmenite( $\text{FeTiO}_3$ ) and an unidentified material as a minor component and a trace of free metal. The XRD pattern of the unidentified material is similar to pseudobrookite ( $\text{Fe}_2\text{TiO}_5$  a brown compound). A solid solution series exists between  $\text{Fe}_2\text{TiO}_5$  (pseudobrookite) and  $\text{FeTi}_2\text{O}_5$ . and has been reported to extend to very low iron content e.g.  $\text{Fe}_{0.05}\text{Ti}_{2.95}\text{O}_5$ . From comparison with other metal titanates (illustrated with BN83/9) we can estimate the unknown minor component to have an orthorhombic structure with the formula  $(\text{FeTi})_3\text{O}_5$ , where the iron content may not be easy to estimate-see below.  $\text{Fe}_2\text{TiO}_5$  (Pseudobrookite) represents the highest possible iron content in this structure.

BN83/8  $\text{TiFeO}_{1.8}$  #992-4 air at HT SN111

The sample was a grey /brown color with a thick crust at one end.

BN83/8 body

The sample contains rutile, the major component, and an  $(\text{FeTi})_3\text{O}_5$  as a minor component. Small shifts in the position of some peaks may suggest that iron content in this component is slightly different from that in BN83/7. No free metal or ilmenite is observed in this sample.

BN83/8B ---Crust

Very similar to BN83/8 but with a higher amount of  $(\text{Fe Ti})_3\text{O}_5$  present.

BN83/9  $\text{TiFeO}_{1.8}$  #992-4 argon at high temperature SN110

The block varied in color from grey to brown.

The sample contains rutile, ilmenite and a  $(\text{FeTi})_3\text{O}_5$  all as major components and a trace of free iron. Small shifts in some of the peaks may suggest that the iron content in the  $(\text{FeTi})_3\text{O}_5$  is slightly different from that in BN83/7.

Please note that the value of the iron content of the  $(\text{FeTi})_3\text{O}_5$  component may not be the same for the three samples but as there does not seem to be an XRD pattern recorded for the  $\text{FeTi}_2\text{O}_5$  and other work has been reported in obscure (eg Russian) journals it would require some investigation to quantify the extent of difference in terms of iron content.

#### Conclusion

The iron titanium oxides are interesting for a variety of reasons. DSIR want to study the valence state and site symmetry with a Mossbauer technique. This may be the basis of a joint paper. Initially they will look at BN83/8. The sample BN83/9 has produced the largest amount of new materials.

21 de laube  
March 30<sup>th</sup> 1992.